

BIOCHEMICAL THERMODYNAMIC MODELLING OF
CELLULAR BIOENERGETICS: A QUANTITATIVE
SYSTEMS PHARMACOLOGY APPROACH

ROSS KELLY

A thesis submitted in partial fulfilment of the
requirements of Liverpool John Moores University for
the degree of Doctor of Philosophy

This research programme was carried out in
collaboration with GlaxoSmithKline

September 2017

Acknowledgements

I would like to start by thanking Steve, Amy and Dom for giving me the opportunity to undertake this PhD, despite a truly awful interview. I would like to thank Dom again for leaving, for without which, I would have never been able to fall in love with Matlab. Thanks also to the BBSRC and GSK for funding this work.

To my supervisory team - Steve, Amy, Joe and Andy – you have all made this a fantastic experience. I certainly won the supervisory lottery with you four. Thank you Amy for your guidance with the experimental work and writing. Thank you Joe for giving up your time to be a part of this project, especially your keen eye for mathematical detail. To Steve – I simply cannot thank you enough for your encouragement, patience, and commitment to developing me as a researcher. Your presence over the last three years transcends academia, rather, you have helped me grow as a person too. I will sorely miss our weekly meetings with Joe. Additionally, I would like to thank Carol for her support in the lab, and Dom for his help with the uncertainty quantification.

To team Webb lab – Dazza, Jonny, Chantelle, “Big papa Sned-dog” and Terry. You guys have made life here beyond enjoyable and I cannot remember a time I did not wish to come to work. I am very lucky to have you all in my life. I must thank my mates from UoL: Jo, Agnès, Harriet, Ali, Abby, Amy, Oisin Jimmy and Jon. I will always miss our lunches together, especially the broad topics of conversation. When I think of Liverpool, I will always think of hockey, especially the Engineers. To Tess, Mol, Hat, Sean and Stan. P&F. Special thanks to Darren for putting up with me as a housemate, we have had some great times and watched some great shows. To Brendan - you’ve helped more than you could imagine, always a good listener. To Hudson – thanks for helping me de-stress at golf. To Nat – thank you so much for your love and support, especially during the last few months. I couldn’t have done it without you.

To my family, Emma and Mum. I would not be the person I am without either of you. Your love and encouragement have kept me going over the last 3 years. To mum – thanks for looking after me while I wrote up this thesis (especially the food). I dedicate this thesis to you.

Abstract

In this thesis, thermodynamic-based mathematical modelling is combined with experimental *in vitro* extracellular flux analysis in order to assess drug redox cycling and cellular bioenergetics. It is widely accepted that pharmacological activity of certain classes of drugs (e.g. anticancer, antimalarial) is related to their ability to accept one or two electrons. However, pharmacological activity via redox cycling is an understated mechanism of toxicity associated with many classes of drugs. In particular, oxidative stress as a result of redox cycling plays a pivotal role in the cause of cardiac toxicity. For example, doxorubicin is an anti-neoplastic drug used to treat cancer. It has strong links to redox cycling-induced cardiac toxicity associated directly with elevated levels of reactive oxygen species (ROS) and oxidative stress within the mitochondria. The underlying mechanisms of redox cycling is very difficult to elucidate, due to the fleeting existence of the radical species. However, assessment of such cellular bioenergetics can be ameliorated with the aid of computational assistance. In chapter 2 the development of a novel thermodynamic-based *in silico* model of doxorubicin redox cycling is described, which is parameterized using data from *in vitro* extracellular flux analysis. The model is used to simulate mitochondrial-specific ROS, with its outputs confirmed against *in vitro* data. Chapter 3 describes construction of a pH-dependent thermodynamic model of hepatic glycolytic flux, used to determine the role of the monocarboxylate transporter 1 flux during extracellular acidification. Finally, chapter 4 describes a thermodynamic-based *in silico* model of mitochondrial bioenergetics, capable of simulating oxygen consumption rates of a cohort of *in vitro* human primary hepatocyte data. The model is finally used to simulate perturbations in key bioenergetic variables and reaction fluxes, illustrating the resulting changes on mitochondrial pH, membrane potential and subsequent oxygen consumption rates.

Contents

1	Chapter 1: General Introduction	7
1.1	Background	8
1.1.1	Quantitative Systems Pharmacology	8
1.1.2	Redox Cycling	9
1.1.3	Redox Cycling Pharmacology & Toxicity	13
1.1.4	Reactive Oxygen Species (ROS) & Bioenergetic Relationship	15
1.1.5	Biochemical Thermodynamics	16
1.1.6	Cellular Bioenergetics	21
1.2	Methods	27
1.2.1	Biochemical Simulation Environment (BISEN)	27
1.2.2	Extracellular flux analysis (EFA)	32
1.2.3	Mitochondrial Superoxide (MitoSOX) Assay	34
1.2.4	Cell Viability Assays – MTT & ATP	35
1.2.5	COSSAN: Sensitivity Analysis	36
1.2.6	Principal Component Analysis & Multinomial Logistic Regression	38
1.3	Pharmacological & Mathematical Motivation	39
1.4	Thesis Outline	40
2	Chapter 2: Modelling Redox Cycling: Model Formulation and Development	42
2.1	Chapter Aims	43
2.2	Mathematical Modelling	43
2.2.1	Quinone Physicochemical & Thermodynamic Model	43
2.2.2	Preliminary Redox Cycling Model	49
2.2.3	Stability Analysis	52
2.2.4	Preliminary Simulations	54
2.3	<i>In vitro</i> Biochemical Redox Cycling	55
2.3.1	Novel EFA Redox Cycling Assay Development	56
2.3.2	EFA Redox Cycling Results & Discussion	58
2.4	<i>In silico</i> – <i>in vitro</i> Model Coupling & Model Expansion	62
2.4.1	Initial Model Fitting	62
2.4.2	Expanded model fitting & stability analysis	66
2.4.3	Sensitivity Analysis	71
2.4.4	Superoxide Detoxification Expansion	73
2.4.5	SOD & ROS Scavenging Expansion	74

2.5	Model predictions & Experimental Validation.....	81
2.5.1	Doxorubicin-Induced Mitochondrial Superoxide Formation.....	81
2.6	Chapter Discussion.....	89
3	Chapter 3: Modelling Cellular Bioenergetics: pH-Dependent Thermodynamic Model of Human Hepatic Glycolytic Flux	92
3.1	Introduction	93
3.2	Mathematical Modelling.....	95
3.2.1	Current Models	95
3.2.2	Pathway Selection	97
3.2.3	Initial Model Construction	100
3.2.4	Preliminary Simulations & Model Development	116
3.2.5	<i>In silico</i> ECAR Simulation	126
3.3	<i>In vitro</i> Hepatocarcinoma ECAR.....	130
3.3.1	Methods	130
3.3.2	Extracellular Flux Analysis Results	132
3.3.3	EFA Media Buffering Power & PPR _{gly} Calculation	133
3.4	<i>In silico</i> – <i>In Vitro</i> Coupling & Sensitivity Analysis.....	136
3.4.1	Sensitivity Analysis	136
3.4.2	Model Parameterization: Cytoplasm Lactate Content	139
3.4.3	Model Validation: Simulating EFA PPR _{gly} & ECAR	140
3.5	Model Predictions	144
3.5.1	The Effects of Extracellular Glucose, Lactate and pH Perturbations on ECAR and PPR _{gly}	144
3.5.2	The Effects of Extracellular Glucose Concentration on Energy Metabolism	145
3.5.3	Suitability of Using MCT1 Flux to Simulate ECAR & PPR _{gly}	147
3.6	Chapter Discussion.....	149
3.6.1	Conclusion	149
4	Chapter 4: Modelling Cellular Bioenergetics: Human Hepatic Mitochondrial Respiration	151
4.1	Introduction	152
4.2	Mathematical Modelling.....	154
4.2.1	Current Models	154
4.2.2	Current Model Construction	156
4.2.3	Preliminary Simulations	181

4.2.4	Modelling EFA OCR	193
4.3	Simulating Mitochondrial Respiration Stress.....	194
4.3.1	Primary Human Hepatocyte <i>in vitro</i> Mitochondrial Stress Test	194
4.3.2	<i>In silico</i> Mitochondrial Stress Test Simulations.....	199
4.4	Statistical Analysis	209
4.4.1	Patient Glycolytic Reserve Capacity.....	209
4.4.2	Multinomial Logistic Regression	213
4.5	Model Predictions	218
4.5.1	Bioenergetic Model Perturbations	218
4.6	Discussion.....	223
4.6.1	Chapter Discussion.....	223
5	Chapter 5: Discussion & Future Work	226
6	Chapter 6: Abbreviations.....	232
7	Chapter 7: Appendix.....	234
7.1	Appendix A	234
8	Chapter 8: Bibliography	241

1 Chapter 1: General Introduction

1.1 Background

1.1.1 Quantitative Systems Pharmacology

Quantitative systems pharmacology (QSP) is a term used to describe a relatively modern interdisciplinary scientific field that has presented itself at the forefront of biological, pharmacological and biomedical based research and development. There are many definitions for QSP. However, the majority tend to conform to a set of fundamental principles which lead to a personal definition based upon my own experience:

Quantitative systems pharmacology is the study of biological systems via the iterative integration of mathematical computational models with experimental techniques, in order to investigate drug pharmacology.

It is no coincidence then that as computational power has rapidly developed, so too has the prominence of systems pharmacology. Although greater computational power is pivotal for the prevalence of systems pharmacology, the true need for this flexible discipline is its ability to explore current experimentally derived knowledge of intricate biological systems by processing this information on a whole cell, network or systematic scale. Furthermore, mathematically probing such systems facilitate quantification and manipulation of often theoretical or inaccessible pharmacological scenarios. The benefits of which go much further than reduction of costs, by guiding experimentation, observing multiple outputs and providing valuable mechanistic insights.

QSP is an essential tool for assessing and predicting mechanisms of adverse drug reactions. The ability to quantitatively assess mechanisms of toxicity is a true accolade for this discipline. For example, measuring biological rates of reactions and the corresponding effects on a systems as a whole is arduous and often impossible. For example drug redox cycling is a common understated mechanism of toxicity, whereby a compound can spontaneously cycle between a reduced and oxidised state at the expense of cellular energy¹. The rate of these reactions can vary over 11 orders

of magnitude, leaving experimental observation an extremely difficult task based on the time scale of these processes alone. However, QSP can account for reactions occurring at such rates, while simultaneously providing a platform for exploration of the effects of such toxicity on a systemic level. QSP can be implemented on the investigation of xenobiotics in extremely complex biological situations, such as within the mitochondria.

1.1.2 Redox Cycling

Redox cycling can be defined as the continuous reduction and oxidation of a compound, moiety or system ². Fundamentally, this can be described on a chemical level as the cycling of single or double electron reduction and oxidations, where oxidation is a loss of electrons, and reduction is the gain of electrons. In the descriptions within this thesis, when describing movement of electrons, double headed arrows denote the movement of a pair of electrons, whereas a single headed or “fish hook” denotes the movement of a single electron. Similarly, once electrons have moved from one compound / moiety to another, a (-) sign indicates two electrons, whereas a (·) dot indicates a single electron or free radical. Note, each electron possesses a relative charge of -1.

1.1.2.1 Redox Cycling Chemistry: Quinones & Radical Species

Redox cycling is a chemical phenomenon associated with many classes of compounds, with the quinone moiety which we denote by (Q), arguably the most well-known ³. Quinones are some of the oldest organic molecules in existence, with traces found on interstellar dust observed on board the NASA spacecraft STARDUST ⁴. That said, it is then unsurprising to find that the quinone structure is not only present physiologically, but is crucial to our survival, playing a fundamental role in mitochondrial energy production in every cell by facilitating electron transfer ⁵.

The ability of the quinone moiety to redox cycle is governed by its ability to stabilize the addition and removal of an electron without deviation from its original structure. Figure 1-1 Shows the classic quinone triad, which includes two sequential single

electron reductions to form the semiquinone radical ($\text{SQ}^{\cdot-}$), and the fully reduced hydroquinone (H_2Q), illustrating how the quinone / quinol ring system remains unchanged.



Figure 1-1: Quinone redox triad. Sequential single electron reductions / oxidations yielding the Q/SQ/ H_2Q triad. Q, SQ and H_2Q are shown in blue, pink and red respectively. R_x describes ring substituents.

1.1.2.1.1 Electronic and Steric Effects, Redox Potential E° and the Nernst Equation

The ability to gain or donate electrons can be categorized into two areas: electronics and sterics ⁶. With respect to electronics, the ease of acceptance of an electron, and therefore reduction of the quinone, can be quantified by the half-cell reduction potential, otherwise known as the redox potential (E°), expressed in either volts (V) or millivolts (mV). E° is the standard reduction potential measured under standard conditions: temperature, $T = 25\text{ }^{\circ}\text{C}$, quinone concentration = 1.0 M, pH 0.0 when in aqueous solution and at a pressure of 100 kPa (0.986 atm). Standard reduction potentials are relative to a standard hydrogen electrode, which is used as a reference as it yields a potential of 0.0 V at all given temperatures ⁷. While this is useful in standard chemistry, it is desirable to describe a reduction potential at non-standard conditions, i.e. physiological conditions: pH 7.0, 37 $^{\circ}\text{C}$. Fortunately, the reduction potential can be described at non-standard conditions in terms of thermodynamics using the Nernst Equation (1-1), where R is the universal gas constant equal to $8.3144598\text{ J mol}^{-1}\text{ K}^{-1}$, T is the temperature in Kelvin, F is the Faraday constant equal

to $9.6485 \times 10^4 \text{ C mol}^{-1}$, n is equal to the number of electrons in the reduction reaction and Q_r is the reaction quotient for the half cell reaction equal to the ratio of the reduced and oxidised species ($[R]/[O]$). If \log_{10} is used rather than natural log, the Nernst equation can be described as Equation (1-2).

$$E = E^{o'} - \frac{RT}{nF} \ln Q_r \quad (1-1)$$

$$E = E^{o'} - \frac{59.1}{n} \log_{10} Q_r . \quad (1-2)$$

It is possible to confuse reduction and redox potentials when changing between chemistry and biological contexts. The term redox potential will refer to the reduction potential for non-standard physiological conditions (denoted $E^{o'}$ henceforth). With this understanding of redox and reduction potentials, it is possible to understand the relationship between redox potential and the likelihood of quinone reduction in terms of electronics.

The overall relationship follows that the more positive the redox potential, the more readily the reduction. Similarly, the more negative the potential, the harder reduction becomes. Like all chemical reactions, the proclivity for a reaction to proceed depends upon the stability of the products. In this instance, how stable is the resulting reduced forms SQ^- or H_2Q . The substituents on the Q or SQ^- ring system directly influence the redox potential in terms of electronics, depending on whether the group is electron donating (EDG) or electron withdrawing (EWG). Common EDGs such as alkyl groups donate electron density into aromatic systems. As a result, the addition of alkyl groups renders the quinone less electrophilic (electron accepting) and therefore harder to reduce. Consequently, the redox potential for a quinone with EDG substituents is expected to become more negative. Conversely, EWGs such as halides Cl or Br, remove electron density from aromatic systems thus increasing the Q or SQ^- electrophilicity. Subsequently, the redox potential tends to become more positive with increased EWG substituents, rendering the Q or SQ^- more readily reduced.

Figure (1-2) shows how the differences in electronics with respect to EWGs and EDGs affect the redox potential of a quinone.

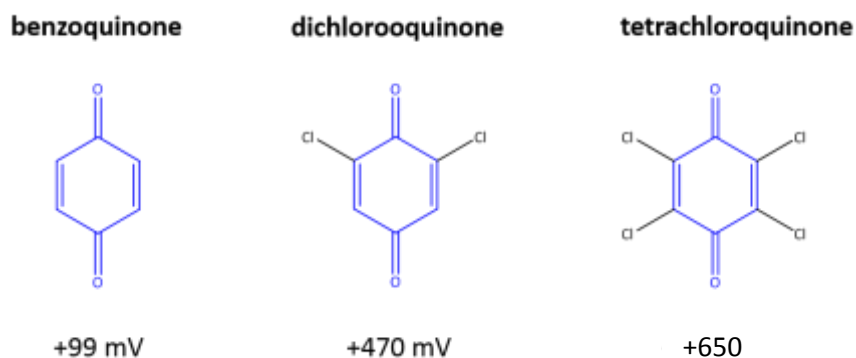


Figure 1-2: Increase in EWG (Cl) renders the E° more positive, more electrophilic and easier to reduce ⁷.

EWGs and EDGs form the majority of the electronic considerations with respect to redox cycling, illustrating how changes in the electronic configuration effects the electrophilicity of a quinone and thus its ability to be reduced or oxidised. Another aspect to consider when analysing factors that dictate whether a chemical reaction will occur is steric effects. Steric effects are the term given to describe the physical chemical space around the molecule and the subsequent effects these have on the proclivity of a successful chemical reaction. Steric effects can be further categorized: steric hindrance (or buttressing effects) and steric shielding. With respect to a quinone, Figure 1-3 illustrates how large groups bonded around the aromatic ring sterically hinders access of an impending nucleophile, thus showing the importance of the physical chemical space of a compound and its ability to react with other compounds.

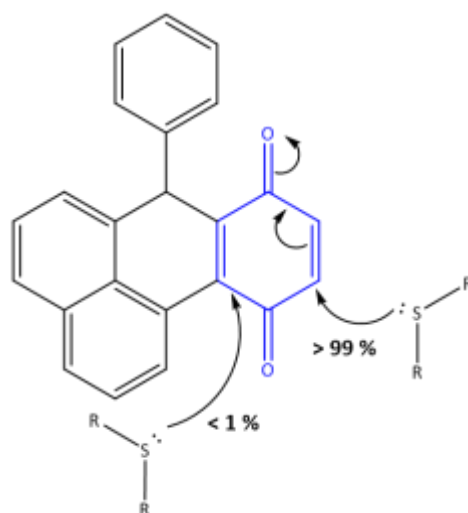


Figure 1-3: Thiol Michael addition at two quinone sites showing relative percentage chance of successful addition dependent on sterical hindrance.

1.1.3 Redox Cycling Pharmacology & Toxicity

1.1.3.1 Redox Cycling Toxicity

Pharmacological activity of many classes of compounds is hinged on their ability to accept one or two electrons ^{8,9}. The need for compound activation via generation of a radical species prompts the formation of unwanted reactive metabolites, mitochondrial toxicity, ROS and futile redox cycling, occurring at the expense of cellular reduction power ¹⁰. The predominant cause of toxicity due to redox cycling compounds rests on their tendency to generate ROS causing oxidative stress, through single electron reduction of molecular oxygen to form a superoxide radical ($O_2^{\cdot-}$), followed by dismutation into hydrogen peroxide (H_2O_2) ^{11,12}. ROS are generated at multiple sources including cytokine activity, NADH/NADPH oxidase, uncoupling of mitochondrial electron transport ¹³. It is no surprise then that redox cycling induced ROS formation is common at sites of high oxygen concentration such as the mitochondria, which also provide a source of electrons for the redox cycle ¹⁴. The quinone motif is arguably the best defined in terms of redox cycling and its associated toxicity and is rightly considered a structural alert ³. A common quinone motif containing redox cycling compound is the anthracycline antibiotic doxorubicin ¹⁵. Doxorubicin is used in a myriad of chemotherapy regimens to treat both

haematological and solid tumours via DNA intercalation, inhibiting topoisomerase II-dependent regulation of double strand breakage¹⁶. Despite its therapeutic purpose, doxorubicin-induced cardiac toxicity is associated with a host of mechanisms: free radical formation, lipid peroxidation, mitochondrial dysfunction and DNA damage to name but a few. Despite this, substantial evidence supports doxorubicin-induced oxidative stress due to redox cycling as the frontrunner in clinically relevant cardiotoxicity. Doxorubicin ROS generation follows the same principals as generic quinone redox cycling, reduction of the doxorubicin quinone motif, facilitated by mitochondrial reductases, yields a semiquinone radical¹⁷, which in turn reduces molecular oxygen forming $O_2^{\cdot-}$ and H_2O_2 while simultaneously reforming the parent doxorubicin¹⁸. Mitochondrial based doxorubicin induced toxicity can be attributed to the high affinity between doxorubicin and the mitochondrial phospholipid cardiolipin, which is located in the inner mitochondrial membrane, playing a major role in mitochondrial structure, function and energy metabolism¹⁹. Cardiac cells are amongst some of the most mitochondria rich cells within the body, consequently, disproportionate amounts of doxorubicin accumulate in the mitochondria, elevating ROS levels, prompting disruption to bioenergetics and subsequently toxicity^{20,21}. This rational can be applied to any mitochondria rich tissue, or cells that utilise mitochondrial bioenergetics as the predominant source of cellular ATP²².

1.1.3.2 Biological Redox Cycling Systems

Biological redox cycling systems fall into three main categories: glutathione redox systems, thioredoxin systems and the pyridine nucleotide system²³. Each of these systems is crucial for cellular homeostasis, with perturbations in them leading to possible cell death.

Glutathione (GSH) is a unique tripeptide that is invulnerable to peptidase cleavage due to its γ -type structure (L- γ -glutamyl-L-cysteinyl glycine). As a result, GSH is a stable molecule with multiple biological responsibilities. For example, GSH serves predominantly as a ROS antioxidant/scavenger, with an affinity to react with electrophiles, ROS and reactive nitrogen species (RNS) alike²⁴. Its thiol chemistry

allows GSH to exist in both a reduced (GSH) and oxidized (GSSH) form, thus completing its own redox cycle system. According to the Nernst Equation (1-1), the reduction potential for most cell types ranges from -150 to -260 mV for the GSH redox couple ²⁵. GSH itself acts as an antioxidant, mopping up ROS and radical species by working in concert with other redox couples such as NAD-NADH, contributing to the overall redox-status of the cell ²⁶.

The pyridine nucleotide (PN) redox couple is inextricably linked to the GSH couple and consequently plays a role in cellular defence against radical species and ROS. The pyridine nucleotide system describes the relationship between reduced and oxidized nicotinamide adenine nucleotide in its non-phosphorylated and phosphorylated form (NADH/NAD⁺ and NADPH/NADP⁺). The PN is essentially the linchpin in maintaining re-reduction of GSSG into useful GSH, with a reduction potential of 400 mV, it provides the electrons necessary to complete the cycle ²³. Together, the GSH couple and PN couple are the foundation for cellular redox status and subsequently anti-oxidative stress defence.

1.1.4 Reactive Oxygen Species (ROS) & Bioenergetic Relationship

Reactive oxygen species (ROS) is a collective term that describes oxygen derived free radical species. ROS play a fundamental role in cell signalling under normal physiological conditions. Consequently, cellular ROS homeostasis is tightly regulated by highly specialized ROS scavenging systems such as superoxide dismutases (SODs), glutathione turnover and general antioxidants ²⁷. Like many biological metabolites, ROS serve as a double edged sword, capable of initiating damage to cells and their organelles, leading to much more severe pathologies including cancer, pulmonary hypertension, heart failure and retinopathy ¹⁴. All of these potential toxicity outcomes depend on several factors: ROS location, ROS radical type and potential obstructions to detoxification such as enzymopathies. The most common ROS cascade has already been eluded to: conversion of molecular oxygen to hydrogen peroxide via superoxide radicals, with processes that uncouple electron transport being a major contributor to the production of ROS ²⁸.

A strong link exists between cellular bioenergetics and ROS, with the mitochondria responsible for the vast majority of ROS formation, specifically from complex I and complex III of the electron transport chain. Approximately 1-2% of all oxygen consumed in the mitochondria is converted into $O_2^{\cdot-}$ which in the presence of metal ions can be converted into the highly reactive hydroxyl radical ($\cdot OH$) through Fenton chemistry²³. Elevated mitochondrial ROS and radical species is known to result in deleterious effects such as MtDNA damage and consequently cell death²⁹. Over 10 different potential mitochondrial ROS forging systems are known, including tricarboxylic acid cycle enzyme α -ketoglutarate dehydrogenase and pyruvate dehydrogenase³⁰. Pharmacological agents that induce ROS, such as redox cycling compounds, have the potential to yield mitochondrial toxicity. Importantly, experimentally assessing redox cycling is very difficult owing to the fleeting existence of radical species, particularly in a biochemical environment, as radical species are recycled back to their original structures as part of cellular redox protective mechanisms.

1.1.5 Biochemical Thermodynamics

1.1.5.1 Thermodynamic Definitions and Concepts

Thermodynamics is a branch of physical chemistry used to describe and understand relationships of multiple forms of energy. This field may be applied in terms of chemical thermodynamics, where concepts such as temperature, chemical potential, free energy and entropy are utilised, or applied to understand transportation and transformation of mass and transduction of free energy.

Thermodynamics are defined by four laws:

0. If two systems have the same temperature as the third, then they have the same temperature as one another
1. The total energy of an isolated system is conserved
2. The entropy of an isolated system does not decrease

3. The minimal entropy of a system is achieved at the temperature of absolute zero.

The zeroth law describes an empirical definition of temperature with respect to the thermal equilibrium of multiple systems, used to decide whether two systems are at equal temperature without bringing them into contact.

The first law of thermodynamics describes essential energy conservation, whereby energy may be converted from one form to another, but is unable to be created or destroyed. This allows the description of a closed thermodynamic system (i.e. it does not exchange any matter with its surroundings, nor is subject to any external forces), whereby the internal energy is equal to the difference between the heat supplied to the system, and the amount of work by the system on its surroundings.

The second law of thermodynamics states that heat energy cannot spontaneously move from a system of low temperature to a system of higher temperature, without additional energy. It also introduces the term *Entropy* (denoted S), which is a thermodynamic quantity that represents the unavailability of a system's thermal energy for conversion into mechanical work. This is also more often referred to as *disorder*. The second law therefore may also describe that entropy always increases with time, meaning thermodynamic equilibrium is a state with maximum entropy.

Finally, the third law states that, as the temperature of a system approaches absolute zero, its entropy (disorder) approaches a constant. The third law may be best likened to the movement of water molecules at different temperatures. For example, at high temperatures, water may exist as a gas whereby its movement is free and essentially random (this may be considered as high entropy or disorder). As it cools, water molecules in the liquid phase move less freely and so the entropy of the system decreases. Finally, at low temperatures, water molecules in solid phase can no longer freely move but instead are only capable of vibrating within ice crystals, meaning lower entropy. If the water reached absolute zero, all molecular motion would cease, meaning a state of zero entropy.

While the laws of thermodynamics may seem abstract and somewhat excessive with respect to biochemical processes, it is the underlying relationships between heat, mass and energy that govern biochemical and biophysical processes ³¹.

1.1.5.2 Gibbs free energy and reaction spontaneity

Gibbs free energy, G , is the energy that can be used to perform work associated with a chemical reaction. The associated Gibbs free energy of a reaction (ΔG) measured in Joules (J), is described in Equation (1-3):

$$\Delta G = \Delta H - T\Delta S , \quad (1-3)$$

where ΔH is enthalpy change (heat change, measured in J), T represents temperature in kelvin (K) and ΔS represents entropy change measures in J/K. This equation can be described in terms of standard-state conditions, which is much more useful for biochemical investigation. Namely, Equation (1-4) describes Gibbs free energy of reaction for standard conditions (ΔG^0):

$$\Delta G^0 = \Delta H^0 - T\Delta S^0 , \quad (1-4)$$

where standard conditions are assumed, namely: $T = 298.15$ K; partial pressures of gasses, (1 atm); and concentration of aqueous solutions are 1 M.

Gibbs free energy of reaction can be used to determine the spontaneity of a biochemical reaction by calculating the change in free energy that occurs when a compound is formed, otherwise known as Gibbs free energy of formation, ΔG_f^0 . Equation (1-5) describes the standard free energy of a reaction from the corresponding standard-state free energies of formation.

$$\Delta G^0 = \Sigma \Delta G_{f\ products}^0 - \Sigma \Delta G_{f\ reactants}^0 . \quad (1-5)$$

The value for ΔG^0 coupled with the value for ΔH^0 , can be used to determine the reaction spontaneity. When $\Delta H^0 > 0$, the reaction is endothermic or consumes heat. When $\Delta H^0 < 0$, the reaction is exothermic or releases heat. This allows classification of a reaction based upon heat changes.

When $\Delta G^\circ > 0$, the reaction is endergonic or non-spontaneous. Conversely, $\Delta G^\circ < 0$, the reaction is exergonic or spontaneous. When $\Delta G^\circ = 0$, the reaction is at equilibrium.

The signs of ΔH° and ΔS° , relate thermodynamics to the likelihood of a reaction to proceed at standard conditions, namely:

- 1) If a reaction is favourable for both entropy ($\Delta S^\circ > 0$) and enthalpy ($\Delta H^\circ < 0$), then the reaction will be spontaneous at any temperature ($\Delta G^\circ < 0$).
- 2) If a reaction is unfavourable for both entropy ($\Delta S^\circ < 0$) and enthalpy ($\Delta H^\circ > 0$), then the reaction will be non-spontaneous at any temperature ($\Delta G^\circ > 0$).
- 3) If a reaction is only favourable for one of either enthalpy or entropy, then equation (1.3) must be used to determine spontaneity.

These relationships are fundamental to the biochemical processes that form cellular bioenergetics. Crucially, not all biochemical processes are spontaneous. In fact, many processes have $\Delta G^\circ > 0$ and therefore must be linked to other reactions with $\Delta G^\circ < 0$ in order to occur. Combined processes occur if the global ΔG° is less than zero. It is worth noting here that although this method allows the description of a processes occurrence, it does not describe the rate at which a process will occur. This concept is pivotal during cellular energy production.

1.1.5.3 Cellular Energy: Negative ΔG° of ATP Hydrolysis

Adenosine triphosphate (ATP) is a small molecule integral for the flow of cellular energy. Free energy is stored in this molecule in the terminal phosphate bond which may be released when hydrolysed, forming adenosine diphosphate (ADP) and inorganic phosphate (Pi) (Figure 1-4). Energetically, it is considerably unfavourable to add a phosphate group to ADP to generate ATP and as such, it is the very same energy that becomes available to do work once the terminal phosphate bond is broken. Ultimately, energy from food is stored in the terminal bond and is utilized by a plethora of cellular reactions including biosynthesis, transport mechanisms and

mechanical work. ATP is therefore commonly known as the energy currency of the cell.

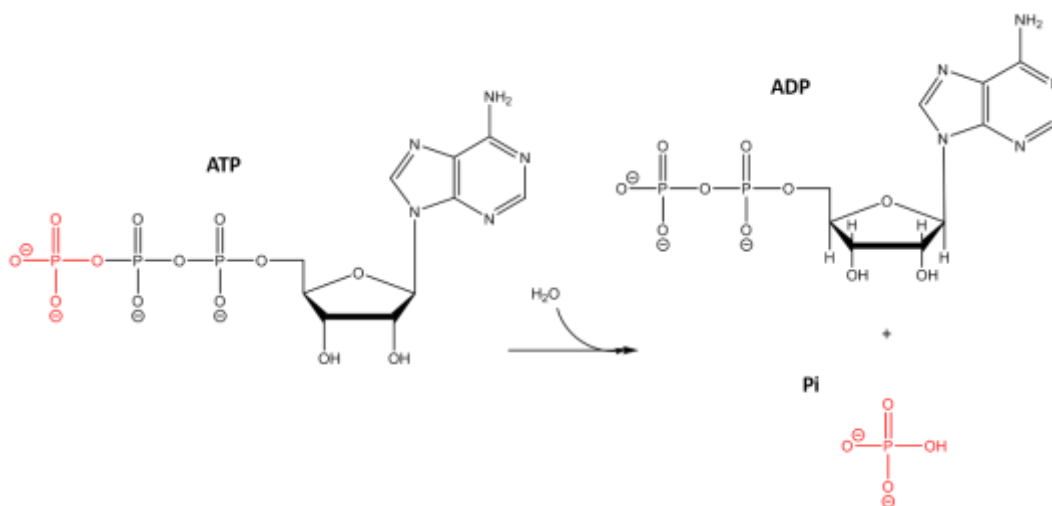


Figure 1-4: ATP hydrolysis. Terminal phosphate bond in ATP is cleaved by water to produce ADP and Pi. Sequential hydrolysis breaks further phosphate bonds until adenosine monophosphate (AMP) is left, releasing chemical energy stored in each of the bonds.

The Gibbs free energy change can be calculated for the ATP hydrolysis reaction: $\text{ATP} \rightleftharpoons \text{ADP} + \text{Pi}$, given for any reversible reaction the equilibrium constant, K_{eq} , is equal to the concentration of the products, divided by the concentration of the reactants, shown in Equation (1-6):

$$K_{eq} = \frac{[\text{ADP}][\text{Pi}]}{[\text{ATP}]}, \quad (1-6)$$

where ΔG^0 and K_{eq} are related by the expression:

$$\Delta G^0 = -RT \ln K_{eq}. \quad (1-7)$$

Equation (1-7) describes the free energy under standard conditions at equilibrium. However, cellular conditions are at neither standard conditions nor are the unit concentrations typically at equilibrium. Instead, calculation of the free energy of ATP hydrolysis under physiological conditions can be calculated using Equation (1-8). ΔG^0

for this reaction is approximately $-31.0 \text{ kJ mol}^{-1}$ ³¹ and so the free energy for ATP hydrolysis under physiological conditions is:

$$\Delta G = \Delta G^{\circ} + RT \ln K_{eq}, \quad (1-8)$$

where

$$\Delta G = -31.0 + 8314 \times 310 \ln[40 \times 10^{-6} \times 5 \times 10^{-3} \times 5 \times 10^{-3}],$$

giving

$$\Delta G = -57.1 \text{ kJ mol}^{-1}.$$

Cellular bioenergetics may be described thermodynamically as such, allowing precise quantification of movement of energy.

1.1.6 Cellular Bioenergetics

Having introduced ATP as the energy currency of the cell, as well as quantitatively describing the chemical energy stored within the phosphate groups using thermodynamics, it is appropriate to now describe the cellular mechanisms whereby ATP is generated: glycolysis and oxidative phosphorylation.

1.1.6.1 Glycolysis

Glycolysis describes the metabolic pathway that produces energy in the form of ATP via the utilization of glucose (schematic shown in Figure 1-5).

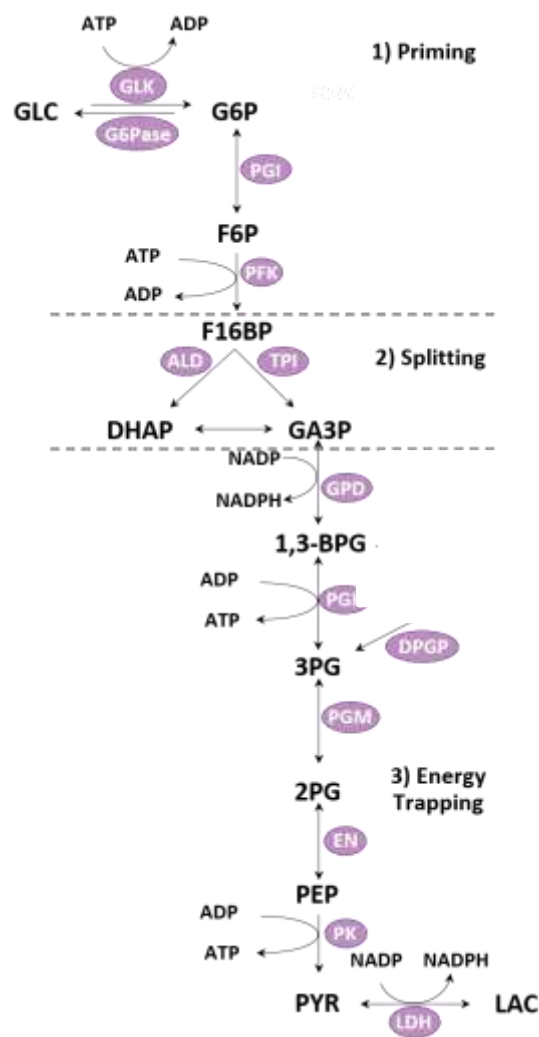


Figure 1-5: Schematic illustrating the catabolism of glucose into pyruvate and lactate with the concomitant generation of ATP. *Enzymes (Purple)*: GLK, Glucokinase ; G6Pase, glucose-6-phosphatase; PGI, Phosphoglucose isomerase; PFK, phosphofructokinase; ALD, aldolase; TPI, triosephosphate isomerase; GPD (GAPDH), glyceraldehyde-3-phosphate dehydrogenase; PGK, phosphoglycerate kinase; PGM, phosphoglycerate mutase; ENO, enolase; PYK, pyruvate kinase; LDH, lactate dehydrogenase. *Metabolites*: GLC, glucose; G6P, glucose-6-phosphate; F6P, fructose-6-phosphate; Pi, inorganic phosphate; F16P, fructose-1,6-phosphate; BPG, 1,3-bisphospho-glycerate; DHAP, dihydroacetone-phosphate; NAD, nicotinamide adenine dinucleotide [O]; NADH, nicotinamide adenine dinucleotide [R]; PG2, 2-phosphoglycerate; PG3, 3-phosphoglycerate; PEP, phosphoenolpyruvate, PYR, pyruvate; LAC, lactate.

Overall, the glycolytic pathway consists of twelve enzymes that catabolise glucose from a 6-carbon molecule to 3-carbon molecules that include pyruvate and lactate. Its primary function is to generate 2 x ATP molecules, 2 x NADH and 2 x pyruvate molecules, which are later processed to form a substantial amount of ATP via the tricarboxylic cycle (TCA) and oxidative phosphorylation. Glycolysis may be considered as three stages; priming, splitting and energy trapping. Priming includes the first three reactions, whereby glucose is trapped in the cell by phosphorylation. Splitting involves cleavage of glucose between carbon 3 and 4, which is achieved by the next two enzymes. Finally, the energy trapping process is completed by the final 6 enzymes of the pathway generating 4 x ATP molecules.

1.1.6.2 Oxidative Phosphorylation

Oxidative phosphorylation (OXPHOS) describes a two tiered process whereby ADP is phosphorylated in an aerobic fashion. Occurring within the mitochondria, OXPHOS is responsible for around 95% of ATP formation in animal cells and as a result, mitochondria are commonly referred to as the powerhouse of the cell ³². ATP is the cellular currency because of the free energy stored in the terminal phosphate bond, the very same bond formed during OXPHOS ³³. Consequently, phosphorylation of

ADP requires energy to occur, delivered by the respiration or oxygen consumption half of OXPHOS, rendering these two processes inextricably linked. OXPHOS occurs within the mitochondrial membrane, a highly specific membrane compared to most other cells that is highly specific with respect to passive permeations across it, allowing small weak acids, water-dissolved gasses and lipophilic compounds through, remaining impermeable to any charged ions, allowing passage only during participation in specialized transport proteins. It is this that gives the membrane its notorious and important potential ($\Delta\Psi_m$). This unique distribution of protons across the membrane, also known as the proton motive force, is the driving force of ATP synthesis linked together by chemiosmotic coupling

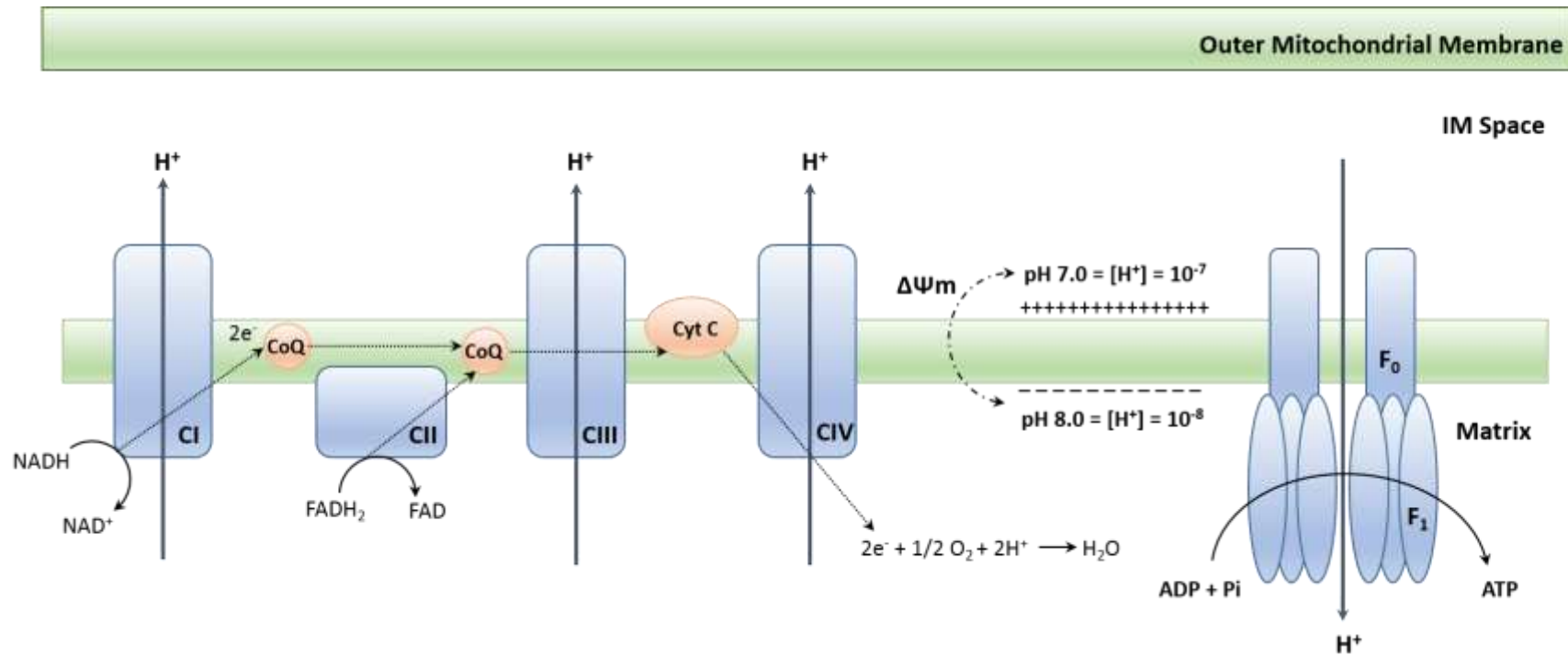


Figure 1-6: Schematic of the electron transport chain and oxidative phosphorylation. Dashed lines represent movements of electrons.

In physiological conditions the respiratory chain acts as a proton pump, catalysing electron transfer from reduced variables NADH and FADH₂ to terminal molecular oxygen, which serves as an electron dump at the end of the chain forming water (Figure 1-6). The concomitant electron flow through the electron transport chain results in a reduction of Gibbs potential. In other words, a large amount of free energy is released, of which the majority is used to pump protons from the matrix to the intermembrane space. The $\Delta\Psi_m$ reflects the unequal distribution of protons and is between -180 to -200 mV on the inside (matrix side) and positive on the outside. It is this very distribution of protons across two mitochondrial compartments with different pH values that forces ATP synthesis to occur, simultaneously driving protons utilising this free energy (Figure 1-6).

1.1.6.3 Warburg Effect

The majority of *in vitro* investigations centre around immortalized carcinoma cell lines due to their robustness and ability to be cultured for extended periods, as opposed to primary cell lines that are relatively short lived and difficult to manipulate. The compromise for this experimental reproducibility is a significant loss of functionality, particularly in hepatocarcinoma cell lines where prominent drug metabolizing enzymes such as the cytochrome (CYP) family have diminished expression³⁴. Nevertheless, immortalized cell lines are used for a large proportion of drug toxicity assays despite their caveats.

The use of cancer cells rather than primary cells presents another problem as they heavily rely on glycolysis as a source of cellular energy. The reason for this metabolic switch favouring glycolysis even in the presence of oxygen is still unknown³⁵. However, switching to “aerobic glycolysis” has been suggested to aid circumvention of several other difficulties. For example, increased cellular proliferation forming solid tumours can promote regions of hypoxia, hindering efficient oxidative phosphorylation. Oncogenic mutations facilitate increased uptake rates of glucose to such an extent that often there is surplus glucose with respect to cellular demands in the form of proliferation or bioenergetics. Although ATP energy demands are high in

proliferating cells, it is counterintuitive for proliferating cells to facilitate oxidative phosphorylation via the conversion of all glucose into CO₂ in order to maximize ATP production, as glucose is needed elsewhere in the cell. For example, aside from energy production, glucose is the primary source of carbon chains that are required to generate other essential macromolecules such as acetyl-CoA for fatty acids, ribose for nucleotides and other biomass. Up to 90% of glucose in carcinoma cell lines is converted into the waste product lactate. However, in doing so, the cell ensures a healthy turnover of NADH ³⁶.

When modelling hepatic glucose metabolism using a hepatocarcinoma cell line it is pivotal to understand the differences between the bioenergetics and driving forces of a primary cell line and that of an immortalized cell line. Primary liver cells will act to buffer extracellular / plasma glucose concentrations via the storage of glucose as glycogen by glycogenolysis. However, hepatocarcinoma cells will bypass this storage mechanism in favour of a more inefficient method of high rate glucose metabolism.

1.2 Methods

1.2.1 Biochemical Simulation Environment (BISEN)

Mathematically modelling large scale systems containing a large number of reactions or transporter processes is inherently difficult, time consuming and error prone ³⁷. The Biochemical Simulation Environment (BISEN) is a tool that generates sets of differential equations and associated computer programs for simulating biochemical systems within the Matlab software. BISEN considers “user-specified multi-compartment systems of enzymes and transporters accounting for the detailed biochemical thermodynamics, rapid equilibria of multiple biochemical species and dynamic proton and metal ion buffering” ³⁷. Such software alleviates the strains of error and inefficiency and is a powerful tool in the arsenal of any mathematical metabolic modeller.

1.2.1.1 Biochemical species and reactants

In order to describe how BISEN works, we must first make some definitions and distinctions. As such, for the duration of this thesis, conventional notation in biochemical thermodynamics will be adopted. First, we must distinguish between a biochemical species and a biochemical reactant. A biochemical *species* refers to a unique chemical compound such as ATP^{4-} , or Mg^{2+} . A biochemical *reactant* is a compound that is the sum of all its interconvertible biochemical species. For example, ATP is a reactant that represents its related species: ATP^{4-} , $HATP^{3-}$, $MgATP^{2-}$ etc. This distinction is important as it allows us to describe with greater clarity the ubiquitous nature of ATP. For example, in its fully dissociated form ATP exists as the ATP^{4-} species, carrying a net -4 charge. However, at a pH of ≈ 7 , ATP can exist in the protonated form $HATP^{3-}$. This is important when modelling changes in pH as BISEN allows computation of a dynamic proton / metal ion time course, also capturing the dynamics of a desired species at different ionic strengths, and the resulting changes on the overall pH and vice versa. For visualization, we can use the example of $HATP^{3-}$ dissociating to yield ATP^{4-} and H^+ , in a solution of ionic strength of ≈ 0.25 M with an acid-base dissociation constant of 6.47, where pK is $-\log_{10}K_{eq}$ and K_{eq} is the dissociation reaction equilibrium constant ³⁸.

The equilibrium expression is:

$$K_{eq} = 10^{-pK} = \frac{[ATP^{4-}][H^+]}{[HATP^{3-}]} . \quad (1-9)$$

Assuming the system is in equilibrium and the total concentration of ATP is equal to the sum of its protonated and unprotonated forms ATP^{4-} , $HATP^{3-}$, then

$$[ATP] = [ATP^{4-}] + [HATP^{3-}], \quad (1-10)$$

$$= [ATP^{4-}] + \frac{[ATP^{4-}][H^+]}{K_{eq}}, \quad (1-11)$$

$$= [ATP^{4-}] \left(1 + \frac{[H^+]}{K_{eq}} \right). \quad (1-12)$$

This then allows us to express molar fractions of ATP as

$$\frac{[ATP^{4-}]}{[ATP]} = \frac{1}{1 + [H^+]/K_{eq}} \quad \& \quad \frac{[HATP^{3-}]}{[ATP]} = \frac{[H^+]/K_{eq}}{1 + [H^+]/K_{eq}} \quad (1-13)$$

Equation (1-13) can be used to track the relative molar fractions of ATP as a function of pH, illustrating how the species fraction may vary as a result of a change in pH. (See Figure 1-7.)

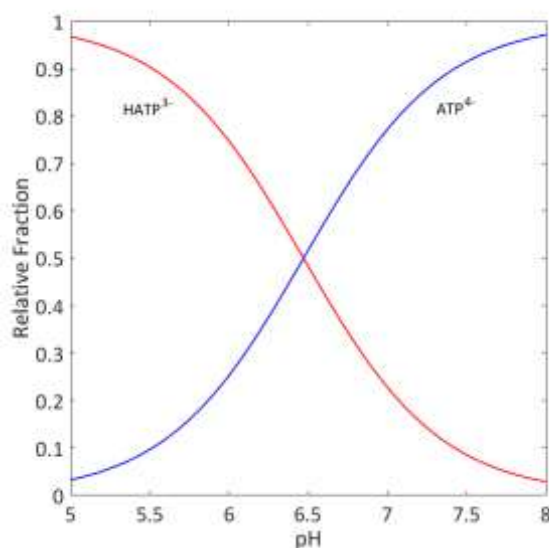


Figure 1-7: Molar fractions of ATP⁴⁻ and HATP³⁻ as a function of pH at pK= 6.7, generated using Equation (1-13).

The ability to have complete control over ionized fractions as a function of pH is crucial when modelling process that may change the pH of a system, as this in turn could alter the state of any species in a system depending on its pKa. Furthermore, when considerably different biological systems, such as the skin or the liver, or biological compartments, such as the cell cytoplasm or the mitochondrial matrix, one must be strict in assigning an accurate pH, as species or any compound will exist in a specific ionized state in these compartments and this may be the difference between an inhibitory or activating, efficacious or toxic effect.

1.2.1.2 Biochemical reactions

Having set out how BISEN treats biochemical species and reactants one can now describe how the suite uses this to describe a biochemical reaction. A chemical reaction that is stoichiometrically correct may be unbalanced in terms of mass and charge. For example, Equation (1-14) represents ATP hydrolysis with unbalanced charge and mass, whereas Equation (1-15) balances charge and mass:



Expressing biochemical equations in the format of Equation (1-15) allows BISEN to apply thermodynamics via the use of ΔG^0 . A complete description of how thermodynamics is incorporated into the system is better explained in Chemical Biophysics³⁸. Briefly, each biochemical equation has its own associated equilibrium constant and $\Delta_r G^0$ that is independent of pH, but dependent upon changes to temperature and ionic strength. Overall, this allows favourability of a reaction to change as a result of a pH change in an environment that has a finite buffer capacity³⁹.

1.2.1.3 Computing a dynamic pH time-course

Having discussed how BISEN treats reactants, species, biochemical reactions and the thermodynamics that surround them, one can use this information to describe their interactions with protons and metal ions to explain how BISEN computes a dynamic pH time course. pH is simply $-\log_{10}[H^+]$ and as a result, is a function of net changes in proton concentration within the system. Therefore, computing a pH time course using BISEN is achieved by accounting for total proton conservation between biochemical reactions and species-proton stoichiometry. The rate of proton consumption in a biochemical reaction is equal to the reaction flux multiplied by its associated proton stoichiometry. The dynamic buffer capacity of the system is also required and this is defined as the number of strong base equivalents in the medium⁴⁰. These are then used to calculate the rate of change of pH by applying this

calculation of proton consumption for all reactions simultaneously, divided by the medium buffer capacity. The rate of change of pH of a BISEN derived system is therefore a function of the sum of proton and metal cation binding with all biochemical species and the overall system buffer capacity.

1.2.1.4 BISEN model construction

In order to use BISEN to construct a pH-dependent thermodynamically driven model, the kinetic equations must be defined in an appropriate file (a BSL file) using the appropriate syntax to allow Matlab to construct a model. Each biochemical reaction or transporter BSL file is then used in a final BSL file which includes all global variables, compartment volumes and their corresponding water fractions, assignment of transporter and biochemical reactions to their corresponding compartment and which kinetic model term to use from each individual BSL file. Using the Glucokinase biochemical reaction BSL file as an example, each BSL file used to house a kinetic term must obey the following format.

```
model E.GLK.1
allosteric_reactants
fructose6phos

    equations
a = ATP;
b = glucose;
p = glucose6phos;
q = ADP;

Vmax_GLK = 0.0252;
KmGLC = 7.5;
KmATP = 0.26;
n = 1.6;
ngkrp = 2;
Kg1c_gkrp = 15;
bgkrp = 0.7;
Kf6p_gkrp = 0.010;

GLKfree = b^ngkrp / (b^ngkrp + (Kg1c_gkrp)^ngkrp) * (1 - bgkrp * fructose6phos

J = Vmax_GLK * GLKfree * a / (KmATP + a) * b^n / (b^n + (KmGLC)^n) ;

EOF
```

First, the model is defined. In this instance, the model is an enzyme kinetic term describing the Glucokinase (GLK) reaction. Multiple versions of this kinetic term are

allowed, but since in this case there is only one version, the notation E.GLK.1 is used. If another model of this enzyme were to be described in this file, the same format would be used but the model would be described as E.GLK.2 etc. This difference is used to distinguish which model of that biochemical reaction is used when BISEN constructs the model. Next, any allosteric reactants are defined under the simple syntax of allosteric-reactants before the equation. After this step, the kinetic term can be described including assignment of parameter values if known. If not, a parameter may be set to “unspecified” allowing later allocation once the model has been constructed in Matlab. BISEN is capable of calculating an equilibrium constant K_{eq} for a biochemical reaction using free energies assigned in an associated database. This is achieved by simply writing the equilibrium constant K_{eq} within the BSL file as K_{eq} . For a user specified value for this constant, the reaction abbreviation can be used as a suffix, for example K_{eq} becomes K_{eq_GLK} .

1.2.2 Extracellular flux analysis (EFA)

Assessment of cellular bioenergetics as a function of whole cell environments is measured via high throughput extracellular flux analysis (EFA) systems that monitor oxidative phosphorylation and glycolytic flux in real time. This is achieved by measuring mitochondrial respiration (oxidative phosphorylation) as cellular oxygen consumption rate (OCR) and glycolytic flux as extracellular acidification rate (ECAR). While OCR remains a robust well used output indicative of oxidative phosphorylation, the true source of ECAR is as yet relatively ambiguous ⁴¹. At present, lactic acid is considered responsible for the majority of ECAR. However, recent studies also show that respiratory acidification may also contribute via the generation of carbonic acid ⁴².

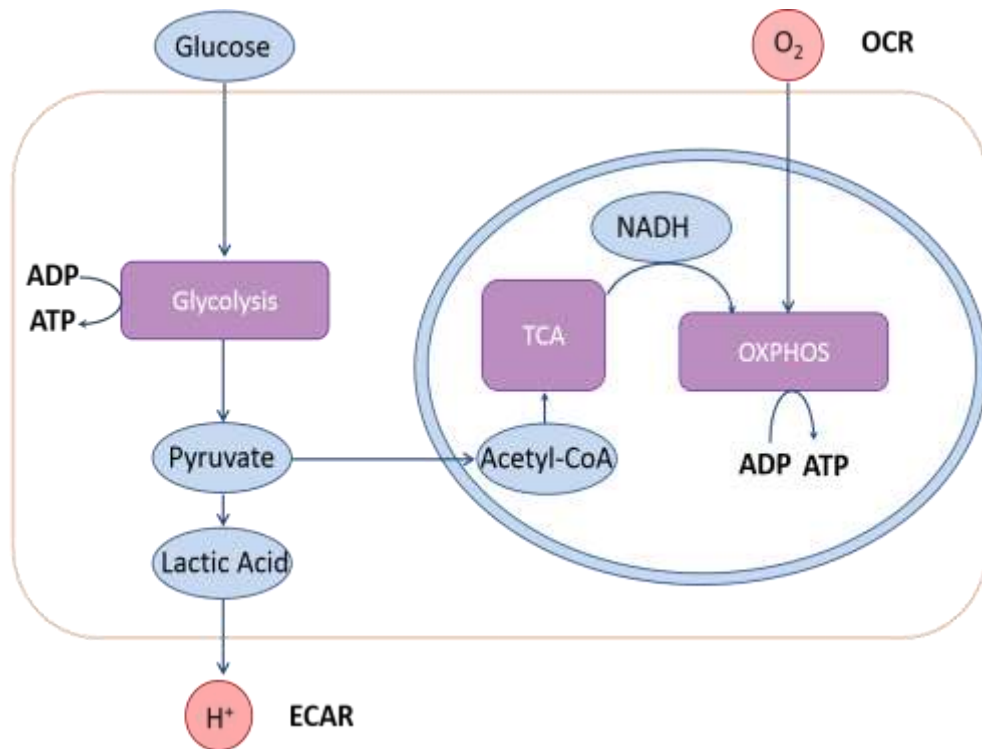


Figure 1-8: Schematic illustrating fundamental components of EFA, with particular emphasis on highlighting EFA outputs ECAR and OCR, as well as the link between the two bioenergetic systems.

Combining OCR and ECAR provides a powerful platform to assess cellular bioenergetics (a schematic of OCR & ECAR and their interactions is shown in Figure 1-8) with OCR and ECAR measurements. It is becoming ever easier to glean information about the underlying mechanisms of drug induced mitochondria toxicity, particularly with respect to oxygen flux⁴³. However, extracellular acidification rate (ECAR) measurements currently are utilized far less regarding cellular bioenergetics than their oxygen consumption counterparts. The nature of cellular ATP production lends credibility to the bias of OCR over ECAR measurements, as approximately 95% of cellular ATP is generated from oxidative phosphorylation in physiological scenarios⁴¹. However, during mitochondrial function impairment, glycolysis accelerates to counteract diminished ATP generation. In some cases however, this compensatory

process simply isn't enough to prevent eventual cell death⁴⁴. Nevertheless, glycolytic flux has been shown to play an important role in cellular bioenergetic homeostasis⁴⁵.

1.2.3 Mitochondrial Superoxide (MitoSOX) Assay

Detection of mitochondrial specific ROS or superoxide is achievable using a specialized fluoroprobe within the MitoSOX assay. This method offers selective detection within live cells that has been validated using confocal microscopy⁴⁶. This approach was used to quantify changes in mitochondrial superoxide / ROS levels after exposure to doxorubicin in order to test the redox cycling models ability to accurately predict organelle specific ROS levels based on thermodynamics. The results were obtained via the following method:

MitoSOX Assay: 5 μ l of MitoSOX reagent (1 μ M) was added to each well and incubated in the dark for 5 minutes. The supernatant was removed and retained before trypsinising the cells. Cells were re-suspended in the retained supernatant before centrifuged at 2000 rpm for 5 minutes. The supernatant was discarded and the cell pellet was re-suspended in HBSS (300 μ l) and then plated in duplicate (100 μ l) in a white flat-bottomed 96-well plate. Fluorescence was measured at an excitation and emission of 396 and 579 nm respectively using a VarioSkan flash plate reader. Cell lysates were prepared from the remainder of the sample using a sonic probe. Protein content was determined using a Bradford assay and all data was normalized to mg of protein/well.

Statistical Analysis: Data values are expressed as mean \pm SD. D'Agostino and Pearson Omnibus normality test was used to detect normality. One-way ANOVA and Dunnett's post-test were used to analyse all parametric data. Statistical analysis was conducted using Graphpad Prism 5 software.

1.2.4 Cell Viability Assays – MTT & ATP

There are many ways in which to detect and quantify cytotoxic effects of compounds on cells *in vitro*, measuring different biological outputs via different detection methods, including tetrazolium reduction, reazurin reduction, protease markers and ATP detection.

The MTT cell viability involves tetrazolium reduction and was the first homogenous cell viability assay developed for high throughput screening. MTT is a positively charged compound that readily penetrates viable eukaryotic cells and has been utilized in thousands of published research papers. Its mechanism of action is quantified via absorbance spectroscopy, where the tetrazolium moiety is reduced into a coloured formazan product. Viable cells convert MTT into this purple formazan product whereas dead cells do not. Exploitation of this factor allows easy quantification of cell viability ⁴⁷.

The ATP assay is an alternative cell viability probe, which measures ATP using firefly luciferase, with ATP having been accepted as a robust marker of viable cells. The ATP assay is the fastest assay to use, the most sensitive and is less susceptible to artifacts than alternative viability assays. Its output is luminescence, which is independent of an incubation step with viable cells whereby a metabolic process is required. The benefit of using two different methods to detect cell viability is minimization of uncertainty of the assay outputs ⁴⁷.

1.2.4.1 MTT & ATP Assay Methods

HepG2 cells (2×10^4) were plated in flat-bottomed 96-well plates in triplicate and allowed to adhere overnight.

MTT Assay: Cells were exposed to a range of concentrations of menadione and doxorubicin (0.005-100 μ M) and incubated for 24 hours. A solution of 3-(4,5-Dimethylthiazol-2-yl)-2,5-diphenyl-tetrazolium Bromide (MTT) in Hanks balanced salt solution (HBSS) was prepared (0.5 mg ml⁻¹) and 20 μ l was added to each well and incubated for a further 2 hours. Finally, 100 μ l of a lysing buffer (*N,N*-

dimethylformamide 50% v/v; sodium dodecyl sulphate 20% w/v) was charged to each well before further incubating for 4 hr. Samples absorbance's were measured at a test and reference wavelength of 570 and 590 nm respectively with a plate reader (MRX, Dynex).

ATP Assay: Cells were exposed to a range of concentrations of menadione and doxorubicin (0.005-100 μ M) and incubated for 24 hours. ATP content of the cells was measured using a Cell Titer-Glo kit following the manufacturer's instructions. 20 μ l of assay reagent was added to each well and shaken for 1 minute. 100 μ l from each well was then plated onto a white 96-well flat-bottomed plate and the luminescence was measured using VarioSkan flash plate reader.

1.2.5 COSSAN: Sensitivity Analysis

Mathematical modelling and simulation is widely applied alongside theory and experimentation during scientific research, with sophistication of model outputs increasing according to development of methods and computational power. That said, perhaps the greatest challenge in using such approaches is the inherent variability and uncertainty that comes from *in silico* modelling. Variability arises from the different sources of information used to construct a model which can be reduced, whereas uncertainty will always be prevalent since it is impossible to perfectly model absolutely everything or predict future outcomes for which there exists no experimental data. Quantification and understanding of model sources of uncertainty is therefore crucial for the credibility of model simulations. Sadly, uncertainty quantification within the biological and pharmacological community is still very much in its infancy, owing predominantly to the computationally intensive and often difficult methods required in order to investigate it. Fortunately, there are sophisticated toolsets available for quantification of uncertainty, with COSSAN arguably one of the best.

COSSAN is an open-source MATLAB based software used to quantify, mitigate and manage uncertainty and risk. The software was developed at the Institute of Risk and

Uncertainty at the University of Liverpool ⁴⁸. This toolset offers advanced algorithms for rational quantification and propagation of model uncertainties, specifically located within parameter selection. COSSAN is an efficient approach to facilitate the linking of deterministic codes with stochastic analysis. Its predominant operations include: uncertainty quantification (UQ), simulation-based reliability analysis, sensitivity analysis, meta-modelling, stochastic finite elements analysis (SFEM) and reliability-based optimization (RBO). These advanced methods allow construction of robust frameworks for the rational treatment of parameter uncertainties.

Sensitivity analysis is the investigation of how variation in the input of a mathematical model leads to uncertainty in its simulated outputs, either qualitatively or quantitatively. Mathematical models often rely on large parameter sets which have the proclivity to be imprecisely known. Moreover, multiple different parameter values or indeed a distribution of parameter values may elicit the desired simulated output. As such, it is important to grasp the relationship between parameter space and model output.

For assessing the uncertainty, sensitivity and quality of experimentally motivated model parameters, the COSSAN toolset can be implemented via the following methodology:

1. For each of the initial parameter estimates, define a parameter sample space by assigning a probability distribution to each parameter.
2. Generate multiple values for each parameter from each distribution using Latin Hypercube Sampling (LHS).
3. Evaluate the model at each combination of parameter values using Monte Carlo simulations and compare outputs to experimental data.
4. Reduce the difference between outputs and error with respect to the experimental data and hone an improved parameter set using a Nelder-Mead approach.

1.2.6 Principal Component Analysis & Multinomial Logistic Regression

1.2.6.1 Principal Component Analysis

Principal component analysis (PCA) is a statistical method that transforms a dataset of possibly correlated variables into groups of linearly uncorrelated called principal components, via an orthogonal transformation. By doing this, each principal component describes the variance sequentially for each dimension of data. This method is commonly used to elucidate strong patterns in dataset, making it easier to explore and visualize. For example, investigating a dataset with two dimensions such as time and concentration, these can be plotted in a plane. However, if it desirable to measure variation, PCA determines a new coordinate system, reducing two coordinate values into a single value for each data point. In doing so, this gives the new single axis scope to view greater variation. Similarly, for 3D situations with 3 sets of data, PCA analysis can be used to project this into a 2-dimensional space, by rotation of the axis. For higher dimensional data, obviously it is impossible to plot more than 3 dimensions, rather, each principal component is ranked, with the first principal component describing the highest variance, with each principal component following sequentially describing less variance.

PCA was used to visualise three sets of percentage change data for a 24 patient cohort of human primary liver cell samples, in order to discern any correlation between these changes and each patients reserve glycolytic capacity before statistical analysis using multinomial logistic regression.

1.2.6.2 Multinomial Logistic Regression

Multinomial logistic regression is a classification-based statistical method used to predict a nominal dependent variable given multiple independent variables, differing from binomial logistic regression by accommodating a dependent variable with more than two categories. For example, multinomial logistic regression can be used to understand which clinical biomarker, X, Y or Z, best describes an endpoint based on

age and length of compound exposure. This method allows both age and length of exposure be used to describe a classification, in this instance X,Y or Z.

1.3 Pharmacological & Mathematical Motivation

Redox cycling is an understated mechanism of toxicity that is associated with many classes of pharmaceutical compounds, ranging from anti-malarial to anti-cancer efforts. Often, efficacy of a compound depends on the ability for it to undergo a single or double electron reduction. The quinone motif is perhaps the most well-known redox cycling moiety and as such, is a structural alert. Doxorubicin is an anti-neoplastic compound that contains the quinone motif with strong links between redox cycling based cardiac toxicity associated specifically within the mitochondria. Unfortunately, detecting and quantifying redox cycling *in vitro* is extremely difficult owing to the fleeting existence of radical species. This prevents predicting this mechanism of toxicity from being easily detected during pre-clinical development of compounds. With the development of mathematical and computational methods, *in silico* representation of redox cycling and complex bioenergetics is achievable, especially when coupled with advanced versatile *in vitro* techniques such as extracellular flux analysis. Combining thermodynamic driven models that represent the fundamental properties of chemical and bioenergetic processes allows detailed mechanistic investigation into redox cycling and cellular bioenergetics, with particular emphasis on the *in vitro* methods used to assess them. To date, no mechanistic deterministic mathematical models of quinone redox cycling exist, nor for any *in silico* models of doxorubicin specific models capable of simulating a dynamic time-course of redox cycling induced ROS formation. With respect to cellular bioenergetics, *in silico* models do exist, however, they are undetailed and lack in mechanistic detail. Furthermore, ambiguity over the source of ECAR during EFA remains prevalent, despite the ability to differentiate between glycolytic and respiratory contributions to acidification. As such, a thermodynamic-based pH-dependent model of cellular bioenergetics would aid better understanding of glycolytic flux output during EFA, as well as lend credibility to ECAR as a valuable

experimental output. Finally, thermodynamic-based models of mitochondrial bioenergetics can be used to better understand the inhibition of electron transport chain complexes and dissipation of mitochondrial membrane potential by mitochondrial poisons. In better understanding these qualitatively compared to experimental data, and being able to accurately recapitulate the *in vitro* EFA representations *in silico*, allows mathematical and computational assistances in novel compound effects on mitochondrial bioenergetics, as well as current poorly understood ones.

1.4 Thesis Outline

Chapter 2 describes a novel thermodynamic-based *in silico* model of quinone redox cycling used to simulate doxorubicin induced ROS formation within the mitochondria. The model is coupled with a novel cell-free extracellular flux analysis assay whereby changes in pH are used to estimate kinetic model parameters. The model is used to successfully predict *in vitro* mitochondrial superoxide formation for 6, 16 and 24-hour data when considering cell viability.

With extracellular flux analysis used throughout this thesis to assess redox cycling and cellular bioenergetics, chapter 3 investigates the role of proton and lactate efflux in the role of extracellular acidification during EFA. The ambiguity over the true source of glycolytic derived acidification coupled with the underutilization of ECAR as an *in vitro* output, prompted the detailed thermodynamic-based pH-dependent model of hepatic glycolytic flux, which is the first of its kind with respect to liver enzyme kinetics capable of simulating a mechanistically accurate pH time-course. The model is validated against *in vitro* EFA data for hepatocarcinoma cells, while considering respiratory contributions to acidification via quantification of media buffering power. The model simulates changes in glycolytic flux as a function of perturbations in extracellular glucose concentration, simulating physiological, hyperglycaemia and hypoglycaemic conditions, showing a switch in monocarboxylate transporter 1 (MCT1) directionality, allowing the model to import lactate as a small

carbon molecule to be processed via gluconeogenesis in order to generate cellular energy ATP.

Finally, chapter 4 describes an *in silico* model of mitochondrial bioenergetics that includes oxidative phosphorylation, the tricarboxylic acid cycle, metabolite transport and passive permeations between three compartments, cytoplasm, intermembrane space and the mitochondrial matrix. The model is again thermodynamic-based and is used to simulate *in vitro* EFA oxygen consumption. The mechanistic detail of the model construction is used to investigate levels of inhibition of mitochondrial complex I, III, IV, V and $\Delta\Psi_m$ as a function of exposure to Rotenone, Antimycin A, oligomycin and FCCP for *in vitro* primary hepatocyte data from 24 human patients. Statistical analysis was used to compare the ability of patient data percentage changes versus model parameter changes to predict glycolytic reserve capacity.

2 Chapter 2: Modelling Redox Cycling: Model Formulation and Development

2.1 Chapter Aims

1. To construct a thermodynamically driven mathematical model of quinone redox cycling, capable of generating time course profiles of radical species formation.
2. To develop a new method to characterize parameter values using extracellular flux analysis *in vitro*.
3. To use the combined *in silico* – *in vitro* platform to investigate the mechanism of quinone redox cycling using known redox-cycler / anti-cancer drug doxorubicin as an example.

2.2 Mathematical Modelling

2.2.1 Quinone Physicochemical & Thermodynamic Model

The proclivity of a quinone to accept an electron, or be reduced, is dependent upon its reduction potential, $E^{\circ'}$, as discussed in 1.1.2. This method of assessing susceptibility via its reduction potential is applicable to all other chemical compounds, most importantly perhaps, it can be applied to reactive oxygen species (ROS). Furthermore, the ability for a quinone, in this case a semiquinone ($SQ^{\cdot-}$), to donate the electron to generate the ROS may also be quantified via the thermodynamic linking of both reduction potentials.

Thermodynamic favourability of the reaction between the $SQ^{\cdot-}$ and molecular oxygen can be gauged by considering $E^{\circ'}$ for the ($Q/SQ^{\cdot-}$) and ($O_2/O_2^{\cdot-}$), where the $E^{\circ'}$ for ($O_2/O_2^{\cdot-}$) is -180 mV ⁴⁹. The reaction equilibrium constant can also be calculated using Equation (2-1).

$$E^{\circ'}(O_2/O_2^{\cdot-}) - E^{\circ'}(Q/SQ^{\cdot-}) = \left(\frac{RT}{F}\right) \ln K_{eq} . \quad (2-1)$$

Where R is the universal gas constant (8.314 J/mol K); T is the temperature in Kelvin and K_{eq} is the reaction equilibrium constant.

In essence, according to Equation (2-1), if the $E^{\circ'}(Q/SQ^{\cdot-})$ is lower than the $E^{\circ'}(O_2/O_2^{\cdot-})$ then the equilibrium will lie to the right-hand-side favouring $O_2^{\cdot-}$ Formation. Similarly, if the $E^{\circ'}(Q/SQ^{\cdot-})$ is higher than the $E^{\circ'}(O_2/O_2^{\cdot-})$ then the opposite is true, favouring the reverse reaction, and thereby leaving superoxide formation ultimately thermodynamically unfavourable. However, it is important to recognize that, regardless of which side of equilibrium is favoured, these reactions are reversible and therefore superoxide formation can occur even if the reverse rate constant is higher than the forward. The production of superoxide is then a function of other biological or chemical factors that influence the position of equilibrium, such as detoxification by superoxide dismutase enzymes (SOD) ⁷.

Reduction potentials for a myriad of quinone compounds have been published, along with their relative forward and reverse rate constants for the formation of superoxide from molecular oxygen, calculated using Equation (2-1) ⁷. Furthermore, these reduction potentials are also inextricably linked to the quinone pKa values, as hydroquinones are weak diacids with pKa values typically in the range of 9-11. pKa values are extremely useful and well utilized for describing the electron density on an atom with which a hydrogen bond is formed. This gives the optimum opportunity to consolidate these crucial physicochemical thermodynamic properties into a mathematical framework from which rate constants may be obtained given any reduction potential or pKa value for a quinone containing compound. This model will be denoted the physicochemical thermodynamic quinone model (PTQM) henceforth.

The PTQM accounts for multiple quinone reduction potentials, rate constants for formation and pKa values for different quinone compounds. 12 structurally different quinone compounds were used to construct the PTQM, covering a large reduction potentials (-500 – 100 mV) and rate constants ($\log 4 - \log 10 \text{ M s}^{-1}$). The model facilitates generation of a rate constant for the formation of superoxide from a semiquinone radical given a reduction potential or pKa, or vice versa by relating the reduction potential of these compounds to their pKa values, and then to the forward and reverse rate constants for superoxide formation. Values for reduction potentials

and pKa values for a group of quinone motif-based compounds, as well as the corresponding rate constants for formation of superoxide from the semiquinone radicals were taken from ⁷, and used to generate the PTQM. From these values, activity relationships were established between pKa, reduction potential, superoxide formation and glutathione conjugate formation.

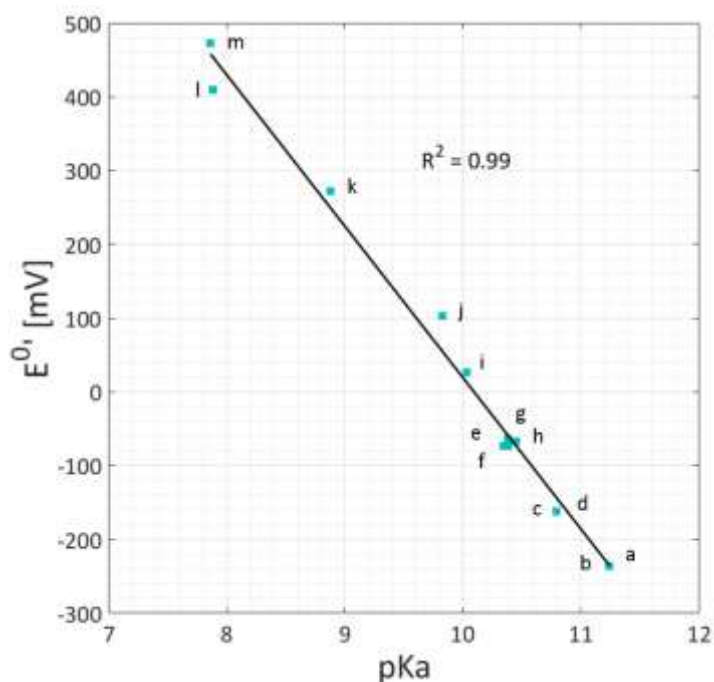


Figure 2-1: Reduction potential – pKa model. Corresponding pKa and reduction potential values for *para*-hydroquinone compounds were consolidated into a mathematical framework, allowing computational estimation of a reduction potential from a pKa value should the reduction potential be unavailable. Compounds: a. ubiquinol-1, coenzyme Q-1; b, tetramethyl-1,4-hydroquinone; c, 2,3,5-trimethyl-1,4-hydroquinone; d, plastoquinol-1; e, 2,6-dimethyl-1,4-hydroquinone; f, 2-methyl-5-isopropyl-1,4-hydroquinone; g, 2,3-dimethyl-1,4-hydroquinone; h, 2,5-dimethyl-1,4-hydroquinone; i, 2-ethyl-1,4-hydroquinone; j, 1,4-hydroquinone; k, 2-chloro-1,4-hydroquinone; l, 2,6-dichloro-1,4-hydroquinone; m, 2,5-dichloro-1,4-hydroquinone ⁷.

Figure 2-1 shows the relationship between pKa and reduction potential, illustrating the general trend of decrease in reduction potential results in an increase in pKa. The electron density of a proton is reflected in its associated pKa value, with the greater

the electron density it shares with the atom it forms the hydrogen bond with, the greater the negative charge remaining once removed, i.e. the greater the negative charge, the higher the pKa value. This directly correlates to the ease of reduction of a quinone, as the more negative the reduction potential, the harder it is to reduce.

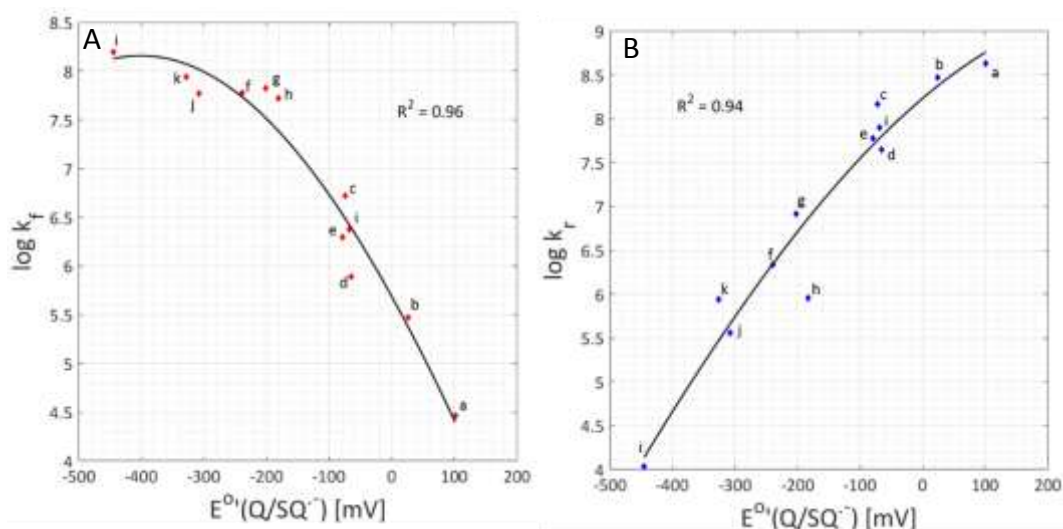


Figure 2-2: Reduction potential superoxide formation rate constant model. Quinone reduction potential thermodynamic data was consolidated into a mathematical framework in order to facilitate superoxide rate constant determination for a range of reduction potentials. The models were fitted using data from ⁷, using the Matlab fitting tool, allowing ameliorated curved fitting compared to source fit. The responsible parent quinone for the semiquinone radicals: a, 1,4-benzoquinone; b, methyl-1,4-benzoquinone; c, 2,3-dimethyl-1,4-benzoquinone; d, 2,5-dimethyl-1,4-benzoquinone; e, 2,6-dimethyl-1,4-benzoquinone; f, duroquinone; g, 2-methyl-1,4-naphthoquinone; h, 2,3-dimethyl-1,4-naphthoquinone; i, anthraquinone; j, Mitomycin; k, Adriamycin; l, AZQ: 2,5-diaziridinyl-3,6-bis(carbethoxyamino)-1,4-benzoquinone.

Figure 2-2 illustrates the relationship between reduction potential and the subsequent rate constants for superoxide formation, generating an activity relationship. The forward rate constant follows the likelihood of electron donation onto molecular oxygen from the relevant $SQ^{\cdot -}$, whereby the more negative the reduction potential, the higher forward the rate constant (k_f). A less readily reduced $SQ^{\cdot -}$ possesses a more negative reduction potential and as such, will seek to rapidly

donate its surplus electron to molecular oxygen if it itself reduced, hence the higher rate constant of formation (k_f) of superoxide. The reverse rate (k_r) constant follows the opposite rational, with the more negative the reduction potential, the slower the rate.

The final set of data to consolidate into this framework is the relationship between the reduction potential and the rate constant for the formation of glutathione adducts (Q-GSH) via irreversible Michael addition. Figure 2-3 shows how increases in reduction potential correspond to a linear increase in the formation rate constant. An increase in reduction potential reflects a more readily reducible quinone, which in turn results in increased proclivity for radical species formation. As such, the rate at which GSH adducts form, is concentration dependent based upon mass action, and therefore will also increase. Figure 2-1, Figure 2-2 and Figure 2-3 form the primary construct of the PTQM model, from which, information regarding reduction potential, pKa, superoxide formation rate constants and glutathione reaction rate constants may be obtained.

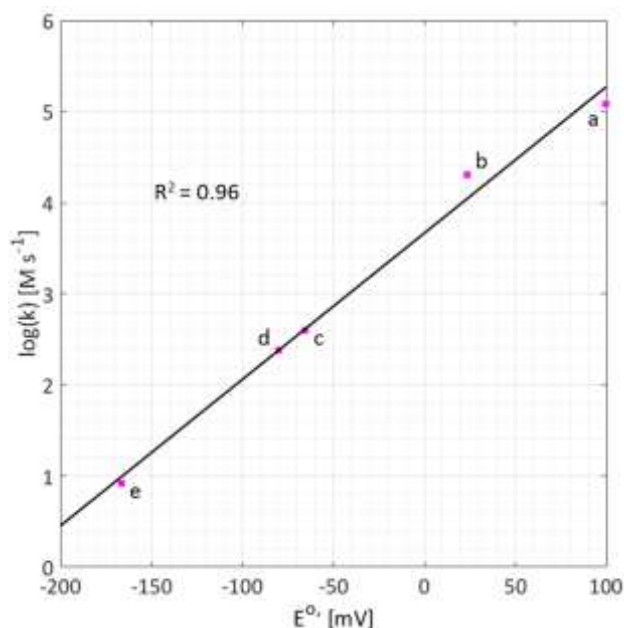


Figure 2-3: Reduction potential GSH adduct rate constant model. Quinone reduction potential thermodynamic data was consolidated into a mathematical framework in order to facilitate superoxide rate constant determination for a range of reduction potentials. The models was fitted using data from ⁷, using the Matlab fitting tool, allowing ameliorated curved fitting compared to source fit. The responsible parent quinone for the semiquinone radicals: a, 1,4-benzoquinone; b, methyl-1,4-benzoquinone; c, 2,6-dimethyl-1,4-benzoquinone; d, 2,5-dimethyl-1,4-benzoquinone; e, 2,3,5-trimethyl-1,4-benzoquinone.

The three models relating reduction potential to superoxide and glutathione adduct formation were then housed in a single model fronted with a graphical user interface (GUI) (Figure 2.4). This facilitates open access for all users, particularly those who are unfamiliar with fitting algorithms or coding. The PTQM GUI works by entering a reduction potential followed by clicking “Generate”, which displays the corresponding forward and reverse rate constants (k_f and k_r) for semiquinone induced superoxide formation and the rate constant for glutathione adduct formation. If the reduction potential for the quinone is unknown, then a pKa value may be entered followed by clicking “Generate” once to generate the reduction potential, then clicking “Generate” a second time to display the rate constants.

Thermodynamic Quinone Rate Constant Generator

Instructions

1. Enter a reduction potential and click generate.
2. If the reduction potential is unknown, enter a pKa value and click generate to give the calculate it. Click generate again to give rate constant values.

Generate

Reduction Potential (mV): **pKa :**

kf [M/s]	kr [M/s]	kGSH [M/s]
1.21545e+08	211942	-1.81146

Figure 2-4: Physicochemical thermodynamic quinone model GUI. Users are able to input a reduction potential or pKa value to obtain specific rate constants for quinone based redox cycling.

2.2.2 Preliminary Redox Cycling Model

The initial chemical redox cycling model was based on the well characterized quinone moiety, notorious for their redox cycling ability as described in Chapter 1. The model was constructed around the $Q/SQ^{\cdot-}/H_2Q$ redox triad (Figure 1-1), coupled with *in vitro* EFA as a method of quantifying the rate of redox cycling experimentally. As mentioned above, the anti-cancer drug doxorubicin was used as the initial quinone containing compound.

Firstly, the redox chemistry was described mathematically using mass action based kinetics, incorporating the thermodynamically derived rate constants for doxorubicin generated from its reduction potential, obtained from the PTQM. The initial model iteration included the redox triad, as well as the double electron reduction from the quinone to the hydroquinone and the formation of $O_2^{\cdot-}$. Table 2-1 and Table 2-2 list

the initial model reactions, along with a description and their corresponding kinetic equations. The model is depicted as a schematic in Figure 2-5.

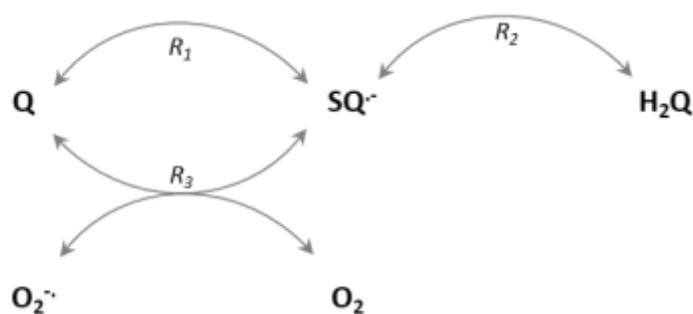


Figure 2-5: Initial redox cycling model schematic. The model captures the redox cycling of a quinone motif and molecular oxygen to form superoxide. Q, quinone; $\text{SQ}^{\cdot-}$, semiquinone radical anion; H_2Q , hydroquinone; $\text{O}_2^{\cdot-}$, superoxide radical anion.

Reaction	Equation	Description
R ₁	$\text{Q} \rightleftharpoons \text{SQ}$	Single electron reduction
R ₂	$\text{SQ} \rightleftharpoons \text{H}_2\text{Q}$	Single electron reduction
R ₃	$\text{SQ} + \text{O}_2 \rightleftharpoons \text{Q} + \text{O}_2^{\cdot-}$	Superoxide formation

Table 2-1: Initial quinone redox cycling model reactions accompanied with a description

Reaction	Equation
R ₁	$k_{f1} [\text{Q}] - k_{r1} [\text{SQ}]$
R ₂	$k_{f2} [\text{SQ}] - k_{r2} [\text{H}_2\text{Q}]$
R ₃	$k_{f3} [\text{SQ}] [\text{O}_2] - k_{r3} [\text{Q}] [\text{O}_2^{\cdot-}]$

Table 2-2: Initial quinone redox cycling model kinetic equations

Using the redox potential $E^{\circ} (\text{Q}/\text{SQ}^{\cdot-}) = -292 \text{ mV}$ for doxorubicin, the corresponding rate constants, calculated by the PTQM (Figure 2-4), k_{f3} and k_{r3} for R₃ are 9.2285×10^7 and $6.6984 \times 10^5 \text{ M s}^{-1}$ respectively^{7,50}. The remaining unknown rate constants were assigned arbitrary values of 1 prior to fitting to experimental data. The initial parameter estimates were varied, but this had no effect on the values of optimized parameters.

The model was constructed by describing the relationship between these reactions in the form of a coupled system of ordinary differential equations (ODEs), namely (2-2):

$$\frac{dQ}{dt} = -R_1 + R_3, \quad (2-2)$$

$$\frac{dSQ}{dt} = -R_2 + R_1 - R_3,$$

$$\frac{dH_2Q}{dt} = R_2,$$

$$\frac{dO_2^{\cdot-}}{dt} = R_3.$$

This model is a reduced representation of quinone redox cycling as stoichiometric accounting for proton H^+ and electron (e^-) is omitted. Instead, it is assumed that proton concentration is constant at pH 7, as this is the pH whereby the $E^{\sigma'}$ has been calculated ⁷. Furthermore, this model assumes that the electrons are abundantly available, allowing dynamics of electron number to be omitted. Molecular oxygen (O_2) concentration is also held constant in the model, allowing simulation of a state of normoxia. In order to ease the inevitable transition from the initial chemical specific model to a pharmacologically relevant experimentally validated model, the oxygen concentration is captured by multiplying the k_{f3} by the oxygen molar saturation 1.3×10^{-4} M, obtained from an 18 % oxygen concentration in unbuffered pH 7 media.

Regardless of the simplicity of the initial model there are fundamental characteristics that must be captured in order to inquisitively model quinone redox cycling. The model has been initially developed to account for two single electron reductions, and one double electron reduction to represent full quinone to hydroquinone reduction. The importance of including both reduction platforms falls into a mechanistic

boundary, as while it is confirmed that the quinone moiety is able to be reduced under both single and double electron reduction methods - how important either mode of reduction will be highlighted below. In this instance, the single-step double electron reduction ($Q \rightleftharpoons H_2Q$) is included implicitly by the two single electron reduction reactions R_1 and R_2 , allowing the double reduction to become a function of the stability of the SQ^\cdot radical species. Thus, a highly unstable radical will further reduce to the H_2Q . Finally, all parameters are positive by definition.

2.2.3 Stability Analysis

Local model stability can be investigated using standard linear stability analysis at for model equilibrium, which occurs at steady state denoted by (Q^{Eq} , $SQ^{\cdot Eq}$, H_2Q^{Eq} , $O_2^{\cdot Eq}$). To facilitate the analysis, the model can be simplified by taking into account that the sum of concentration of the three quinone derived variables Q , SQ^\cdot and H_2Q is equal to the initial amount of Q placed in the system, Q_i . Therefore, the variable H_2Q can now be replaced in Table 2-2 with Equation (2-3):

$$H_2Q = Q_i - Q - SQ. \quad (2-3)$$

Now, by setting the right-hand sides of the equations in the system Equations (2-2) to zero, and after simplification, we get the following steady state concentrations:

$$Q^{Eq} = \frac{Q_i k_{r1} k_{r2}}{k_{r1} k_{r2} + k_{r2} k_{f1} + k_{f1} k_{f2}}, \quad (2-4)$$

$$SQ^{Eq} = \frac{Q_i k_{r1} k_{f2}}{k_{r1} k_{r2} + k_{r2} k_{f1} + k_{f1} k_{f2}},$$

$$O_2^{\cdot Eq} = \frac{k_{f1} k_{f4}}{k_{r1} k_{r4}}.$$

In particular, we note that there is only one steady state for this system.

Calculating the Jacobian matrix (J) for this system (2-2), we get:

$$J = \begin{pmatrix} -k_{f1} - O_2^- k_{r3} & k_{r1} + k_{r3} & -Q k_{r3} \\ k_{f1} - k_{r2} + O_2^- k_{r3} & -k_{r1} - k_{r2} - k_{f2} - k_{p4} & Q k_{r3} \\ -O_2^- k_{r3} & k_{p3} & -Q k_{r3} \end{pmatrix}.$$

Evaluating the eigenvalues of J in the case where $Q = Q^{EQ}$, O_2^{-EQ} , and considering the sign of the real parts of the resulting eigenvalues allows local stability to be determined. The expressions for these eigenvalues (λ) in the general case are rather lengthy, but with the preliminary parameters set as outlined in on page 49, we have:

$$\lambda_1 = -0.9728 + 0.000850i,$$

$$\lambda_2 = -2.7846 + 0.0007650i,$$

$$\lambda_3 = -2.4727 \times 10^5.$$

Information regarding stability of the steady state system can be ascertained by examination of the eigenvalues, specifically, if the real parts are negative then the steady state is locally stable. Conversely, if the real parts are positive then the steady state is locally unstable. In this instance, the preliminary model complex eigenvalues, with negative real parts. Therefore, the unique equilibrium point is asymptotically stable, with its critical point being a spiral point, with trajectories decaying towards the critical point.

These eigenvalues however, are a function of partial arbitrarily set parameter values. While these parameter values will always be positive, different parameter sets may yield unstable unique equilibrium points. At this point, the model is not representative of any experimental data and therefore to investigate parameter selection would be trivial. A range of parameter values were substituted to determine whether they change the sign of the real part, which showed that the real parts remained negative over a wide range of parameter variations.

2.2.4 Preliminary Simulations

Calculation of doxorubicin specific rate constants for k_{f3} and k_{r3} , leaves 4 unknown parameters, which as we describe above were initially assigned arbitrary values of 1. Initial simulations therefore are arbitrary by definition. Nevertheless, model simulation provides a graphical platform stimulating motivation for further model development once experimental data has been generated. Furthermore, initial simulations provide qualitative intuition regarding the suitability of the model in its current form. The preliminary time course simulation and steady state simulations were generated by integration of the ODE system using the variable-order stiff solver ode15s in Matlab. Initial simulations depicted in Figure 2-6 show chemical transition from the initial quinone (Q ; 1 M) to the fully reduced hydroquinone (H_2Q) via the semiquinone radical ($SQ^{\cdot-}$) including generation of the superoxide radical ($O_2^{\cdot-}$) Regardless of the model being in its infancy, qualitative insights can be made. As expected, the model captures the thermodynamically favourable formation of superoxide from the $SQ^{\cdot-}$ given the doxorubicin specific rate constants.

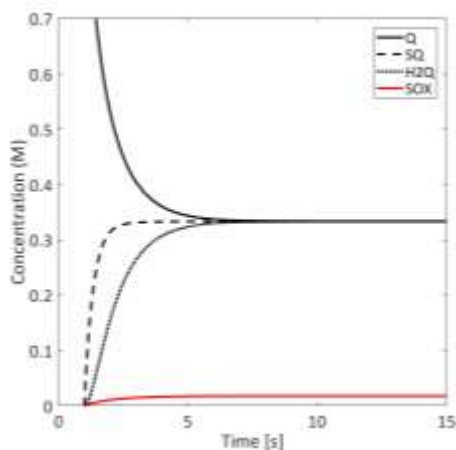


Figure 2-6: Combined initial variable time course simulation illustrating final variable product destination.

The preliminary model at this stage is unable to quantitatively capture chemical redox cycling without experimentally informed parameter derivation. However, preliminary model simulation outputs can be compared to the calculated variable

steady state values obtained during the stability analysis to confirm numerical accuracy of the ODE solution. Substituting the parameter set on page 49 into the unique equilibrium steady state on page 52, yields numerical values for variable steady states (Q^* , SQ^* , SOX^*) which can be compared to the simulated steady state values (Q_{sim}^* , SQ_{sim}^* , SOX_{sim}^*).

$$Q^* = 0.3333 \text{ M},$$

$$Q_{sim}^* = 0.3333 \text{ M};$$

$$SQ^* = 0.3333 \text{ M},$$

$$SQ_{sim}^* = 0.3333 \text{ M};$$

$$O_2^{-*} = 0.0179 \text{ M},$$

$$SOX_{sim}^* = 0.01791 \text{ M}.$$

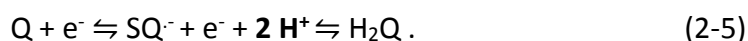
Which are therefore in agreement.

Now, in order to parameterize the model more accurately, it must be aligned with experimental data.

2.3 *In vitro* Biochemical Redox Cycling

As described in chapter 1, detecting and quantifying radical chemistry kinetics is extremely difficult owing to the fleeting existence of the radical species. This motivates alternative approaches, whereby rather than measuring concentration of radical species, chemical stoichiometry can be monitored as a function of reaction flux.

According to the initial model, for complete reduction from Q to H₂Q, a total of 2 H⁺ atoms are consumed. Conversely, for every complete oxidation, two protons will be ejected. This reaction stoichiometry can be exploited as a method of quantifying the rates of these reactions. In particular, if proton flux can be measured as a function of time and quinone concentration Equation (2-5), namely using:



2.3.1 Novel EFA Redox Cycling Assay Development

EFA is an experimental technique used to measure the rate of change of proton and oxygen concentration outside of a cellular environment, as described in chapter 1. In this instance, the technique can be implemented in a cell free environment measuring the PPR of the solution within the transient microchamber.

EFA proton efflux output can be expressed either as a function of pH or as a proton production rate PPR, with a rate of change in proton concentration rather than a rate of change of pH preferable when mathematical alignment is the overall endpoint. Considering the transient microchamber and the method by which the EFA measures the PPR, it is imperative that the EFA measures PPR flux prior to addition of the quinone compound so as to capture the immediate chemical dynamics. Therefore, the inbuilt injection system was used to charge the compound to the solution, providing the best platform to capture the rapid kinetic changes expected.

Arguably the most critical consideration to make when attempting to measure compound redox cycling is the reaction pH. Changes in pH can affect the ionic form of a drug depending upon its pKa value, by presenting opportunity to exist purely in its unionized, completely ionized or as an equilibrium of both. In *in vitro* pharmacological experiments, a physiological pH of 7.4 is preferred, facilitating a closer physiological relationship. Here, solution pH may affect whether an auto reduction or auto oxidation will occur to initiate a redox cycle. Furthermore, should redox cycling in a specific bio-compartment wish to be investigated where the pH deviates from 7.4, such as the stomach where the pH is considerably more acidic (pH 1.5 – 3.5) or within an erythrocyte where the pH is a function of oxygen saturation, this can be accomplished by adjusting the reaction solvent pH accordingly.

In order to maximize the ability to translate the assay into a pharmacologically relevant scenario, the assay was designed to mimic a typical EFA assay. As such, unbuffered seahorse EFA medium was used as the reaction solvent, devoid of glucose, with the pH set to 7.0.

The initial mathematical model is again centred on the thermodynamic driven kinetics of doxorubicin as the initial quinone of interest, as the generation of $O_2^{\cdot-}$ is favourable according to its redox potential at pH 7, and doxorubicin is also proven to be capable of redox cycling in pharmacological scenarios. As such, the assay was performed using doxorubicin as the test compound.

In order to facilitate future comparisons of the combined system to pharmacologically relevant information, compound concentration and solvent selection were influenced by toxicological studies of doxorubicin administration to cellular systems, namely, using biologically relevant concentrations.

2.3.1.1 Materials

All seahorse consumables were purchased from Seahorse Biosciences (North Billerica, Ma, USA), doxorubicin was purchased from sigma Aldrich (Dorset, UK).

2.3.1.2 Injection preparation

Doxorubicin stock solution (10 mM), was serially diluted in unbuffered seahorse assay medium to prepare 6 concentrations: 400, 300, 200, 100, 80 and 40 μ M in 100 % DMSO. Compound solutions were set to a final pH of 7 using HCl and KOH when necessary. Final compound dilution occurs post injection giving a final concentration of 50, 35, 25, 12.5, 10 and 5 μ M inside the well.

2.3.1.3 Extracellular flux analysis

200 μ l of XF calibrant was added to each well of a 96 well XF utility plate. The sensor cartridge was then placed on top of the utility plate, submerging the sensors fully in the calibrant. The utility plate and sensor cartridge was then incubated overnight at 37°C in a CO₂ free incubator.

The pH of the unbuffered XF assay medium was set to 7.4 using HCl and KOH when necessary and then incubated at 37°C in a CO₂ free incubator. 25 μ l of each doxorubicin concentration was added to the injection port A of each well of the sensor cartridge. Each doxorubicin concentration was plated in triplicate. Ports above

wells devoid of media were charged with the equivalent volumes of assay media in order to maintain injection pressure across the plate. The utility plate was inserted into the flux analyser and allowed to calibrate, and then removed once complete. Prior to analysis, the XFe96 instrument (Seahorse Biosciences, North Billerica, MA, USA) mixed the assay media in each well for 10 min to allow the oxygen partial pressure to reach equilibrium. Extracellular flux analysis was conducted simultaneously measuring ECAR (PPR) and OCR. The first three measurements were used to establish a baseline rate. All measurements include a 3 min mix, allowing the probe to retract and collapse the transient micro chamber. This allows oxygen tension and pH in the microenvironment to restore to normal.

Doxorubicin was injected after the third measurement (16 min) and the resulting changes in PPR and OCR were measured for a further 20 measurements (150 min) yielding the basal response.

2.3.2 EFA Redox Cycling Results & Discussion

EFA was used to measure the rate of change of proton production / consumption before and after injection of doxorubicin into unbuffered XF media at pH 7. Three different concentrations of doxorubicin 50, 25 and 12.5 μM were analysed for an $n = 3$. Compound injection occurred at $t = 16$ min Figure 2-7.

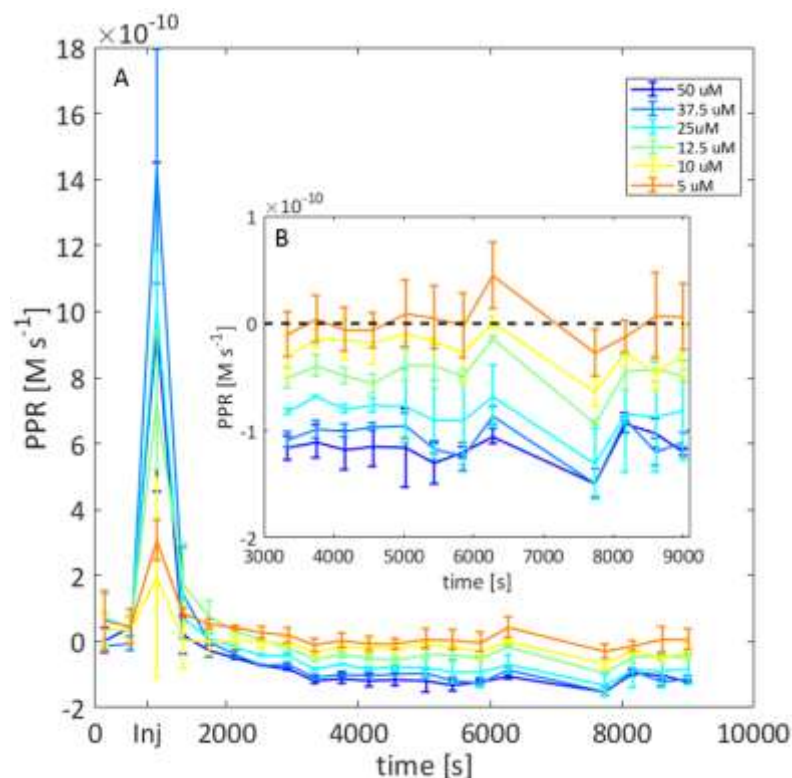


Figure 2-7: EFA PPR profile for doxorubicin at 50, 37.5, 25, 12.5, 10 and 5 μM . Negative PPR indicates proton consumption rather than production. Each dataset is the average of $n=3$ experiments expressed with its standard deviation. A) Shows entire EFA results including compound injection peak. B) Shows steady negative PPR from $t=3000$ s onwards. Compound injection time is labelled "Inj" on the x-axis.

Changes to overall well pH were also measured (e.g. using conventional EFA as rates of change of proton concentration to pH via $-\log [\text{H}^+]$). Figure 2-8 shows the pH profile for the same experiment.

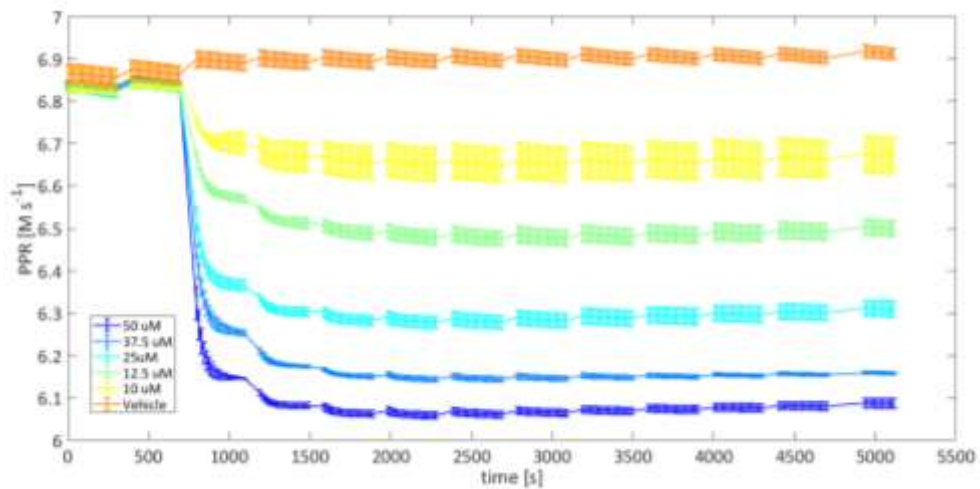


Figure 2-8: pH profile for doxorubicin at 50, 25 and 12.5 μM shown in blue, red and green respectively. Control compound free data is shown in purple. Each dataset is the average of $n=3$ experiments expressed with its standard deviation.

There are three predominant characteristics of the doxorubicin EFA profile. The first and most obvious is the initial spike increase in PPR for all six concentrations immediately after compound injection (Figure 2-7). Each data point on the plot represents the PPR directly after a 3-minute solution mix within the well, specifically measured in the transient microchamber. Compound injection occurs at $t = 16$ min, in between measurements 2 and 3. Therefore, the increase in proton production rate is caused by introduction of doxorubicin to the media. The resulting change in pH is due to the increased dissociation of the hydroxyl group as depicted in Figure 2-9.

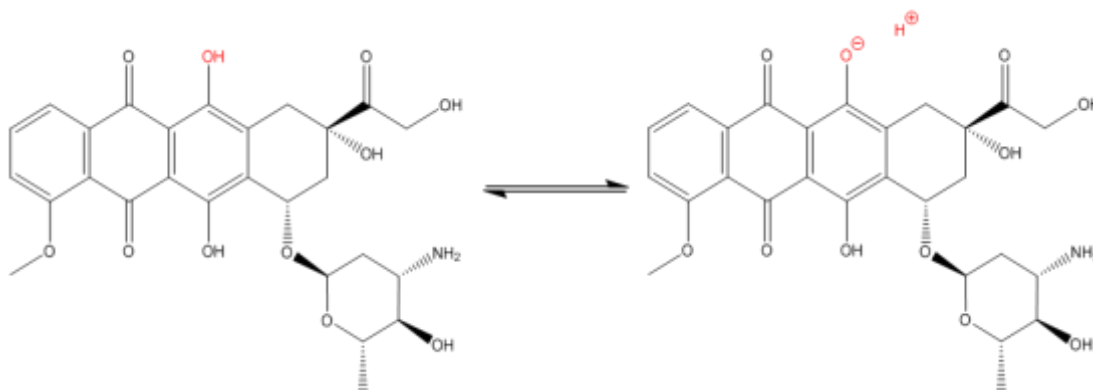


Figure 2-9: Doxorubicin phenol acid dissociation. Phenol hydroxyl group highlighted in red in both scenarios, with the right-hand side representing the phenol anion and dissociated proton.

Proton dissociation from doxorubicin would therefore increase the measured PPR and subsequently increase the acidity of the well, represented by a decrease in pH. Indeed, the concomitant measurement of system pH in Figure 2-8 shows this exact decrease in pH, which is relative to the concentration of doxorubicin charged thus confirming that the acid dissociation is responsible for the initial increase in PPR at measurement 3.

The second characteristic is the trend between the different concentrations of doxorubicin. As the concentration of doxorubicin decreases, so too does the relative PPR, specifically after injection (as seen in Figure 2-7). Moreover, the pH profile in Figure 2-8 shows that the increase in acidity, and decrease in pH, is relative to the concentration of doxorubicin injected, i.e. the greater the concentration of doxorubicin charged, the more protons able to dissociate from the compound resulting in an increase in acidity (drop in pH).

The final important characteristic of the doxorubicin PPR EFA profile is the eventual negative PPR shown for all concentrations. Negative PPR indicates a proton consumption, rather than production. In this experiment, increasing the concentration of doxorubicin increases the amount of protons available to dissociate, which yields a more negative PPR output.

Additionally, interpretation of the pH plot in Figure 2-8 indicates that the EFA well acidity does not return to that of prior to the introduction of doxorubicin, further lending credibility to the hypothesis parent compound remains dissociated.

With regards to the reduction chemistry, the consumption of protons yielding a reduction reaction is shown in Equation (2-5). This equation illustrates that 2 H⁺ are used in the final reductive step in the quinone redox triad, whereby the SQ⁻ is fully reduced to the H₂Q. Utilization of this chemistry would therefore suggest that the rate of proton consumption measured in Figure 2-7, is equal to the rate of reduction of the SQ⁻ to the H₂Q. Similarly, should the PPR profile have remained positive, this flux would be representative of the reverse reaction.

2.4 *In silico* – *in vitro* Model Coupling & Model Expansion

PPR data generated in (2.3) provides an *in vitro* platform to which our mathematical model could be aligned with. The PPR shown in Figure 2-7 corresponds to the reduction reaction in Equation (2-5). With respect to the mathematical model, this corresponds to the reaction R₂ from Table 2-1. Regardless of the omission of H⁺ as a model variable, the PPR is implicit within this reaction and may expressed as R₂ reaction flux, providing stoichiometric balance is maintained by doubling the flux output, as two H⁺ are consumed for every unit flux.

It is visible from (2.2) that the model in its current form is unable to simulate a negative flux for the reaction R₂, with the model at steady state, R₂ = 0 = R₃ (from the H₂Q and O₂⁻ equations), which then gives R₁ = 0 = R₂ from the Q and SQ⁻ equations.

2.4.1 Initial Model Fitting

As outlined above, the preliminary model uses arbitrary values of 1 for the four unknown parameters k , k_{f1} , k_{r1} , k_{f2} and k_{r2} . New values for these parameters were obtained by fitting the model to the doxorubicin EFA data (Figure 2-7) for 50 μM, using the non-linear optimization function, *fminsearch*, in Matlab.

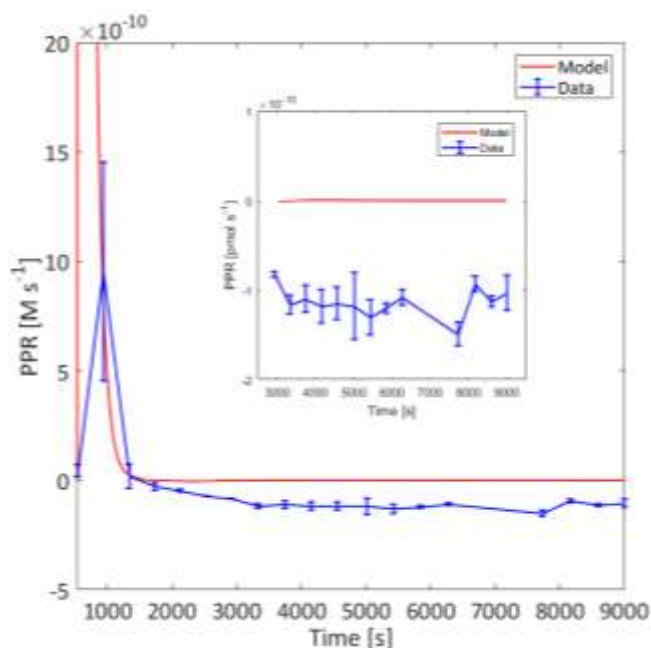


Figure 2-10: Initial model fitting to doxorubicin 50 μM EFA data. Main plot illustrates the entire EFA time course, with the insert figure illustrating steady state region.

The *fminsearch* function finds the minimum of an unconstrained multivariable function using a derivative-free method, using the Nelder-Mead simplex algorithm⁵¹. In essence, it finds the minimum distance between the model and the data by perturbing the assigned parameters. In this instance, all initial parameter values were equal to 1, with changes in initial starting parameters having no effect on final parameter selection.

The initial fit between the model and the *in vitro* data captures the qualitative profile, but falls considerably short of recapitulating the EFA data quantitatively (Figure 2-10). As we can see, the model is unable to produce a negative PPR output. The inability of the model to match the data in its current form may be a result of one of two things: either the model is lacking in mechanistic detail with respect to redox cycling chemistry, or the approach to link proton consumption / production to quinone redox cycling via a surrogate *in vitro* method is not feasible, or both. To assess these issues, the chemistry of quinone redox cycling was assessed and compared to the mathematical model.

2.4.1.1 Redox cycling model expansion

The initial redox cycling model provided an initial platform to compare the qualitative changes in the redox cycling EFA data, including the fundamental chemical reactions between Q, SQ^- , H_2Q and O_2^- in the form of single electron reductions. However, this model is incapable of reproducing the quantitative dynamics of the experimental data (namely, negative PPR, i.e. $R_2 < 0$ at steady state). This has led to the derivation of an improved description of the model in order to incorporate an additional redox reaction known as comproportionation.

Comproportionation is also known as synproportionation and is used to describe the potential chemical reaction between two reactants of the same element or moiety when they exist in different oxidation states, forming a product with the same oxidation state. Depending upon the thermodynamics, comproportionation of Q and H_2Q to form SQ^- is possible, when the value of the mass action expression is not equal to the equilibrium constant. This unique property of a redox cycling reaction will change the overall reaction stoichiometry, as two SQ^- comproportionation to yield the parent Q and the fully reduced H_2Q as shown in Equation (2-6). The result of the addition of the comproportionation reaction is that when Q and H_2Q are present, SQ^- will always exist:



Figure 2-11 shows the new model schematic, with new reaction equations shown in Table 2-3.

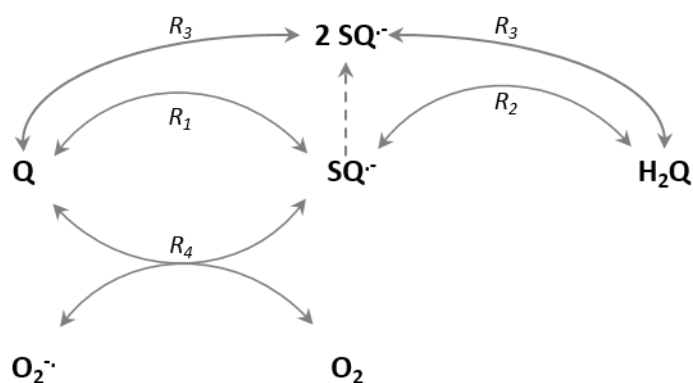


Figure 2-11: Quinone redox cycling model. All reactions are reversible and denoted with a solid double-headed arrows. The dashed single-headed arrow does not represent a reaction, rather, effective accumulation of SQ^{•-} in order to facilitate the comproportionation reaction R₃. Each reaction is denoted R₁₋₄ with corresponding term found in Table 2-3.

Reaction	Equation	Description
R ₁	$Q \rightleftharpoons SQ^{\bullet-}$	Single electron reduction
R ₂	$SQ^{\bullet-} \rightleftharpoons H_2Q$	Single electron reduction
R ₃	$2 SQ^{\bullet-} \rightleftharpoons Q + H_2Q$	Comproportionation
R ₄	$SQ^{\bullet-} + O_2 \rightleftharpoons Q + O_2^{\bullet-}$	Superoxide formation

Table 2-3: Expanded quinone redox cycling model. All reactions are reversible and denoted with double-headed arrows. Each reaction is accompanied with a description of its mechanism.

The new set of reaction equations are shown in Equations (2-7):

$$\frac{dQ}{dt} = -R_1 + R_4 + R_3, \quad (2-7)$$

$$\frac{dSQ}{dt} = -R_2 + R_1 - R_4 - 2R_3,$$

$$\frac{dH_2Q}{dt} = R_2 + R_3 ,$$

$$\frac{dO_2^{\cdot-}}{dt} = R_4 .$$

Initial parameter values remained the same as the preliminary model, with the addition of the comproportionation parameters assigned arbitrary values of 1 prior to model fitting.

2.4.2 Expanded model fitting & stability analysis

New values for the model parameters were obtained by fitting the model to the doxorubicin EFA data (Figure 2-7) for 50 μM , using the same method described in 2.5.1. With the comproportionation reaction added, the model was better able to align with 50 μM EFA data (Figure 2-12).

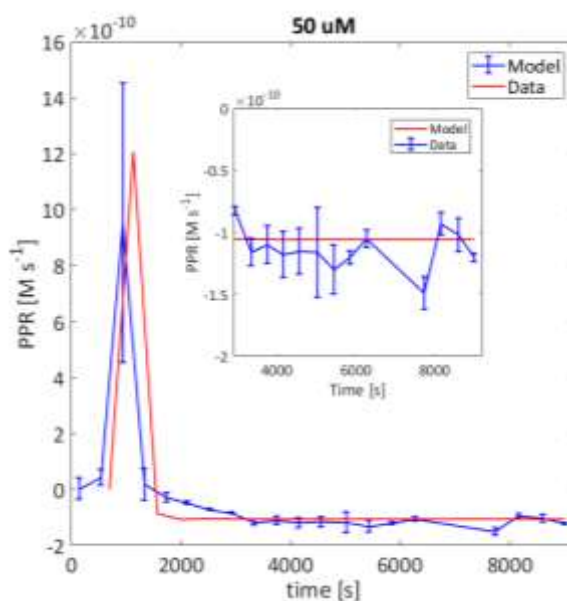


Figure 2-12: Expanded model fitting to doxorubicin 50 μM EFA data. Main plot illustrates the entire EFA time course, with the insert figure illustrating steady state region.

The expanded model including the comproportionation reaction was significantly better at fitting the EFA data with respect to the 50 μM doxorubicin concentrations than the initial model, namely, negative PPR is possible. The fitting generated new values for the rate constants shown in Table 2-4. The new parameter values can be assessed as reaction pairs, as each pair can be converted into an equilibrium constant K_{eq} , using $K_{\text{eq}} = k_f/k_r$. For reactions 1, 4 and 7, the forward rate constant k_f is larger than the reverse rate constant k_r and therefore favours the forward reaction, that is, the production of SQ^- and O_2^- . For reactions 2 and 3, the opposite is true, i.e. the reverse rate is favoured. If $k_{f1} < k_{r1}$, then redox cycling would be thermodynamically unfavourable. The predominant caveat with this fit is the recapitulation of the initial ionization, i.e. the PPR spike at $t = 1000$. The model grossly over estimates this feature during simulation. However, the most important feature is the steady state redox cycling occurring at $t = 3000$ s onwards, depicted in the figure insert. For this, the model is capable of not only reaching the same order of magnitude as the data, but recapitulating the actual data at specific time points.

Rate		
Constant	Value	Units
k_{f1}	11.1785	s^{-1}
k_{r1}	9.7857	s^{-1}
k_{f2}	10.9181	s^{-1}
k_{f2}	13.4391	s^{-1}
k_{f3}	7.8184	$\text{M}^{-1} \text{s}^{-1}$
k_{r3}	10.7783	$\text{M}^{-1} \text{s}^{-1}$
k_{f4}	9.2285×10^7	s^{-1}
k_{r4}	6.6984×10^5	s^{-1}

Table 2-4: Expanded quinone redox cycling model parameters.

With these new set of parameters, the model was simulated at the experimental concentrations 50, 37.5, 25, 1235, 10 and 5 μM as an initial test of parameter adequacy. Figure 2-13 shows the models ability to recapitulate the *in vitro* EFA data with the fitted parameter set for this wide range of concentrations. It is important to note that this parameter set coupled with the comproportionation is necessary to replicate the experimental data. Before investigating the uncertainty of these parameters, the stability analysis can now be repeated to include the experimentally derived parameters along with the additional reaction.

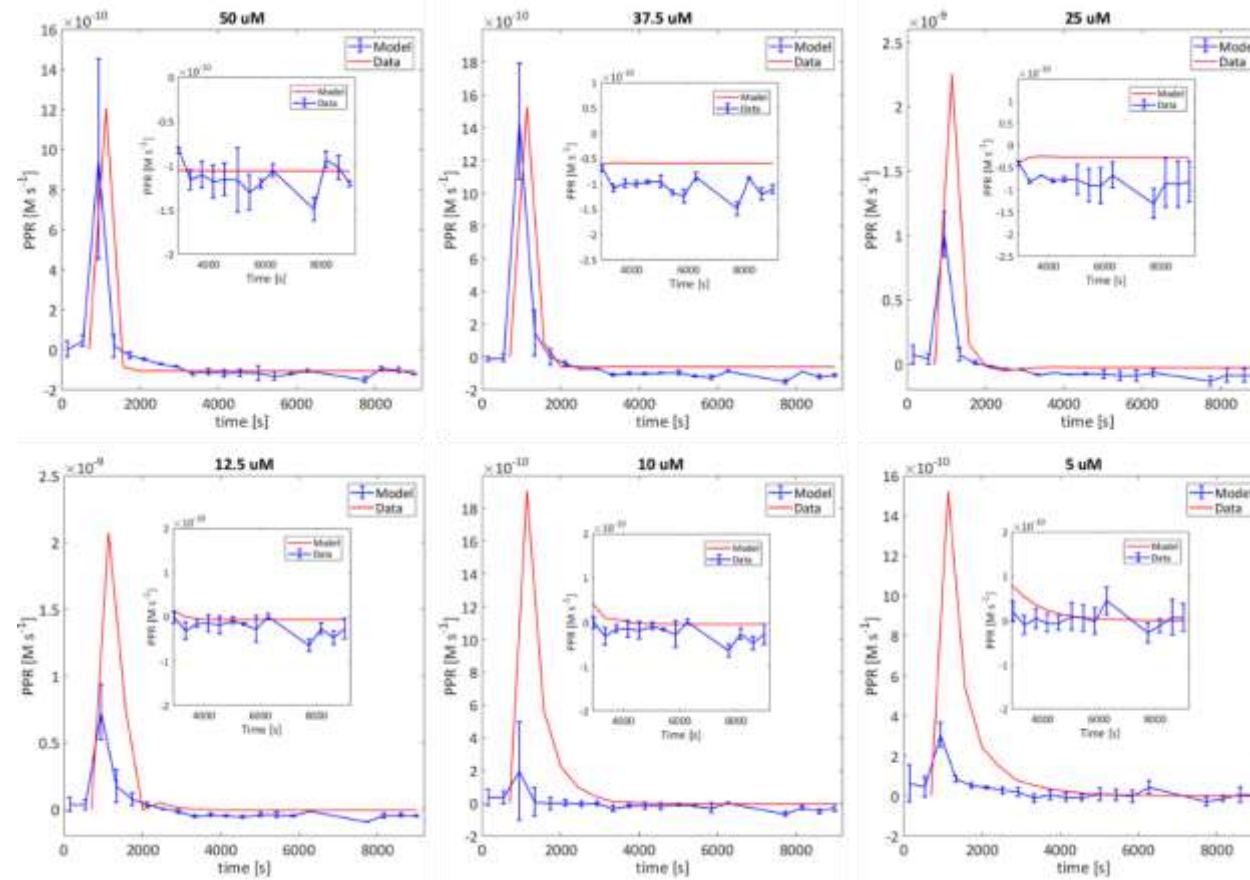


Figure 2-13: EFA doxorubicin experimental concentration simulations. Parameters generated through initial 50 μM data fitting were used to simulate the 5 other concentration outputs, compared to experimental data.

2.4.2.1 Stability analysis

Local model stability was investigated using the method described in 2.3.3. By setting the right-hand sides of the equations in the system (2-7) to zero allows the steady states to be calculated. In this instance, two steady states are possible. This leads to two possible steady state concentrations for each variable in the model, namely:

$$Q^{Eq} = 1.628 \times 10^{-5} \text{ \& } 1.862 \text{ M,} \quad (2-8)$$

$$SQ^{Eq} = 1.860 \times 10^{-5} \text{ \& } -3.145 \text{ M,}$$

$$O_2^{-Eq} = 0.0204 \text{ \& } -0.0302 \text{ M.}$$

Using the optimized parameters obtained in the previous section.

Obviously, it is impossible to have negative variable concentrations. As such, the unique equilibrium point that yields positive variable concentrations was used to calculate system stability.

Calculating the Jacobian matrix (J) for the equilibrium point allows the local stability to be determined, which in turn allows calculation of the corresponding eigenvalues (λ), this yields:

$$\lambda_1 = -0.0088856 ,$$

$$\lambda_2 = -19.259 ,$$

$$\lambda_3 = -2.57386 \times 10^4 .$$

Distinct negative real eigenvalues yield a node phase portrait, suggesting the equilibrium point is locally asymptotically stable. From this information, the trajectories of the phase portrait will move towards the equilibrium point, without oscillating about the equilibrium. This stability analysis can be compared to the preliminary model for insight into the importance of the comproportionation reaction. Both sets of eigenvalues for the preliminary and expanded model have negative real parts, suggesting both system unique stability points are asymptotically

stable. However, the preliminary model includes imaginary parts which means the trajectories spiral towards the critical point, which is not observed in the experimental data, e.g. Figure 2-7.

2.4.3 Sensitivity Analysis

Sensitivity analysis describes the process whereby the output of a model is assessed as a function of its inputs. That is to say, sensitivity analysis allows determination of uncertainty within the model parameter space, which in turn influences the reliability of the model output. Sensitivity analysis can be conducted locally or globally. Local sensitivity analysis assesses one factor at a time, i.e. changes in a single parameter and the resulting effects on the model output. This method can be limiting, as results may be sensitive on location in the parameter space. Global sensitivity analysis, however accounts for a wider range of possible parameter variations, while also considering parameter interactions. As such, global sensitivity analysis was performed on the redox cycling model in order to determine the most sensitive model parameters and will now be described.

2.4.3.1 Parameter sensitivity

The COSSAN toolset was used to conduct global sensitivity analysis on the doxorubicin quinone model using the following workflow:

1. Definition of model and its input and output parameters.
2. Assignment of a probability density function to each input parameter.
3. Generate an input matrix through which an appropriate random sampling method e.g. (Latin Hypercube).
4. Assess the influence or relative importance of each input parameter on the output variable.

This method elucidates the effect of the input parameter variability on the model output, while simultaneously investigating the interaction between parameters. This is accomplished using Sobol sampling, yielding sensitivity indices (Sobol indices) which are importance measures for quantifying sensitivity.

The COSSAN software platform was used for this sensitivity analysis. First, to assign a probability distribution around each of the model parameters, (k_{f1} , kr_1 , k_{f2} , kr_2 , k_{f3} , kr_3). 1000 parameter sets were then generated using Latin Hypercube sampling from these sampling distributions. The global sensitivity analysis was then performed, with “PPR” as the model output used for comparison. Estimation of sensitivity / Sobol indices using these 1000 samples was then performed, followed by uncertainty propagation where the uncertainty in input parameter values were translated into model output variances with respect to PPR, as shown in Figure 2-14. The quantitative contribution for each parameter to model output variance is given by the total effect index, showing positive and negative relations on model outputs for each parameter. The larger the normalised sensitivity measure is, the more sensitive this parameter is to model output.

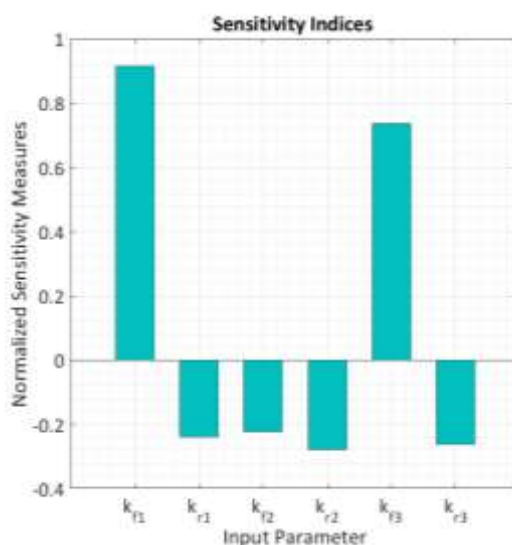


Figure 2-14: Sensitivity indices versus input parameters for model PPR production. Each bar represents the normalized total effect index.

The total sensitivity effect in Figure 2-14 highlights the most sensitive parameters with respect to model PPR output, with k_{f1} and k_{f3} the most sensitive, both of which positively effect PPR output. It makes sense that k_{f1} is the most sensitive parameter, as this governs essentially all conversion of Q to SQ^- and H_2Q , ultimately responsible for all reactions downstream of the initial reduction. The forward rate constant for

the comproportionation reaction, R_3 , is ranked as the second most sensitive parameter, giving credibility to the importance of including the comproportionation reaction to the model, also suggesting that the comproportionation reaction may in fact be the predominant mechanism in which the parent Q is regenerated. All other model parameters have similar sensitivity index size as well as having a negative effect on PPR model output, suggesting that increases in parameters k_{r1} , k_{f2} , k_{r2} and k_{r3} reduce the model PPR output.

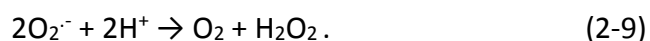
2.4.4 Superoxide Detoxification Expansion

Reactive oxygen species formation and detoxification is a very tightly regulated process within the cell, responsible for pivotal signalling processes including programmed cell death ²³. Furthermore, cellular defence mechanisms against oxidative stress as a function of elevated ROS levels is extremely efficient, with highly specialized enzymes such as superoxide dismutases and glutathione peroxidases at the forefront, adept at swiftly quenching further radical species formation ⁵². However, regardless of the rapidity of these processes, thresholds exist whereby ROS can overwhelm detoxification processes, especially when futile redox cycling occurs at the expense of cellular reducing power (NADH) in catalytic fashion, causing toxicity in many forms, often resulting in cell death ¹. One example includes superoxide induced mitochondrial dysfunction, as these organelles are highly aerobic and electron rich around the electron transport chain ⁵³. Increased levels of superoxide within the mitochondria activate mitochondrial K_{ATP} channels, which increase membrane potential $\Delta\Psi$, and in turn generates more ROS ⁵⁴.

In order for the redox cycling model to be applicable within a toxicological setting, such detoxification processes must be included in order for the model to provide quantitative pharmacological insights. As such, we now explore superoxide dismutase mediated $O_2^{\cdot-}$ detoxification within the model framework.

2.4.4.1 Superoxide Dismutase Role in Redox Signalling and Oxidative Stress Defence

Superoxide dismutases (SODs) form the predominant cellular defence against elevated cellular superoxide anions⁵⁵. There are three different isoforms in mammals, specific to different cellular compartments. These consist of: Mitochondrial SOD, which has a manganese (Mn) catalytic active metal (MnSOD); cytoplasmic SOD, (Cu/ZnSOD) which utilizes copper-zinc catalytic metals; and, extracellular SOD, which utilizes only copper metal for its activation (CuSOD)⁵⁵. The responsibility of SOD is to convert $O_2^{\cdot-}$ into hydrogen peroxide (H_2O_2) which then prevents both further radical species formation such as the highly reactive hydroxyl radical ($\cdot OH$), as well as facilitating protective cellular signalling and gene expression via H_2O_2 . Even though ROS such as $O_2^{\cdot-}$ and H_2O_2 are pivotal for such bio-function, ROS levels actually act as a double-edged sword, possessing desirable and toxic effects:



Equation (2-9) describes the reaction between superoxide and SOD, with consumption of H^+ and reformation of molecular oxygen included. The initial redox cycling model was constructed and parameterized with the omission of SOD, since this reaction also consumes protons, which could have obstructed determining the kinetics of the redox cycling. Fortunately, SOD enzyme kinetics are well described, parameterized and validated within the literature⁵². Perhaps the best example of this lies within the integration of mitochondrial energetics by Kembro *et al.*⁵². In this publication, the kinetics of both cytoplasmic and mitochondrial isoforms of SOD are described. SOD will be added to the model, specifically, mitochondrial SOD, in order to allow the model to simulate organelle specific superoxide detoxification.

2.4.5 SOD & ROS Scavenging Expansion

In order to simulate ROS / superoxide profiles with physiological relevance, the complementary ROS scavenging systems must be considered and included. Complete

detoxification of superoxide ends after SOD mediated H_2O_2 formation is converted into H_2O by glutathione (GSH) ²⁶ shows the complete detoxification pathway along with the enzymes used accomplish it.

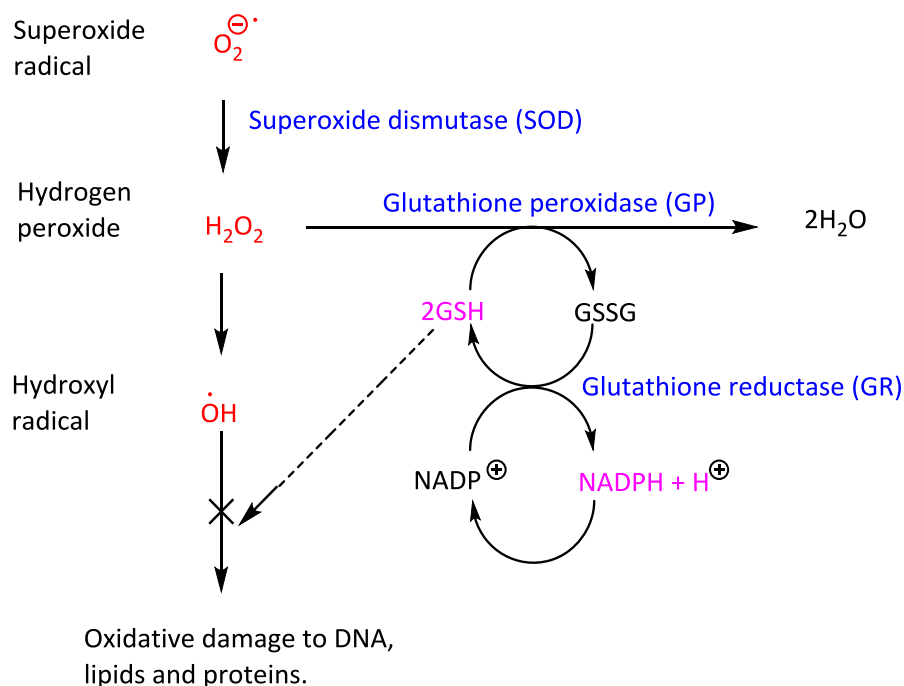


Figure 2-15: Schematic process illustrating superoxide radical detoxification / scavenging. ROS, enzymes and reducing agents are coloured red, blue and pink respectively. X shows the downstream results of GSH depletion and the resulting cellular damage.

Three enzyme mediated reactions facilitate superoxide / ROS scavenging: SOD; glutathione peroxidase (GP); and, glutathione reductase (GR) ²⁶. GP mediates the final detoxification of hydrogen peroxide by using GSH as the reducing agent, generating H_2O and oxidised glutathione (GSSG) simultaneously. GR then is responsible for the reformation of the GSH reducing / scavenging agent, accomplished by reducing GSSG at the expense of cellular reducing power, NADPH. Fundamentally, this scavenging process is a cascade of redox reactions whereby concomitant reduction and oxidation of cellular metabolites facilitate the complete reduction of $\text{O}_2^{\ominus\cdot}$ into harmless water. ROS induced toxicity as a function of a futile redox cycle may occur as a result of overwhelmed scavenging ability in the form of depleted GSH or NADPH. This form of

toxicity is prevalent in many situations, such as ionizing radiation herbicides, antimalarial and sulfadruugs to name but a few ¹.

In order to model removal/detoxification of superoxide, all three enzyme mediated radical scavenging processes must be included. Unfortunately, modelling the dynamic processes that synthesize and maintain cellular redox state, NADPH/NAD lies outside the scope of this work and as such, NADPH/NAD redox state can be maintained. This then allows the GSH/GSSG ratio to be to be the focus of the modelling, which is extremely useful, as GSH depletion work is a staple in assessing compound toxicity within both academic research and the pharmaceutical industry.

Fortunately, research and kinetic modelling of these ROS scavenging systems are extensive therefore allowing swift recapitulation of this process mathematically into our modelling framework. Kinetic terms and parameters for mitochondrial SOD, GR and GP were taken from Kembro *et al.* ⁵². The combined ROS/redox cycling model illustrated in Figure 2-16.

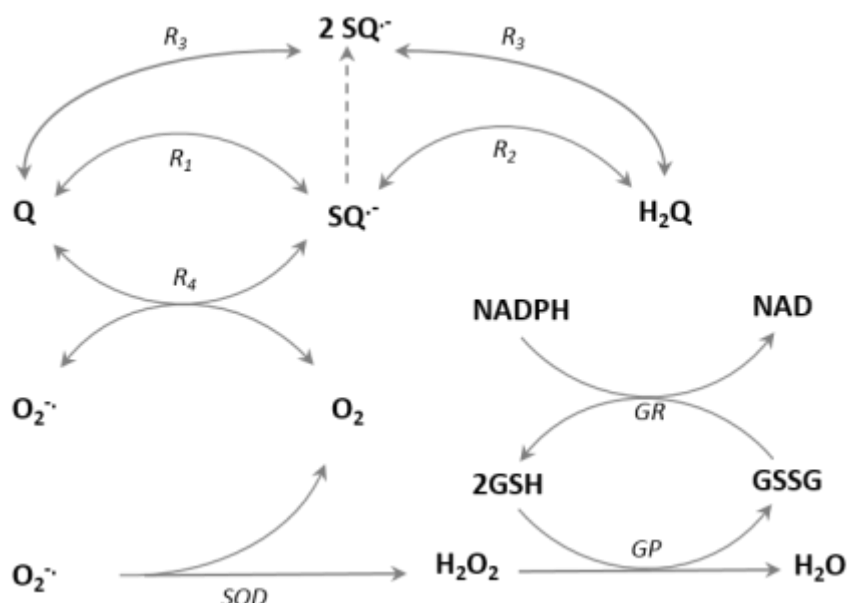


Figure 2-16: Redox cycling / ROS detoxification expansion model schematic.

New kinetic terms for each of the scavenging reactions (SOD, GP and GR) taken from Kembro *et al.* ⁵², were added to the model as follows:

Superoxide Dismutase

$$SOD = \frac{2 k^1 k^5 \left(k^1 + k^3 \left(1 + \frac{[P]}{K_i} \right) \right) e_t [A]}{k^5 \left(2 k^1 + k^3 \left(1 + \frac{[P]}{K_i} \right) \right) + [A] k^1 k^3 \left(1 + \frac{[P]}{K_i} \right)}$$

Where [A] = [O₂⁻], and [P] = [H₂O₂]

Parameter	Value	Units
k^1	1.2×10^3	M ⁻¹ s ⁻¹
k^3	24	M ⁻¹ s ⁻¹
k^5	2.4×10^{-4}	s ⁻¹
K_i	5.0×10^{-4}	M
e_t	3.0×10^{-4}	M

Glutathione Peroxidase

$$GP = \frac{e_t [P] - [A]}{\Phi [A] + \Phi_2 [P]}$$

Where [A] = [GSH], and [P] = [H₂O₂]

Parameter	Value	Units
e_t	1.0×10^{-4}	M
ϕ	5.0×10^{-3}	Ms ⁻¹
ϕ_2	0.75	Ms ⁻¹

Glutathione Reductase

$$GR = \frac{k^1 e_t}{1 + \frac{K_{mA}}{[A]} + \frac{K_{mB}}{[B]} + \frac{K_{mA}}{[A]} + \frac{K_{mB}}{[B]}}$$

Where [A] = [GSSG], and [B] = [NADPH]

Parameter	Value	Units
e_t	8.0×10^{-4}	M
k^1	2.5×10^{-3}	Ms^{-1}
K_{mA}	6.0×10^{-5}	M
K_{mB}	15	M

The model system of ODEs can be described by Equations (2-10). Note, reactions are redefined with respect to Figure 2-16:

$$\frac{dQ}{dt} = -R_1 + R_4 + R_3, \quad (2-10)$$

$$\frac{dSQ}{dt} = -R_2 + R_1 - R_4 - 2R_3,$$

$$\frac{dH_2Q}{dt} = R_2 + R_3,$$

$$\frac{dO_2^-}{dt} = R_4 - SOD,$$

$$\frac{dH_2O_2}{dt} = SOD - GP,$$

$$\frac{dGSH}{dt} = -GP + GR,$$

$$\frac{dGSSG}{dt} = 0.5 (GP - GR),$$

$$\frac{dNADPH}{dt} = 0,$$

$$\frac{dNAD}{dt} = 0.$$

Initial variable conditions are taken from the same source as the kinetic parameters⁵², and are shown in Table 2-5.

Variable	Value	Units
GSH	1.65×10^{-3}	M
GSSG	1.32×10^{-3}	M
NADPH & NADH	7.50×10^{-5}	M
O_2^-	6.39×10^{-9}	M
H_2O_2	8.23×10^{-7}	M
Q	5.00×10^{-7}	M
SQ	0	M
H_2Q	0	M

Table 2-5: Model initial conditions for ROS scavenging system.

The model is now able to simulate basal ROS devoid of the presence of doxorubicin. Note, NADPH and NAD are fixed at constant values by setting their ODE to equal zero.

Simulation of the model without the presence of quinone predicts basal scavenging dynamics. Figure 2-17 illustrates the model's ability to simulate detoxification mitochondrial ROS in the form of superoxide and hydrogen peroxide. Note that while cellular / mitochondrial ROS will always exist, complete removal occurs in our model as production of superoxide (i.e. basal superoxide formation) as a function of quinone redox cycling is not considered. The most important aspect of this simulation is the maintenance of steady concentrations of GSH/GSSG which is in-line with literature values⁵², as it is GSH that will fundamentally be responsible for complete detoxification, as GSH detoxifies the hydrogen peroxide ROS SOD by-product.

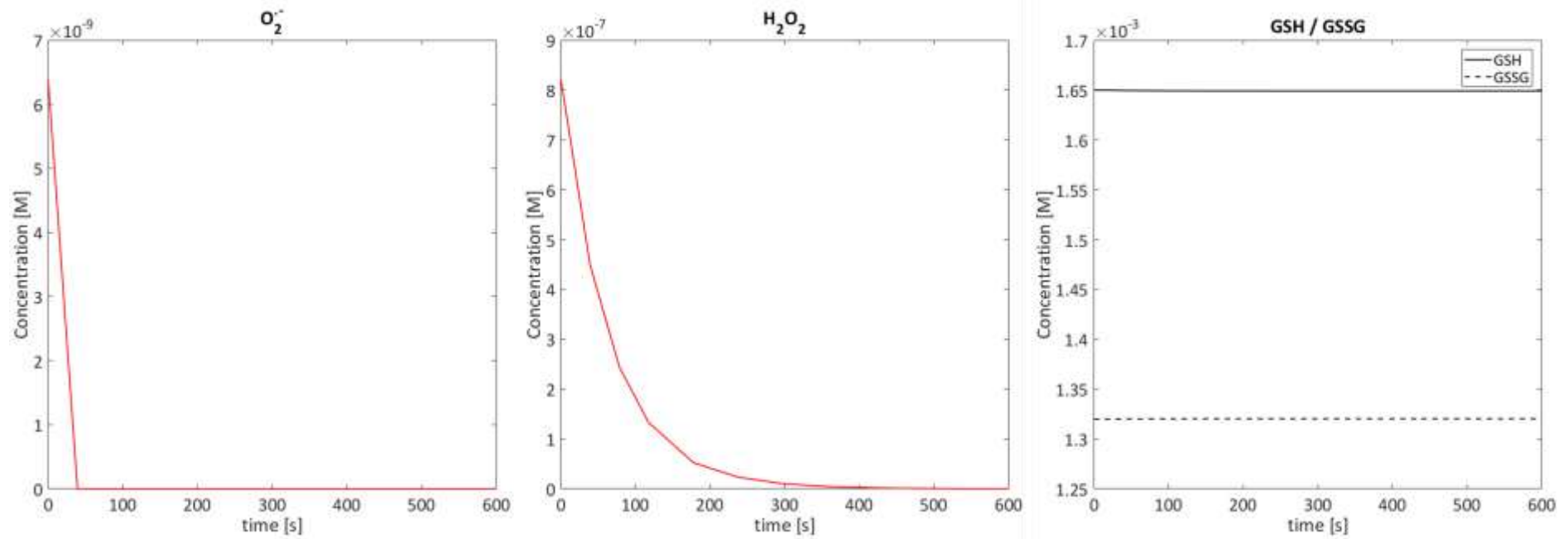


Figure 2-17: ROS scavenging simulations. Model simulation shows detoxification of superoxide into hydrogen peroxide resulting in complete ROS removal. GSH/GSSG scavenging couple remains steady.

2.5 Model predictions & Experimental Validation

The doxorubicin specific quinone redox cycling model is capable of simulating a time course profile of radical species that exist fleetingly *in vitro* and *in vivo*. In order to assess the quality of the model, it is desirable to validate against additional experimental data. Unfortunately, time course data of quinone redox cycling is unavailable, hence the construction of this model. However, it is possible to measure superoxide levels in cellular compartments, such as the mitochondria, using the MitoSOX assay. Superoxide formation within the mitochondria is exceptionally common, with between 1 and 3% of all oxygen consumption forming $O_2^{\cdot-}$ as a function of electron leakage from the electron transport chain ²⁸. Furthermore, elevated ROS within the mitochondria as a result of doxorubicin redox cycling is a postulated mode of cardiotoxicity, due to the mitochondria rich highly energetic cardiomyocyte cells ¹⁶. As such, its administration is severely limited regardless of its antineoplastic properties for a host of malignancies ⁵⁶. Doxorubicin is capable of auto oxidation, however, in a buffered physiological environment it may be reduced by mitochondrial completing the redox cycle and, in turn, initiating a ROS cascade that overwhelms cellular / organelle oxidative stress defences. The most useful application of our new mechanistic mathematical model would therefore be to simulate the increase in mitochondrial $O_2^{\cdot-}$ levels, considering basal superoxide formation, whilst simultaneously assuming mitochondrial reduction as implicit.

2.5.1 Doxorubicin-Induced Mitochondrial Superoxide Formation

Prior to determination of mitochondrial ROS levels, cell viability must be ascertained for a series of concentrations of doxorubicin, followed by calculation of the drug IC50 value for the cell type (see pages 81-84). The IC50 concentration describes the concentration which results in 50 % cell viability. Cell viability as a function of exposure to doxorubicin was determined using HepG2 cells a 24 hours utilizing the MTT and ATP assays as separate methods of assessing cytotoxicity.

All drug solutions were prepared in Me₂SO and diluted leaving the final solvent concentration <5% (v/v) for each incubation. Measurement of Cytotoxicity using MTT and ATP Assays: HepG2 cells (2×10^4) were plated in flat-bottomed 96-well plates in triplicate and allowed to adhere overnight. Cells were maintained in DMEM high glucose medium supplemented with foetal bovine serum (10% v/v), sodium pyruvate (1% v/v), HEPES buffer (1% v/v) and pen-strep (1% v/v). Cells were incubated at 37°C in 5% CO₂ humidified air.

MTT Assay: Cells were exposed to a range of concentrations of doxorubicin (0.005-100 μ M) and incubated for 24 hours. A solution of 3-(4,5-Dimethylthiazol-2-yl)-2,5-diphenyl-tetrazolium Bromide (MTT) in Hanks balanced salt solution (HBSS) was prepared (0.5 mg ml⁻¹) and 20 μ l was added to each well and incubated for a further 2 hours. Finally, 100 μ l of a lysing buffer (N,N-dimethylformamide 50% v/v; sodium dodecyl sulphate 20% w/v) was charged to each well before further incubating for 4 hr. Samples absorbance's were measured at a test and reference wavelength of 570 and 590 nm respectively with a plate reader (MRX, Dynex).

ATP Assay: Cells were exposed to a range of concentrations of doxorubicin (0.005-100 μ M) and incubated for 24 hours. ATP content of the cells was measured using a Cell Titer-Glo kit following the manufacturer's instructions. 20 μ l of assay reagent was added to each well and shaken for 1 minute. 100 μ l from each well was then plated onto a white 96-well flat-bottomed plate and the luminescence was measured using VarioSkan flash plate reader. Data values are expressed as mean \pm SD. D'Agostino and Pearson Omnibus normality test was used to detect normality. One-way ANOVA and Dunnett's post-test were used to analyse all parametric data. Statistical analysis was conducted using Graphpad Prism 5 software.

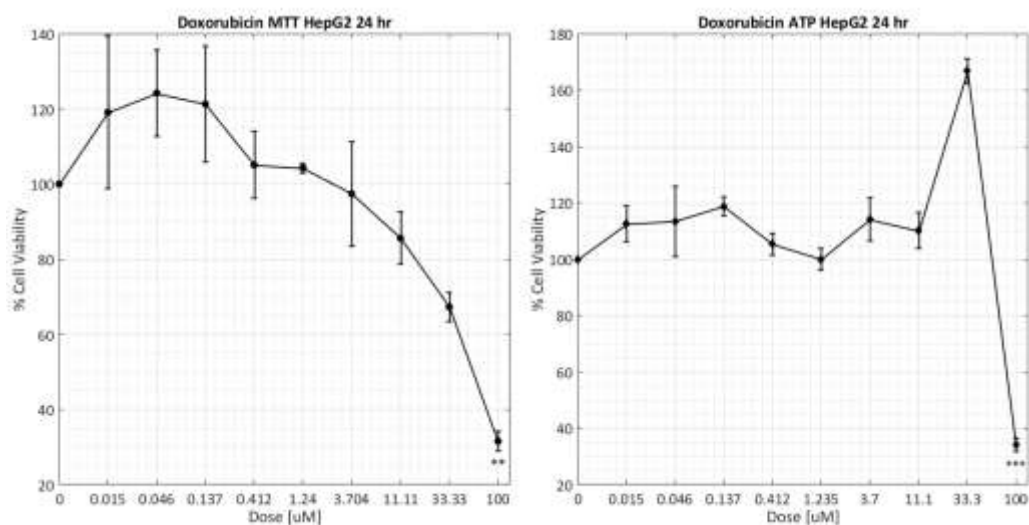


Figure 2-18: Chemosensitivity of HepG2 cells towards Doxorubicin Exposure. Cytotoxicity was assessed using MTT and ATP assays after exposure to doxorubicin for 24hr at a range of concentrations (0.005-100 μM), for 3 independent experiments. Increase in dosing concentrations of doxorubicin leads to an overall decrease in % cell viability for all graphs. * = <0.05 P; ** = <0.01 P; *** = <0.001 P confidence.

Figure 2-18 shows the doxorubicin induced cytotoxicity in HepG2 cells determined using the MTT and ATP cell viability assays. From these data sets, the IC₅₀ value for doxorubicin in HepG2 cells for 24 hour exposure was calculated to be 13.36 μM . The results from the cell viability assay provide a platform from which appropriate concentrations of doxorubicin may be used during the assessment of mitochondrial superoxide levels using the MitoSOX assay. There are, however, considerations to be made. The initial model was constructed using concentrations which, according to the cytotoxicity assays, may cause significant reduction in cell viability. It is important to capture the changes in ROS at these concentrations regardless of the cytotoxicity evident *in vitro* as doing so will allow investigation of the model's ability to cope with a known cytotoxic concentration, especially in terms of model GSH depletion. Also, as described in 1.2.3, the MitoSOX assay is notorious for detecting other ROS specific to the mitochondria. This should be taken into consideration when trying to replicate results within the model.

2.5.1.1 *In vitro* doxorubicin-induced mitochondrial superoxide formation

Doxorubicin induced mitochondrial superoxide concentration changes were determined using the MitoSOX assay. HepG2 cells (1×10^5) were plated in flat-bottomed 24-well plates and allowed to adhere overnight. Incubation conditions were identical to that described in the cytotoxicity investigation.

MitoSOX Assay: 5 μ l of MitoSOX reagent (1 μ M) was added to each well and incubated in the dark for 5 minutes. The supernatant was removed and retained before trypsinising the cells. Cells were re-suspended in the retained supernatant before centrifuged at 2000 rpm for 5 minutes. The supernatant was discarded and the cell pellet was re-suspended in HBSS (300 μ l) and then plated in duplicate (100 μ l) in a white flat-bottomed 96-well plate. Fluorescence was measured at an excitation and emission of 396 and 579 nm respectively using a VarioSkan flash plate reader. Cell lysates were prepared from the remainder of the sample using a sonic probe. Protein content was determined using a Bradford assay and all data was normalized to mg of protein/well.

Figure 2-19 shows the fold increases of mitochondrial superoxide as a function of doxorubicin exposure after 6, 16 and 24 hours in HepG2 cells. Concentrations above 75 μ M yielded significant increases compared to the control which is devoid of doxorubicin for all time points. Additional significance is predicted for 50 μ M at 6 hours. Overall, increases in concentration in doxorubicin at each time-point yields a proportional increase in mitochondrial superoxide. Levels of superoxide increase between 6 and 16 hours, followed by subsequent decreases in fold changes between 16 and 24 hours. This decrease is most likely accredited to the cell cytotoxicity as confirmed in Figure 2-18, where at 24 hours concentrations greater than 13.33 μ M are predicted to result in 50 % cell death. The correlation between elevated mitochondrial superoxide levels as a function of doxorubicin concentration and cell death suggest that both concentration and length of exposure play a role in potential increased mitochondrial superoxide concentration mediated cell death.

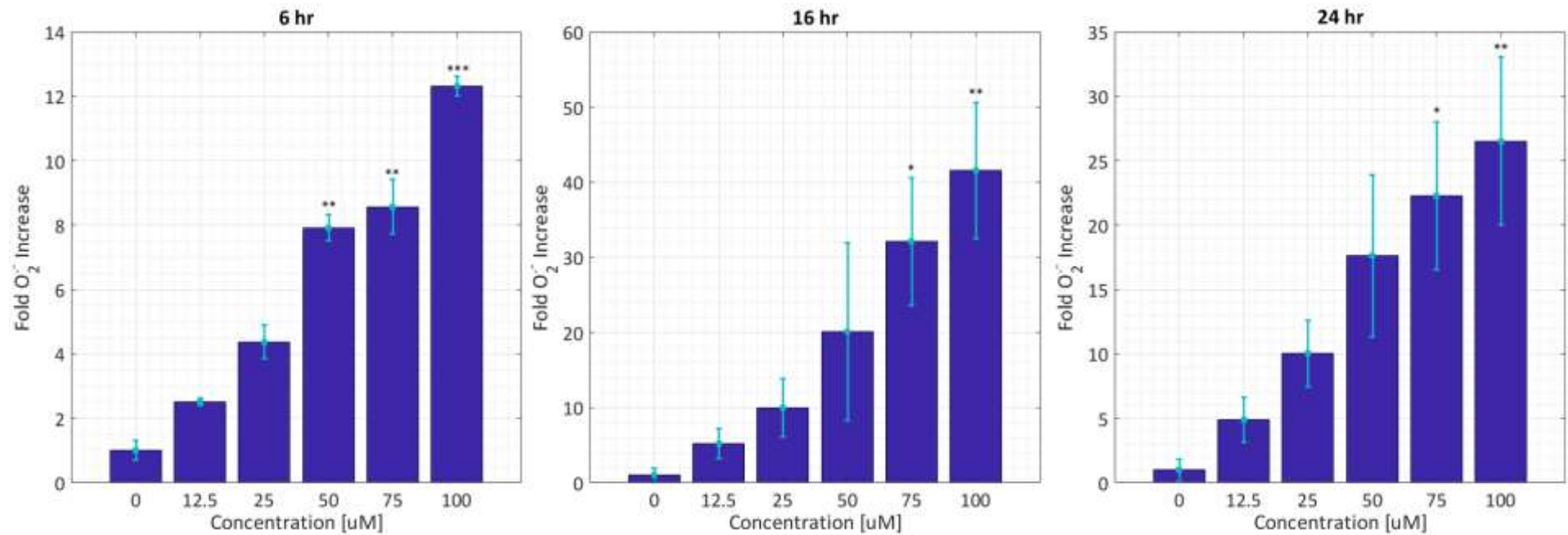


Figure 2-19: Assessment of doxorubicin induced mitochondrial superoxide. Mitochondrial superoxide fold increases as a function of doxorubicin exposure was measured using the MitoSOX assay at a range of concentrations (12.5 – 100 μM) for three independent experiments. Results yielded significant increases in mitochondrial superoxide. * = $p < 0.05$ P, ** = $p < 0.01$ P, *** = $p < 0.001$ P confidence.

The final experiment was to assess the *in silico* models ability to recapitulate the increases in mitochondrial superoxide given as the inputs of the concentration of doxorubicin, its reduction potential, duration of exposure, coupled with the mitochondrial specific ROS scavenging mechanisms.

Figure 2-20 shows the comparison between the MitoSOX data and model simulations for various concentrations of doxorubicin (12.5 – 100 μM) at 6, 16 and 24 hours. For the 6 hour simulations, the model adequately simulates fold increase in ROS for the lower concentration range, with overestimation of ROS between 50 and 100 μM . For the 16 hour simulation, the model accurately simulates ROS increase as a function of doxorubicin concentration, with almost all simulations falling within the error bars of the MitoSOX data. The simulations for 24 hours, however, exceed the MitoSOX data considerably, especially for the higher concentration ranges. It should be noted that the model does not consider cell viability, especially at that time point for the high doxorubicin concentrations. Figure 2-18 shows the decreases in cell viability as a function of these concentrations and as such, the model failing to recapitulate the reduced cell output is a good potential reason for such excessive ROS levels predicted at 24 hours by the mathematical model.

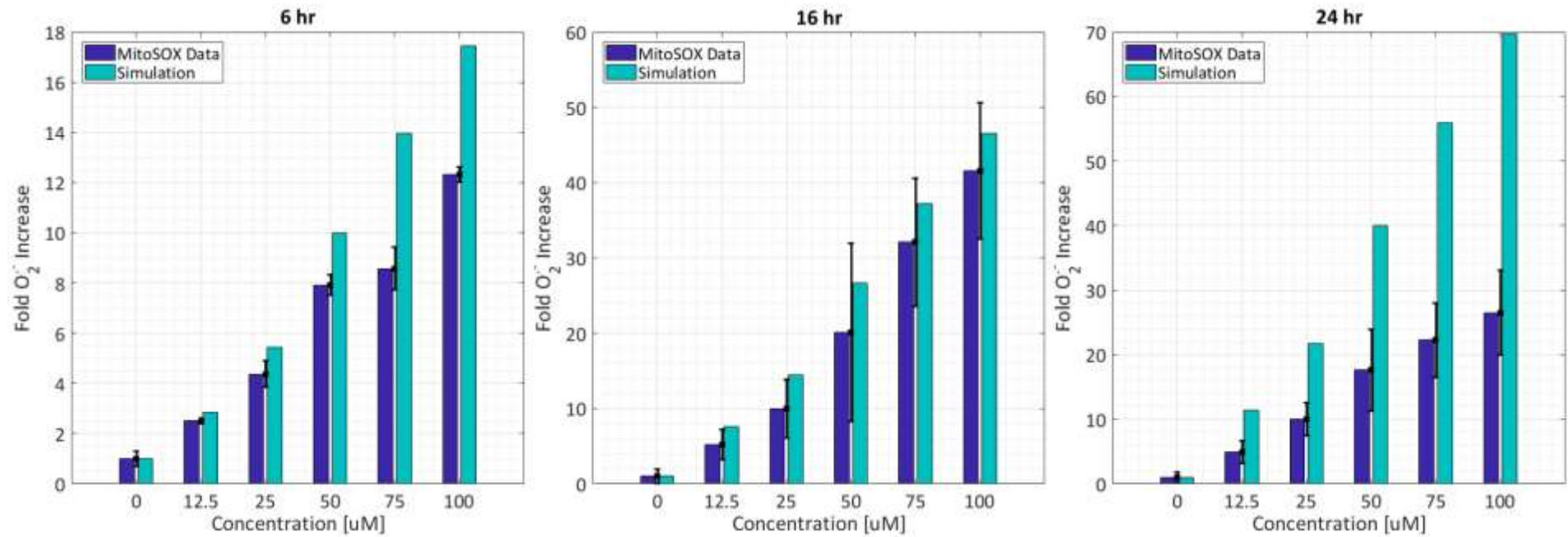


Figure 2-20: MitoSOX assay vs model simulations for doxorubicin redox cycling. Fold increases in mitochondrial superoxide as a function of doxorubicin exposure was compared to the fold increase in model ROS for doxorubicin at 12.5, 25, 50, 75 and 100 μM at 6, 16 and 24 hours. Black error bars are from the MitoSOX data Figure 2-19.

In order to test this hypothesis, the *in silico* model ROS output was normalized at 24 hours according to the predicted experimental decreases in cell viability. First, a simple model was constructed by fitting a line to the cell viability data in Figure 2-18 in order to be able to enter a concentration of doxorubicin and generate a % decrease in cell viability. A single order polynomial fit described by (2-11) fit the model with an R^2 value of 0.96:

$$f(x) = P_1x^2 + P_2x + P_3, \quad (2-11)$$

where $P_1 = -2.05$, $P_2 = 15.01$, $P_3 = 91.96$ and $x = \text{dose}$.

The model was re-simulated accounting for depletion of cell viability by reducing model output as a function of calculated cell death, and compared to the previous 24 hour simulations show in Figure 2-21.

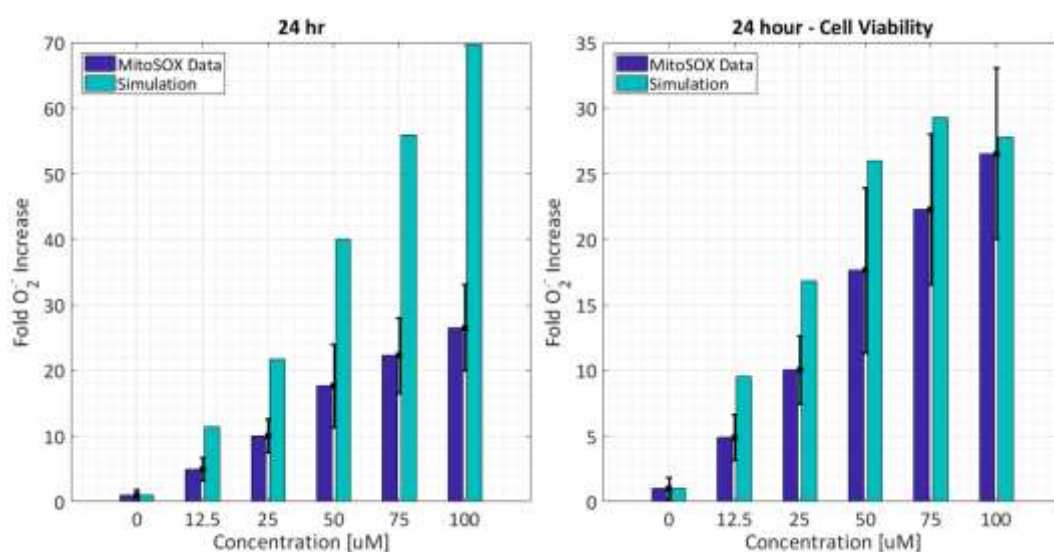


Figure 2-21: Normalizing model ROS output according to *in vitro* cell viability data. Black error bars are from MitoSOX data, simulations after cell viability normalisation show significantly improved resemblance to *in vitro* MitoSOX data.

As we can observe in Figure 2-21, accounting for cell death as a function of doxorubicin concentration at 24 hours allows significantly better model predictions of mitochondrial ROS levels.

2.6 Chapter Discussion

This chapter describes the development of a novel *in silico* model of quinone redox cycling, specifically doxorubicin, that is thermodynamically based in mechanistic in construction, and mechanistic in nature. The physiochemical properties of a plethora of quinones are consolidated into a mathematical framework from which compound specific reduction potentials and the corresponding equilibrium rate constants can be obtained. Unknown kinetic parameters for the doxorubicin redox cycling model were obtained using a novel surrogate *in vitro* extracellular flux analysis assay where the rates of proton consumption and production are measured in real time. The use of cell-free EFA as a surrogate to predict rate constants is not without its uncertainty. This approach is hinged upon doxorubicin's ability to auto-oxidate, as well as re-reduction without the presence or aid of reducing agents or reductase enzymes. It is well documented in the literature that doxorubicin is capable of auto-oxidation in cellular compartments which are well tightly buffered. Within the cell-free *in vitro* EFA method, doxorubicin redox cycling is possible due to two crucial reasons: First, the unbuffered assay media, which allows doxorubicin to dissociate at pH 7 and second, free dissolved oxygen in the media for which electrons may be dumped allowing auto-oxidation. Unbuffered assay media assists in the dissociation of electron density around the quinone and adjacent hydroquinone motifs, prompting formation of a stable semiquinone radical. Auto-oxidation can be confirmed through oxygen consumption during EFA which is doxorubicin concentration dependent.

The model required additional mechanistic information in order to recapitulate the EFA data, specifically, the addition of the comproportionation reaction where iterations of the same variable in different oxidation states are able to rearrange themselves. This addition allowed the model to simulate 6 different concentrations of EFA data using only one dataset to parameterize the model. The model was

expanded to include mitochondrial specific ROS detoxification mechanisms, centred around glutathione metabolism and superoxide dismutase, the kinetic terms and parameters for which were taken from the literature. The model was simulated to illustrate its ability to detoxify literature based levels of ROS while simultaneously keeping the GSH/GSSG redox couple in-tact. The final test for the model was to be able to predict *in vitro* doxorubicin-induced mitochondrial ROS formation. For this, *in vitro* levels of mitochondrial ROS were quantified using the MitoSOX assay on HepG2 cells after exposure to doxorubicin for 6, 16 and 24 hours. The MitoSOX assay probe detects mitochondrial superoxide via a reaction with a specialized hydroethidine compounds and superoxide, which yields fluorescence. This probe is able to localize to the mitochondria as it contains a triphosphonium salt, which targets the mitochondrial membrane. Unfortunately, the major caveat with using this probe is that there can be considerable overlap between fluorescence spectral outputs. That is, fluorescence from reactions between the probe and other ROS cannot be completely distinguished. This can be circumvented to some extent using high performance liquid chromatography (HPLC) but in this instance, it is easier and acceptable to assume that output from the MitoSOX assay is representative of mitochondrial ROS in general. With that in mind, model simulations of mitochondrial ROS are equal to the sum of mitochondrial superoxide and hydrogen peroxide.

Simulations of these time-points proved the model able to predict mitochondrial ROS well for 6 and 16 hours, but overestimates for 24 hours, due to the model not accounting for cell viability. ATP and MTT cytotoxicity assay data for 24 hours exposure to doxorubicin was used to normalize model ROS production, bringing 24 hour simulation to within the error bounds of the *in vitro* data. The ability to simulate this *in vitro* data suggests several important things: EFA *in vitro* cell-free assay is a suitable to ascertain kinetic parameters based on proton consumption and production in this instance. It proves that using thermodynamic and chemistry based methods, combined with experimental data, can facilitate *in silico* prediction of cellular organelle-specific doxorubicin induced ROS formation is possible, despite the

fleeting existence of radical species. Finally, it lends credence to the non-specificity of the MitoSOX assay, as the model uses total ROS to simulate the MitoSOX data.

**3 Chapter 3: Modelling Cellular Bioenergetics: pH-
Dependent Thermodynamic Model of Human
Hepatic Glycolytic Flux**

3.1 Introduction

Extracellular flux analysis (EFA) is gaining momentum as a versatile, high throughput method of assessing cellular bioenergetics for a plethora of biological points of interest, boasting inclusion in over 1500 peer reviewed publications, and is commonly used as a method of investigating drug-induced mitochondrial dysfunction in a wide variety of different cellular systems^{43,57,58}. EFA, using any of the XF analysers (Seahorse instruments), is accomplished by the use of biosensors within a specialised sensor cartridge that measure rates of oxygen consumption and proton efflux. The majority of investigations centre on changes in cellular respiration, quantified by deviations in oxygen consumption rate (OCR), with up until recently, the concomitant ECAR measurements which are assumed to be indicative of glycolytic flux. Respiratory contributions to ECAR may be easily quantified by measuring the buffering power (BP) of the EFA media, allowing quantification of the media's ability to manage changes in pH, while also considering the maximum amount of H⁺ generated per oxygen molecule consumed^{41,42}. Depending upon the experimental conditions and cell type ECAR may be either almost entirely respiratory, or almost entirely glycolytic⁴¹. Despite this, separation of glycolytic specific acidification remains largely underutilized. Such neglect to differentiate between the two outputs may stem from the ambiguities surrounding the source of ECAR. Glycolytic acidification is widely accepted to be a function of lactic acid efflux into the extracellular space, with subsequent weak acid dissociation occurring at physiologically relevant media pH (7.0 – 7.4) as a result of lactic acid having a pKa value of 3.86⁵⁹.

The biological complexity of cellular bioenergetics coupled with EFA intricacies has prompted the construction and use of the mathematical-based approach described in this chapter. Mathematical models present notable benefits to biological research, often by stimulating the logical consolidation of the essential elements of a complex system needed to construct a model, in turn eliciting useful reduced representations. The application of these mathematical techniques enables a deeper understanding

of the fundamental qualitative and quantitative features of a complex system. Consequently, mathematical modelling can guide experimentation, generate testable hypotheses and simulate sometimes difficult biological scenarios in a time- and effort-efficient manner. Several mathematical models of hepatic glucose metabolism exist with an exciting variety of uses including hormonal regulation of glucose metabolism, hepatocellular respiration and bioenergetics and even a comprehensive model of the human hepatocyte used to explore liver physiology^{60–62}. However, current models of hepatic glucose metabolism fail to include pH-dependence and the resulting changes to reaction equilibria and enzyme kinetics. Furthermore, current mathematical models that focus specifically on hepatic cellular bioenergetics in combination with EFA are lacking in metabolic network depth and as a result, authors tend to link ECAR to pyruvate generation, rather than proton release into an extracellular environment, and omit respiratory contributions to ECAR altogether⁶².

This chapter describes a unique pH-dependent, thermodynamically-driven kinetic model of hepatic glycolysis, capable of computing a comprehensive dynamic pH time course that is representative of EFA ECAR measurements. The model captures the rapid binding and unbinding of protons and metal ions with all modelled biochemical species in order to compute a total proton stoichiometry. Accounting for complete proton stoichiometry is crucial, as model ECAR/PPRgly output is calculated by using lactate/H⁺ efflux through the liver-specific monocarboxylate transporter 1 (MCT1)⁶³. The model is aligned with *in vitro* liver specific experimental data, such that simulated ECAR changes are a function of lactate/H⁺ efflux. ECAR sensitivity is determined during sensitivity analysis, yielding the most sensitive model parameters coupled to the respective biochemical reactant. The model was subsequently used to predict changes in extracellular acidification during *in vitro* media removal, eliciting the potential metabolic and physical consequences with respect to ECAR that would not be possible experimentally. This model is the first of its kind with respect to simulating ECAR/PPRgly via the MCT1 as a function of hepatic glycolytic rate only, by deducting respiratory contributions to extracellular acidification.

Aims:

1. To construct a pH-dependent thermodynamic model of hepatic glycolytic flux.
2. Measure glycolytic flux of HepG2 cells *in vitro* accounting for respiratory contributions to acidification.
3. To align the model with *in vitro* experimental data
4. To compare model outputs to ECAR and proton production rate *in vitro* outputs.
5. To use the model to explore the role of lactic acid, compartment volume and the extracellular concentration of glucose on ECAR, to assess the sensitivity of ECAR with respect to extracellular pH, and to investigate model areas responsible for redox state sensitivity.

3.2 Mathematical Modelling

3.2.1 Current Models

With the liver being the fundamental organ in regulating plasma glucose concentrations *in vivo*, coupled with the clinical relevance of glucose related diseases such as diabetes, mechanistic mathematical models of hepatic glucose metabolism already exist. For example, the MitoSYM model ⁶², uses a “pyruvate-to-lactate” metabolic flux to compute ECAR, essentially modelling ECAR as a function of pyruvate metabolism. While the MitoSYM model manages to recapitulate experimental ECAR trends using this method, taking this approach allows for very little mechanistic interpretation regarding the glycolytic status. The MitoSYM model is particularly basic in its inclusion of glycolysis, modelling only glucose uptake and glucose-6-phosphate (G6P) production, the first two of ten enzyme-mediated reactions in the glycolytic pathway. As a result, production and utilisation of NADH is not explicitly modelled. This is a cause for concern as NADH is an integral linking molecule between glycolysis and oxidative phosphorylation via the TCA cycle. Consequently, a vital component that links the two dominant bioenergetic pathways is instead represented as a phenomenological element that is once again dependent upon

pyruvate. Using pyruvate to represent ECAR, NADH turnover and the NADH/NAD ratio, coupled with expressing glycolytic flux via glucose uptake and G6P production, is somewhat ambitious in a model that aims to support the evaluation of compounds in drug development. It is noted, however, that ECAR as a function of glycolytic flux in the MitoSYM model is not the primary focus of the model. Moreover, it is appreciated that in the realm of systems biology one always strives to construct the simplest model that may yield robust insights. This is particularly true as the MitoSYM model is a smaller Tenon in the larger DILI-SYM Mortise ⁶².

Perhaps the most comprehensive model hepatic glucose metabolism is the 2012 König model ⁶¹, which accounts for glucose metabolism in its entirety, including hormonal regulation of hepatic glucose production (HGP) and hepatic glucose utilisation (HGU) used to quantify hepatic contribution to glucose homeostasis ⁶¹. This is a kinetic model validated using 25 different experimental data sets capable of simulating hepatic glucose metabolism under varying physiological states. Furthermore, this model simulates primary hepatic situations with the inclusion of all major glucose metabolism pathways such as glycolysis, gluconeogenesis and glycogen metabolism within human hepatocytes. The model utilizes integrated hormonal regulation via the inclusion of interconvertible phosphorylation states of key enzymes used to simulate changes in insulin, epinephrine and glucagon and their resulting hormonal effects on glucose metabolism. The model reveals the high capacity of the liver to buffer extracellular glucose concentrations during dynamic fasting and postprandial situations. Undoubtedly a powerful tool, the model is not without caveats of its own. It is obvious that the focus of this model is glucose homeostasis, however, this has been accomplished at the expense of setting integral metabolites as constant. For example, the model sets ATP, ADP, AMP, NADH, H⁺ and inorganic phosphate (Pi) as constant values throughout simulations, arguably the most important variables in cellular bioenergetics. Preventing dynamic variation of these model constituents could perhaps encumber overall function of glycolysis as a source of cellular energy in the form of ATP, which in turn, artificially regulates redox

and energy homeostasis within the model. Yet, this remains the most comprehensive kinetic model with a copious amount of experimental liver-specific validation.

In essence, the MitoSYM model is aligned with our intention of describing hepatic glycolytic flux using EFA, but lacks mechanistic depth, whereas the König model presents outstanding mechanistic metabolic detail, but is centred on hormonal regulation of glucose metabolism, rather than bioenergetic output. Furthermore, both of these models fail to include pH-dependence, and thermodynamics during their enzyme kinetics. Including thermodynamic control, and as a result, pH-dependence is crucial when modelling cellular bioenergetics as it is fundamental thermodynamics in the form of proton gradients and free energies that govern the majority of ATP synthesis within the cell during oxidative phosphorylation.

The overall *in silico* motivation to modelling hepatic glycolysis is to generate a thermodynamic driven, pH-dependent model of cellular glycolytic flux that is detailed enough to provide mechanistic insights into cellular bioenergetics, while simultaneously being able to recapitulate *in vitro* EFA measurements. The model will be the first of its kind to achieve this, whilst also accounting for the respiratory contributions to acidification during EFA.

3.2.2 Pathway Selection

Hepatic glycolytic flux describes the utilization of glucose via glycolysis and as such, the *in silico* model will primarily comprise of glycolysis, described in Chapter 1. However, the liver is the predominant organ responsible for maintaining plasma glucose homeostasis, therefore, other subsidiary pathways must be considered when constructing a model that essentially recapitulates glucose metabolism.

3.2.2.1 Glycogenolysis

During times of diminished glucose plasma concentrations, glucose can be generated from glycogen stores as a source of intermediary energy. This process is called glycogenolysis and occurs predominantly in the liver and muscle tissue. This process plays a key role in aiding the liver in its function of buffering plasma glucose levels

and is stimulated by the hormones glucagon and epinephrine. The overall pathway proceeds via Figure 3-1.

Glycogenolysis

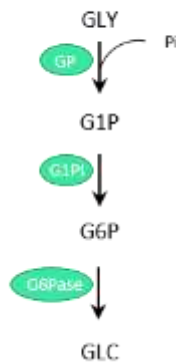


Figure 3-1: Schematic illustrating fundamental components of glycogenolysis. Enzyme-mediated reactions are shown in green. Enzymes: GP, glycogen phosphorylase; G1P, glucosephosphate isomerase; G6Pase, glucose-6-phosphatase. Substrates: GLY, glycogen; Pi, inorganic phosphate; G1P, glucose-1-phosphate; G6P, glucose-6-phosphate and GLC, glucose.

3.2.2.2 Gluconeogenesis

As well as depleting glycogen stores, glucose can be generated from small short chain carbon molecules such as lactate, pyruvate and oxaloacetate. In essence, this may be considered as reverse glycolysis as many of the steps are the opposite of those found in the glycolytic pathway (Figure 3-2). This metabolic process occurs predominantly in the liver where up to 70 % of extracellular lactate is removed from the plasma and catabolized via gluconeogenesis.

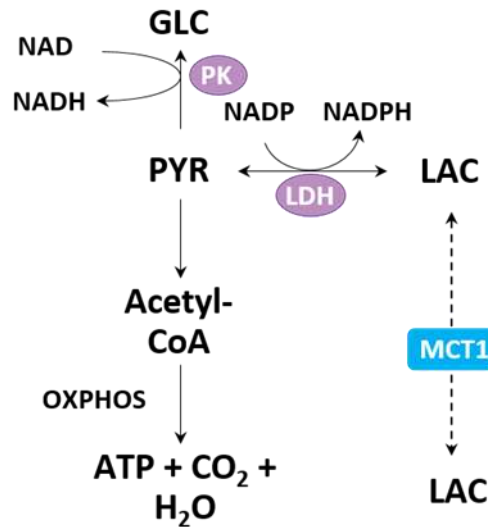


Figure 3-2: Gluconeogenesis. Double-headed reaction arrows illustrate reaction reversibility and as such, subsequent conversion of lactate via pyruvate into glucose.

Figure 3-2 illustrates the transformation of lactate into glucose via a series of enzyme-mediated reactions. Lactate re-enters the cell via the MCT1 transporter, which is then converted back into pyruvate via LDH. Pyruvate is versatile, it can be utilized in the mitochondria via oxidative phosphorylation generating ATP, or converted back into glucose, depending upon what is physiologically needed.

After establishing the pivotal pathways in human hepatic glycolytic flux, one must decide which pathways will be included in the model. The glycolysis pathway forms the backbone of glycolytic flux and so must be included in the model. If modelled carefully, the reverse of the glycolysis pathway will inherently yield a form of gluconeogenesis and therefore this will also be included in the model. Enzymes: PK, pyruvate kinase; LDH, lactate dehydrogenase; MCT1, monocarboxylate transporter 1; OXPHOS, oxidative phosphorylation. Substrates: PYR, pyruvate and LAC, lactate.

Glycogenolysis is arguably the most important part of glucose metabolism in the liver as the majority of glucose is stored as glycogen. Furthermore, *in vivo*, the liver plays perhaps the most important role in buffering plasma glucose concentration during periods of fasting or hypoglycaemia maintaining a strict concentration range

between 3 and 9 mM. This is achieved by using hepatic glycogen stores in order to export glucose when it is needed *in vivo*. However, considering the Warburg effect in carcinoma cell lines and the diminished amount of glycogen storage, glycogenolysis as a metabolic system will be omitted, better allowing our model to represent glycolytic flux within an immortalized cell predominately used for bioenergetic toxicity assessment such as HepG2 cells.

3.2.3 Initial Model Construction

The glycolytic flux model is based on the kinetic model of human hepatic glucose metabolism presented by König *et al.*⁶¹, gaining its pH-dependency and interwoven thermodynamics by constructing it using the BISEN toolset. The model comprises of 14 enzyme mediated kinetic reactions and 2 transport fluxes between a two-compartment system representing the cellular cytoplasm where glycolysis is located and the extracellular space (Figure 3-3)(Table 3-2). Through these 16 enzyme-mediated processes a total of 26 biochemical reactants are utilised, with their compartment location denoted with the suffix *_c* and *_e* for cytoplasm and extracellular species respectively (Table 3-1 and Table 3-2). Model variables are described in mM units and time is represented as minutes yielding reaction and transport fluxes, *J*, with the units: mM min⁻¹.

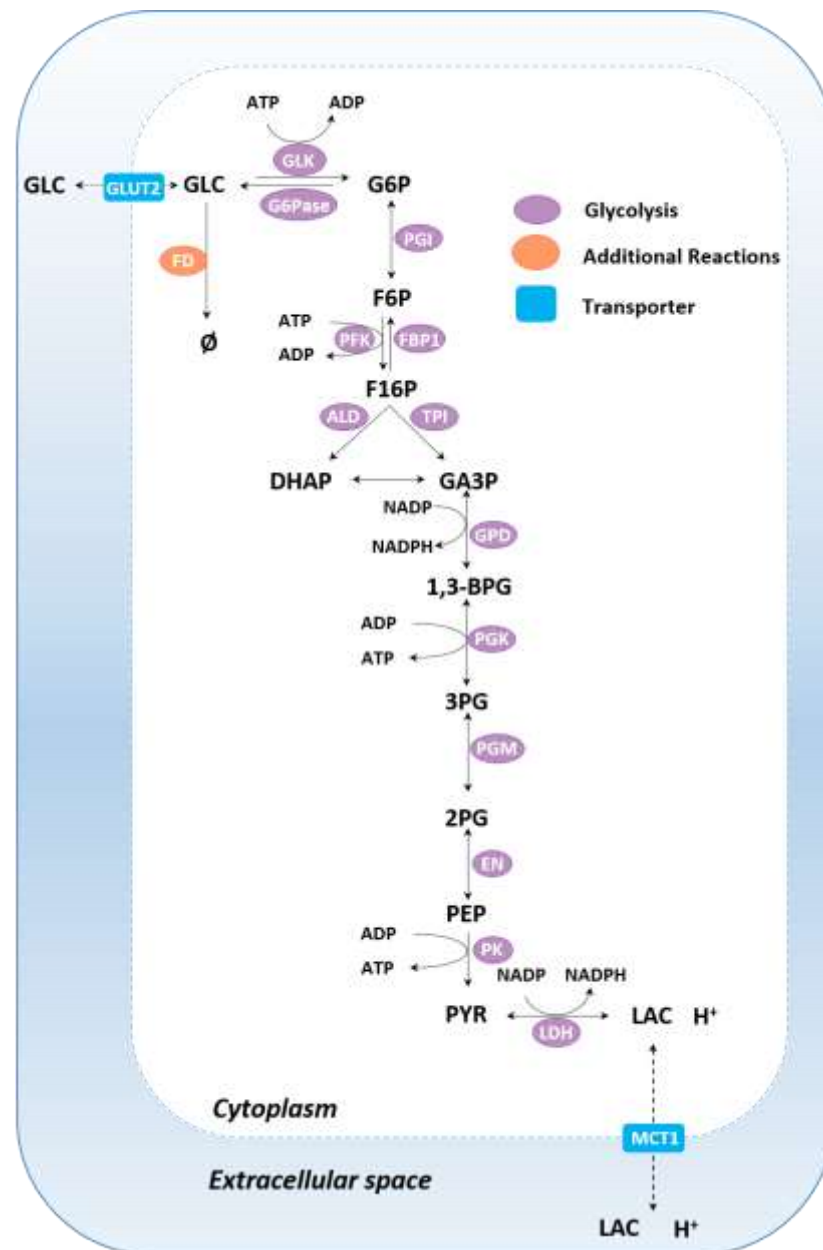


Figure 3-3: Schematic of human hepatic glycolytic flux model. Biochemical model comprising of two compartments: cytoplasm and extracellular space. Glycolytic enzymes are shown in purple, transporter reactions are depicted as blue rectangles and oxidative phosphorylation is portrayed in orange. Reaction descriptions can be found in Table 3-2.

Chapter 3: Modelling Cellular Bioenergetics: Hepatic Glycolytic Flux Model

Variable	Abbreviation	Compartment	Initial Concentration (mM)
Glucose	GLC	Cytoplasm	5.000
ATP	ATP	Cytoplasm	2.800
ADP	ADP	Cytoplasm	0.800
Glucose-6-phosphate	G6P	Cytoplasm	0.120
Fructose-6-phosphate	F6P	Cytoplasm	0.005
Inorganic phosphate	Pi	Cytoplasm	5.000
Fructose-1,6-phosphate	F16P	Cytoplasm	0.020
1,3-bisphospho-glycerate	BPG	Cytoplasm	0.300
Fructose-2,6-phosphate	F26P	Cytoplasm	0.004
Dihydroxyacetone-phosphate	DHAP	Cytoplasm	0.300
Glyceraldehyde-phosphate	GHAP	Cytoplasm	0.100
NAD	NAD	Cytoplasm	1.220
NADH	NADH	Cytoplasm	0.00056
2-phospho-D-glycerate	PG2	Cytoplasm	0.030
3-phospho-D-glycerate	PG3	Cytoplasm	0.270
Phosphoenolpyruvate	PEP	Cytoplasm	0.150
Pyruvate	PYR	Cytoplasm	0.100
Lactate	LAC	Cytoplasm	0.500
Protons	H	Cytoplasm	6.8 (pH)
Magnesium ions	Mg	Cytoplasm	5.000
Potassium ions	K	Cytoplasm	8.000
Glucose	GLC _e	Extracellular	5.000
Lactate	LAC _e	Extracellular	0.000
Protons	H _e	Extracellular	7.4 (pH)
Magnesium ions	Mg _e	Extracellular	0.000
Potassium ions	K _e	Extracellular	0.000

Table 3-1: Model biochemical reactants including their corresponding abbreviation, allocated compartment and initial concentration.

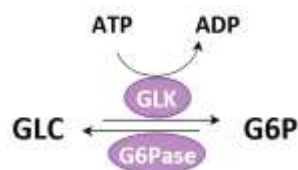
Reaction	Abbreviation	Description
Glucokinase	GLK	$GLC + ATP \rightarrow ADP + G6P + H$
Glucose-6-phosphatase	G6Pase	$G6P + H_2O \rightarrow GLC + Pi$
Phosphoglucose isomerase	PGI	$G6P \rightleftharpoons F6P$
Phosphofructokinase	PFK	$F6P + ATP \rightarrow F16P + ADP + H$
Fructose-1,6-bisphosphatase	FBP1	$F16P + H_2O \rightarrow F6P + Pi$
Aldolase	ALD	$F6P \rightleftharpoons DHAP + GAPH$
Triosephosphate isomerase	TPI	$DHAP \rightleftharpoons GAPH$
Glyceral-3-P dehydrogenase	GAPDH	$GAPH + Pi + NAD \rightleftharpoons BPG + NADH + H$
Phosphoglycerate kinase	PGK	$BPG + 2 ADP \rightleftharpoons PG3 + 2 ATP$
Phosphoglycerate mutase 1	PGYM	$PG3 \rightleftharpoons PG2$
Enolase / phosphopyruvate hydratase	ENO	$PG2 \rightleftharpoons PEP$
Pyruvate kinase	PYK	$PEP + 2 ADP + H \rightleftharpoons PYR + 2 ATP$
Lactate dehydrogenase	LDH	$PYR + NADH + H \rightleftharpoons LAC + NAD$
Glucose Storage (Glycogenolysis)	FD	$GLC \rightarrow \emptyset$
Glut-2-transporter	GLUT2	$GLC_e \rightleftharpoons GLC$
Monocarboxylate transporter 1	MCT1	$LAC + H \rightleftharpoons LAC_e + H_e$

Table 3-2: Model enzyme-mediated reactions including abbreviation and description. Single-headed reaction arrows indicate irreversible, double arrows indicate reversible reactions.

A complete mathematical description of all kinetic rate equations and their allocated parameter values used to construct the model will now be presented, followed by a description of the enzyme role within the pathway and model. All terms and values are derived from the Konig model ⁶¹, unless stated otherwise. Units for each parameter are also presented. Biochemical reactants are presented in square brackets, for example GLC is [GLC]. A schematic of the complete model is shown in Figure 3-3, where biochemical reactants are positioned in their corresponding compartments.

3.2.3.1 Glycolytic Flux Reactions

Glucokinase (GLK):



$$J_{GLK} = v_{max} gk_{free} \frac{[ATP]}{k_m^{ATP} + [ATP]} \frac{[GLC]^n}{[GLC]^n + (k_m^{glc})^n},$$

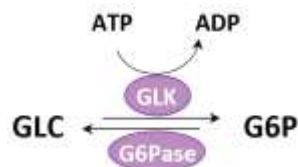
where

$$gk_{free} = \frac{[GLC]^{n_{gkrp}}}{[GLC]^{n_{gkrp}} + (k_{gkrp}^{GLC})^{n_{gkrp}}} \left(1 - \frac{b_{gkrp}[F6P]}{[F6P] + k_{gkrp}^{F6P}} \right).$$

Parameter	Value	Units
n	1.60×10^0	
k_m^{glc}	7.50×10^0	mM
k_m^{ATP}	2.60×10^{-1}	mM
n_{gkrp}	2.00×10^0	
k_{gkrp}^{GLC}	1.50×10^1	mM
k_{gkrp}^{F6P}	1.00×10^{-2}	mM
b_{gkrp}	7.00×10^{-1}	
v_{max}	2.52×10^{-2}	mM min ⁻¹

Glucokinase (GLK) is regulated by the glucokinase regulator protein which is a competitive inhibitor for glucose. The regulatory binding mechanism of this protein is dependent upon glucose and fructose-6-phosphate (F6P) and in turn alters the k_m for glucose.

Glucose-6-phosphatase (G6Pase):



$$J_{G6PASE} = v_{max} \frac{[G6P]}{k_m^{G6P} + [G6P]}.$$

Parameter	Value	Units
k_m^{G6P}	2.00×10^0	mM
v_{max}	1.89×10^{-2}	mM min ⁻¹

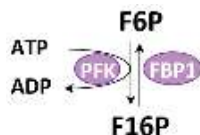
Glucose-6-phosphate isomerase (PGI):



$$J_{PGI} = \frac{\frac{v_{max}}{k_m^{G6P}} \left([G6P] - \frac{[F6P]}{K_{eq}} \right)}{1 + \frac{[G6P]}{k_m^{G6P}} + \frac{[F6P]}{k_m^{F6P}}}$$

Parameter	Value	Units
K_{eq}	5.17×10^{-1}	
k_m^{G6P}	1.82×10^{-1}	mM
k_m^{F6P}	7.10×10^{-2}	mM
v_{max}	4.20×10^{-1}	mM min ⁻¹

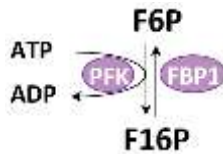
Phosphofructokinase (PFK):



$$J_{PFK} = v_{max} \left(1 + \frac{[F16P]}{k_a^{F16P}} \right) \left(\frac{[G6P][ATP]}{k_i^{F16P} k_m^{ATP} + k_m^{F6P} [ATP] + k_m^{ATP} [F6P] + [ATP][F6P]} \right)$$

Parameter	Value	Units
k_m^{ATP}	1.11×10^{-1}	mM
k_m^{F6P}	7.70×10^{-2}	mM
k_i^{F16P}	1.20×10^{-2}	mM
v_{max}	7.18×10^{-2}	mM min ⁻¹
k_a^{F16P}	1.00×10^{-3}	mM

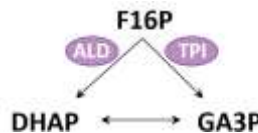
Fructose-1,6-bisphosphatase (FBP):



$$J_{FBP} = \frac{v_{max}}{1 + \frac{[F26P]}{k_i^{F26P}}} \left(\frac{[F16P]}{[F16P] + k_m^{F16P}} \right).$$

Parameter	Value	Units
k_i^{F26P}	1.00×10^{-3}	mM
k_m^{F16P}	1.30×10^{-3}	mM
v_{max}	4.33×10^{-1}	mM min ⁻¹

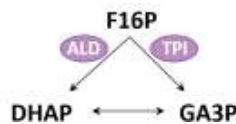
Aldolase (ALD):



$$J_{ALD} = \frac{\frac{v_{max}}{k_m^{F16P}} \left([F16P] \frac{[GAPDH][DHAP]}{K_{eq}} \right)}{1 + \frac{[F16P]}{k_m^{F16P}} + \frac{[GAPDH]}{k_i^{GAPDH}} + \frac{[DHAP]([DHAP] + k_m^{GAPDH})}{k_m^{DHAP} k_i^{GAPDH}} + \frac{[F16P][GAPDH]}{k_m^{F16P} k_{i2}^{GRAP}}}$$

Parameter	Value	Units
K_{eq}	9.76×10^{-5}	mM
k_m^{F16P}	7.10×10^{-3}	mM
v_{max}	4.20×10^{-3}	mM min ⁻¹
k_m^{DHAP}	3.64×10^{-2}	mM
k_m^{GAPDH}	7.10×10^{-3}	mM
k_i^{GAPDH}	5.72×10^{-2}	mM
k_{i2}^{GRAP}	4.2×10^{-1}	mM

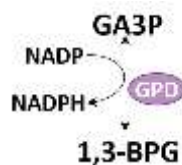
Triosephosphate isomerase (TPI):



$$J_{TPI} = \frac{v_{max}}{k_m^{DHAP}} \left(\frac{[DHAP] - \frac{[GAPDH]}{K_{eq}}}{1 + \frac{[DHAP]}{k_m^{DHAP}} + \frac{[GAPDH]}{k_m^{GAPDH}}} \right)$$

Parameter	Value	Units
K_{eq}	5.45×10^{-2}	mM
k_m^{DHAP}	5.90×10^{-1}	mM
v_{max}	4.20×10^{-3}	mM min ⁻¹
k_m^{GAPDH}	4.20×10^{-1}	mM

Glyceraldehydphosphate dehydrogenase (GAPDH):



$$J_{GAPDH} = \frac{\frac{v_{max}}{k_{NAD} k_{GAPDH} k_{Pi}} \left([NAD][GAPDH][Pi] - \frac{[BPG][NADH]}{K_{eq}} \right)}{\left(1 + \frac{[NAD]}{k_{NAD}} \right) + \left(1 + \frac{[GAPDH]}{k_{GAPDH}} \right) + \left(1 + \frac{[Pi]}{k_{Pi}} \right) + \left(1 + \frac{[NADH]}{k_{NADH}} \right) \left(1 + \frac{[BPG]}{k_{BPG}} \right) - 1}$$

Parameter	Value	Units
K_{eq}	8.68×10^{-2}	
k_{NAD}	5.00×10^{-2}	mM
v_{max}	4.20×10^{-3}	mM min ⁻¹
k_m^{GAPDH}	5.00×10^{-4}	mM
k_{Pi}	3.90×10^0	mM
k_{NADH}	8.30×10^{-3}	mM
k_{BPG}	3.50×10^{-12}	mM

Phosphoglycerate Kinase (PGK):



$$J_{PGK} = \frac{\frac{v_{max}}{k_{ADP} k_{BPG}} \left([ADP][BPG] - \frac{[ATP][PG3]}{K_{eq}} \right)}{\left(1 + \frac{[ADP]}{k_{ADP}} \right) + \left(1 + \frac{[BPG]}{k_{BPG}} \right) + \left(1 + \frac{[ATP]}{k_{ATP}} \right) + \left(1 + \frac{[PG3]}{k_{PG3}} \right) - 1}$$

Parameter	Value	Units
K_{eq}	7.00×10^0	
k_{ADP}	3.50×10^{-1}	mM

v_{max}	4.20×10^{-3}	mM min ⁻¹
k_{BPG}	2.00×10^{-3}	mM
k_{ATP}	4.80×10^{-1}	mM
k_{PG3}	1.20×10^0	mM

Phosphoglycerate mutase (PGM):



$$J_{PGM} = \frac{v_{max} \left([PG3] - \frac{[PG2]}{K_{eq}} \right)}{[PG3] + k_{PG3} \left(1 + \frac{[PG2]}{k_{PG2}} \right)}$$

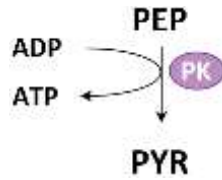
Parameter	Value	Units
K_{eq}	1.84×10^{-1}	
k_{PG3}	5.00×10^0	mM
v_{max}	4.20×10^{-3}	mM min ⁻¹
k_{PG2}	1.00×10^0	mM

Enolase (ENO):



$$J_{ENO} = \frac{v_{max} \left([PG2] - \frac{[PEP]}{K_{eq}} \right)}{[PG2] + k_{PG2} \left(1 + \frac{[PEP]}{k_{PEP}} \right)}$$

Parameter	Value	Units
K_{eq}	5.45×10^{-1}	
k_{PG2}	1.00×10^0	mM
v_{max}	3.60×10^{-3}	mM min ⁻¹
k_{PEP}	1.00×10^0	mM

Pyruvate Kinase (PK):


$$J_{PK} = (1 - \gamma)v^{dp} + \gamma v^p,$$

where

$$v^{dp} = v_{max} \alpha_{inp}^{dp} \left(\frac{[PEP]^{n^{PEP}}}{[PEP]^{n^{PEP}} + (k_{pep,inp}^{dp})^{n^{PEP}}} \right) \left(\frac{[ADP]}{[ADP] + k_{ADP}} \right),$$

and

$$v^p = v_{max} \alpha_{inp}^p \left(\frac{[PEP]^{n^{PEP}}}{[PEP]^{n^{PEP}} + (k_{pep,inp}^p)^{n^{PEP}}} \right) \left(\frac{[ADP]}{[ADP] + k_{ADP}} \right),$$

given

$$(\alpha_{base}^p + (1 - \alpha_{base}^p)f),$$

$$(\alpha_{base}^{dp} + (1 - \alpha_{base}^{dp})f),$$

and

$$\alpha_{inp}^{dp} = (1 - f)(\alpha^{dp} - \alpha_{end}) + \alpha_{end},$$

$$\alpha_{inp}^p = (1 - f)(\alpha^p - \alpha_{end}) + \alpha_{end} ,$$

$$k_{pep,inp}^{dp} = (1 - f)(k_{pep}^{dp} - k_{pep}^{min}) + k_{pep}^{min} ,$$

$$k_{pep,inp}^p = (1 - f)(k_{pep}^p - k_{pep}^{min}) + k_{pep}^{min} ,$$

with

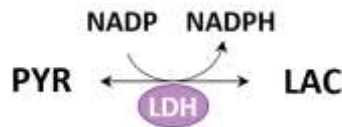
$$f = \frac{[F16P]^{n_{fbp}}}{[F16P]^{n_{fbp}} + (k_{fbp}^{dp})^{n_{fbp}}} .$$

Parameter	Value	Units
n^{PEP}	3.50×10^0	
n^{FBP}	1.80×10^0	
v_{max}	4.62×10^{-2}	mM min ⁻¹
k_{pep}^{dp}	1.10×10^0	mM
k_{min}^{dp}	8.00×10^{-2}	mM
α^{dp}	1.00×10^0	
α^p	1.10×10^0	
α_{end}	1.00×10^0	
k_{fbp}^{dp}	1.60×10^{-4}	mM
k_{fbp}^p	3.50×10^{-4}	mM
α_{base}^{dp}	8.00×10^{-2}	
α_{base}^p	4.00×10^{-2}	
k_{ADP}	2.30×10^0	mM

Phosphofructokinase is one of several integral enzymes involved in hepatic glycolysis as it has an interconvertible phosphorylation state denoted γ . If $\gamma = 1$, the enzyme is modelled in its phosphorylated state and therefore simulates the presence of the hormone insulin leading to increased glycolytic flux. If $\gamma = 0$, the enzyme is modelled in its dephosphorylated state and therefore simulates the presence of the hormones epinephrine and glucagon which reduce glycolytic flux. When modelling carcinoma

cells such as HepG2 cells, glycolytic flux is increased compared to that of normal cells due to the Warburg effect explained earlier. Therefore, when modelling hepatocarcinoma glycolytic flux, any interconvertible phosphorylation states kinetic equations use $\gamma = 1$.

Lactate dehydrogenase (LDH):



$$J_{LDH} = \frac{\frac{v_{max}}{k_m^{PYR} k_m^{NADH}} \left([PYR][NADH] - \frac{[LAC][NAD]}{K_{eq}} \right)}{\left(1 + \frac{[NADH]}{k_m^{NADH}} \right) \left(1 + \frac{[PYR]}{k_m^{PYR}} \right) \left(1 + \frac{[LAC]}{k_m^{LAC}} \right) \left(1 + \frac{[NAD]}{k_m^{NAD}} \right) - 1}$$

Parameter	Value	Units
K_{eq}	2.78×10^{-4}	
k_m^{PYR}	4.95×10^{-1}	mM
v_{max}	1.26×10^{-2}	mM min ⁻¹
k_m^{NADH}	2.70×10^{-2}	mM
k_m^{LAC}	3.20×10^{-1}	mM
k_m^{NAD}	9.84×10^{-1}	mM

Glucose transporter 2 (GLUT2):



$$J_{GLUT2} = \frac{\frac{v_{max}}{k_m^{GLC}} \left([GLC_e] - \frac{[GLC]}{K_{eq}} \right)}{1 + \frac{[GLC_e]}{k_m^{GLC}} + \frac{[GLC]}{k_m^{GLC}}}$$

Parameter	Value	Units
K_{eq}	1.00×10^0	
k_m^{GLC}	4.20×10^1	mM
v_{max}	4.20×10^{-3}	mM min ⁻¹

Monocarboxylate transporter 1 (LACT):



$$J_{LACT} = \frac{\frac{v_{max}}{k_m^{LAC}} \left([LAC_e] - \frac{[LAC]}{K_{eq}} \right)}{1 + \frac{[LAC_e]}{k_m^{LAC}} + \frac{[LAC]}{k_m^{LAC}}}$$

Parameter	Value	Units
K_{eq}	1.00×10^0	
k_m^{LAC}	8.00×10^{-1}	mM
v_{max}	5.42×10^{-3}	mM min ⁻¹

Monocarboxylate transporter 1 is the liver specific enzyme responsible for transport of lactic acid. Lactate is transported in its anionic form as LAC⁻ with co-transportation of a proton. This is due to the lactic acid having a pKa value of 3.82 which as a result

means at pH 7.4 this weak carboxylic acid will exist in its dissociated form. This is very important when modelling extracellular acidification.

Glycogenolysis (FD):



$$J_{FD} = \frac{v_{max} [GLC]^n}{k_m^{GLC^n} + [GLC]^n}$$

Parameter	Value	Units
n	1.00×10^0	
k_m^{GLC}	9.00×10^0	mM
v_{max}	1.00×10^0	mM min ⁻¹

Glycogen storage in HepG2 cells is almost non-existent due to effects previously described in this chapter. However, there will be a level of storage and glucose regulation within the cell that exists outside the scope of this model. To account for intracellular glucose regulation, the essence of glycogenolysis has been captured using the glycogenolysis term J_{FD} . This expression is used to prevent intracellular glucose concentrations from exceeding physiological levels of intracellular glucose for the model. HepG2 cells in standard *in vitro* cell culture are exposed to glucose concentrations approximately 5-fold higher than physiologically realistic levels. In order to prevent intracellular glucose concentration from inevitably equilibrating to that of the extracellular environment, a k_m value of 9 mM has been estimated (hyperglycaemic condition). The other two parameters n and v_{max} have been assigned

arbitrary values of 10 and 1 respectively for the initial model, with the view to amend these values to match experimental data in later work.

3.2.3.2 BISEN Inputs

Each kinetic term was written into corresponding biochemical BSL file as described in 1.2.4.1. Compartment volumes and corresponding water fractions were set in the overall BSL construction file. In this model, the cytoplasm compartment represents the total intracellular volume occupied by 25×10^3 cells, calculated using the density of liver tissue and the average radius of a HepG2 cell. Using a value of 9×10^{-6} m for the cell radius r ⁶⁴, and assuming cells are spherical, the volume of 25×10^3 cells V_1 , was calculated using Equation (3-1).

$$V_1 = \frac{4}{3} \pi (9.0 \times 10^{-6})^3. \quad (3-1)$$

This yields a single cell intracellular volume of 3.0536×10^{-15} m³. The density of liver tissue is 1.077 g ml⁻¹⁶⁵ and 1 m⁻³ = 1 L at this density. Using these values and scaling up from a single cell to 25×10^3 cells gives a total intracellular volume of 7.364×10^{-8} L. The extracellular volume in this model does not represent the entire well volume but the microchamber volume. This is because EFA lowers a fluorescent measuring probe approximately 200 μ m above the cell monolayer at the bottom of the well to measure OCR and ECAR creating a transient microchamber. These measurements are repeated every 3 minutes, until the gradient of OCR / ECAR is linear. This indicates a constant rate of consumption / production in the microchamber before the probe is retracted. The contents of the well are then allowed to equilibrate before the next measurement cycle. As a result, all measurements are a function of the microchamber volume as opposed to the entire well. Therefore, the extracellular compartment volume is equal to the microchamber volume which is 2.0×10^{-6} L⁶⁶. The compartments are set in the BSL construction file as a fraction of the total volume. The total volume occupied by the cells and microchamber as a percentage of the total model volume is 0.0368 and 99.9632 % respectively, with the total water fraction for both compartments being initially set to 1 . There are 2 variables set constant in the

cytoplasm compartment: H^+ and P_i . As the tricarboxylic cycle (TCA) has not been modelled, the source of intracellular proton production is also therefore omitted. To prevent complete intracellular proton depletion, intracellular pH was fixed at pH 6.8 by keeping H^+ constant, however, for the initial simulation intracellular pH was not clamped in order to observe the variable time course and determine if its changes were qualitatively sound. Intracellular inorganic phosphate was held constant at 5 mM, as it was also held constant in the Konig model ⁶¹. Intracellular free phosphate is carefully maintained in cellular physiology by mechanisms not included within this model and was therefore held constant also. In the extracellular compartment, free magnesium and potassium ions were also held constant as the media used in EFA is an unbuffered solution.

3.2.4 Preliminary Simulations & Model Development

The BISEN toolset generated a pH-dependent model of hepatic glycolytic flux represented as a system of ordinary differential equations (ODEs) (Table 3-3), that are pH-dependent with respect to enzyme kinetics.

$d[GLC]/dt =$	$-J_{GLK} + J_{G6PASE} - J_{FD} + J_{GLUT2}$
$d[ATP]/dt =$	$-J_{GLK} - J_{PFK} + 2 J_{PGK} + 2 J_{PYK}$
$d[ADP]/dt =$	$J_{GLK} + J_{PFK} - 2 J_{PGK} - 2 J_{PYK}$
$d[G6P]/dt =$	$J_{GLK} - J_{G6PASE} - J_{PGI}$
$d[F6P]/dt =$	$J_{PGI} - J_{PFK} + J_{FBP1}$
$d[P_i]/dt =$	0
$d[F16P]/dt =$	$J_{PFK} - J_{FBP1} - J_{ALD}$
$d[BPG]/dt =$	$J_{GAPDH} - J_{PGK}$
$d[F26P]/dt =$	0
$d[DHAP]/dt =$	$J_{ALD} - J_{TPI}$
$d[GHAP]/dt =$	$J_{ALD} + J_{TPI} - J_{GAPDH}$
$d[NAD]/dt =$	$-J_{GAPDH} + J_{LDH}$
$d[NADH]/dt =$	$J_{GAPDH} - J_{LDH}$
$d[PG2]/dt =$	$J_{PGK} - J_{PGYM}$
$d[PG3]/dt =$	$J_{PGYM} - J_{ENO}$
$d[PEP]/dt =$	$J_{ENO} - J_{PYK}$
$d[PYR]/dt =$	$J_{PYK} - J_{LDH}$
$d[LAC]/dt =$	$J_{LDH} - J_{LACT}$
$d[GLC_e]/dt =$	$-J_{GLUT2}$
$d[LAC_e]/dt =$	J_{LACT}

Table 3-3: Hepatic glycolytic flux model ODEs, excluding ion equations.

Variable time course and reaction flux simulations were generated by integration of model equations using the variable-order stiff solver ode15s in Matlab 2015b, coupled with relative integration and absolute integration tolerances of 1.0×10^{-4} and 1.0×10^{-10} respectively. An additional solver option setting the maximum solver step size "MaxStep" was used, set to 5.0×10^{-2} . For time course simulations, steady state solutions are reached when changes in all variable concentrations do not exceed the size of the absolute integration tolerance for a time interval of ≥ 2000 seconds. Rather than derive a steady state mathematically, this definition of a steady state is better suited to represent a large scale dynamic system. The initial preliminary simulation was conducted over a 300 minute time period. The primary aim of the initial simulations was to establish whether or not the BISEN toolset could successfully construct a model that could reproduce the well-defined states previously achieved in the literature.

Initial model simulations over a duration of 300 minutes yielded dynamic variable curves that deviate from initial conditions only slightly for the majority of the variables, predominantly remaining within the same order of magnitude, shown in Figure 3-4. A dynamic pH time course was simulated accounting for differences in pH in both cytoplasm and extracellular compartment. This was accomplished using the method described in chapter 1 and is a function of total proton stoichiometry within the model. The initial decrease in intracellular pH suggest an increase of intracellular proton concentration caused by an imbalance in the intracellular proton stoichiometry. Extracellular pH also decreased as a result of the MCT1 transporter successfully pumping protons into the extracellular environment.

Variable time course solutions failed to equilibrate by the end of the simulation. The reactions that influence the variables F16P, GAP, and DHAP were examined and altered in order to correctly reflect the homeostasis conditions in the unperturbed system.

In order to investigate variables of concern, the reaction fluxes of the model were simulated as a method of assessing which reactions, aside from those directly linked

to these variables, which may be causing instability. Figure 3-5 shows the total flux, J , of each reaction within the model during the simulation. The majority of the reaction fluxes were constant over the simulation, however, FBP and PYK were still in a dynamic state as the simulation concluded. Unsteady flux through the FBP reaction shown in the FPB flux plot in Figure 3-5 presented a possible explanation for instability of the F16P variable and therefore this variable and its associated reactions were examined first.

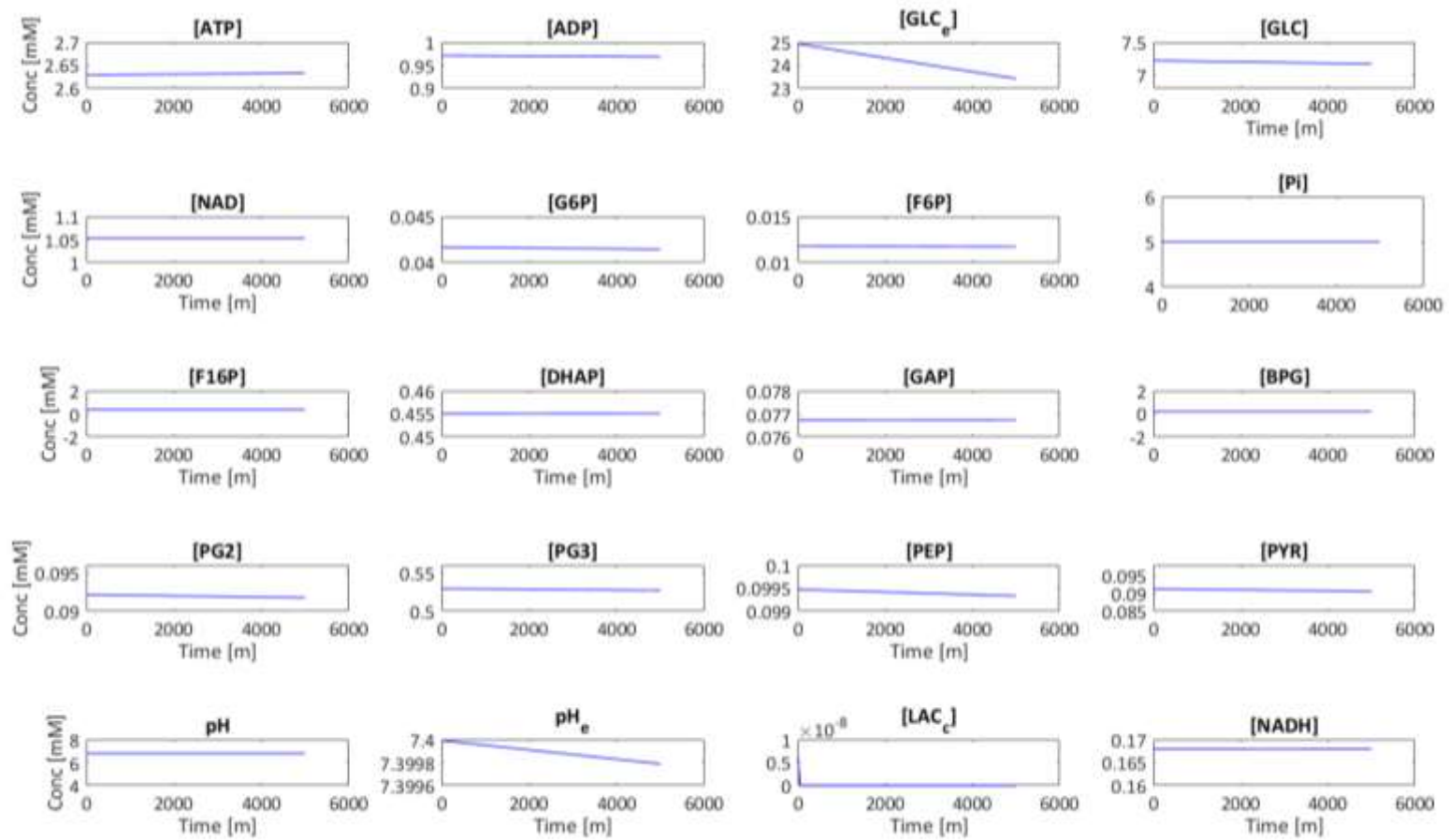


Figure 3-4: Plots showing the initial variable time course simulation of the hepatic glycolytic flux model.

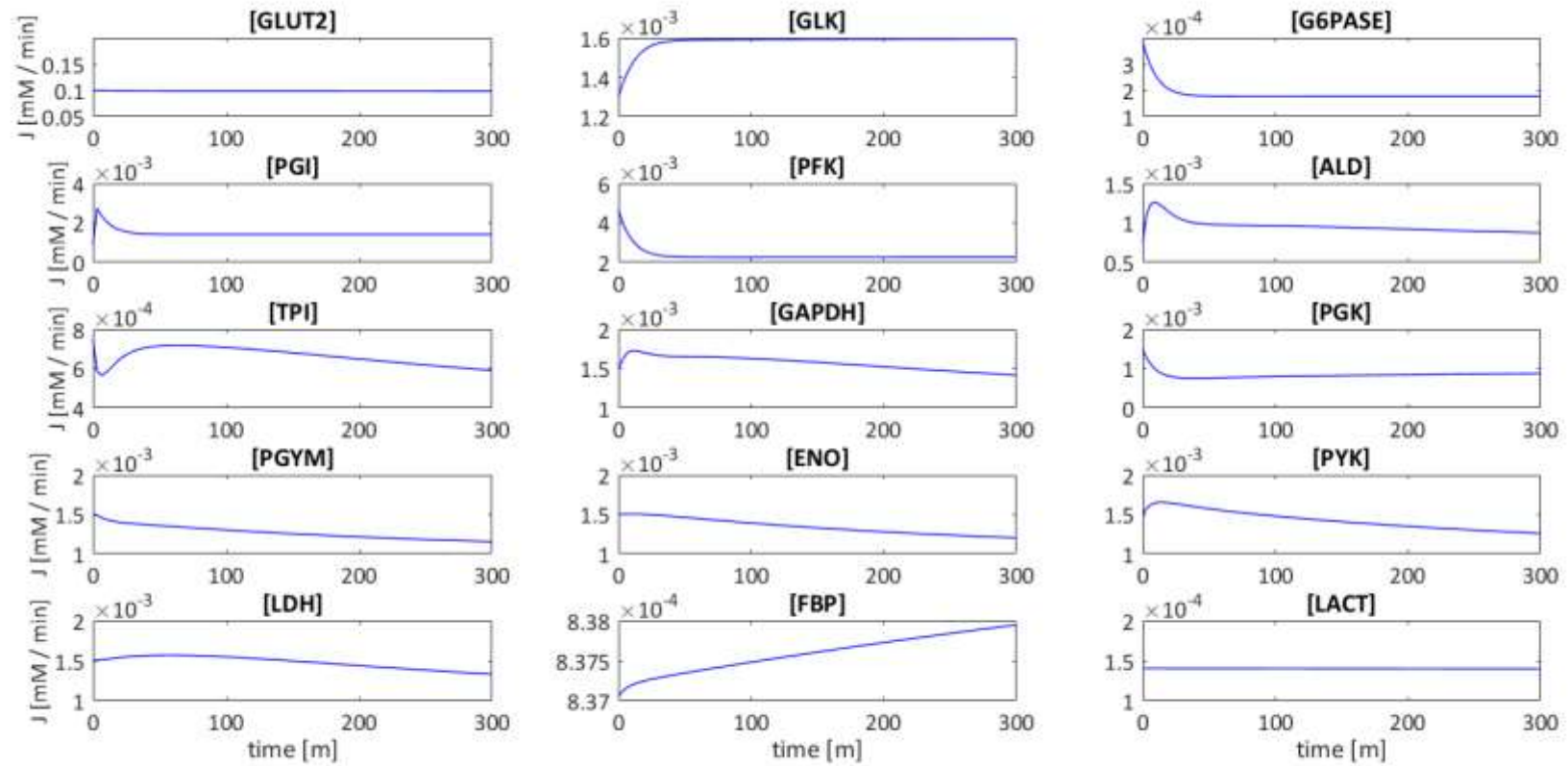


Figure 3-5: Plots showing the initial reaction flux time courses of the hepatic glycolytic model.

Plotting the individual reaction fluxes shows discrepancies in production and consumption fluxes specific to the variables of concern. Figure 3-6 highlights the reaction fluxes responsible for three variables of concern and one flux balanced variable BPG. The most important part of these simulations are the black cross and red circle plots that are the total production and consumption fluxes respectively. If the model were at steady state, these two plots would be the same shown in the F6P plot. The GAP plot shows only slight imbalance between the production and consumption with the two plots almost aligned. The DHAP flux plot clearly shows an imbalance of production and consumption fluxes, with the red consumption flux approximately 0.5 mM min^{-1} lower.

The F16P flux terms are of higher concern as the production and consumption terms are neither close nor appear to be converging. In fact, towards the latter stages of the simulation they appear to diverge. From this qualitative flux balance analysis, it was decided that F16P is at this point the variable of highest concern, provoking investigation of the reactions responsible for its consumption and production.

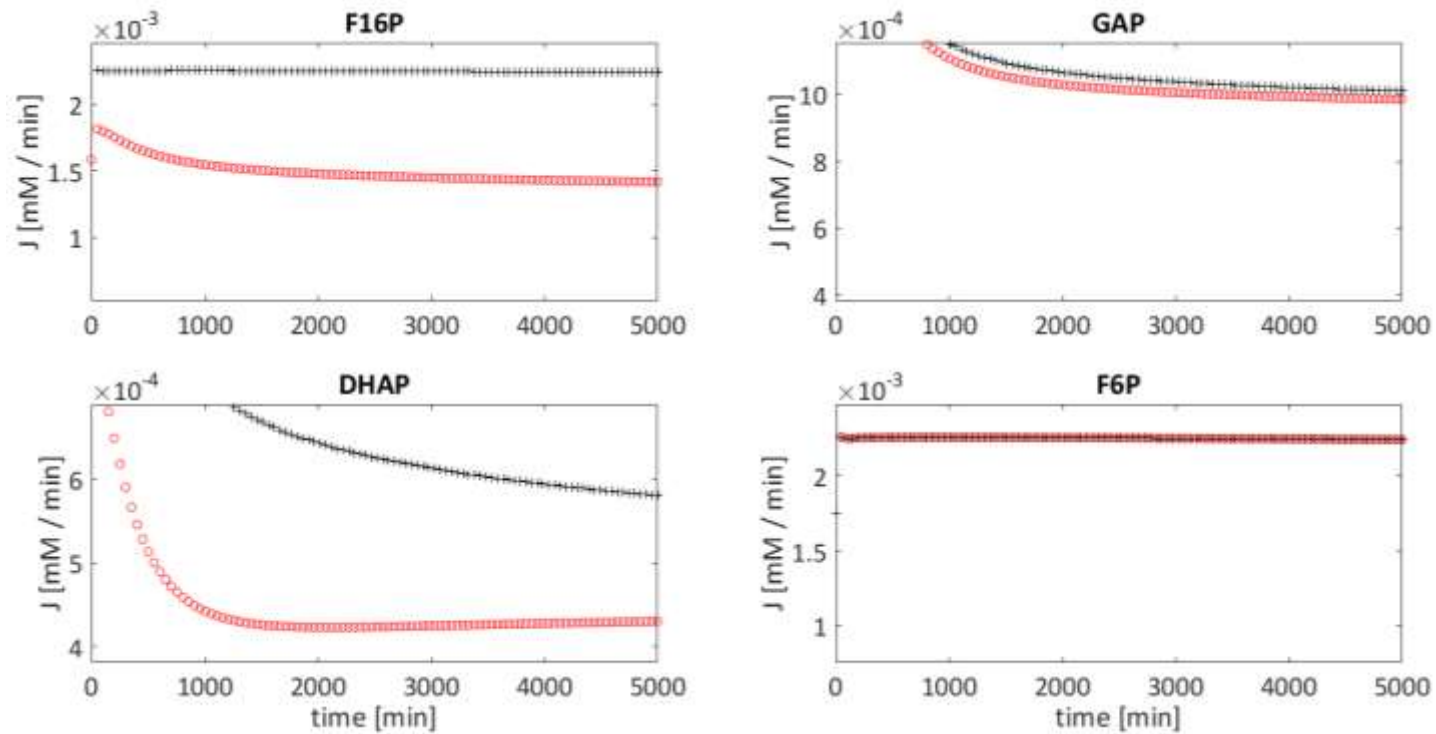


Figure 3-6: Variable specific flux analysis: Reaction fluxes responsible for production and consumption of specific variables were separated by showing production flux simulations in black and consumption fluxes in red. The sum of all production and consumption fluxes are plotted with crosses and circles respectively. F16P, DHAP and GAP are variables of concern, with F6P plotted as an example of balanced production and consumption

As previously discussed, there are significant pathway omissions in the BISEN generated pH-dependent model compared to the glucose metabolism model from which the kinetic terms were selected. For example, the pH-dependent model excludes glycogenolysis and the mitochondria along with its components. Focusing on differences between the two models around the F16P variable, two enzyme reactions were omitted directly linked to the production and consumption of F16P, phosphofructokinase (PFK2) and fructose-2,6-bisphosphatase 2 (F26P) (Figure 3-7).

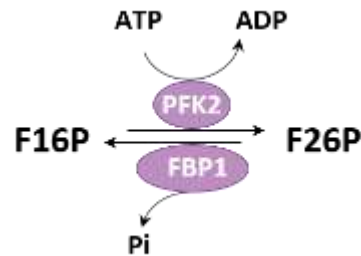


Figure 3-7: Enzyme mediated removal and production omitted from the pH-dependent model.

Omission of these enzymes may be responsible for the discrepancy highlighted in the flux balance analysis of F16P either by decreasing production flux of F16P via the FBP reaction from F26P, or increasing the consumption flux via the PFK2 reaction. Since F26P is held constant within the pH-dependent model used only as an allosteric reactant, it was decided to implement a removal term in the model for F16P in the form of a linear decay within the FBP reaction. The new kinetic term for FBP now includes a mass-action-based decay term with a new parameter k_{fbp1} which was manually adjusted to 2.0×10^{-3} .

$$J_{FBP} = \frac{v_{max}}{1 + \frac{[F26P]}{k_i^{F26P}}} \left(\frac{[F16P]}{[F16P] + k_m^{F16P}} \right) + k_{fbp1}[F16P]. \quad (3-2)$$

The initial simulation was repeated to include the new FBP kinetic term, as well as setting any variable that is devoid of a sink to constant. This included extracellular pH, extracellular lactate and extracellular glucose. Furthermore, the simulation duration was extended to 3.0×10^4 minutes to allow the model to reach a steady state. A steady state of the model was shown by this extended variable time course simulation and flux balance analysis simulation in Figure 3-8 and Figure 3-9 respectively. Using both variable and flux simulations allows the model to be viewed on a component and system scale, as the fluxes are often described as the variables of the system. The variable concentrations must conform to the demands of the system in order to balance its fluxes in a steady state. Figure 3-8 and Figure 3-9 illustrate the models capability of having a steady state that satisfies both a component and system level.

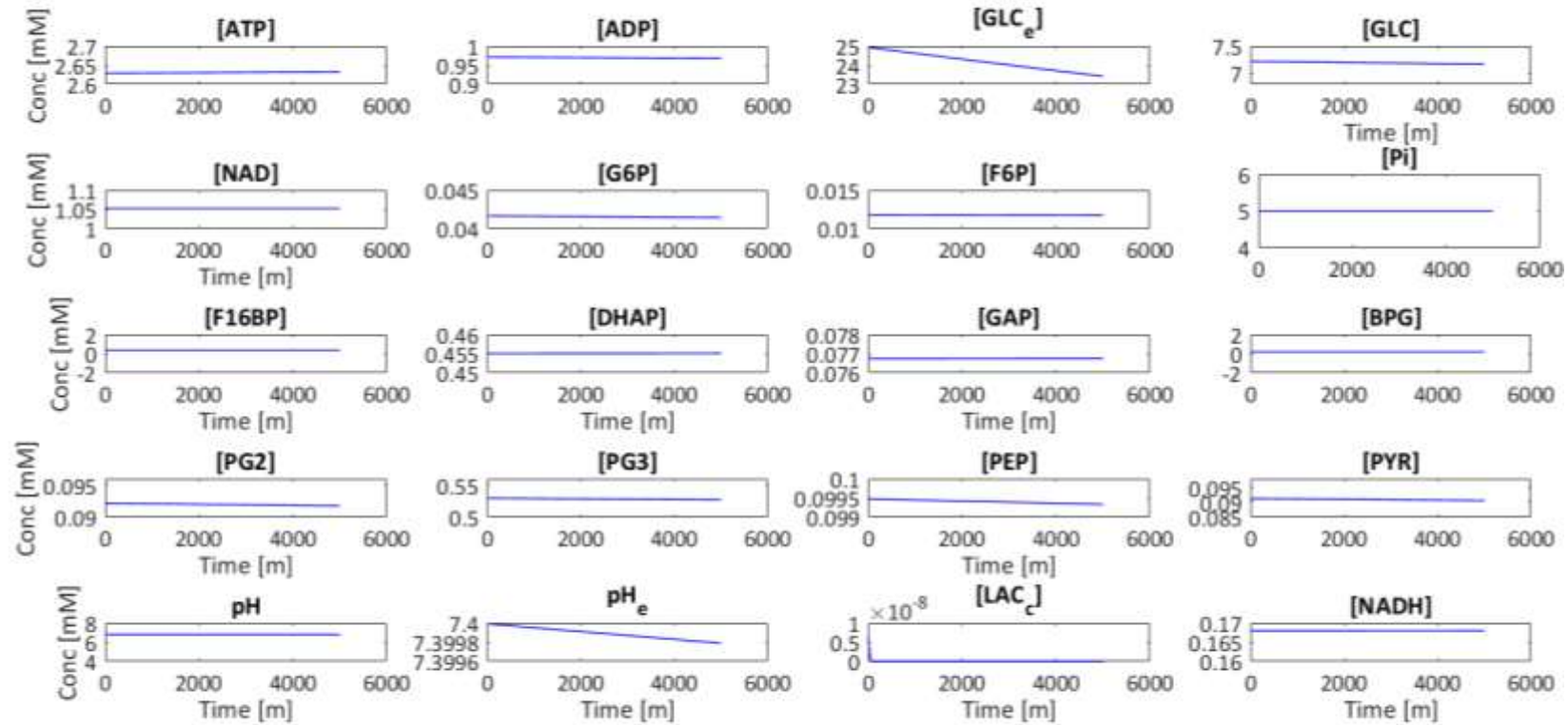


Figure 3-8: Plots showing variable quasi-steady state time courses with amended FBP reaction.

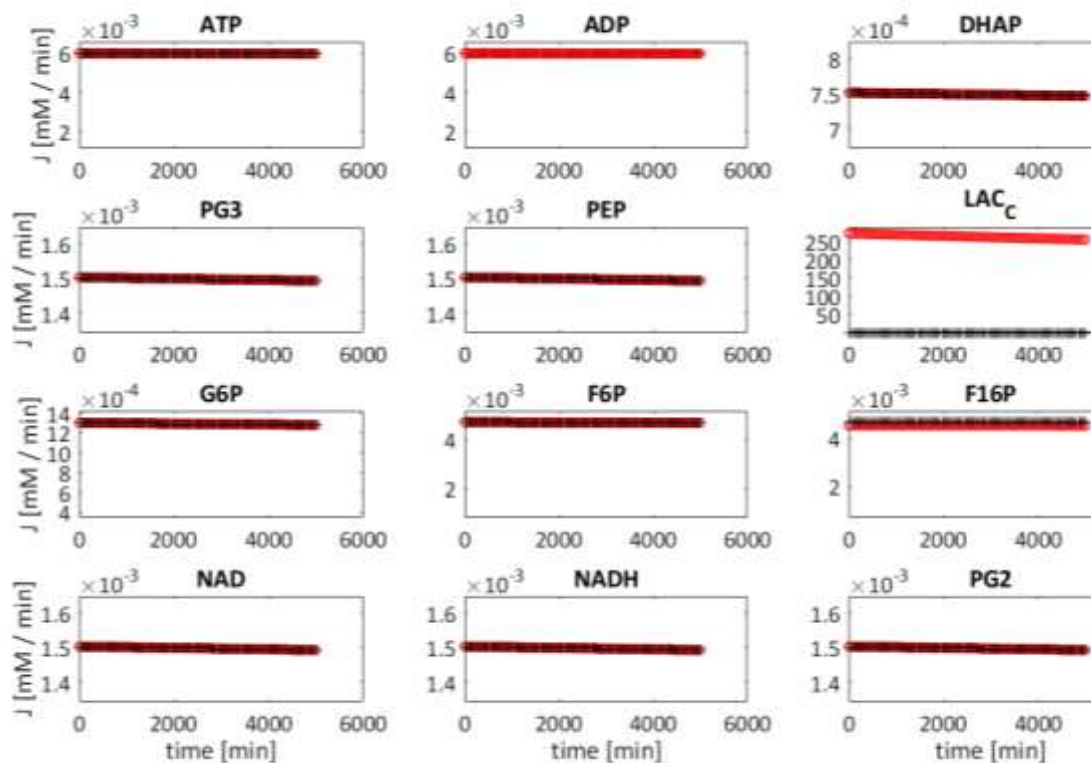


Figure 3-9: Plots showing variable specific flux balance analysis time courses for the hepatic glycolytic model. Reaction fluxes responsible for production and consumption of specific variables were separated by showing production flux simulations in black and consumption fluxes in red. The sum of all production and consumption fluxes are plotted with crosses and circles respectively.

3.2.5 *In silico* ECAR Simulation

The first aim of this chapter was to construct a pH-dependent model of hepatic glycolytic flux capable of accurately generating ECAR outputs to be used synergistically with *in vitro* extracellular flux analysis. Now that a model has been constructed and shown to reach a quasi-steady state that makes qualitative and quantitative sense for both variable and reaction fluxes, a preliminary plot of ECAR may be simulated. That is, having model steady state values that are near to the initial conditions that are measured.

ECAR is a measurement used to indicate overall glycolytic flux during EFA, used in combination with OCR. It is widely accepted that increased ECAR, often as a response to impaired mitochondrial function, is reflective of cellular capability to circumvent compromised energy metabolism. Regardless of the complexity of cellular energy metabolism, cancer cell energy metabolism has gained interest as a therapeutic target ⁶⁷. In EFA, ECAR is measured by a sensor probe containing a fluorophore capable of detecting proton extraction from a monolayer of cells. The probe itself descends into the well trapping approximately 2 μl of media above the monolayer creating a transient microchamber 200 μm above the cell surface. This process occurs at 5 to 8 minute intervals allowing the probe to measure the proton concentration change continuously for 2 to 5 minutes until the rate of change is linear. The gradient of this slope is calculated to determine the rate of proton efflux (ECAR). Once this process is complete, the probe is withdrawn from the well allowing the contents of the microchamber to re-equilibrate with the rest of the well.

The pH-dependent model computes a dynamic pH time course by accounting for total proton stoichiometry enabling accurate simulation of proton efflux into the extracellular compartment. Having already discussed how liver systems use the MCT1 co transporter to facilitate the transportation of lactic acid in the form of lactate and protons at physiological pH, the efflux of protons and lactate are stoichiometrically equal and therefore the MCT1 flux values as a function of time were used to model ECAR.

In silico ECAR and PPRgly was simulated as a function of the MCT1 transport flux, JMCT1, expressed in mM min^{-1} . Conversion from *in silico* transport flux of mM min^{-1} to the *in vitro* PPR pmol min^{-1} measurement was accomplished using Equation (3-4), and total model ECAR (mpH min^{-1}) was converted using Equation (3-3). Note, this conversion equation also includes normalization for experimental protein content, where *PNF* is the protein normalization factor which is equal to the total protein content per well:

$$ECAR = \frac{\left(-\log_{10}\left(\frac{J_{MCT1}}{1 \times 10^3}\right)\right) 1 \times 10^{-3}}{PNF}, \quad (3-3)$$

$$PPR = \frac{1 \times 10^9 (J_{MCT1})}{PNF}. \quad (3-4)$$

This first converts the flux concentration from mM to M, followed by transforming mM into pH and then into mpH, yielding mpH min⁻¹. The changes in volume from the cell to cytoplasm was also accounted for as the ECAR measurement is taken in the microchamber and is therefore not a function of the whole well volume. To account for this, the flux is then expressed as a function of the size difference of the microchamber compared to the total well volume. The total amount of media in the well is 200 µl and the microchamber volume is 2 µl therefore the flux was multiplied by 1.0 × 10⁻³ thus scaling the flux to the size of the microchamber. Finally, like most experiments involving cells, final output values are normalized by protein content. EFA ECAR data is usually expressed as mpH min⁻¹ µg protein⁻¹ or mpH min⁻¹ well protein⁻¹. For this reason, the scaling factor must be malleable depending on which format the ECAR data is returned.

Model ECAR was simulated for *PNF* values that encompasses both mpH min⁻¹ µg protein⁻¹ and mpH min⁻¹ well protein⁻¹ for the 25×10³ cell seeding densities. At that seeding density, biologically relevant *PNF* values range between 1 and 10 (Figure 3-10).

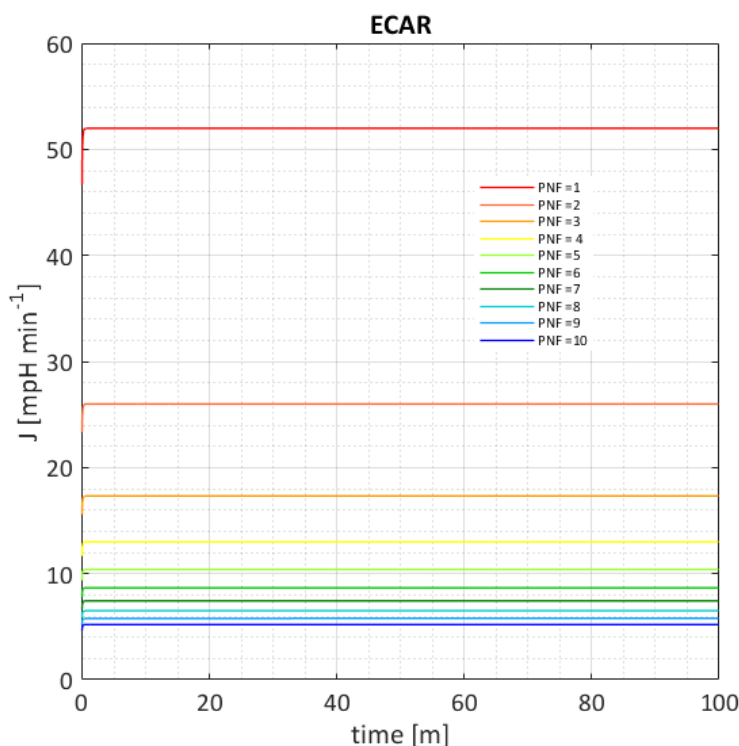


Figure 3-10: Changes in ECAR as a function of cellular protein content. PNF represents the protein normalisation factor in Equation (3-3).

When ECAR is a positive value and remains positive during experimentation, this conversion method is appropriate. However, converting proton concentration in mM into pH involves using a logarithmic transformation, which can lead to imaginary or complex solutions if the ECAR passes from negative to zero yielding an infinite ECAR. This is evidently not present in *in vitro* experimentation but the problem is not inherent in the model, rather, in the experimentation itself. The benefit of mathematically simulating ECAR directly from a transporter flux rather than calculating after measuring a change in concentration is that it is possible to ignore the role of the probe, thus generating an immediate and unhindered flux. As such, *in vitro* experimentation does not require such unit conversion as mpH min⁻¹ is the unit output as a result of having to measure ECAR rather than calculate the transporter flux. Regardless, infinite ECAR is unacceptable. Therefore, calculation of ECAR will include absolute values allowing circumvention of this problem, providing care is taken when expressing the direction of the flux.

3.3 *In vitro* Hepatocarcinoma ECAR

Having constructed a liver specific pH-dependent model of glycolytic flux that is capable of simulating ECAR, the next step was to align it with *in vitro* data in order for it to be considered mechanistically useful. The experimental plan was designed to investigate the effects of extracellular glucose and lactate on ECAR, and to generate an ECAR profile representative of glycolysis only. In order to generate data comparable to outputs from the literature, the HepG2 cells used were cultured in high glucose (25 mM) before and during plating onto the 96 well assay plate. The experimental objective was to inject 10 different concentrations of glucose after the 1 hour glucose free assay media incubation prior to EFA while measuring ECAR before and after injection.

3.3.1 Methods

3.3.1.1 Materials

All seahorse consumables were purchased from Seahorse Biosciences (North Billerica, Ma, USA). Human hepatocarcinoma (HepG2) cell line was purchased from the European Collection of Cell Cultures (Salisbury, UK). DMEM (high glucose, 25 mM), HEPES buffer, foetal bovine serum and collagen (1 Rat tail) were purchased from Invitrogen (ADDRESS). Acetic acid, Hanks balanced buffer solution and sodium pyruvate were purchased from sigma Aldrich (Dorset, UK). All other reagents were purchased from Sigma Aldrich (Dorset, UK).

3.3.1.2 Cell Culture

HepG2 cells were maintained in DMEM high-glucose media (glucose 25 mM) supplemented with foetal bovine serum (10% v/v), L-glutamine (2 mM), sodium pyruvate (1 mM) and HEPES (1 mM). Cells were incubated at 37°C under humidified air containing 5% CO₂. Cells were used up to passage 17.

3.3.1.3 Extracellular Flux Analysis

HepG2 cells were collected on the day of the experiment by trypsinisation and then washed thrice with serum- and glucose-free media. The cells were then plated onto a collagen coated (50 µg/ml in acetic acid 0.02 M), XF 96-well cell culture microplates (2.5×10^4 cells /100 µl medium/well) overnight in high glucose (25 mM). Culture medium was removed from all wells and replaced with 175 µl of unbuffered glucose free Seahorse Assay media, supplemented with sodium pyruvate (1 %v/v) and L-glutamate (1% v/v) pre-warmed to 37°C. Cells were incubated in a CO₂ free incubator at 37°C for 1 h. Before rate measurement, the XFe96 Instrument (Seahorse biosciences, North Billerica, MA) mixed the assay media in each well for 10 min, allowing the oxygen partial pressure to equilibrate. OCR and ECAR were measured simultaneously thrice, establishing a baseline rate. For each measurement, there was a 3 min mix followed by 3 min wait time to restore normal oxygen tension and pH in the transient microenvironment surrounding the cells. Glucose injections (0.1 – 25 mM) occurred at the end of the basal measurement cycles at 16 min, followed by 10 further measurements. The overall assay duration was 95 min.

3.3.1.4 BCA Protein Quantification

Post-extracellular flux analysis, assay medium was removed from all wells. 50 µl of ATP releasing agent was charged to each well and the plate was shaken (1 min, 300 RPM). A standard curve was prepared using the BSA stock (2 mg BSA/ml in ATP releasing agent). Working reagent (WR) was prepared by adding 50 parts bicinchonic acid to 1 part copper sulphate. 5 µl of cell lysate was plated into a clear 96 well plate followed by the addition of 200 µl of WR before incubation (37°C, 30 min). The absorbance was then measured at 580 nm on a Labsystems Multiskan plate reader. Protein content was then calculated by comparing known protein concentration absorbance from the standard curve. Protein concentrations were then used to normalize the extracellular flux data giving overall rates of ECAR and OCR as mpH min⁻¹ well protein⁻¹ and pmol min⁻¹ well protein⁻¹, respectively.

3.3.1.5 Buffering Capacity

EFA assay media buffering capacity was measured at 37 °C using a pH probe. HCL (0.1 M) was charged in 6 x 20 µl aliquots to 10 ml of assay media, while changes in pH were recorded. Media buffering power was calculated from the gradient of the line of best fit after plotting the change in pH vs nmol H⁺ added per 7 µl.

3.3.1.6 Statistical Analysis

Statistical significance was ascertained using Prism 5 software via a one way ANOVA, with values expressed as a mean ± standard deviation (S.D) taken from four independent experiments (n=4).

3.3.2 Extracellular Flux Analysis Results

The effects of changes in extracellular glucose concentration (0-25 mM) on ECAR and OCR for HepG2 cells was examined. ECAR was expressed in mpH min⁻¹ mg protein⁻¹, including respiratory contributions to acidification, and OCR as pmol/min per mg protein. In this experiment, bioenergetic measurements are normalized to total well protein content and for basal readings prior to glucose injection (Figure 3-11). Prior to EFA, the cells were starved for 60 min in media devoid of glucose. While the relationship between glucose concentration and ECAR/OCR is minimal, there is a definitive switch in energetic metabolism from respiratory to glycolytic, prior to accounting for respiratory acidification, post exposure to glucose. The introduction of glucose following a minor starvation period induces an increase in ECAR and decrease in OCR. This is hypothesized to be the result of an increase in glycolytic energy metabolism, which generates ATP from glucose at a faster rate than oxidative phosphorylation. The ability of carcinoma cell lines, including HepG2, to exhibit this phenomena is well characterized and has been reported previously⁶⁷. Average ECAR increased significantly after introduction of all concentrations of glucose compared to no introduction of glucose (P-values < 0.001). Average OCR after the introduction of all concentrations of glucose apart from 0.1 and 1 mM, was a significant decrease

compared to no introduction of glucose (P-values < 0.001). Complete description of significant changes can be found in the Appendix A.

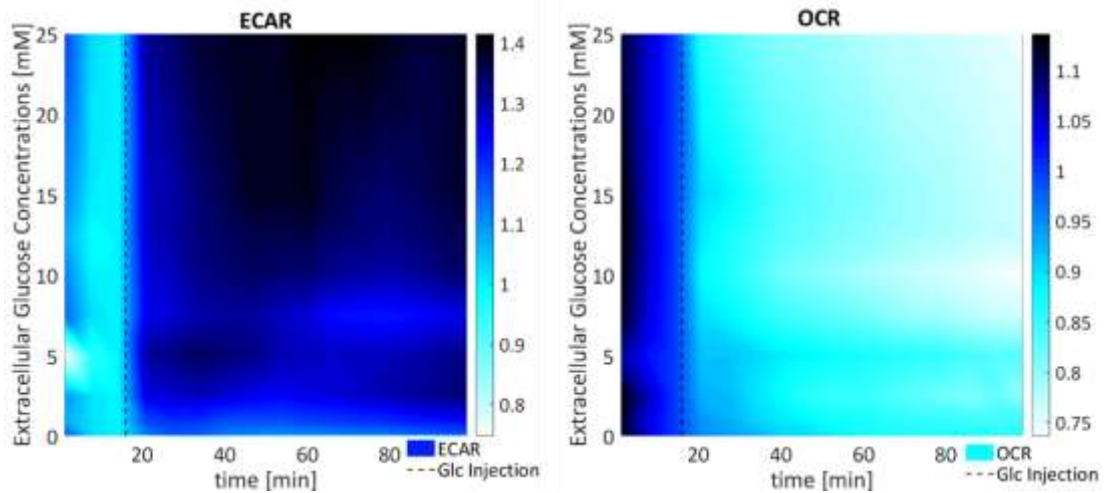


Figure 3-11: The effect of extracellular glucose on ECAR and OCR. HepG2 cells were exposed to serial concentrations of glucose (0.1-25mM) at $t = 16$ min (dashed line). ECAR and OCR is expressed in colour according to the colour bar in mpH/min per mg protein (basal) and pmol/min per mg protein (basal), respectively. Measurements indicated are an average of $n=4$.

3.3.3 EFA Media Buffering Power & PPR_{gly} Calculation

EFA glucose-free media buffering power (BP) was calculated after measuring changes in pH after the addition of hydrochloric acid (HCL), using the gradient of the line of best fit for the data (Figure 3-12). The calculated value for EFA unbuffered media of 0.0005 mpH/nmol H^+ in 7 μ l, calculated as the gradient of the line of best fit, ranks considerably lower than for various other types of media, as shown in Table 3-4. However, this is somewhat unsurprising as EFA media is inherently unbuffered by default to facilitate the detection of small changes in acidity rather than mask them.

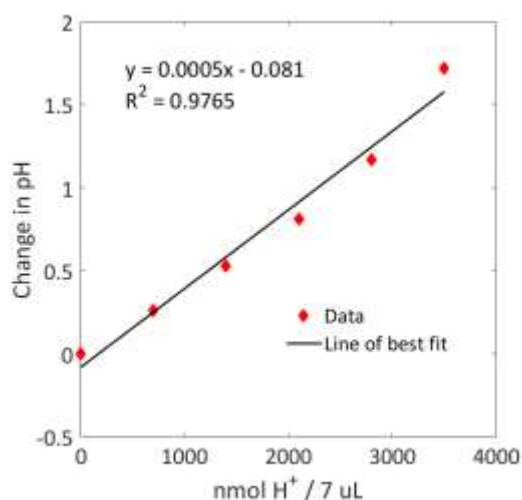


Figure 3-12: The buffering power of unbuffered glucose-free EFA media was measured by adding 0.1 M HCl aliquots to 10 ml of media, followed by calculating the gradient of the slope from the resulting pH change.

Assay medium	BP	Composition	Reference
EFA unbuffered medium	5×10^{-4}	sodium pyruvate (1 %v/v) and L-glutamate (1% v/v), pH 7.4 37oC	This chapter
KRPH 0.1% BSA	4.5×10^{-2}	2 mM HEPES, 136 mM NaCl ₂ , 2 mM NaH ₂ PO ₄ , 3.7 mM KCl, 1 mM MgCl ₂ , 0.1% w/v fatty-acid-free BSA, pH 7.4, 37°C	68
KRPH 1.0% BSA	3.5×10^{-2}	2 mM HEPES, 136 mM NaCl, 2 mM NaH ₂ PO ₄ , 3.7 mM KCL, 1 mM MgCl ₂ , 0.1% w/v fatty-acid-free BSA, pH 7.4, 37°C	68
minimal TES Buffer	1×10^{-2}	1.3 mM CaCl ₂ , 120 mM NaCl, 0.4 mM KH ₂ PO ₄ , 3.5 mM KCL, 2 mM MgCl ₂ , 20 mM TES, 15 mM glucose 0.1% w/v fatty-acid-free BSA, pH 7.4, 37°C	68
XF DMEM	1×10^{-1}	5 mM glucose, 2 mM glutamine, 0.4 mM sodium pyruvate, pH 7.4, 35°C	68
XF RPMI	4.10×10^{-2}	(Bicarbonate-free) 11 mM glucose, 2 mM glutamine, 1 mM NaH ₂ PO ₄ , pH 7.4, 35°C	68

Table 3-4: Buffering power and composition of different types of media.

Determination of the media BP allows for the calculation of the buffering capacity (BC) and respiratory contributions to ECAR. The BC can be entered directly into the EFA analyser to account for the media BP for its readings and is therefore extremely useful for future experiments. Buffering capacity is calculated from the experimentally determined BP using (3-6).

$$BC = \frac{1.0 \times 10^{-9}}{BP} = 2.0 \times 10^{-6} \left(\frac{\text{pH}}{\text{nmol}} \text{H}^+ \text{in } 7\mu\text{L} \right), \quad (3-5)$$

where

$$BP = 5.0 \times 10^{-4} \left(\frac{\text{pH}}{\text{nmol}} \text{H}^+ \text{in } 7\mu\text{L} \right). \quad (3-6)$$

Total proton production rate (PPR_{tot}) was calculated in Equation (3-7), using the average experimentally derived ECAR post glucose injection for 5 mM glucose ($10.2 \text{ mpH min}^{-1} \text{ mg protein}^{-1}$) (Figure 3-11) divided by the BP.

$$PPR_{tot} = \frac{ECAR}{BP} = 2.04 \times 10^4 \left(\frac{\text{pmol H}^+}{\text{min mg protein}} \right). \quad (3-7)$$

Subsequently, the respiratory contributions PPR_{resp} were calculated using Equation (3-7), where pK_1 is the overall pK_a for $\text{CO}_2(\text{aq}) + \text{H}_2\text{O} \rightarrow \text{HCO}_3^- = 6.093$, $\text{max H}^+/\text{O}_2$ is the derived acidification for the metabolic transformation of glucose oxidation = 1, $OCR_{tot} = 17.78 \text{ pmol O}_2 \text{ min}^{-1} \text{ mg protein}^{-1}$ for 5 mM over 10 measurements, $OCR_{rot} = 5.17 \text{ pmol O}_2 \text{ min}^{-1} \text{ mg protein}^{-1}$. Thus,

$$\begin{aligned} PPR_{resp} &= \left(\frac{10^{\text{pH}-\text{p}K_1}}{1 + 10^{\text{pH}-\text{p}K_1}} \right) \left(\frac{\text{max H}^+}{\text{O}_2} \right) (OCR_{tot} - OCR_{rot}), \\ &= 1.09087 \times 10^1 \left(\frac{\text{pmol H}^+}{\text{min mg protein}} \right). \end{aligned} \quad (3-8)$$

Finally, using Equations (3-9) and (3-10), PPR_{gly} was calculated by subtracting respiratory acidification contributions from the total proton production rate giving a PPR_{gly} value of 3.0389×10^4 pmol H^+ min⁻¹ mg protein⁻¹:

$$PPR_{tot} = PPR_{gly} + PPR_{resp}, \quad (3-9)$$

giving

$$PPR_{gly} = PPR_{tot} - PPR_{resp} = 2.0389 \times 10^4 \left(\frac{\text{pmol } H^+}{\text{min mg protein}} \right). \quad (3-10)$$

The difference between PPR_{gly} and PPR_{resp} of 11 pmol H^+ / min per mg protein is relatively small. This is unsurprising as the unaltered EFA data in Figure 3-11 implies an inverse relationship between ECAR and OCR and therefore minimal respiratory contributions to ECAR. Nevertheless, regardless of this particular cell lines proclivity to fund ECAR with predominantly glycolytic acidification, it is a worthy and facile endeavour for the sake of understanding the cellular bioenergetic output.

3.4 *In silico* – *In Vitro* Coupling & Sensitivity Analysis

3.4.1 Sensitivity Analysis

Testing the sensitivity of a metabolic model with respect to its parameters is a crucial way of assessing its robustness. Variables that are most receptive to parameter perturbations can be identified by measuring changes in time-course simulations following parameter variation and, consequently, parameters that must be treated with care when measured and used can also be defined. Sensitivity analysis may be presented in many forms depending upon the state of the system. For this model, we elected to measure the percentage mean change of the j^{th} variable with respect to a -99% to +400% change in the i^{th} parameter (Equation (3-11)). We define V_j as the j^{th} variable over time; V_j^{base} is the j^{th} variable over time with the base value for the i^{th} parameter; V_j^{ival} is the j^{th} variable over time with a perturbed value for the i^{th} parameter; with ival \in [-99,400%] of its base value. We denote Mean ($V_j(t)$) as the

mean value of the j th variable over the time course $t \in [0,300]$ mins, where $||$ denotes absolute value.

% absolute change
relative to
parameter change (3-11)

$$= \max \left[\frac{\left| \frac{\text{mean}(V_j^{ival}(t)) - \text{mean}(V_j^{ibase}(t)) \times 100}{\text{mean}(V_j^{ibase}(t))}}{\left| \frac{(ival - ibase)}{ibase} \times 100 \right|} \right]}{1} \right]$$

A parameter is classed as mildly sensitive (*MS*) if a change in any variable as a result of parameter manipulation is between 1 - 10% absolute mean change relative to the parameter change, and sensitive (*S*) if >10% is observed over a 300-minute simulation (Figure 3-13). Sensitivity analysis presented 8 sensitive parameters: phosphofructokinase (PFK) V_{\max} (*MS*), triosephosphate isomerase (TPI) K_{eq} (*MS*), dihydroxy-acetone phosphate (DHAP) K_m (*MS*), glyceraldehyde dehydrogenase (GAPDH) K_{eq} (*MS*), K_m NAD (*MS*), lactate dehydrogenase (LDH) V_{\max} (*MS*), MCT1 K_{eq} (*S*) and V_{\max} (*S*). The two most sensitive parameters with respect to lactate, K_{eq} and V_{\max} for the MCT1 transporter are expressed as % mean change of its initial value, (Figure 3-14). With two out of three MCT1 transporter parameters registering as sensitive, parameter selection for this enzyme mediated reaction must be carefully considered, especially when MCT1 transporter flux is to be used for simulating ECAR.

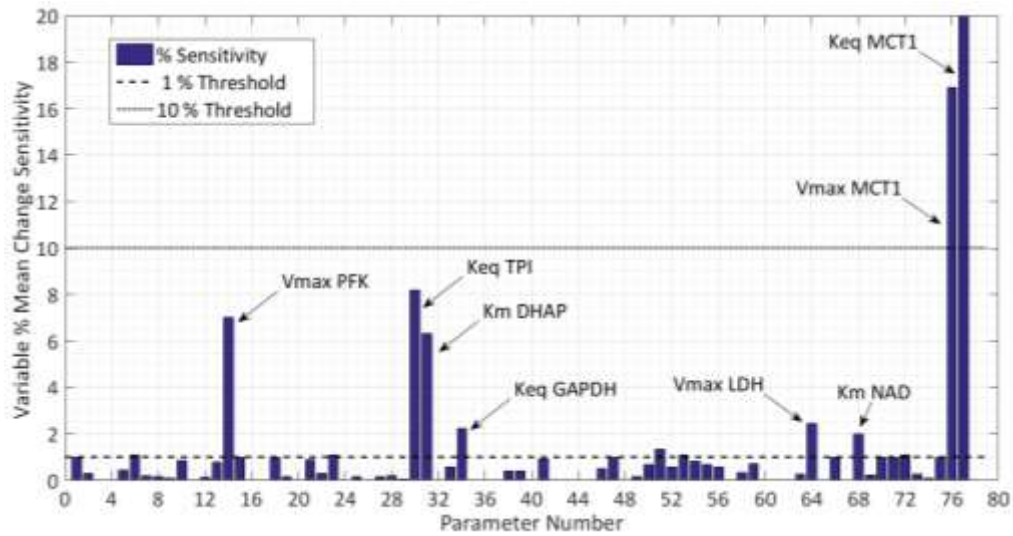


Figure 3-13. Sensitivity analysis. 78 model parameters were varied between -99% to +400% of their default values to identify the maximum % mean change in any variable and provide a measure of sensitivity relative to parameter change variation. The 8 most sensitive parameters are annotated.

Figure 3-14 shows the effects of changes in V_{max} MCT1 and K_{eq} MCT1 on intracellular lactate concentrations. The initial parameter was altered from -99 % to +400 % in 21 iterations, as shown with the 21 bars for each plot. Evidently, intracellular lactate concentration is more sensitive to the MCT1 equilibrium constant than the V_{max} . However, both parameters satisfy the sensitive criteria threshold (Figure 3-13).

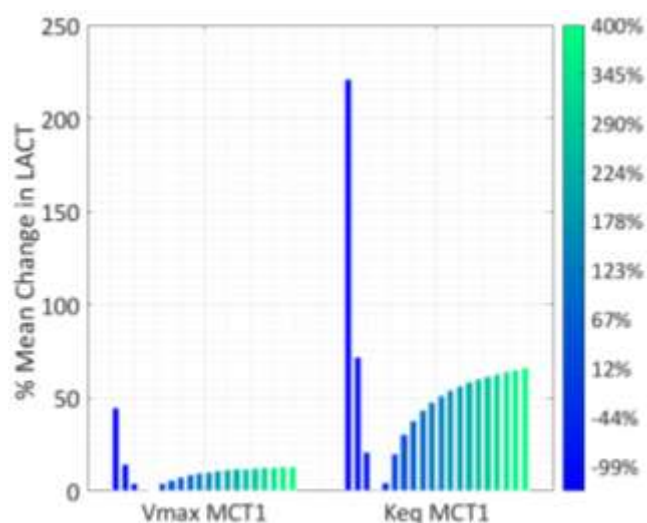


Figure 3-14. Sensitive model parameters illustrating changes in intracellular lactate concentration. % mean changes in intracellular lactate concentration as a function of sensitive parameter manipulation are shown compared to their initial steady state condition. Lactate is more susceptible to changes in the equilibrium constant, K_{eq} , than to the V_{max} of MCT1 co-transporter kinetics.

3.4.2 Model Parameterization: Cytoplasm Lactate Content

In order to accurately choose the values for the identified sensitive parameters, the model was fitted to *in vitro* intracellular lactate concentration. Luk et al. measured the intracellular lactate concentration of HepG2 cells during their study of the effects of miR-122 on pyruvate kinase⁶⁹. Their data was used for comparison of the model simulations of the cytoplasm concentration of lactate over an extended time course of 48 h. Initial simulations were improved upon by fitting the two sensitive parameters of the MCT1 (Figure 3-15). Parameter adjustment was performed using unconstrained nonlinear optimization as described in the methods section, such that $V_{max\ MCT1}$ and $K_{eq\ MCT1}$ values adjusted from $33\ \text{mM}\ \text{min}^{-1}$ and 1, to $2.0 \times 10^{-3}\ \text{mM}\ \text{min}^{-1}$ and 1.15×10^2 respectively, where equilibrium constants are unitless.

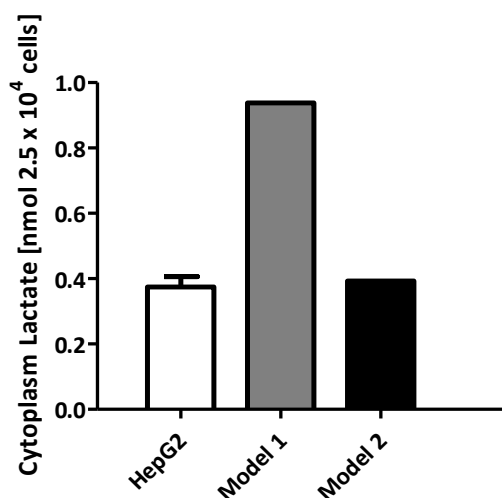


Figure 3-15: Intracellular lactate concentration after 48 h: Model intracellular lactate concentration was aligned with experimental data from HepG2 cells after 48 hr. Model 1 simulation represents the lactate concentration pre-parameter adjustment with all model parameters obtained from the literature, with Model 2 simulation indicative of post-parameter adjustment.

Steady state cytoplasm levels of lactate in the model prior to parameter adjustment were approximately three times higher than *in vitro* amounts. Minor adjustment to the MCT1 Vmax parameter provided a more comparable *in vitro* – *in silico* intracellular steady state concentration of lactate, while simultaneously leaving other variable and flux steady state concentrations largely unaltered (% changes in steady states given in the supplementary information).

3.4.3 Model Validation: Simulating EFA PPR_{gly} & ECAR

The model was validated by comparison of EFA PPR_{gly} and ECAR experimental data that was not used for the original parameterization. The model was used to recreate EFA analysis data obtained experimentally (Figure 3-11) generating both profiles for ECAR and PPR_{gly} using the MCT1 flux term. Furthermore, the model was used to simulate EFA, capturing the cell incubation and media change prior to EFA, assessing the model's ability to respond to extracellular changes that are cannot be measured experimentally. The *in vitro* experiment therefore consists of a 1440 min (24 h)

incubation in high glucose environment (25 mM), followed by extracellular lactate and glucose removal during a 60 min incubation in unbuffered media prior to EFA. Glucose is reintroduced at $t = 1500$ min after the end of the glucose-free incubation, followed by 120 min of measurements. The model simulation was normalized to the average protein content of the respective wells (Figure 3-16).

Simulated ECAR and PPR_{gly} is in good accordance with experimental observations. Simulated ECAR was expectedly short of experimental values, owing to the omission of respiratory contributions within the model. The model was able to accurately simulate PPR_{gly} using the MCT1 flux only, suggesting that lactate/ H^+ is likely responsible for glycolytic extracellular acidification, which is in good agreement with the literature⁷⁰⁻⁷². As is apparent in Figure 3-16, the model is better suited to recapitulate PPR_{gly} rather than ECAR, likely due to the model comprising of glycolytic acidification mechanisms only. It is then unsurprising that simulated ECAR falls short of experimental data. The model simulates the changes in extracellular acidification as a function of changes in extracellular environment at t_1 where extracellular glucose and lactate are removed, as well as t_2 when 5 mM of glucose is introduced (Figure 3-16). The resulting PPR_{gly} is therefore a function of extracellular homeostasis, suggesting that extracellular glucose and lactate concentration play a greater role in ECAR and PPR_{gly} levels than expected.

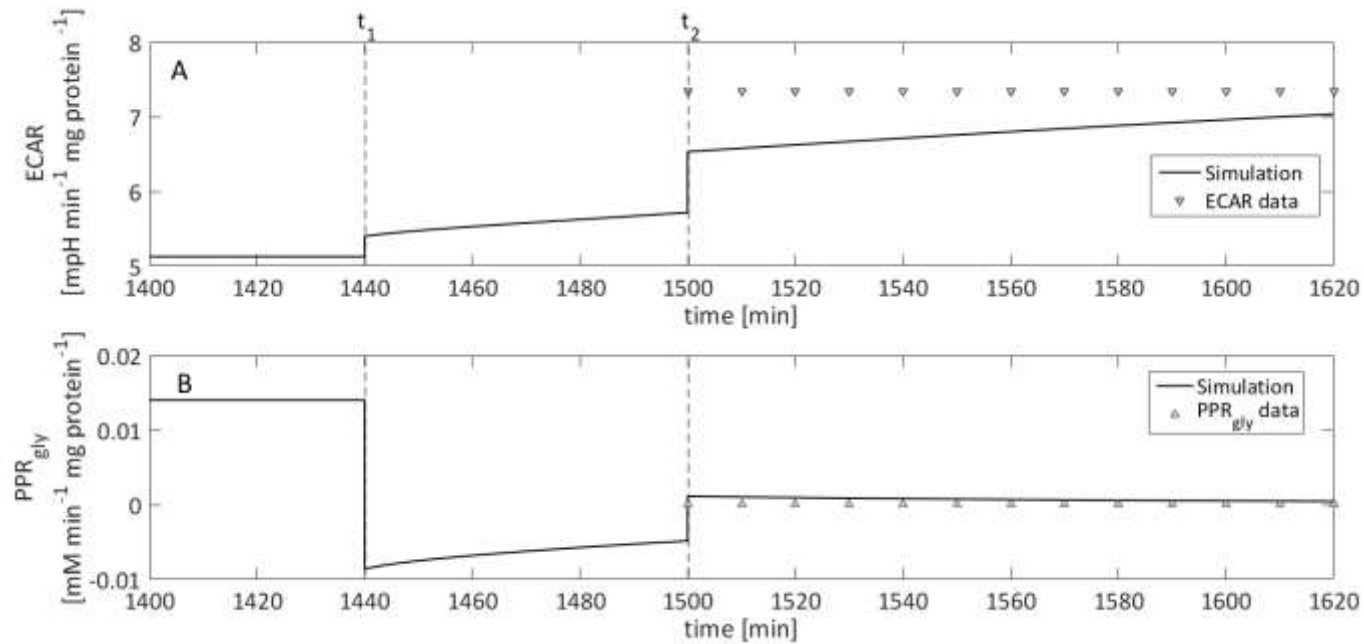


Figure 3-16: ECAR and PPR_{gly} simulation. A, model simulation of ECAR (solid line) compared to *in vitro* ECAR (triangles) normalized to protein content, taken from 5 mM glucose EFA results (Figure 3-11) B, model simulation of PPR_{gly} (solid line) compared to *in vitro* PPR_{gly} (triangles) normalised to protein content for 5 mM glucose experiments. PPR_{gly} data was taken from EFA results (Figure 3-11) followed by adjusting each ECAR measurement for respiratory contributions, as well as extracellular media buffering power. At t_1 all extracellular model variables are reset to zero to mimic *in vitro* media change, at t_2 glucose is reintroduced at 5 mM, using this concentration as the initial parameter and rate expressions from the literature are based on this concentration. Full simulation time course can be found in the supplementary information.

Model concentration steady state values are compared to a range of possible values sourced from the literature. In general, the model is in good accordance with these ranges, however, several values are situated outside of the ranges. It should be noted that this model is designed to recapitulate a specific *in vitro* scenario, rather than a generic *in vivo* / *in vitro* system such as generic monolayer cell culture or isolated hepatocytes. Furthermore, the effects of the extracellular volume that this model is tasked with replicating is obviously different to a physiological situation. For example, intracellular lactate concentration in the model is a function of the extracellular concentration in the transient micro chamber of EFA. Consequently, when simulating a media change, removal of lactate in its entirety drastically affects the intracellular lactate concentration by the laws of mass action. Regardless, variables of bioenergetic importance such as ATP, ADP, and PYR are located within the bounds of literature ranges.

Variable	Model [mM]	Literature range [mM]
GLC	4.7996	3.61 – 6.85
ATP	2.7203	0.49 – 3.430
ADP	0.8797	0.5 – 1.38
G6P	0.0336	0.06 – 0.205
F6P	0.0096	0.011 – 0.1
Pi	5.0000	3.64 – 5.74
F16P	0.3699	0.016 – 0.03
BPG	0.0040	0.3
F26P	0.4560	0.004
DHAP	0.0769	0.012 – 0.052
GHAP	1.0519	0.0014 – 0.228
NAD	0.2049	1.2200
NADH	0.1687	0.0006
PG2	0.4637	0.007 – 0.049
PG3	0.0810	0.048 – 0.41
PEP	0.0956	0.092 – 0.27
PYR	0.1146	0.059 – 0.271
LAC	0.0054	0.12 – 2.347

Table 3-5: Literature and model variable concentration comparison. All literature values for variables are sourced from the liver specific glucose metabolism models, compiled within the supplementary materials of ⁶¹.

3.5 Model Predictions

3.5.1 The Effects of Extracellular Glucose, Lactate and pH Perturbations on ECAR and PPR_{gly}

Simulated extracellular acidification is representative of both lactate and H^+ and as such, the effects of changes in extracellular glucose, lactate and H^+ concentrations on PPR were simulated in order to determine the effects on extracellular acidification.

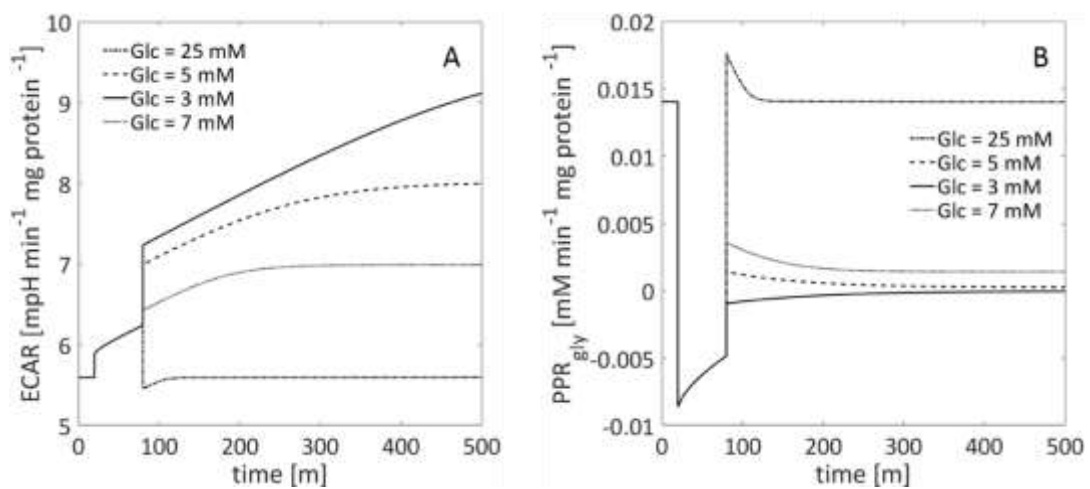


Figure 3-17. Effects of extracellular glucose concentration on ECAR and PPR_{gly} experimental simulations. Simulation follows *in vitro* setup, with all extracellular variables removed at $t=20$ followed by a glucose-free 60 min incubation before reintroduction of glucose at $t=80$. A, model simulation of ECAR as a function of 3, 5, 7 and 25 mM extracellular glucose. B, model simulation of PPR_{gly} as a function of 3, 5, 7 and 25 mM extracellular glucose. Concentration selection is based on *in vitro* conditions simulating high glucose 25 mM, hyperglycaemia (7 mM), physiological (5 mM) and hypoglycaemia (3 mM).

Our model predicted no change in either ECAR or PPR_{gly} with respect to perturbations in extracellular lactate concentration or pH (data not shown). Adjustment of extracellular glucose concentrations yielded diversity in both ECAR and PPR_{gly} . Extracellular acidification was simulated at four specific extracellular glucose concentrations in order to simulate hypoglycaemia (3 mM), physiological basal (5 mM), hyperglycaemia (7 mM) and the *in vitro* standard high glucose (25 mM). The simulated experiments follow the same protocol of that used in Figure 3-16, where

the model is simulated devoid of glucose followed by extracellular glucose exposure, in this instance at $t = 80$ min. Figure 3-17 highlights the simulated differences between PPR_{gly} and ECAR. As glucose concentration increases, ECAR decreases. However, as glucose concentration increases, PPR_{gly} increases. While ECAR and PPR_{gly} may appear to be inversely related with respect to extracellular glucose concentration, this is not the case, as ECAR output fails to recapitulate MCT1 directionality. The liver is the predominant organ responsible for maintaining blood concentrations; capable of releasing glucose during periods of hypoglycaemia, and storing/utilizing glucose during hyperglycaemia⁷³. Furthermore, the liver is especially capable of utilizing extracellular lactate as a fuel source to generate glucose under the process of gluconeogenesis^{74,75}. It is unsurprising then that the model is capable of generating a negative flux during PPR_{gly} simulations during hypoglycaemia (Figure 3-17 B).

3.5.2 The Effects of Extracellular Glucose Concentration on Energy Metabolism

The resulting changes in model energy metabolism as a function of extracellular glucose perturbation were simulated in the form of ATP, ADP and pyruvate concentrations (Figure 3-18). ATP and ADP are directly related and simulations exhibit an inverse relationship between the two variables: as expected due to gluconeogenesis, as extracellular glucose concentration decreases, ATP concentration increases with ADP concentration decreasing. Similarly, cytoplasm pyruvate concentrations also decrease suggesting pyruvate utilisation. With respiratory energy production omitted in this model the fact that as extracellular glucose decreases the MCT1 transporter instead favours the uptake of lactate (Figure 3-17), suggests that gluconeogenesis is responsible for increases in ATP.

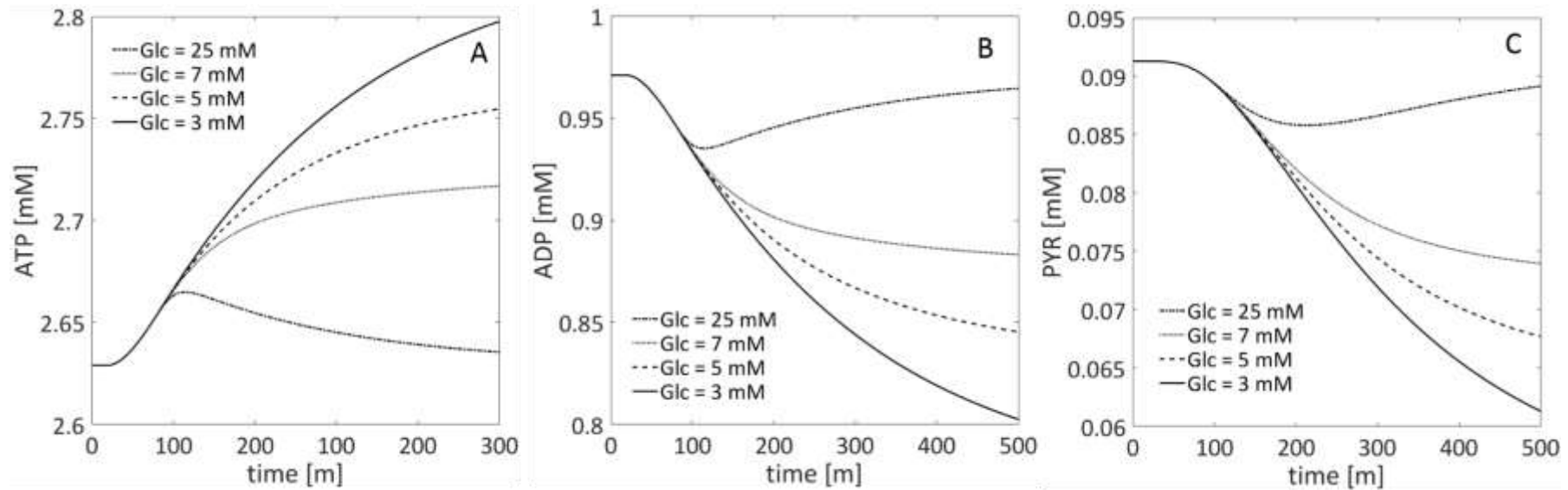


Figure 3-18. Effects of extracellular glucose concentration on model energy metabolism. A, model simulation of ATP as a function of 3, 5, 7 and 25 mM extracellular glucose. B, model simulation of ADP as a function of 3, 5, 7 and 25 mM extracellular glucose and C, model simulation of pyruvate as a function of 3, 5, 7 and 25 mM extracellular glucose. Concentration selection is based on *in vitro* conditions simulating high glucose 25 mM, hyperglycaemia (7 mM), physiological (5 mM) and hypoglycaemia (3 mM).

Decreases in cytoplasm pyruvate concentrations will also affect respiratory energy metabolism, as cytoplasmic pyruvate is an indirect precursor for oxidative phosphorylation ^{76,77}.

3.5.3 Suitability of Using MCT1 Flux to Simulate ECAR & PPR_{gly}

MCT1 is one of several isoforms of the MCT family that is liver specific, responsible for the rapid proton-linked movement of monocarboxylates, such as L-lactate, across the plasma membrane. In general, tumour cells express higher levels of MCT to maintain an appropriate intracellular pH environment for growth ⁶³. This is crucial for tumour homeostasis as energy production tends to be glycolytically sourced rather than respiratory owing to hypoxia / anoxia. Consequently, efflux of protons is essential to regulate intracellular pH. Furthermore, lactic acid is metabolised via gluconeogenesis ⁷⁸. As such, the model must be capable of recapitulating these biologically important scenarios when aligned with cell line data.

The model is able to switch MCT1 flux direction during simulation as a function of changes in extracellular glucose concentration. The method used to apply the MCT1 flux term to PPR_{gly} is therefore very suitable. However, the concomitant ECAR simulations for the same perturbations in extracellular glucose concentration give asymptotic peaks (Figure 3-19). Switching between a positive and negative flux when simulating influx to efflux using MCT1, causes asymptotic artefacts when using the proposed method of converting model flux output in mM min⁻¹ to mpH min⁻¹, due to the use of the logarithms. It is therefore reasonable to expect such artefacts in the *in vitro* data as the lactate / H⁺ flux direction changes.

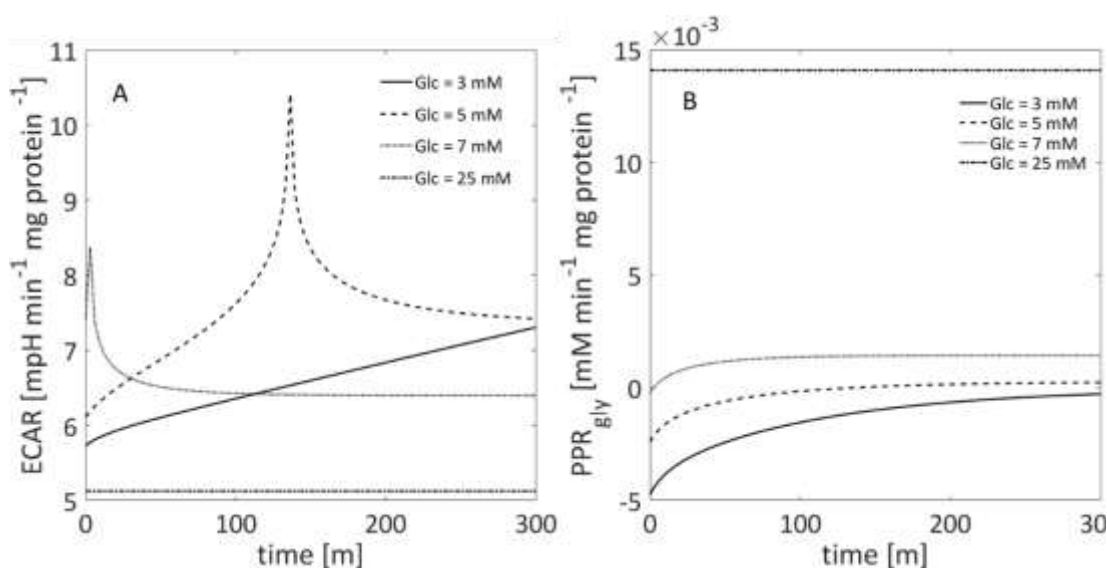


Figure 3-19: Effects of MCT1 directionality on ECAR and PPR_{gly} simulations. A, model simulation of ECAR as a function of 3, 5, 7 and 25 mM extracellular glucose. B, model simulation of PPR_{gly} as a function of 3, 5, 7 and 25 mM extracellular glucose. Concentration selection is based on *in vitro* conditions simulating high glucose (25 mM), hyperglycaemia (7 mM), physiological (5 mM) and hypoglycaemia (3 mM).

In practice, *in vitro* ECAR EFA outputs will avoid such spikes when using high glucose (25 mM) which ensures ample substrate for glycolysis. However, switches in metabolic direction from glycolysis to gluconeogenesis are more probable during glucose-free experiments where galactose is used as the sugar source. Such experiments are commonly utilised when assessing drug-induced mitochondrial toxicities when cells are often exposed to a glucose free environment in order to inhibit net ATP production from glycolytic activity so that cells are completely reliant on oxidative phosphorylation for ATP production⁷⁹. However, in this instance it is very likely that small substrates such as extracellular lactate will be utilised as a respiratory substrate via gluconeogenesis which, in turn, may lead to asymptotic ECAR artefacts in the data. As a result, the model implies that PPR data is a more robust method of assessing extracellular acidification as such artefacts are avoided such as that observed in Figure 3-19 (5 mM).

3.6 Chapter Discussion

3.6.1 Conclusion

A novel pH-dependent model of hepatic glycolytic flux was constructed and used to simulate *in vitro* HepG2 ECAR and PPR_{gly} . Mathematically expressing glycolytic rate as a function of the MCT1 is unique to this work and as such, gives credence to lactate and proton efflux as the predominant driving force of PPR_{gly} . Extracellular flux analysis using HepG2 cells elucidated the relationship between ECAR and OCR dependent upon extracellular glucose concentrations. Specifically, a distinct metabolic switch was observed from respiratory to glycolytic activity when cells were exposed to glucose after brief fasting (60 min). Measuring the buffering power of EFA media allowed for the determination of respiratory contributions to ECAR thus enabling the separation of ECAR due strictly to glycolytic acidification. These calculations highlighted that glycolysis is the predominant driver for extracellular acidification. This work illustrates the important discrepancies between ECAR and calculated PPR_{gly} , with ECAR simulations falling short of experimental data. Furthermore, the occurrence of asymptotic peaks, produced as a result in changes in transporter directionality as a function of using logarithms when converting from molarity to pH, were illustrated. Direct use of PPR_{gly} is therefore shown to be more accurate when simulating experimental data, as well as providing better clarity during the metabolic switch from glycolysis to gluconeogenesis. We therefore strongly recommend the use of PPR_{gly} rather than ECAR as an indicator of cellular glycolytic rate. Effects of extracellular glucose on ECAR, PPR_{gly} and energy metabolism suggest that the model is capable of simulating switches in metabolic state depending upon extracellular environments, specifically, switching to gluconeogenesis during hypoglycaemia in order to generate ATP. Overall, the model demonstrates that MCT1 flux, and subsequently H^+ /lactate flux, in the context of glycolytic flux is more than capable of recapitulating *in vitro* PPR_{gly} . These findings support lactic acid as the predominant source of glycolytic acidification, while simultaneously illuminating the shortcomings of using ECAR as an indicator of glycolytic rate. The construction and simulations of

this model are testament to the quality of parameterized models currently available in the literature, as well as the development of toolsets such as BISEN that aid the generation of multi-compartment systems of ODE's that account for dynamic ionic buffering and thermodynamics. Overall, the model highlights the inadequacy of using ECAR as an indicator of glycolytic rate when glycolytic specific acidification is so readily accessible. Furthermore, modelling the glycolytic rate as a function of the MCT1 transporter flux in terms of PPR_{gly} facilitates negative flux expression depending upon transporter directionality, avoiding asymptotic results when using logarithms to recapitulate ECAR. Finally, this work could impact the way extracellular flux analysis results are expressed in the field of bioenergetics, recommending the use of PPR_{gly} rather than ECAR when measuring glycolytic energy metabolism.

4 Chapter 4: Modelling Cellular Bioenergetics: Human Hepatic Mitochondrial Respiration

4.1 Introduction

Drug induced liver injury (DILI) is a leading cause of attrition during drug development. According to the World Health Organisation (WHO), DILI is one of the most serious adverse drug reactions and is the fifth leading cause of death related to liver diseases, accounting for 20-40% of all instances of clinical hepatic failure^{80,81}. As such, pre-clinical assessment of DILI during drug development is essential. DILI is both compound- and patient- dependent with a plethora of possible causes. Mitochondrial toxicity has emerged as one of the multifactorial contributors to DILI, the understanding and prediction of which has been recently improved due to the amelioration of screening methods, including the glu/gal assay and, extracellular flux analysis through Seahorse Bioscience XF analysers^{44,82-84}. The role of mitochondrial toxicity within DILI appears to be a mechanistic liability as drug induced mitochondrial dysfunction can lead to oxidative stress by de-energizing the cell and inducing apoptosis^{85,86}.

Drug induced mitochondrial toxicity (DIMIT) presents itself as a major aetiology of DILI, with a considerable number of metabolic based mechanistic points of interest. The scale of this problem is apparent, as 50% of drugs with black-box warnings for DILI contain mitochondrial liabilities⁸⁷. Perhaps the most notable classification of mitotoxic compounds are those that inhibit the electron transport chain, thereby directly preventing ATP synthesis⁸⁸. Extracellular flux analysis, in the form of a "Mito-Stress test" (Figure 4-9), whereby the electron transport complexes and chemiosmotic coupling are sequentially inhibited and uncoupled respectively using classical mitotoxic poisons, is particularly suited to examining the mechanism of such compounds. The resulting changes in oxidative phosphorylation during the Mito-Stress test are captured in the form of an oxygen consumption rate (OCR) profile and this profile may then be used to investigate new DIMIT by simple comparison, allowing specific electron transport complex inhibition to be assigned. This method of detection and quantification of DIMIT is performed using whole, intact cells and is therefore a function of its whole cell environment, allowing compensatory

mechanisms such as glycolysis, when applicable, to alleviate toxicity. This provides a realistic physiologically relevant framework from which to better understand and predict DIMT⁴³.

The identification of mitochondrial liabilities early in the drug development pipeline is crucial to the prevention of DIMT and potential DILI. Subsequently, pharmaceutical companies are now actively exploring new *in vitro*, *in vivo* and *in silico* tools and technologies in order to tackle drug safety⁸⁹. Unfortunately, although DIMT is screened early during preclinical development, current screens suffer from low specificity, and there is little translational power to predict whether the presence of DIMT will lead to DILI. This is compounded by a distinct lack of animal models available, as well as the idiosyncratic nature of most DIMT. This, coupled with the complexity of mitochondrial biology which differs tissue to tissue, makes investigation of DIMT extremely difficult. In order to circumvent this, the current model for mitochondrial toxicity screening is an iterative process which utilises *in vitro* almost entirely. Initial *in vitro* screens facilitate early structure activity relationship (SAR) studies and cell-based assays illuminate initial compound toxicity. If after these initial screens mitochondrial aetiology is suspected, further studies using isolated mitochondria are performed. If a positive result follows, mechanistic studies are performed which examine OXPHOS respiration, permeability transition, ROS and RNS, membrane potential ($\Delta\Psi$) and mitochondrial DNA status (mtDNA)⁹⁰.

The efficiency and translatability of this process could be significantly increased with the application of a highly mechanistic, thermodynamically-driven model of mitochondrial bioenergetics. This would be particularly powerful if linked directly to the output of EFA. This chapter describes the development of such a model, as well as its ability to recapitulate primary hepatocyte bioenergetics responses to the classical ETC inhibitors oligomycin, FCCP, rotenone and antimycin A. The model is then used to explore the relationships between ETC complexes and OCR, as well as the potential mode of action of doxorubicin on mitochondrial activity as a function of elevated mitochondrial ROS.

4.2 Mathematical Modelling

4.2.1 Current Models

Arguably the most relevant mathematical model with respect to mitochondrial toxicity, quantified in terms of OCR, is the MitoSYM model. This model is liver specific and was developed specifically to translate *in vitro* compound screening data into predictions of DILI, via combination with DILIsym⁶². DILIsym is a multiscale computational model of DILI, designed to be used during drug development to provide enhanced understanding of DILI hazard posed by individual molecules. The model boasts inclusion of the essential biochemical pathways associated with hepatocellular bioenergetics such as glycolysis, mitochondrial respiration, electron transport chain activity and mitochondria membrane potential. In the study by Yang et al., the authors investigate the ability of the DILIsym model to reproduce the EFA outputs of HepG2 cells following perturbations in extracellular glucose, oligomycin and FCCP concentrations. The authors openly state that their model comprises only of the basic requirements. For example, they use only 8 state variables and 7 reaction fluxes to describe hepatocellular bioenergetics. While the ability of the MitoSYM model to reproduce the *in vitro* data using such reduced representation of the biological complexity, the capability of the model to yield any detailed mechanistic insight is limited due to this simplicity. It should be noted that the MitoSYM model is a smaller cog in the overall DILIsym machinery, as such it can be speculated that this simplified model would be more suitable to incorporate. However, claims that such a rudimentary model can “help reduce the resources burden associated with screening compounds for DILI risk” should be treated with caution. Overall, MitoSYM represents a strong first step to link *in silico*, and *in vitro* outputs in order to assess and bioenergetic toxicity with respect to extracellular flux analysis and DIMT.

A considerably more detailed model of mitochondrial respiration is the 2013 model from Kembro *et al.*, which focuses on mitochondrial energetics, redox and ROS metabolic networks⁵². This model is a two-compartment model that considers OXPHOS and matrix-based processes within the mitochondria, while focusing

predominantly on ROS formation, scavenging and effects on ETC. Importantly, the model recapitulates the essential bioenergetic mitochondrial processes, including specific modelling of all ETC complexes, $\Delta\Psi$ and the TCA cycle. The model itself is used to simulate the qualitative features and order of magnitude of hydrogen peroxide emission, as well as and the dynamics observed after treatment of GSH scavenging inhibitors. The model is elegant in terms of its mechanistic detail and ability to explore ROS dynamics within the mitochondria. However, it is unfortunately not specific to any particular organ, rather, the authors provide a set of parameters with a focus to mainly on qualitative outputs rather than quantitative. Furthermore, the authors do not strive to match the model outputs to the *in vitro* EFA outputs.

Finally, perhaps the most detailed and mechanistically relevant models of mitochondrial bioenergetics are those constructed by the Beard group which include several iterations of models for cardiac mitochondrial bioenergetics, constructed to include pH-dependence and thermodynamic control using the BISEN software (see introduction for details). This model has had several iterations and expansion from 2005. It began life as a relatively simple biophysical model of mitochondrial respiratory system and oxidative phosphorylation ⁹¹. In 2006, it was expanded to include modelling of oxygen transport and cellular energetics in order to explain observations on *in vivo* cardiac energy metabolism ⁹². Of particular interest and relevance to this thesis, is in the study of computational modelling of the mitochondrial tricarboxylic acid cycle, oxidative phosphorylation, metabolite transport and electrophysiology ⁹³.

The model has then further been applied to the study of detailed enzyme kinetics ⁹⁴, and also investigating phosphate metabolite concentrations and ATP hydrolysis potential in normal and ischemic hearts ⁹⁵. The model has been expanded and utilized to simulate experimentally observed phenomena on cardiac energetics during heart failure ⁹⁶, and also to explore feedback regulation and time hierarchy of oxidative phosphorylation in cardiac mitochondria ⁹⁷. The most recent use of this model was to

explore catalytic coupling of oxidative phosphorylation, ATP demand and reactive oxygen species generation⁵³.

These models have been parameterized and validated with a myriad of experimental data and as such, after over a decade of being used for research, are highly regarded in the field.

Ultimately, all of the described models are based on the fundamental thermodynamics that govern enzyme kinetics and subsequently variable concentrations. These models encompass cellular metabolites as moieties defined by their unique binding constants to proton and metal ions and, as a result, generate a unique proton stoichiometry that is inherently pH-dependent. Gibbs free energy and effects of changes in temperature on the equilibria and kinetics of biochemical reactions are incorporated into the models in order to give thermodynamic control^{39,98}. This sophisticated level of mechanistic detail, accompanied by the detail with respect to mitochondrial bioenergetics, TCA cycle and metabolite/ion transport makes these models the ideal starting place to develop a combined *in vitro* – *in silico* effort to investigate DIMT.

4.2.2 Current Model Construction

In this study, the construction of our mitochondrial respiration model (Figure 4-1) was based on the kinetic model of oxidative phosphorylation, TCA cycle, metabolite transport and passive permeations presented by the Beard group. Additionally, the model was constructed using the BISEN toolset, thus providing its pH-dependency and interwoven thermodynamics. Our version comprises of 62 state variables, the metabolism of which are described by 11 enzyme mediated TCA reactions, 7 transporters, 9 passive membrane permeation reactions, 4 substrate / ion transport reactions and 12 enzyme / transporter mediated oxidative phosphorylation reactions, that include proton leaking. These processes are contained within a 3 compartment model comprising of cytoplasm, denoted by (_c), intermembrane space (_i) and mitochondrial matrix (_x). Model variables are described using

molarity as units and time is represented as seconds, yielding reaction and transport fluxes, J , with the units: $M s^{-1}$.

Aims

1. Construct a thermodynamic, pH-dependent model of human hepatic mitochondrial respiration.
2. Simulate hepatic cellular oxidative phosphorylation, represented via OCR.
3. Simulate perturbations in oxidative phosphorylation as a function of classic mitochondrial stress poisons, recapitulating *in vitro* primary human hepatic OCR changes.

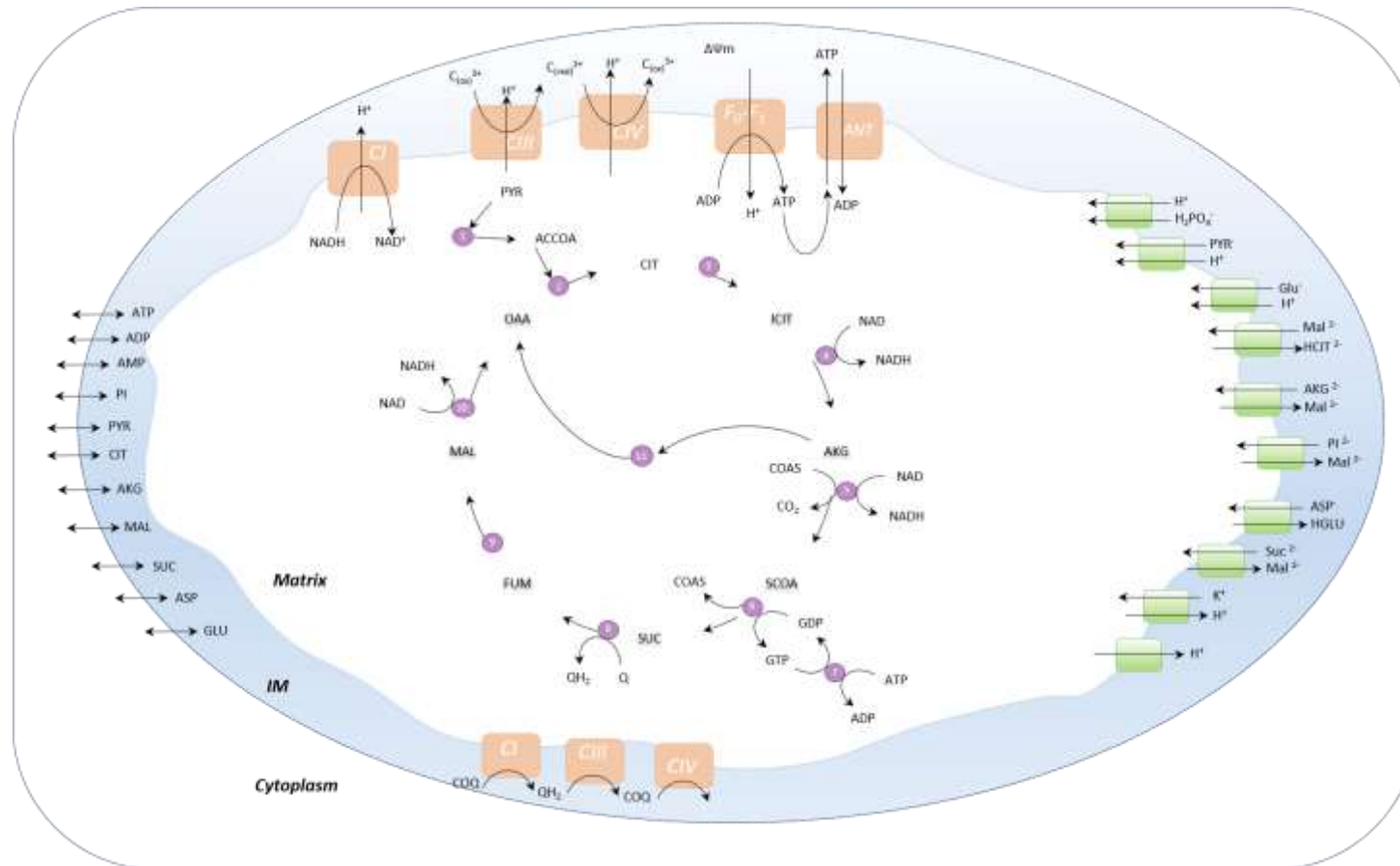


Figure 4-1: Mitochondrial respiration model. Orange rectangles represent ETC, purple circles represent TCA cycle and green rectangles represent transporters and double headed arrows represent membrane passive permeations. Detailed descriptions of the enzyme and transport reactions are found in Table 4-3.

Model state variables are described according to their compartment, concentration and unit. A full list of model variables, parameters and reactions are given in Table 4-1, Table 4-3 and Table 4-4.

Variable	Description	Initial Value	Units
<i>IM Space Species (i)</i>			
[Cred]i	Reduced cytochrome c concentration in the IM space	3.49×10^4	M
[ATP]i	ATP concentration in the IM space	1.13×10^2	M
[ADP]i	ADP concentration in the IM space	7.24×10^{-5}	M
[AMP]i	AMP concentration in the IM space	4.03×10^{-7}	M
[PI]i	Inorganic phosphate concentration in the IM space	2.28×10^{-4}	M
[H ⁺]i	H ⁺ concentration in the IM space	7.94×10^{-8}	M
[Mg]i	Mg ²⁺ concentration in the IM space	1.00×10^{-3}	M
[K]i	K ⁺ concentration in the IM space	1.30×10^{-1}	M
[PYR]i	Pyruvate concentration in the IM space	7.48×10^{-5}	M
[CIT]i	Citrate concentration in the IM space	1.66×10^{-4}	M
[AKG]i	α -ketoglutarate concentration in the IM space	9.75×10^{-8}	M
[SUC]i	Succinate concentration in the IM space	3.58×10^{-5}	M
[MAL]i	Malate concentration in the IM space	1.27×10^{-4}	M
[ASP]i	Aspartate concentration in the IM space	1.19×10^{-5}	M
[GLU]i	Glutamate concentration in the IM space	7.38×10^{-5}	M
[FUM]i	Fumarate concentration in the IM space	1.50×10^{-5}	M
[ICIT]i	Iso-citrate concentration in the IM space	1.50×10^{-5}	M
[PO2]	concentration in the IM space	2.50×10^{-1}	M
dPsi	concentration in the IM space	1.78×10^{-2}	M
<i>Matrix Variables (x)</i>			
[H ⁺]x	H ⁺ concentration in the matrix	5.73×10^{-8}	M
[ATP]x	ATP concentration in the matrix	2.84×10^{-3}	M
[NADtot]x	NAD concentration in the matrix	2.97×10^{-3}	M
[ADP]x	ADP concentration in the matrix	7.16×10^{-3}	M
[AMP]x	AMP concentration in the matrix	1.00×10^{-6}	M
[GTP]x	GTP concentration in the matrix	1.43×10^{-3}	M

Chapter 4: Modelling Cellular Bioenergetics: Human Mitochondrial Respiration

[GDP]x	GDP concentration in the matrix	3.57×10^{-3}	M
[PI]x	Inorganic Phosphate concentration in the matrix	3.92×10^{-4}	M
[NADH]x	NADH concentration in the matrix	2.49×10^{-3}	M
[QH2]x	Reduced Ubiquinol concentration in the matrix	5.14×10^{-4}	M
[OAA]x	Oxaloacetate concentration in the matrix	5.12×10^{-11}	M
[ACCOA]x	Acetyl-CoA concentration in the matrix	2.98×10^{-3}	M
[CIT]x	Citrate concentration in the matrix	4.21×10^{-4}	M
[ICIT]x	Iso-citrate concentration in the matrix	1.16×10^{-5}	M
[AKG]x	α -ketoglutarate concentration in the matrix	1.80×10^{-7}	M
[SCOA]x	Succinyl-CoA concentration in the matrix	2.18×10^{-7}	M
[COASH]x	CoA-SH concentration in the matrix	9.47×10^{-6}	M
[SUC]x	Succinate concentration in the matrix	6.35×10^{-5}	M
[FUM]x	Fumarate concentration in the matrix	7.41×10^{-5}	M
[MAL]x	Malate concentration in the matrix	2.34×10^{-4}	M
[GLU]x	Glutamate concentration in the matrix	1.02×10^{-4}	M
[ASP]x	Aspartate concentration in the matrix	1.53×10^{-8}	M
[K]x	K ⁺ concentration in the matrix	9.37×10^{-2}	M
[Mg]x	Mg ²⁺ ion concentration in the matrix	9.86×10^{-4}	M
[CO2tot]x	Total CO ₂ concentration in the matrix	2.14×10^{-2}	M
[PYR]x	Pyruvate concentration in the matrix	9.69×10^{-5}	M
[COQ]x	Oxidised Ubiquinol concentration in the matrix	5.12×10^{-11}	M

Cytoplasmic Species (c)

[PYR]_c	Pyruvate concentration in the cytoplasm	7.50×10^{-5}	M
[CIT]c	Citrate concentration in the cytoplasm	1.66×10^{-4}	M
[AKG]c	α -ketoglutarate concentration in the cytoplasm	9.75×10^{-8}	M
[SUC]c	Succinate concentration in the cytoplasm	3.58×10^{-5}	M
[MAL]c	Malate concentration in the cytoplasm	1.27×10^{-4}	M
[ASP]c	Aspartate concentration in the cytoplasm	1.19×10^{-5}	M
[GLU]c	Glutamate concentration in the cytoplasm	7.38×10^{-5}	M
[FUM]c	Fumarate concentration in the cytoplasm	1.50×10^{-5}	M
[ICIT]c	Iso-citrate concentration in the cytoplasm	1.50×10^{-5}	M
[PCr]c	Phosphate creatine concentration in the cytoplasm	2.68×10^{-2}	M
[AMP]c	AMP concentration in the cytoplasm	4.03×10^{-7}	M
[Cr]c	Creatine concentration in the cytoplasm	3.44×10^{-2}	M
[ATP]c	ATP concentration in the cytoplasm	1.13×10^{-2}	M

[ADP]c	ADP concentration in the cytoplasm	7.49×10^{-5}	M
[PI]c	Inorganic Phosphate concentration in the cytoplasm	2.29×10^{-4}	M
[H ⁺]c	H ⁺ concentration in the cytoplasm	7.94×10^{-8}	M
[Mg]c	Mg ²⁺ concentration in the cytoplasm	1.00×10^{-3}	M
[K]c	K ⁺ concentration in the cytoplasm	1.30×10^{-1}	M

Table 4-1: Mitochondrial respiration model. All state variables were adopted from ^{93,96}.

Parameter	Description	Value	Units
RT	Universal Gas Constant (R) Temperature (T)	2.5775	kJ mol ⁻¹
F	Faraday constant	0.096484	kJ mol ⁻¹ mV ⁻¹
Vcyto	Cytoplasm volume	0.6801	(ml mito / ml cell)
Vmito	Mitochondria volume	0.2882	(ml mito / ml cell)
Wx	Matrix water space fraction	0.8425	ml water (ml cytoplasm ⁻¹)
Wi	IM water space fraction	0.0724	ml water (ml mitochondria ⁻¹)
Wm	Mitochondrial water space	0.7238	ml water (ml mitochondria ⁻¹)
Wc	Cytoplasm water space fraction	0.6514	ml water (ml mitochondria ⁻¹)
γ	Outer membrane area per mito volume	5.99	μm ⁻¹
Pm	Mitochondria protein density	2.73×10^5	(mg Protein) (l mito) ⁻¹
nA	H ⁺ stoichiometric coefficient	3	Unitless
PPI	Mt membrane inorganic phosphate permeability	327	μm sec ⁻¹
PA	Mt membrane nucleotide permeability	85	μm sec ⁻¹
ϑ	ANT Parameter		
kO2	Kinetic constant for complex IV	1.20×10^4	M
β	Matrix buffer capacity	0.01	M
CIM	Inner membrane capacitance	6.75×10^{-6}	mol (l mito) ⁻¹ mV ⁻¹
Bx	Matrix buffering parameter	0.02	M
KBx	Matrix buffering parameter	1.00×10^7	M
ψ	Mitochondrial membrane potential	1.77×10^2	mV

Table 4-2: Model parameters not related to reaction terms. All parameters that are fixed within the model including thermodynamic constants, compartment volume and water fractions are described here and taken from ^{93,96}.

Flux	Description	Units
Mitochondrial		
Reactions		
J _{CI}	Complex I	M s ⁻¹
J _{C3}	Complex I	M s ⁻¹
J _{C4}	Complex IV	M s ⁻¹
J _{F0-F1}	F0F1-ATPase (ATP Synthase) (Complex V)	M s ⁻¹
J _{ANT}	Adenine nucleotide translocase	M s ⁻¹
J _{PIHT}	Phosphate-hydrogen co-transporter	M s ⁻¹
J _{HL}	Proton leak	M s ⁻¹
J _{KH}	Mitochondrial K ⁺ / H ⁺ release	M s ⁻¹
J _{PD}	Pyruvate Dehydrogenase	M s ⁻¹
J _{CS}	Citrate synthetase	M s ⁻¹
J _{AC}	Aconitase	M s ⁻¹
J _{ISOD}	Isocitrate dehydrogenase	M s ⁻¹
J _{AKG}	α-ketoglutarate dehydrogenase	M s ⁻¹
J _{SU}	Succinyl-CoA synthetase	M s ⁻¹
J _{SC}	Succinate dehydrogenase	M s ⁻¹
J _{FUM}	Fumarase	M s ⁻¹
J _{MA}	Malate dehydrogenase	M s ⁻¹
J _{NDK}	Nucleoside diphosphokinase	M s ⁻¹
J _{GO}	Glutamate oxaloacetate transaminase	M s ⁻¹
J _{AK}	Adenylate kinase	M s ⁻¹
Mitochondrial Transport Fluxes		
J _{PYRH}	Pyruvate - H ⁺ co-transporter	M s ⁻¹
J _{GLUH}	Glutamate - H ⁺ co-transporter	M s ⁻¹
J _{CITMAL}	Citrate - Malate antiporter	M s ⁻¹
J _{AKGMAL}	α-ketoglutarate - malate antiporter	M s ⁻¹
J _{SUCMAL}	Succinate - malate antiporter	M s ⁻¹

J_{MALPI}	Malate - phosphate antiporter	$M s^{-1}$
J_{ASPGLU}	Aspartate - glutamate antiporter	$M s^{-1}$
J_{PiT}	Phosphate transport across outer membrane	$M s^{-1}$
J_{ATPt}	ATP transport across outer membrane	$M s^{-1}$
J_{ADPt}	ADP transport across outer membrane	$M s^{-1}$
J_{AMPt}	AMP transport across outer membrane	$M s^{-1}$
J_{PYRt}	Pyruvate transport across outer membrane	$M s^{-1}$
J_{CiTt}	Citrate transport across outer membrane	$M s^{-1}$
J_{MALt}	Malate transport across outer membrane	$M s^{-1}$
J_{AKGt}	α -ketoglutarate transport across outer membrane	$M s^{-1}$
J_{SUct}	Succinate transport across outer membrane	$M s^{-1}$
J_{GLUt}	Glutamate transport across outer membrane	$M s^{-1}$
J_{ASPt}	Aspartate transport across outer membrane	$M s^{-1}$

Cytoplasm Reactions

J_{ATPase}	Cytoplasmic ATP consumption rate	$M s^{-1}$
J_{AKc}	Cytoplasmic adenylate kinase	$M s^{-1}$
J_{CK}	Creatine kinase	$M s^{-1}$

Table 4-3: Mitochondrial respiration model reaction descriptions. Reaction flux abbreviations are accompanied by a description and units.

4.2.2.1 Kinetic Parameters & Model Equations

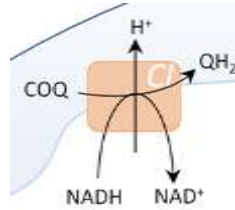
Descriptions of each of the reaction/flux terms will now be presented in detail:

Binding Polynomials:

Binding polynomials are represented using P , where the subscript indicates the reactant. This describes the binding between biochemical species and metal ions. For example,

$$P_{ATP} = 1 + \frac{[H^+]}{K_{H-ATP}} + \frac{[K^+]}{K_{K-ATP}} + \frac{[Mg^{2+}]}{K_{Mg-ATP}}$$

Complex 1 flux:



$$J_{C1} = X_{C1} (K_{eq,C1} [NADH]_x [COQ]_x - [NAD]_x [QH_2]_x),$$

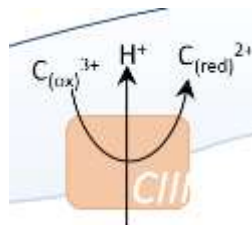
$$K_{eq,C1} = \frac{K_{eq,C1}^0 [H^+]_x^5}{[H^+]_i^4},$$

$$K_{eq,C1}^0 = \exp(-(\Delta_r G_{C1}^0 + 4 F \Delta\psi) / RT),$$

$$\Delta_r G_{C1}^0 = \Delta_f G_{NAD}^0 + \Delta_f G_{QH_2}^0 - \Delta_r G_{NADH}^0 - \Delta_r G_{COQ}^0 = -109.$$

Parameter	Value	Units
X_{C1}	2.47×10^4	$\text{mol s}^{-1} \text{M}^{-2} (1\text{mito})^{-1}$
$\Delta_r G_{C1}^0$	-109.7	kJ mol^{-1}
F, RT	Table 4-2	

Complex 3 flux:



$$J_{C3} = X_{C3} \left(\left(\frac{1 + [PI]_x / k_{PI,1}}{1 + [PI]_x / k_{PI,2}} \right) (K_{eq,C3}^{1/2} [COX]_i [QH_2]_x^{1/2} - [Cred]_i [COQ]_x^{1/2}) \right)$$

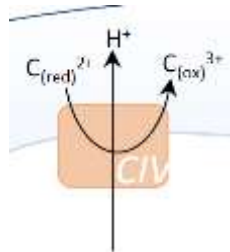
$$K_{eq,C3} = K_{eq,C3}^0 [H^+]_x^2 / [H^+]_i^4$$

$$K_{eq,C3}^0 = \exp(-(\Delta_r G_{C3}^0 + 2 F \Delta\psi) / RT)$$

$$\Delta_r G_{C3}^0 = \Delta_f G_{Cred}^0 + \Delta_f G_{COQ}^0 - \Delta_r G_{QH_2}^0 - \Delta_r G_{COX}^0 = 46.69$$

Parameter	Value	Units
X_{C3}	6.65×10^{-1}	$\text{mol s}^{-1} \text{M}^{-2} (1\text{mito})^{-1}$
$\Delta_r G_{C3}^0$	46.69	kJ mol^{-1}
$k_{PI,1}$	2.81×10^{-5}	M
$k_{PI,2}$	3.14×10^{-3}	M
F, RT & Ψ	Table 4-2	

Complex 4 flux:



$$J_{C4} = X_{C4} \left(\left(\frac{1}{1+k_{O_2}/[O_2]} \right) \exp\left(\frac{F \Delta\psi}{RT}\right) \left(\frac{[Cred]_i}{C_{yt} C_{tot}} \right) \left(K_{eq,C4}^{1/2} [Cred]_i [O_2]_x^{1/4} - [COX]_i \right) \right),$$

Where $[O_2]_x$ is assumed to be equal to $C_{O_2,cell}$

$$K_{eq,C4} = \frac{K_{eq,C4}^0 [H^+]_x^4}{[H^+]_i^2},$$

$$K_{eq,C4}^0 = \exp(-(\Delta_r G_{C4}^0 + 2 F \Delta\psi) / RT),$$

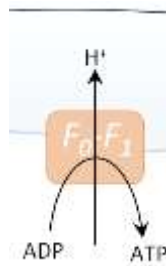
$$\Delta_r G_{C4}^0 = \Delta_f G_{COX}^0 + \Delta_f G_{H_2O}^0 - \Delta_r G_{Cred}^0 - \Delta_r G_{O_2}^0 = -202.2.$$

Parameter	Value	Units
X_{C4}	9.93×10^{-5}	$\text{mol s}^{-1} \text{M}^{-2} (1\text{mito})^{-1}$

$\Delta_r G_{C4}^0$	-202.2	kJ mol ⁻¹
k_{O_2}	1.20×10^{-4}	M
$CytC_{tot}$	2.70	Mol (1 IM water) ⁻¹
$F, RT \text{ \& } \psi$	Table 4-2	

F₀F₁-ATPase flux flux:

(Complex V)



$$J_{F_0-F_1} = X_{F_1} (K_{eq,F_1} [ADP]_x [PI]_x - [ATP]_x),$$

where

$$K_{eq,F_1} = K_{eq,C1}^0 \left(\frac{[H^+]_i^{N_A}}{[H^+]_x^{N_A-1}} \right),$$

$$K_{eq,F_1}^0 = \exp(-(\Delta_r G_{F_1}^0 + N_A F \Delta \psi) / RT),$$

$$\Delta_r G_{F_1}^0 = \Delta_f G_{ATP}^0 + \Delta_f G_{H_2O}^0 - \Delta_r G_{ADP}^0 - \Delta_r G_{PI}^0 = -4.51.$$

Parameter	Value	Units
X_{F_1}	5.95×10^3	mol s ⁻¹ M ⁻² (1mito) ⁻¹
$\Delta_r G_{F_1}^0$	-4.51	kJ mol ⁻¹
N_A	3	Unitless
F, RT	Table 4-2	

Mitochondrial adenylate kinase flux:

$$J_{AKi} = X_{AKi} (K_{eq,AK} [ADP]_x [ADP]_i - [AMP]_i [ATP]_i).$$

Parameter	Value	Units
X_{AKi}	1.00×10^{10}	$\text{mol s}^{-1} \text{M}^{-2} (1\text{mito})^{-1}$
$\Delta_r K_{eq,AK}$	3.97×10^{-1}	Unitless
F, RT	Table 4-2	

Adenine nucleotide translocase flux:


$$J_{ANT} = \frac{k_2^{\text{ANT}} q \frac{[ATP]_x [ADP]_i}{K_0^D} - k_3^{\text{ANT}} q \frac{[ATP]_i [ADP]_x}{K_0^D}}{\left(1 + \frac{[ATP]_i}{K_0^T} + \frac{[ADP]_i}{K_0^D}\right) \left(1 + \frac{[ATP]_x}{K_0^T} + \frac{[ADP]_x}{K_0^D}\right)},$$

where

$$k_2^{\text{ANT}} = k_2^{\text{ANT},0} \exp((-3a_1 - 4a_2 + a_3)F\Delta\psi/RT),$$

$$k_3^{\text{ANT}} = k_3^{\text{ANT},0} \exp((-4a_1 - 3a_2 + a_3)F\Delta\psi/RT),$$

$$K_0^D = k_0^{D,0} \exp(3\delta_D RT/F\Delta\psi),$$

$$K_0^T = k_0^{T,0} \exp(4\delta_T RT/F\Delta\psi),$$

$$q = \frac{k_3^{\text{ANT}} K_0^D}{k_2^{\text{ANT}} K_0^T} \exp(F\Delta\psi/RT).$$

Parameter	Value	Units
$K_2^{ANT,0}$	0.159	s^{-1}
$K_3^{ANT,0}$	0.501	s^{-1}
K_0^D	38.89	mM
K_0^T	56.05	mM
a_1	0.2829	Unitless
a_2	0.2086	Unitless
a_3	0.2372	Unitless
δ_D	0.0699	Unitless
δ_T	0.0167	Unitless
$\Delta_r K_{eq,AK}$	3.97×10^{-1}	Unitless

Hydrogen-Phosphate co-transporter flux:



$$J_{PIHT} = X_{PIHT} \left(\frac{[H_2PO_4]_i [H^+]_i - [H_2PO_4]_x [H^+]_x}{k_{PIHT} ((1 + [H_2PO_4]_i / k_{PIHT}) (1 + [H_2PO_4]_x / k_{PIHT}))} \right)$$

Parameter	Value	Units
X_{PIHT}	3.01×10^6	$\text{mol s}^{-1} \text{M}^{-2} (1\text{mito})^{-1}$
k_{PIHT}	1.01×10^{-3}	M

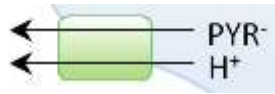
Hydrogen-Potassium exchange flux:



$$J_{KH} = X_{KH} ([K^+]_i [H^+]_x - [K^+]_x [H^+]_i)$$

Parameter	Value	Units
X_{KH}	5.65×10^6	$\text{mol s}^{-1} \text{M}^{-2} (1\text{mito})^{-1}$

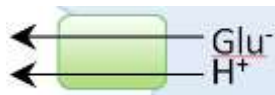
Hydrogen-Pyruvate co-transporter flux:



$$J_{PYRt} = X_{PYR}([PYR]_i[H^+]_i - [PYR]_x[H^+]_x).$$

Parameter	Value	Units
X_{PYR}	4.12×10^8	$\text{mol s}^{-1} \text{M}^{-2} (1\text{mito})^{-1}$

Hydrogen-Glutamate co-transporter flux:



$$J_{GLUht} = X_H([GLU]_i[H^+]_x - [GLU]_x[H^+]_i).$$

Parameter	Value	Units
X_{GLUht}	3.26×10^8	$\text{mol s}^{-1} \text{M}^{-2} (1\text{mito})^{-1}$

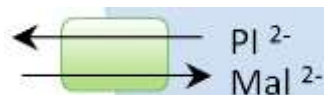
Malate-Citrate exchange flux:



$$J_{CM} = X_{CM}([CIT]_i[MAL]_x - [CIT]_x[MAL]_i).$$

Parameter	Value	Units
X_{CM}	7.31×10^1	$\text{mol s}^{-1} \text{M}^{-2} (1\text{mito})^{-1}$

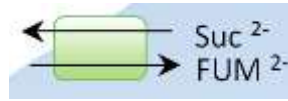
Malate-phosphate exchange flux:



$$J_{MALPI} = X_{MALPI}([MAL]_i[PI]_x - [MAL]_x[PI]_i).$$

Parameter	Value	Units
X_{MALPI}	1.58×10^1	$\text{mol s}^{-1} \text{M}^{-2} (1\text{mito})^{-1}$

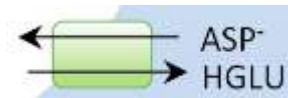
Succinate-Fumarate exchange flux:



$$J_{SUCFUM} = X_{SUCFUM}([SUC]_i[FUM]_x - [SUC]_x[FUM]_i).$$

Parameter	Value	Units
X_{SUCFUM}	9.54×10^1	$\text{mol s}^{-1} \text{M}^{-2} (\text{1mito})^{-1}$

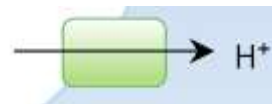
Aspartate-Glutamate exchange flux:



$$J_{ASPGLU} = X_{ASPGLU}([ASP]_i[GLU]_x - [ASP]_x[GLU]_i).$$

Parameter	Value	Units
X_{ASPGLU}	7.48×10^{-5}	$\text{mol s}^{-1} \text{M}^{-2} (\text{1mito})^{-1}$

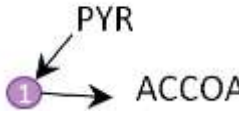
Proton leak flux:



$$J_{PL} = X_{PL} \Delta\psi \left(\frac{[H^+]_c \frac{e^{F\Delta\psi}}{RT} - [H^+]_x [GLU]_i}{\frac{e^{F\Delta\psi}}{RT} - 1} \right).$$

Parameter	Value	Units
X_{PL}	3.05×10^2	$\text{mol s}^{-1} \text{M}^{-2} (\text{1mito})^{-1}$
F, RT	Table 4-2	

Pyruvate dehydrogenase flux:



$$J_{pdh} = \frac{V_{mf} \left(1 - \frac{1}{K_{eq,pdh}} \frac{[P][Q][R]}{[A][B][C]} \right)}{K_{mC} [A][B] + K_{mB} [A][C] + K_{mA} [C][B] + [A][B][C]},$$

where [A] = [PYR]x, [B] = [COASH]x, C = [NAD]x, [P] = [CO₂]x, [Q] = [ACCOA]x, and [R] = [NADH]x

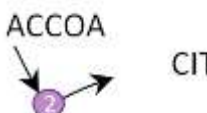
and

$$K_{eq,pdh} = K_{eq}^0 \frac{1}{[H^+]} \frac{P_{CO_2,tot} P_{ACCOA} P_{NADH}}{P_{PYR} P_{COASH} P_{NAD}},$$

$$K_{eq,pdh}^0 = 5.02 \times 10^{-4}.$$

Parameter	Value	Units
V_{mf}	0.205093	
K_{mA}	38.30×10^{-6}	M
K_{mB}	14.00×10^{-6}	M
K_{mC}	3.33×10^{-6}	M
F, RT	Table 4-2	

Citrate Synthase flux:



$$J_{CS} = \frac{V_{mf} \left([A][B] - \frac{[P][Q]}{K_{eq,cits}} \right)}{K_{iA} K_{mB} + K_{mA} [B] + K_{mB} [A] + [A][B]},$$

where [A] = [OAA]x, [B] = [ACCOA]x, [P] = [COASH]x and [Q] = [CIT]x

and

$$K_{eq,cits} = K_{eq,cits}^0 \frac{1}{[H^+]_x} \frac{P_{COA}P_{CIT}}{P_{OAA}P_{ACCOA}},$$

$$K_{eq,cits}^0 = 7.34 \times 10^{-8}$$

Parameter	Value	Units
V_{mf}	9.8253	
K_{mA}	4.00×10^{-6}	M
K_{mB}	9.9×10^{-6}	M
K_{iA}	60.7×10^{-6}	M
F, RT	Table 4-2	

Aconitase flux:



$$J_{AC} = \frac{V_{mf}V_{m4} \left([A] - \frac{[P]}{K_{eq,acon}} \right)}{K_{mA}V_{mr} + V_{mr}[A] + \frac{V_{mf}}{K_{eq,acon}} [P]},$$

where $[A] = [CIT]_x$, and $[P] = [ICIT]_x$,

and

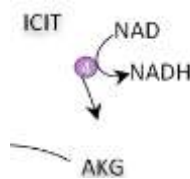
$$K_{eq,acon} = K_{eq,acon}^0 \frac{P_{ICIT}}{P_{CIT}},$$

$$K_{eq,acon}^0 = 7.59 \times 10^{-2}.$$

Parameter	Value	Units
V_{mf}	0.02766	
V_{mr}	0.02766	

F, RT	Table 4-2	
K_{mA}	1.1×10^{-4}	M

Isocitrate dehydrogenase flux:



$$J_{isod} = \frac{V_{mf} \left(1 - \frac{1}{K_{eq,isod}} \frac{[P][Q][R]}{[A][B]} \right)}{1 + \frac{K_{mB}}{[B]} \frac{K_{mA}}{[A]} \left(\left(1 + \frac{K_{iB}}{[B]} \right)^{N_A} \frac{[Q]}{K_{iq}} \right)},$$

where $[A] = [NAD]_x$, $[B] = [ICIT]_x$, $[P] = [AKG]_x$, $[Q] = [NADH]_x$, and $[R] = [CO_2]_x$,

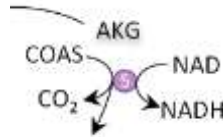
and

$$K_{eq,isod} = K_{eq,isod}^0 \frac{1}{[H^+]_x} \frac{P_{AKG} P_{NADH} P_{CO_2}}{P_{NAD} P_{CIT}},$$

$$K_{eq,isod}^0 = 3.50 \times 10^{-16}.$$

Parameter	Value	Units
V_{mf}	0.49204	
K_{mA}	7.40×10^{-7}	
K_{mB}	1.83×10^{-8}	
K_{iq}	2.90×10^{-7}	
$F, RT \ \& \ \psi$	Table 4-2	
K_{iB}	7.66×10^{-6}	M
N_A	3.0	

α -ketoglutarate dehydrogenase flux:



$$J_{akg} = \frac{V_{mf} \left(1 - \frac{1}{K_{eq,akg}} \frac{[P][Q][R]}{[A][B][C]} \right)}{1 + \frac{K_{mA}}{[A]} \frac{K_{mB}}{[B]} \left(1 + \frac{[Q]}{K_{iq}} \right) + \frac{K_{mC}}{[C]} \left(1 + \frac{[R]}{K_{ir}} \right)},$$

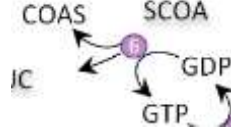
where $[A] = [AKG]$, $[B] = [COASH]_x$, $[C] = [NAD]_x$, $[P] = [CO_2]_x$, $[Q] = [SCOA]_x$, and $[R] = [NADH]_x$,

and

$$K_{eq,AKG} = K_{eq,AKG}^0 \frac{1}{[H^+]_x} \frac{P_{CO_2} P_{SCOA} P_{NADH}}{P_{AKG} P_{COASH} P_{NAD}},$$

$$K_{eq,AKG}^0 = 6.93 \times 10^{-3}.$$

Parameter	Value	Units
V_{mf}	0.0876	
K_{mA}	8.00×10^{-7}	
K_{mB}	5.50×10^{-7}	
K_{mC}	2.10×10^{-7}	
K_{ir}	4.50×10^{-6}	
K_{iq}	6.90×10^{-6}	
F, RT	Table 4-2	

Succinyl-CoA synthase flux:

 J_{sc}

$$\begin{aligned}
 &= \frac{V_{mf}V_{mr} \left([A][B][C] - \frac{[P][Q][R]}{[A][B][C]} \right)}{V_{mr}K_{ia}K_{ib}K_{mc} + V_{mr}K_{ib}K_{mc}[A] + V_{mr}K_{ia}K_{mb}[C] + V_{mr}K_{mc}[A][B] + V_{mr}K_{mB}[A][C] + V_{mr}[A][B][C] + \frac{V_{mf}K_{ir}K_{mq}[P]}{K_{eq,su}} + \frac{V_{mf}K_{iq}K_{mP}[R]}{K_{eq,su}} + \frac{V_{mf}K_{mR}[P][Q]}{K_{eq,su}} + \frac{V_{mf}K_{mq}[P][R]}{K_{eq,su}} + \frac{V_{mf}K_{mp}[P][Q]}{K_{eq,su}} + \frac{V_{mf}[P][Q][R]}{K_{eq,su}} + \frac{V_{mf}K_{mq}K_{ir}[P][A]}{K_{eq,su}} + \frac{V_{mf}K_{ia}K_{mB}[C][R]}{K_{eq,su}} + \frac{V_{mf}K_{mQ}K_{ir}[A][B][P]}{K_{ia}K_{ib}K_{eq,su}} + \frac{V_{mf}K_{mA}[B][C][R]}{K_{ir}} + \frac{V_{mf}K_{mR}[A][P][Q]}{K_{ia}K_{eq,su}} + \frac{V_{mr}K_{mB}K_{ia}[C][Q][R]}{K_{iq}K_{ir}} + \frac{V_{mf}K_{mQ}K_{ir}[A][B][C][P]}{K_{ia}K_{ib}K_{ic}K_{eq,su}} + \frac{V_{mf}K_{ip}K_{mR}[A][B][C][Q]}{K_{ia}K_{ib}K_{ic}K_{eq,su}} + \frac{V_{mf}K_{mR}[A][B][P][Q]}{K_{ia}K_{ib}K_{eq,su}} + \frac{V_{mr}K_{mA}[B][C][Q][R]}{K_{iq}K_{ir}} + \frac{V_{mr}K_{mA}K_{ic}[B][P][Q][R]}{K_{ip}K_{iq}K_{ir}} + \frac{V_{mr}K_{mB}K_{ia}[C][P][Q][R]}{K_{ip}K_{iq}K_{ir}} + \frac{V_{mf}K_{mR}[A][B][C][P][Q]}{K_{ia}K_{ib}K_{ic}K_{eq,su}} + \frac{V_{mf}K_{mA}[B][C][P][Q][R]}{K_{ip}K_{iq}K_{ic}}
 \end{aligned}$$

where $[A] = [GDP]x$, $[B] = [SCOA]x$, $[C] = [PI]x$, $[P] = [COASH]x$, $[Q] = [SUC]x$, and $[R] = [GTP]x$,

and

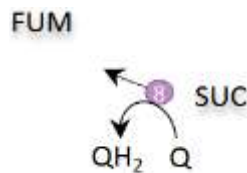
$$K_{eq,SU} = K_{eq,isod}^0 \frac{1}{H^+} \frac{P_{COASH}P_{SUC}P_{GTP}}{P_{GDP}P_{SCOAP}P_{PI}}$$

$$K_{eq,isod}^0 = 9.54 \times 10^{-9}.$$

Parameter	Value	Units
V_{mf}	0.0876	
K_{ma}	1.60×10^{-6}	M
K_{mb}	5.50×10^{-6}	M
K_{mc}	6.60×10^{-8}	M
K_{mp}	8.80×10^{-6}	M
K_{mq}	1.11×10^{-7}	M

K_{ir}	4.50×10^{-6}	M
K_{ia}	5.50×10^{-6}	M
K_{ib}	1.00×10^{-8}	M
K_{ic}	2.000×10^{-9}	M
K_{ip}	2.00×10^{-7}	M
K_{iq}	3.00×10^{-9}	M
F, RT	Table 4-2	

Succinate dehydrogenase flux:



$$J_{SC} = \frac{V_{mf}V_{mr} \left([A][B] - \frac{[P][Q]}{K_{eq,SC}} \right)}{V_{mr}K_{ia}K_{iB} + V_{mr}K_{mB}[A] + V_{mr}K_{mA}[B] + \frac{V_{mf}K_{mB}}{K_{eq,SC}}[P] + \frac{V_{mf}K_{mP}}{K_{eq,SC}}[Q] + V_{mr}[A][B] + \frac{V_{mf}K_{mQ}}{K_{eq,SC}K_{ia}}[A][P] + \frac{V_{mf}K_{mA}}{K_{iq}}[B][Q] + \frac{V_{mf}}{K_{eq,SC}}[P][Q]}$$

where $[A] = [SUC]x$, $[B] = [COQ]x$, $[P] = [QH_2]x$, and $[Q] = [FUM]x$

and

$$K_{eq,SC} = K_{eq,SC}^0 \frac{P_{QH_2} P_{FUM}}{P_{COQ} P_{SUC}}$$

$$K_{eq,SC}^0 = 1.69.$$

Parameter	Value	Units
V_{mf}	0.08578	
K_{mA}	4.67×10^{-8}	M

K_{mB}	4.80×10^{-8}	M
K_{mP}	2.45×10^{-6}	M
K_{mQ}	1.20×10^{-9}	M
K_{ia}	1.20×10^{-8}	M
K_{iq}	1.28×10^{-9}	M

Fumarase flux:



$$J_{FUM} = \frac{V_{mf}V_{mr} \left([A] - \frac{[P]}{K_{eq,FUM}} \right)}{K_{mA}V_{mr} + V_{mr}[A] + \frac{V_{mf}[P]}{K_{eq,FUM}}}$$

where $[A] = [FUM]x$, [and $[P] = [MAL]x$,

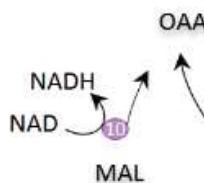
and

$$K_{eq,FUM} = K_{eq,SC}^0 \frac{P_{MAL}}{P_{FUM}},$$

$$K_{eq,FUM}^0 = 4.04 .$$

Parameter	Value	Units
V_{mf}	0.00707	
K_{mA}	4.47×10^{-7}	M

Malate dehydrogenase flux:



$$J_{MAL} = \frac{V_{mf}V_{mr} \left([A][B] - \frac{[P][Q]}{K_{eq,MAL}} \right)}{V_{mr}K_{ia}K_{iB} + V_{mr}K_{mB}[A] + V_{mr}K_{mA}[B] + \frac{V_{mf}K_{mB}[P]}{K_{eq,MAL}} + \frac{V_{mf}K_{mP}[Q]}{K_{eq,MAL}} + V_{mr}[A][B] + \frac{V_{mf}K_{mQ}}{K_{eq,MAL}K_{ia}}[A][P] + \frac{V_{mf}K_{mA}}{K_{iq}}[B][Q] + \frac{V_{mf}K_{mA}}{K_{ip}}[A][B][P] + \frac{V_{mf}}{K_{ib}K_{eq,MAL}}[B][P][Q]}$$

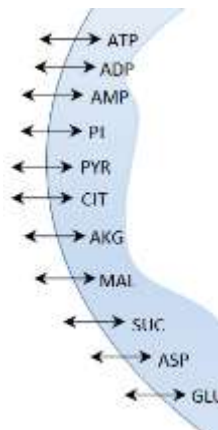
where [A] = [NAD]x, [B] = [MAL]x, [P] = [OAA]x, and [Q] = [NADH]x,

$$K_{eq,MAL} = K_{eq}^0 \frac{P_{OAA}P_{NADH}}{P_{NAD}P_{MAL}},$$

$$K_{eq,MAL}^0 = 2.27 \times 10^{-12}.$$

Parameter	Value	Units
V_{mf}	0.07706	
K_{mA}	9.06×10^{-8}	M
K_{mB}	2.50×10^{-9}	M
K_{mP}	6.13×10^{-8}	M
K_{mQ}	2.58×10^{-6}	M
K_{ia}	2.79×10^{-9}	M
K_{ib}	3.60×10^{-9}	M
K_{ip}	5.5×10^{-6}	M
K_{iq}	3.18×10^{-6}	M

Passive permeation fluxes:



Adenine nucleoside permeation:

$$J_{ATPt} = \gamma P_A ([ATP]_c - [ATP]_i) ,$$

$$J_{ADPt} = \gamma P_A ([ADP]_c - [ADP]_i) ,$$

$$J_{AMPt} = \gamma P_A ([AMP]_c - [AMP]_i) .$$

Inorganic Phosphate permeation:

$$J_{PIt} = \gamma P_A ([PI]_c - [PI]_i) .$$

TCA cycle intermediate permeation:

$$J_{PYRt} = \gamma P_A ([PYR]_c - [PYR]_i) ,$$

$$J_{CITt} = \gamma P_A ([CIT]_c - [CIT]_i) ,$$

$$J_{MALt} = \gamma P_A ([MAL]_c - [MAL]_i) ,$$

$$J_{AKGt} = \gamma P_A ([AKG]_c - [AKG]_i) ,$$

$$J_{SUCt} = \gamma P_A ([SUC]_c - [SUC]_i) ,$$

$$J_{FUMt} = \gamma P_A ([FUM]_c - [FUM]_i) ,$$

$$J_{GLUt} = \gamma P_A ([GLU]_c - [GLU]_i) ,$$

$$J_{ASPt} = \gamma P_A ([ASP]_c - [ASP]_i) .$$

Parameter	Value	Units
γ	Table 4-2	
P_A	Table 4-2	

The corresponding ODEs are described in Table 4-4:

$$\begin{aligned}
 d[\text{ATP}]_x / dt &= (J_{NU} + J_{F1} - J_{ANT}) / W_x \\
 d[\Delta\Psi] / dt &= (1.48E+05)(+4 J_{C1} + 2 J_{C3} + 4 J_{C4} - N_A * J_{F1} - J_{ANT} - J_{PL} + J_{AHG}) / C_{im} \\
 d[\text{ADP}]_x / dt &= (-J_{NU} - J_{F1} + J_{ANT}) / W_x \\
 d[\text{Pi}]_x / dt &= (-J_{SU} - J_{F1} + J_{H2PI} - J_{MALPI} - J_{SUCPI}) / W_x \\
 d[\text{NADH}]_x / dt &= (+J_{PDH} + J_{IC} + J_{AK} + J_{MA} - J_{C1}) / W_x \\
 d[\text{QH2}]_x / dt &= (+J_{SC} + J_{C1} - J_{C3}) / W_x \\
 d[\text{OAA}]_x / dt &= (-J_{CS} + J_{MA} + J_{GO}) / W_x \\
 d[\text{ACCOA}]_x / dt &= (-J_{CS} + J_{PDH}) / W_x \\
 d[\text{CIT}]_x / dt &= (+J_{CIT} - J_{AC} + J_{CITMAL}) / W_x \\
 d[\text{ICIT}]_x / dt &= (+J_{AC} - J_{IC}) / W_x \\
 d[\text{AKG}]_x / dt &= (+J_{IC} - J_{AK} - J_{GO}) / W_x \\
 d[\text{SCOA}]_x / dt &= (+J_{AK} - J_{SU}) / W_x \\
 d[\text{COASH}]_x / dt &= (-J_{PDH} - J_{AK} + J_{SU} + J_{CS}) / W_x \\
 d[\text{SUC}]_x / dt &= (+J_{SU} - J_{SC} + J_{SUCMAL}) / W_x \\
 d[\text{FUM}]_x / dt &= (+J_{SC} - J_{FU}) / W_x \\
 d[\text{MAL}]_x / dt &= (+J_{FU} - J_{MA} + J_{MALPI} - J_{AKGMAL} - J_{CITMAL} - J_{SUCMAL}) / W_x \\
 d[\text{GLU}]_x / dt &= (+J_{GO} + J_{AHG}) / W_x \\
 d[\text{ASP}]_x / dt &= (-J_{GO} + J_{AHG}) / W_x \\
 d[\text{Cred}]_i / dt &= (-J_{GO} + J_{AHG}) / W_x \\
 d[\text{ASP}]_x / dt &= (+2 J_{C3} - 2 J_{C4}) / W_i \\
 d[\text{ATP}]_i / dt &= (J_{ATP} + J_{ANT} + J_{AKFi}) / W_i \\
 d[\text{ADP}]_i / dt &= (J_{ADP} - J_{ANT} - 2 J_{AKFi}) / W_i \\
 d[\text{AMP}]_i / dt &= (J_{PERM} + J_{AKFi}) / W_i \\
 d[\text{Pi}]_i / dt &= (-J_{H2PI} + J_{PIH} + J_{MALPI}) / W_i \\
 d[\text{ATP}]_c / dt &= (-Rm_{cyto} (J_{ATPt} + J_{CK} + J_{AK} - J_{PGK} + J_{PK} - J_{AK} - J_{PFK})) / W_c \\
 d[\text{ADP}]_c / dt &= (-J_{ADPt} - J_{ANT} - 2 J_{AKFi}) / W_i \\
 d[\text{Pi}]_c / dt &= (-Rm_{cyto} (-J_{Pit})) / W_c \\
 d[\text{PYR}]_x / dt &= (-J_{PDH}) / W_x \\
 d[\text{PYR}]_i / dt &= (-J_{PDH}) / W_x \\
 d[\text{PYR}]_c / dt &= (-Rm_{cyto} (J_{PYRt})) / W_c \\
 d[\text{CIT}]_i / dt &= (-J_{CITt}) / W_i \\
 d[\text{CIT}]_c / dt &= (-Rm_{cyto} (J_{CITt})) / W_c \\
 d[\text{AKG}]_i / dt &= (-J_{AKGMAL} + J_{AKGt}) / W_i \\
 d[\text{AKG}]_c / dt &= (-Rm_{cyto} (J_{AKGt})) / W_c
 \end{aligned}$$

$$\begin{aligned}
 d[\text{SUC}]_i / dt &= (+ J_{\text{SUCt}} - J_{\text{SUCMAL}}) / W_i \\
 d[\text{SUC}]_c / dt &= (- Rm_{\text{cyto}} (J_{\text{SUCt}})) / W_c \\
 d[\text{MAL}]_i / dt &= (- J_{\text{MALPI}} + J_{\text{MALt}} + J_{\text{AKGMAL}} + J_{\text{CITMAL}} + J_{\text{SUCMAL}}) / W_i \\
 d[\text{MAL}]_c / dt &= (- Rm_{\text{cyto}} (J_{\text{MALt}})) / W_c \\
 d[\text{ASP}]_i / dt &= (- J_{\text{ASPLU}} + J_{\text{ASPt}}) / W_i \\
 d[\text{ASP}]_c / dt &= (- Rm_{\text{cyto}} (J_{\text{ASPt}})) / W_c \\
 d[\text{GLU}]_i / dt &= (- J_{\text{GLUH}} + J_{\text{ASPLU}} + J_{\text{GLUt}}) / W_i \\
 d[\text{GLU}]_c / dt &= (- Rm_{\text{cyto}} (J_{\text{GLUt}})) / W_c \\
 d[\text{FUM}]_i / dt &= (J_{\text{FUMt}}) / W_i \\
 d[\text{FUM}]_c / dt &= (- Rm_{\text{cyto}} (J_{\text{FUMt}})) / W_c \\
 d[\text{ICIT}]_i / dt &= (J_{\text{CITMAL}} + J_{\text{ICTt}}) / W_i \\
 d[\text{ICIT}]_c / dt &= (- Rm_{\text{cyto}} (J_{\text{ICTt}})) / W_c \\
 d[\text{PCr}]_c / dt &= (- J_{\text{CK}}) / W_c \\
 d[\text{AMP}]_c / dt &= (- Rm_{\text{cyto}} (J_{\text{AMPt}} + J_{\text{AK}})) / W_c \\
 d[\text{Cr}]_c / dt &= (+ J_{\text{CK}}) / W_c
 \end{aligned}$$

Table 4-4: Mitochondrial respiration model ODEs.

While the model is constructed using kinetic terms and parameters exclusively from Vinnakota *et al.* ⁹⁶, this model differs from the original through the coupling with *in vitro* extracellular flux analysis, whereby oxygen consumption rate (OCR) outputs are a function of the transient microchamber volumes. This adaptation allows for simulation of EFA outputs relative to an extracellular environment, which is not achieved in the Wu *et al.* model ⁹⁶. The simulation of OCR including the transient microchamber volume is described in 4.2.4.

4.2.3 Preliminary Simulations

Time-course simulations were generated variable-order stiff solver ode15s in Matlab, with initial conditions as denoted in Table 4-1. For time course simulations, steady state solutions are assumed to have been reached when changes in all variable concentrations do not exceed the size of the absolute integration tolerance (10^{-10}) for a time interval of 2000 seconds. This definition of a steady state is used because of the intractability of an analytical solution for such a large-scale dynamic system. The

initial preliminary simulations were conducted over a 5000 second time period. The primary aim of the initial simulations was to establish whether or not the model could recapitulate the well-defined physiologically reported levels previously achieved in the literature. Figure 4-2, Figure 4-3 and Figure 4-4 show the time-course simulations for all model variables (matrix ($_x$), intermembrane space ($_i$) and cytoplasm ($_c$) respectively), with Figure 4-5 and Figure 4-6 illustrating model reaction and transporter flux terms varying over time.

4.2.3.1 Variable & Reaction Flux Steady States

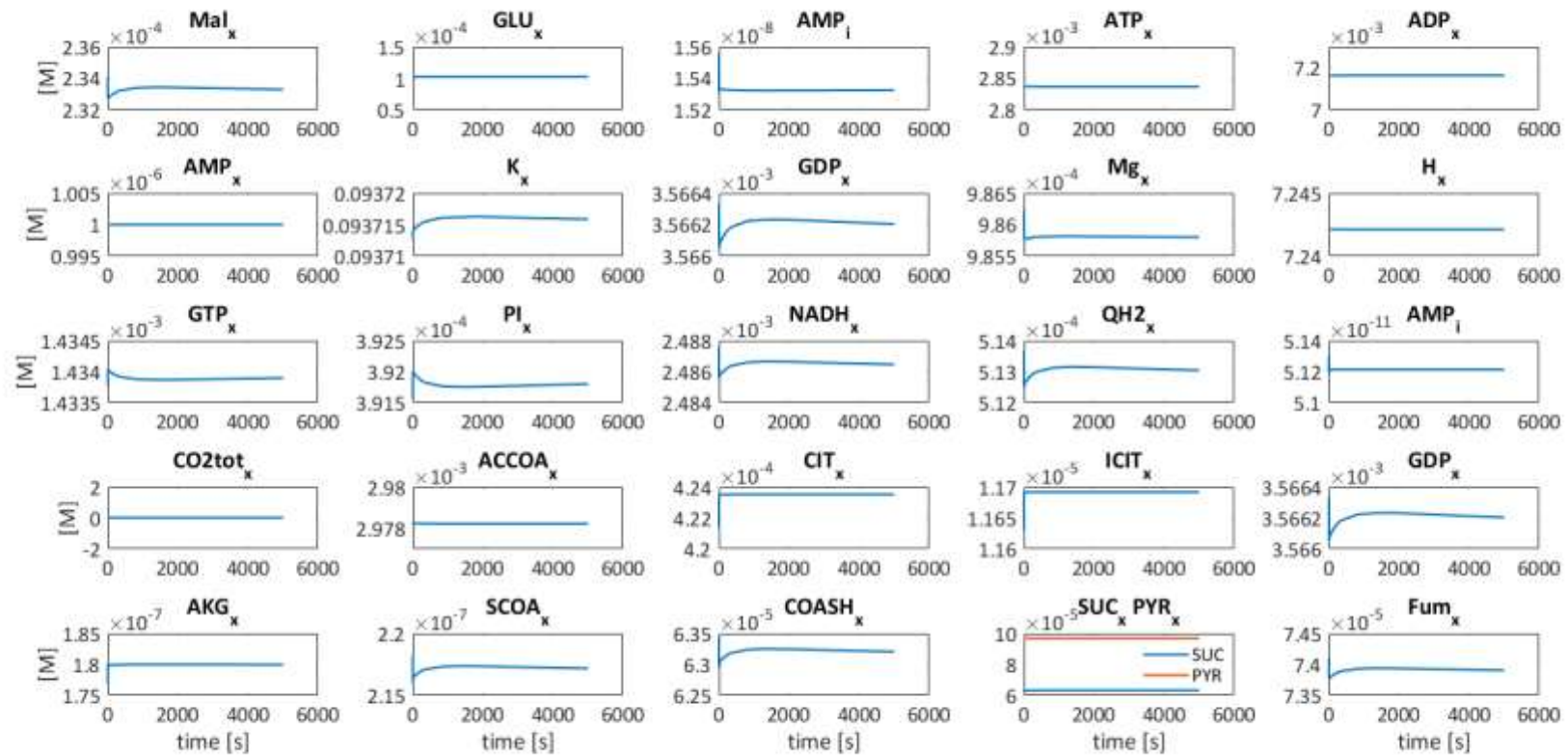


Figure 4-2: Mitochondrial respiration model matrix variable time course simulation. All concentrations are expressed in [M] and time [s].

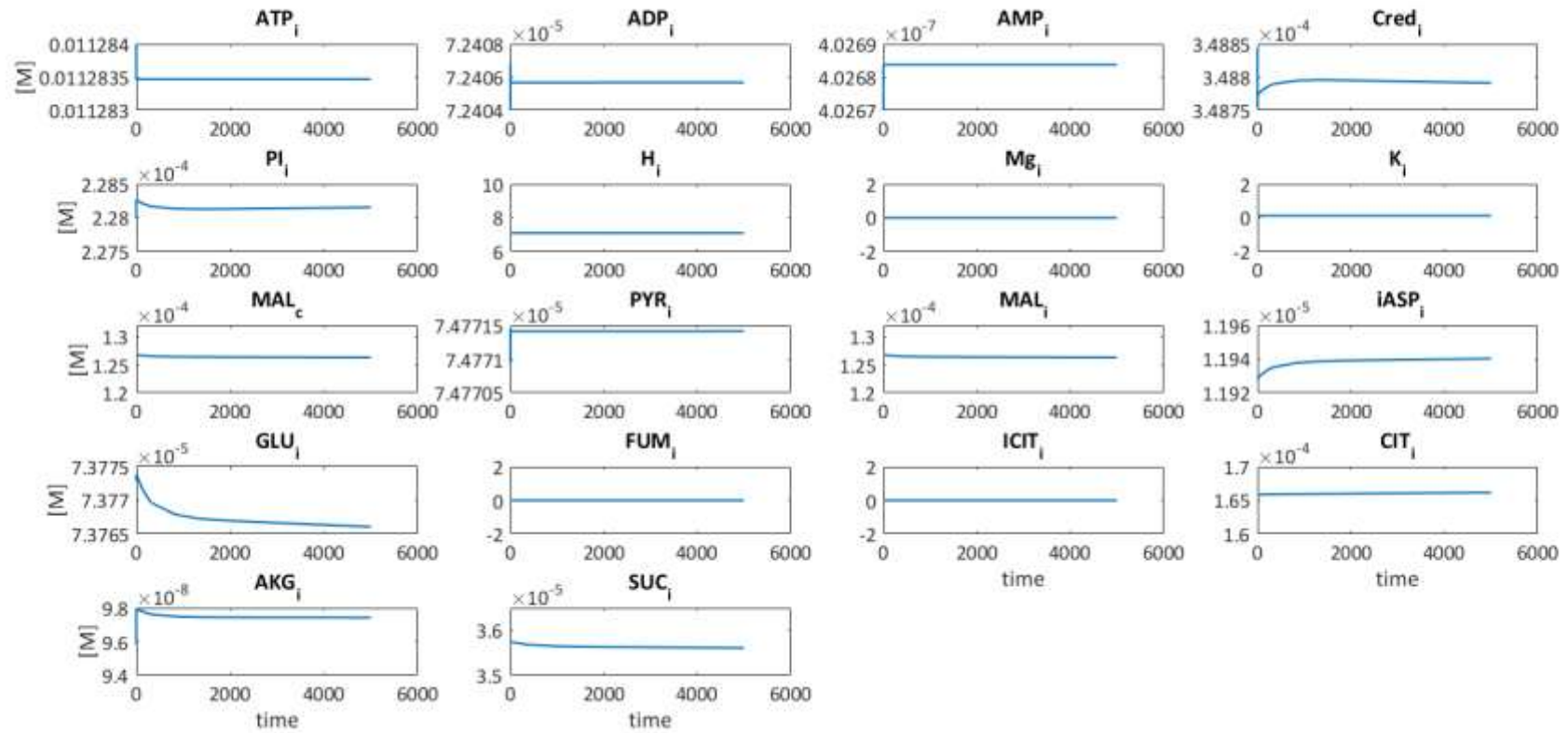


Figure 4-3: Mitochondrial respiration model intermembrane space variable time course simulation.

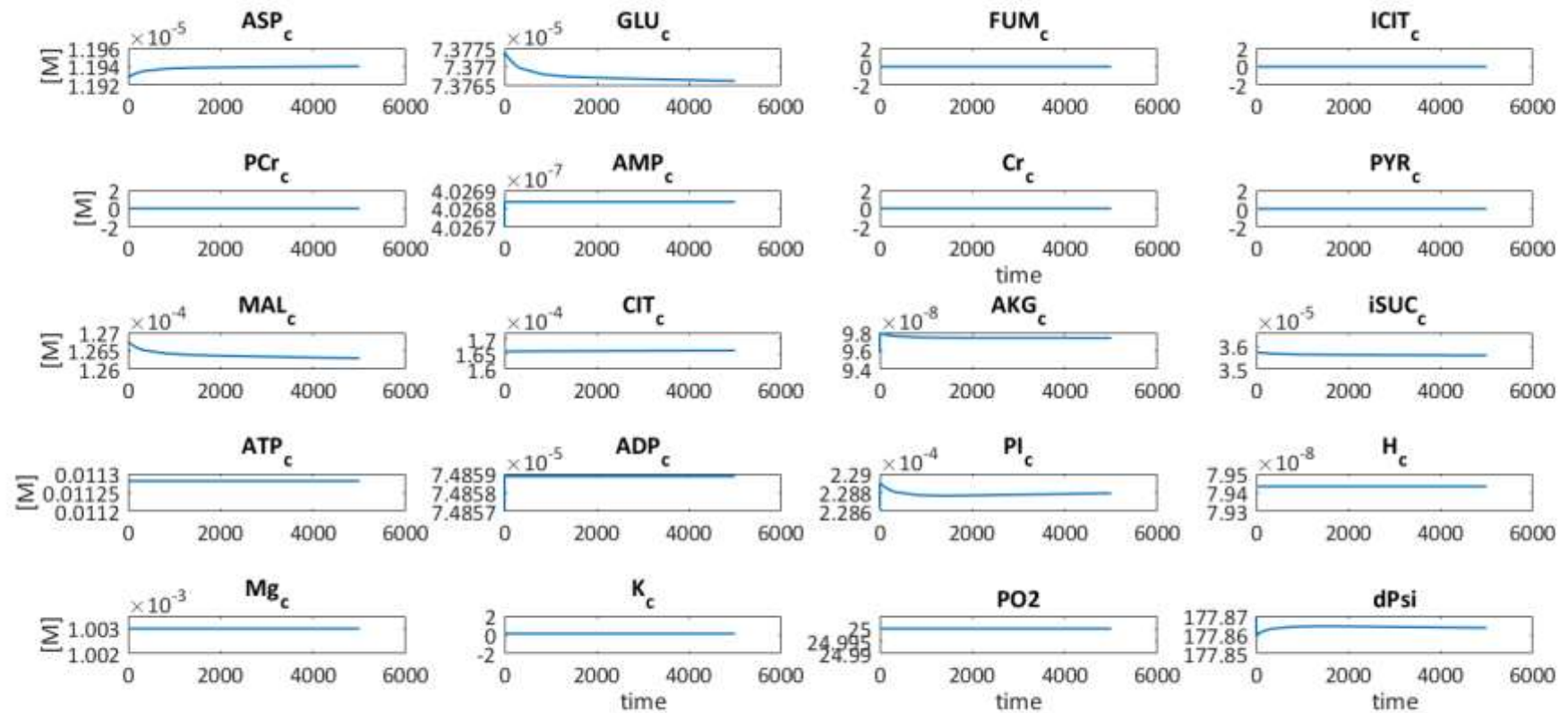


Figure 4-4: Mitochondrial respiration model cytoplasm and membrane potential ($\Delta\Psi_m$) time course profile.

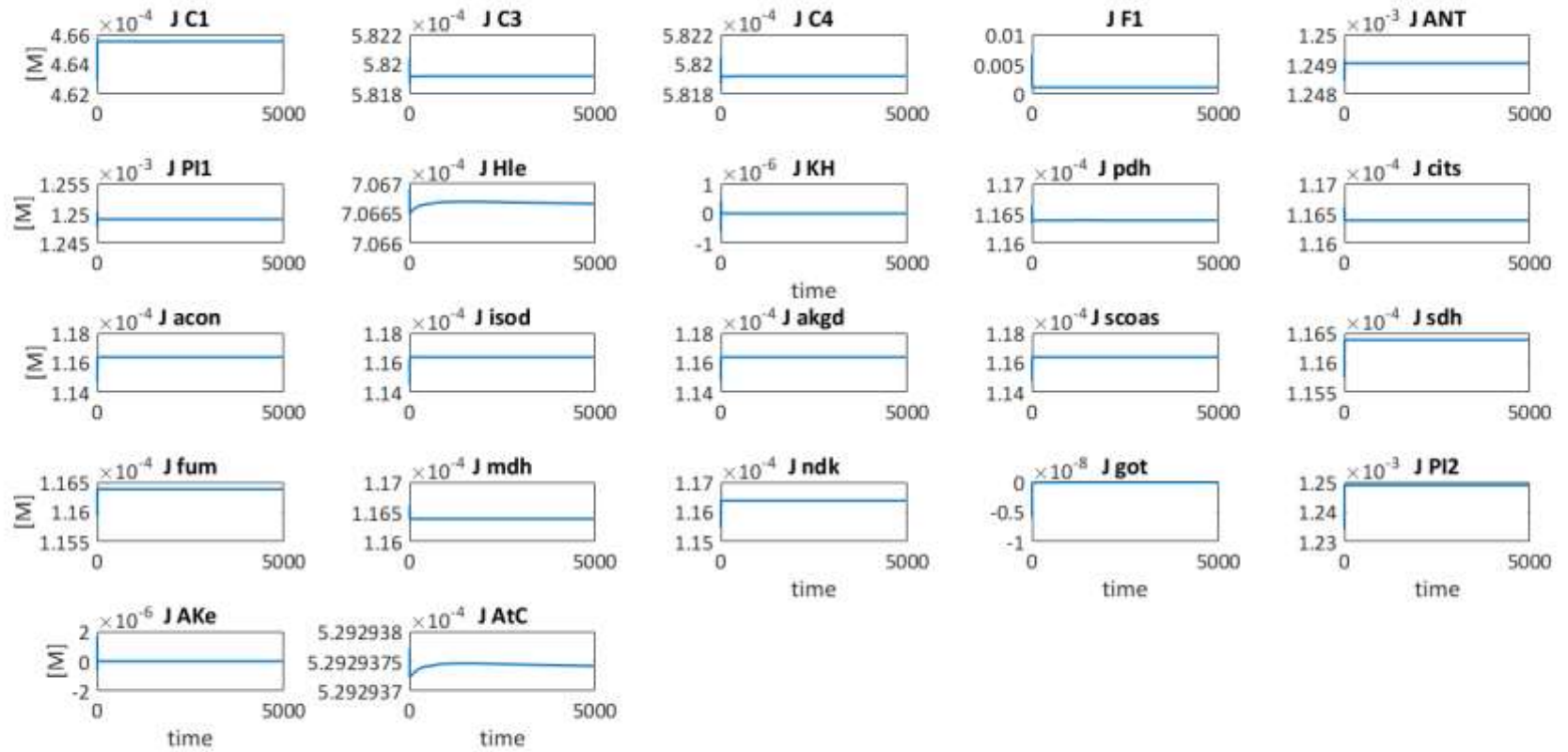


Figure 4-5: Mitochondrial respiration model ETC TCA reaction flux time course profiles.

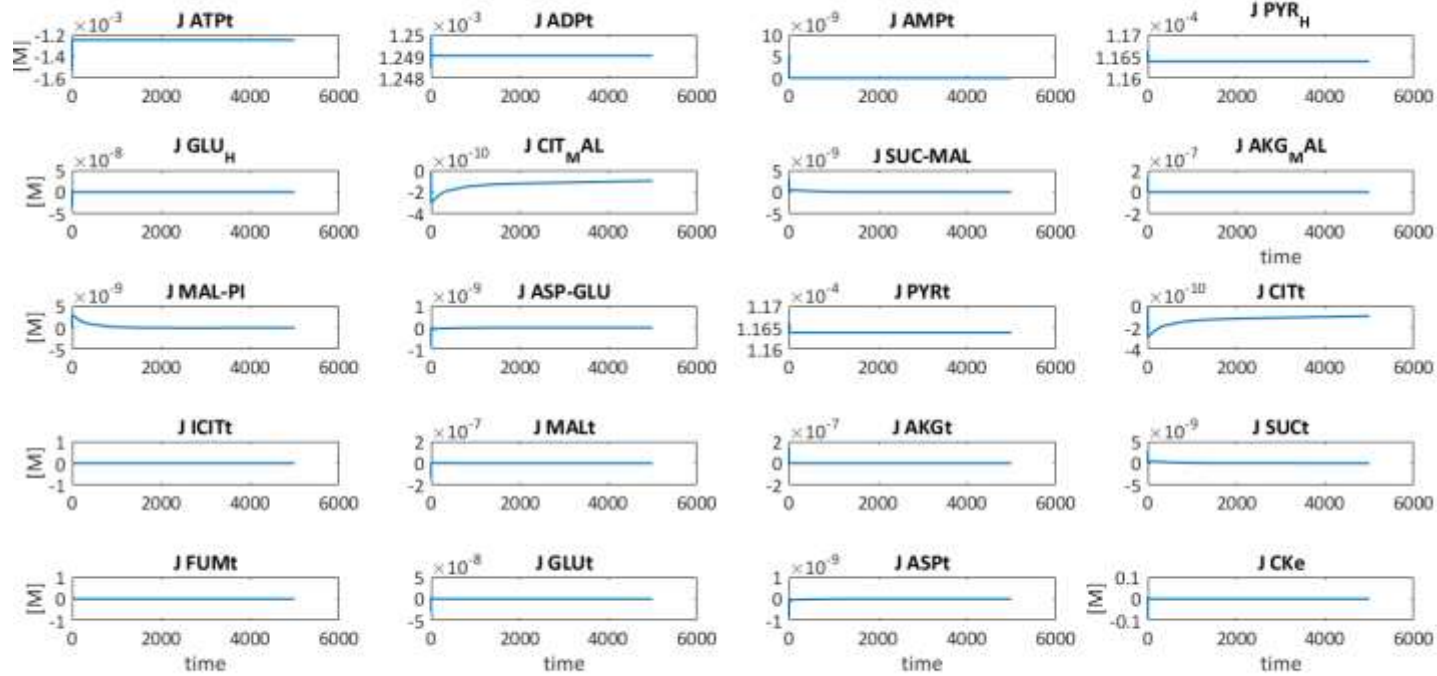


Figure 4-6: Mitochondrial respiration transporter and permeation reaction flux time course plots.

In order to establish how close to the literature values our simulated outputs are, our simulated steady state concentrations were subtracted from literature values and the differences are shown in Table 4-5.

Variable	Difference	Relative % Difference	Units
<i>IM Space Species (i)</i>			
[Cred]i	4.20×10^{-6}	1.2	M
[ATP]i	1.65×10^{-10}	0	M
[ADP]i	-6.00×10^{-9}	0.05	M
[AMP]i	3.20×10^{-10}	0.08	M
[PI]i	-3.00×10^{-7}	0.13	M
[H ⁺]i	0	0	M
[Mg]i	-3.00×10^{-6}	0.3	M
[K]i	0	0	M
[PYR]i	3.00×10^{-8}	0.04	M
[CIT]i	-2.00×10^{-7}	0.12	M
[AKG]i	7.00×10^{-11}	0.07	M
[SUC]i	1.90×10^{-7}	0.53	M
[MAL]i	1.44×10^{-5}	11.34	M
[ASP]i	-4.00×10^{-8}	0.34	M
[GLU]i	3.00×10^{-8}	0.04	M
[FUM]i	0	0	M
[ICIT]i	0	0	M
[PO2]	0	0	M
[$\Delta\Psi_m$]	1.00×10^{-1}	0.06	M
<i>Matrix Variables (x)</i>			
[H ⁺]x (pH)	-0.1781546	2.46	M
[ATP]x	3.00×10^{-6}	0.11	M

[ADP]x	-3.00×10^{-6}		M
[AMP]x	0	0.10	M
[GTP]x	-4.00×10^{-6}	0	M
[GDP]x	4.00×10^{-6}	400	M
[PI]x	2.00×10^{-7}	0.28	M
[NADH]x	4.00×10^{-6}	0.01	M
[QH2]x	1.00×10^{-6}	1.02	M
[OAA]x	-1.00×10^{-14}	0.19	M
[ACCOA]x	2.00×10^{-6}	0.02	M
[CIT]x	-3.814×10^{-3}	0.07	M
[ICIT]x	-5.30×10^{-6}	904.99	M
[AKG]x	0	45.69	M
[SCOA]x	8.00×10^{-8}	0	M
[COASH]x	-5.374×10^{-5}	36.7	M
[SUC]x	2.9×10^{-7}	567.05	M
[FUM]x	2.00×10^{-7}	0.46	M
[MAL]x	7.00×10^{-7}	0.27	M
[GLU]x	-2.00×10^{-7}	0.30	M
[ASP]x	0	0.01	M
[K]x	-2.00×10^{-5}	0.02	M
[Mg]x	2.00×10^{-7}	0.02	M
[CO2tot]x	-0.1926	11.54	M
[PYR]x	5.00×10^{-8}	0.05	M

Cytoplasmic Species (c)

[PYR]c	0	0	M
[CIT]c	-2.00×10^{-7}	0.12	M
[AKG]c	7.00×10^{-11}	0.07	M
[SUC]c	1.90×10^{-7}	0.74	M

[MAL]c	7.00×10^{-7}	0.55	M
[ASP]c	-4.00×10^{-7}	3.36	M
[GLU]c	3.00×10^{-8}	0.04	M
[FUM]c	0	0	M
[ICIT]c	0	0	M
[PCr]c	4.00×10^{-5}	0.15	M
[AMP]c	3.00×10^{-10}	0.07	M
[Cr]c	1.00×10^{-7}	0	M
[ATP]c	2.00×10^{-5}	0.18	M
[ADP]c	4.00×10^{-8}	0.05	M
[PI]c	2.00×10^{-7}	0.09	M
[H ⁺]c	-3.00×10^{-11}	0.04	M
[Mg]c	-3.00×10^{-7}	0.03	M
[K]c	0	0	M

Table 4-5: Molarity differences between simulated variable concentrations and literature values from ⁹⁶.

Table 4-5 shows that most of the model variables are within 10^{-5} of literature values. For variables such as $\Delta\Psi_m$, the difference is relative to the size of the variable, 10^{-1} difference for a value around 177 mV is accurate. The most deviant variable is [CIT]x, which is 10^{-3} M different to the literature value. This may be to use of different parameter values for citrate synthase. ⁹⁶ present multiple sources from which they obtain their parameter values. For citrate synthase, they use values from ⁹⁹, however, the values used in this model are taken indirectly from ¹⁰⁰. This may explain why we obtain a slightly different steady state value for [CIT]x. Recapitulating the basal model output is the first step in model validation. The next step is to be able to replicate situations presented in the literature of system perturbations.

4.2.3.2 Model Validation

The ability of the model to simulate experimental literature data, the model was used to recreate changes in membrane potential $\Delta\Psi_m$, matrix ATP, oxygen consumption

rate (OCR) and changes in pH as a function of cytoplasmic inorganic phosphate concentration whilst placing the model in “state 2”, where cytoplasm ADP concentration is set to zero. This provides a true test of the model's ability to handle several perturbations while simulating bioenergetic relevant outputs. Experimental data was taken from ⁹³, with the original experiments performed by ¹⁰¹. For these simulations, OCR is modelled as a function of ETC complex 4 flux. Thus, the model was used to simulate experimental outputs from the literature, in particular, testing its ability to reproduce outputs under stress conditions relevant to mitochondrial specific bioenergetic outputs Figure 4-7.

These comparisons between model simulations and experimental data demonstrate that the model is effective at replicating changes in $\Delta\Psi_m$, pH and OCR. Deviations from the experimental data were observed when model simulations of matrix ATP concentration, expressed as a fraction of total ATP and ADP content, were performed. This is most likely a function of how we simulated “state 2” compared with the literature values. However, these deviations were deemed to fall within an acceptable range, displaying the key qualitative features of the literature data.

Combining the validation steps in Table 4-5 and Figure 4-7 provides confidence of our model construction and bioenergetic output.

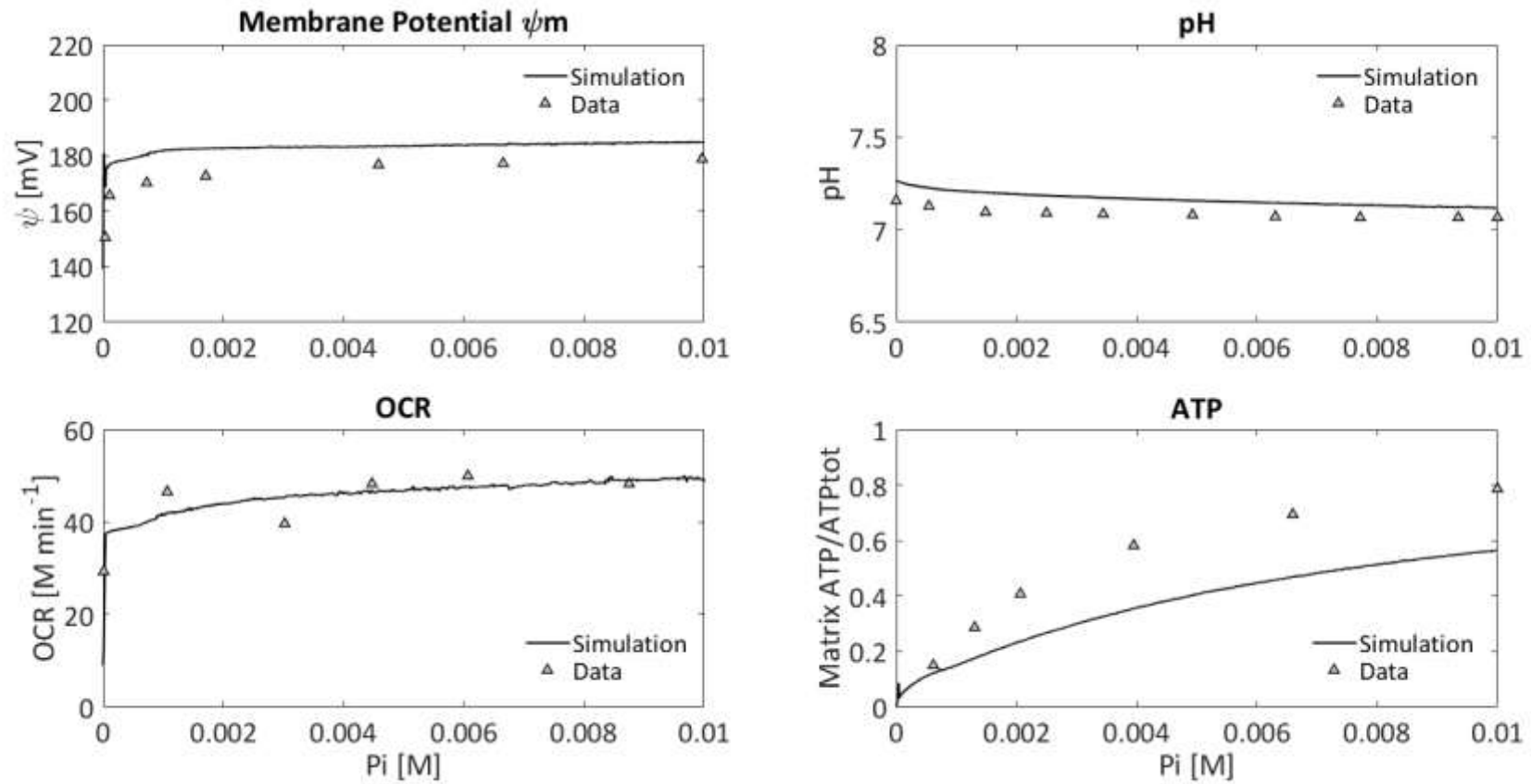


Figure 4-7: Model simulations of $\Delta\Psi_m$, matrix pH, oxygen consumption rate (OCR) and matrix ATP as a function of cytoplasmic inorganic phosphate concentrations during state 2 metabolism. Experimental data (triangles) was taken from ⁹³.

4.2.4 Modelling EFA OCR

In our framework, oxygen consumption rate is modelled as a function of cytoplasmic inorganic phosphate using the flux of ETC complex IV (J_{C4}). The primary role of oxygen within the mitochondria is to accept two electrons from the transport chain per single oxygen atom in a net 4 electron reduction of molecular oxygen to form water at complex IV. This process is well studied; the x-ray structure of the oxygen reduction site on complex IV reveals covalent links between histidine residues and a tyrosine residue to ensure retention ¹⁰². Alongside this, there are other fates of oxygen in relation to the activity of the electron chain, including the formation of ROS, detailed later. *In vitro*, the measurement of OCR can be deemed a direct measurement of mitochondrial respiration when measured in in-tact or permeabilised cells or tissue, which can be achieved using an EFA with an XFe Seahorse analyser. *In silico*, simulating OCR is straight forward, as the exact reaction flux of OCR at only complex IV can be tracked quantitatively. One important thing to note is that with respect to EFA, our model does not consider non-mitochondrial respiration (NMr), which describes all other cellular consumptions of oxygen, usually in the form of oxidative enzymes. As such, when simulating OCR in our model, NMR may be addressed by simply adding a basal rate which can be derived experimentally. Furthermore, the experimental measurement of OCR cannot capture OCR due to complex IV flux directly. Instead, consumption of oxygen from the extracellular media environment is approximated from the 2 μ L transient microchamber directly above the cells. This feature, particularly the microchamber volume, must be taken into account when attempting to replicate experimental EFA outputs *in silico*. Finally, our *in silico* model output is $M s^{-1}$ and therefore must be converted into the EFA format of $pmol min^{-1}$ (or vice versa) for comparison. Figure 4-8 shows a representative model OCR output for a 10 minute simulation. As stated above, OCR was simulated using the complex IV flux (J_{C4}), coupled with NMr (to implicitly account for non-mitochondrial respiration) with the transient microchamber volume (tmcV), to allow comparison with *in vitro*, as outlined in Equation (4-1).

$$OCR = J_{C4} + NMr \times tmcV, \quad (4-1)$$

where

$$NMr = 8.6 \times 10^{-14} \text{ M s}^{-1}, \text{ and } tmcV = 2.0 \times 10^{-6} \text{ L}$$

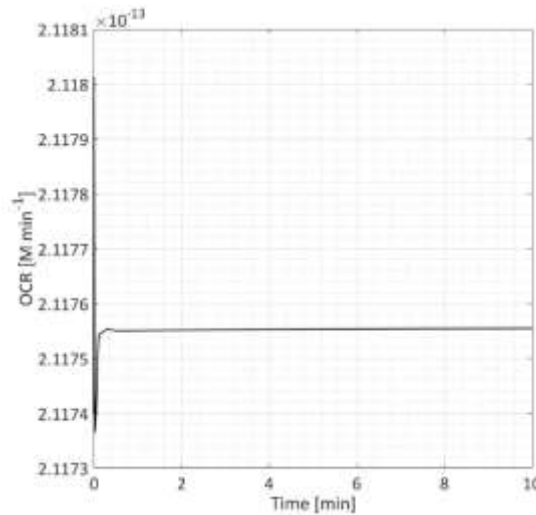


Figure 4-8: Simulation of basal model OCR. OCR was simulated as the electron transport chain complex IV flux combined with a non-mitochondrial respiration. Note, while the model output is M s^{-1} , the figure shows OCR converted in M min^{-1} .

NMr for the model simulation was taken from EFA data generated in chapter 2 (Page 132) during glucose experiments, $tmcV$ is taken from the Agilent EFA analyser website ¹⁰³.

4.3 Simulating Mitochondrial Respiration Stress

4.3.1 Primary Human Hepatocyte *in vitro* Mitochondrial Stress Test

The final stage of validation is to test the models ability to recapitulate *in vitro* EFA OCR, we compare the model output to experimental data. In order to test the utility of this model in the investigation and prediction of DILI the ideal experimental data would be taken from human liver. While there exists much data in the literature for

numerous different carcinoma cell types this lacks physiological relevance due to the tumourigenic origin and thus altered bioenergetic phenotype ⁶⁷. Such a validation was possible using EFA data collected from freshly isolated primary hepatocytes (24 donors), available by collaboration with the Chadwick group based MRC Centre for Drug Safety Science at the University of Liverpool (unpublished). These samples were prepared from healthy tissue during liver resection and represents a rare opportunity as this data is not available in the literature. The dataset contains the parameters of the response of each donor sample when subject to a mito-stress test using EFA (Figure 4-9).

4.3.1.1 Mitochondrial Respiration Stress Test

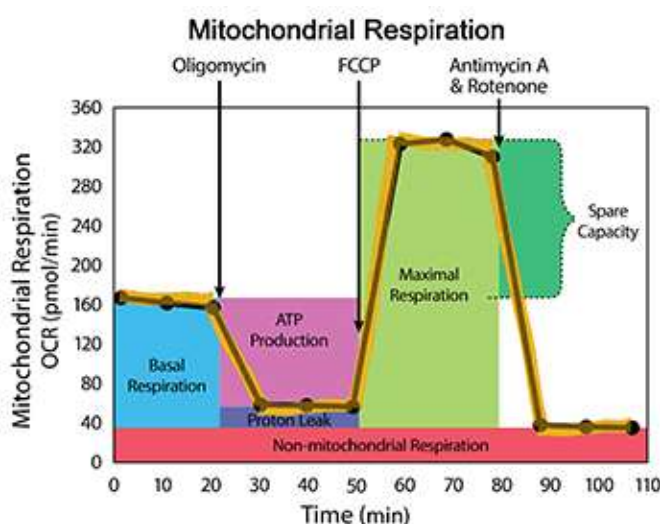


Figure 4-9: Schematic of mitochondrial respiration stress test. Sequential exposure to mitochondrial toxicants oligomycin, FCCP, Antimycin A & Rotenone yield a profile that allows basal respiration, ATP production, proton leak, maximal respiration, spare capacity and non-mitochondrial respiration to be discerned. Figure was taken from Agilent Technologies ¹⁰⁴.

Oligomycin is a potent H⁺-ATP synthase (complex V) inhibitor and is amongst the top 0.1% cancer cell selective cytotoxic agents against 60 human cancer cell lines. Its selectivity arises from its mode of action; binding to a 23kd polypeptide (OSCP) located in the F₀ baseplate blocking ATP synthesis ¹⁰⁵. Exposure of cells to oligomycin inhibits mitochondrial ATP synthesis, yielding the level of ATP produced in the

mitochondria. FCCP (carbonyl cyanide *p*-trifluoromethoxyphenylhydrazone) is a chemiosmotic uncoupler, which functions to separate ATP production from the thermodynamic driven membrane proton gradient, effectively depolarizing the mitochondrial membrane potential ($\Delta\Psi_m$)¹⁰⁶. FCCP in this instance is used to reveal the maximal respiration via the removal of the proton motive force¹⁰⁷. Antimycin A (AMA) is a complex III inhibitor produced by *Streptomyces kitazawensis* which blocks electron transport between cytochromes *b* and *c*¹⁰⁸, and inhibiting succinate and NADH oxidase¹⁰⁸. Finally, rotenone is a well-known mitochondrial complex I inhibitor, but its exact mechanism of action remains ambiguous¹⁰⁹. Rotenone has however been proven to induce apoptosis via elevated ROS levels²⁴. Combined exposure to AMA and rotenone inhibits the final two ETC complexes (I & III) complete ETC inhibition, allowing non-mitochondrial respiration levels to be determined.

4.3.1.2 Primary Human Hepatocyte Mitochondrial Stress Test Data

The raw experimental data for each donor is illustrated as OCR in $M s^{-1}$ against time, devoid of protein content normalization (Figure 4-10).

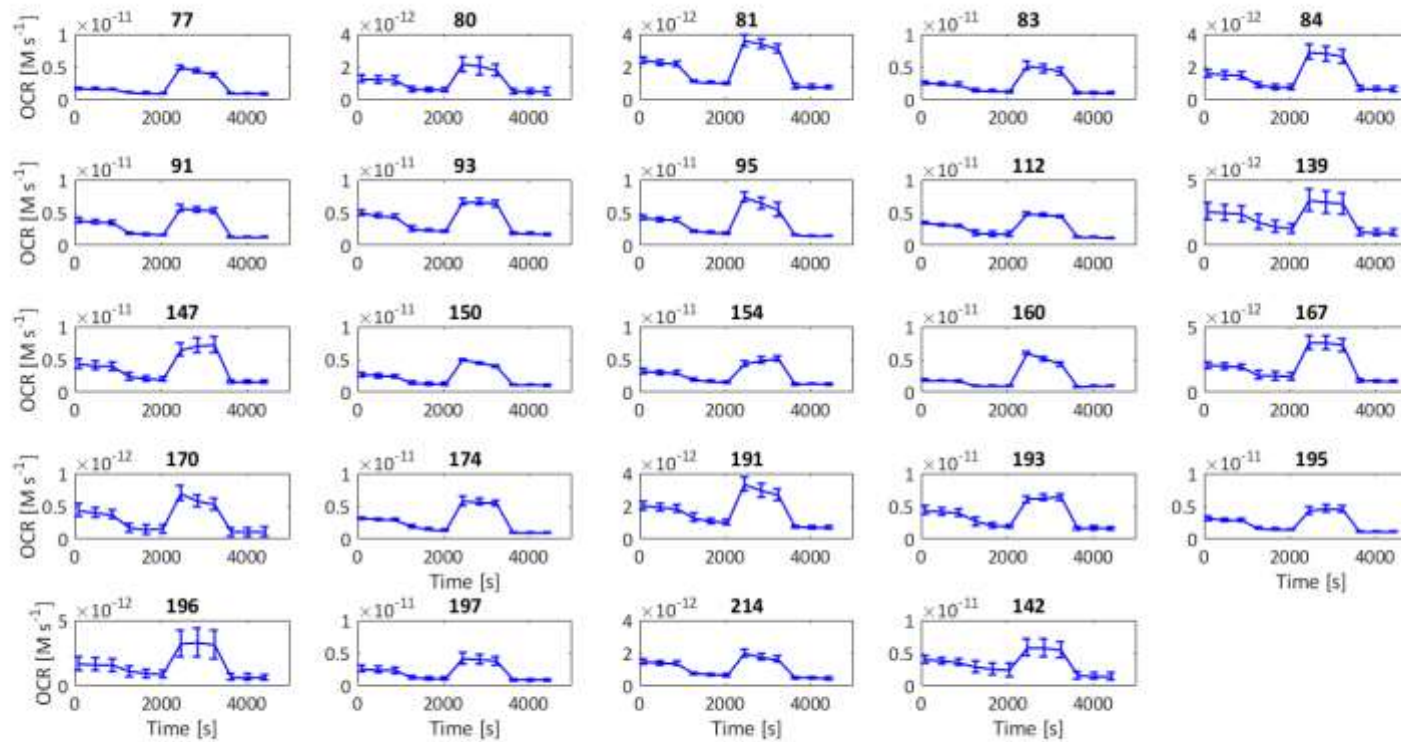


Figure 4-10: Human primary hepatocyte mitochondrial respiration stress test OCR data, provided by the Chadwick Lab University of Liverpool. The bold number titles for each plot is the patients ID's in this study.

The parameters of interest from a mito-stress test arise from the changes in OCR after exposure to a mitochondrial toxicant, with each transition separated by 3 EFA measurements between injections of mitotoxics. In addition, the unique basal OCR of each patient is an important parameter. Although, in order to compare between each patient, the basal OCR reading should be normalized to protein content in these calculations each transition was converted to a percentage change as a normalization method to be used for mathematical linkage. In order to achieve this, each of the three measurements for each stage can be converted into a single value by taking the mean, followed by calculating the percentage change between each compound injection. This yields a plot possessing three points: A, percentage decrease from basal OCR after exposure to oligomycin; B, percentage increase after exposure to FCCP and C, percentage decrease after exposure to AMA and rotenone (Figure 4-11). Visualization of the data in this way facilitates immediate comparison between each patient in the cohort without protein normalization, as well as reducing the number difficulty of model simulation of the data.

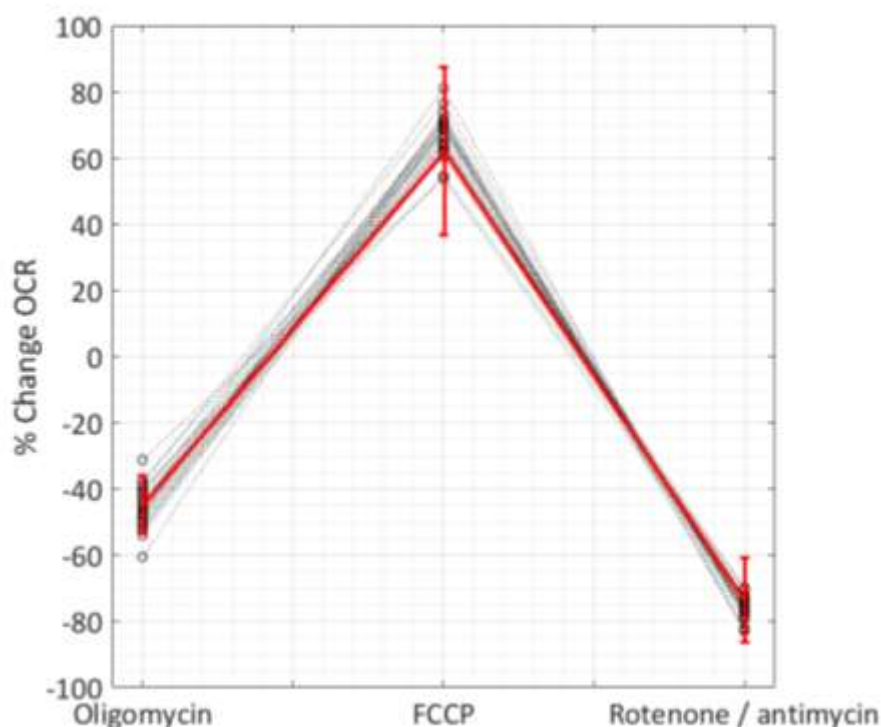


Figure 4-11: Three point reduced representation of *in vitro* mitochondrial stress test data. Relative percentage changes in OCR for each patient after exposure to oligomycin, FCCP, AMA and rotenone are shown in black dashes. Solid red line shows cohort average accompanied with the standard deviation.

Figure 4-11 shows the percentage changes in OCR for the all patients as a function of mitochondrial respiration poisoning. Furthermore, this representation simplifies differences in basal OCR between patients, thereby, allowing a simple comparison between all patients in the cohort.

4.3.2 *In silico* Mitochondrial Stress Test Simulations

The simulation of the mito-stress test begins with accounting for the mechanisms of action and pharmacological changes of the mitotoxicants oligomycin, FCCP, AMA and rotenone. Simulating exposure to oligomycin, AMA and rotenone can be achieved by inhibiting fluxes through complex V (F_0F_1 -ATP synthase), III and I respectively, which may be accomplished by reducing the total flux through each enzyme pathway, namely, reducing parameters $X_{F_0-F_1}$, X_{C_3} and X_{C_1} respectively to the $J_{F_0-F_1}$, J_{C_3} and J_{C_1}

flux terms. Simulating FCCP requires decoupling of the ETC from the proton motive force, thereby permeabilising the membrane. In our model, this can be achieved by reducing the pH gradient between the mitochondrial matrix and mitochondrial intermembrane space membranes and reducing the membrane potential itself ($\Delta\Psi_m$). Modelling mitochondrial respiration in the first instance with such mechanistic detail allows a better representation of the pharmacological modes of action of the compounds of interest.

4.3.2.1 Preliminary Simulation of Mitochondrial Respiration Stress Test

Figure 4-12 shows the effect of complete inhibition of mitochondrial complexes V, I and III as well as reduction of $\Delta\Psi_m$ and decoupling OXPHOS from the proton gradient (achieved by setting $X_{F0-F1} = X_{C3} = X_{C1} = 0$, fixing term of each mitochondrial complex by 100%, setting the matrix pH equal to the IM pH and reducing the $\Delta\Psi_m$ by 20%).

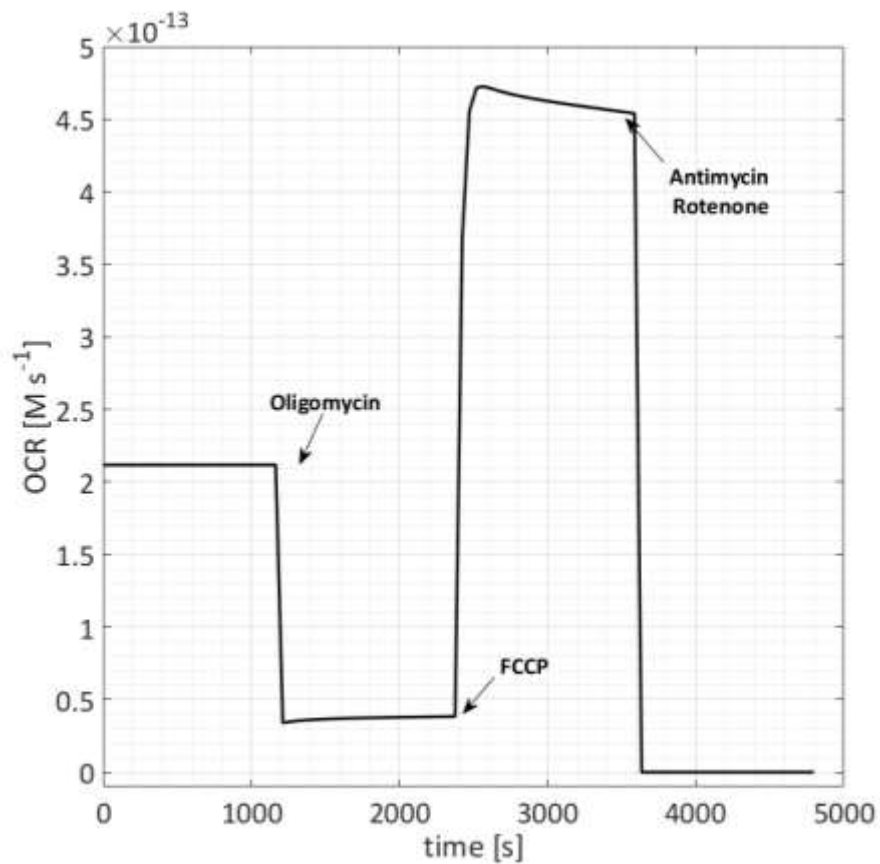


Figure 4-12: Preliminary simulation of mitochondrial respiration stress test. Figure is annotated to illustrate injections of compounds oligomycin, FCCP, AMA and Rotenone.

Perturbing the model according to the pharmacological mechanisms of action of the stress compounds allows simulation of a basic OCR stress test profile. Inhibiting complex I produces a drop in simulated OCR comparable to EFA data. Uncoupling the ETC from the membrane potential allows the model to simulate maximal respiration, illustrated by the large increase in OCR after simulated FCCP “exposure”. Finally, complete inhibition of the ETC by inhibiting complex I and III, reduces respiration to the non-mitochondrial level. The extreme nature of the preliminary simulation can be compared to the average three-point representation of the percentage changes from the human test data (Figure 4-11). Figure 4-13 shows the comparison.

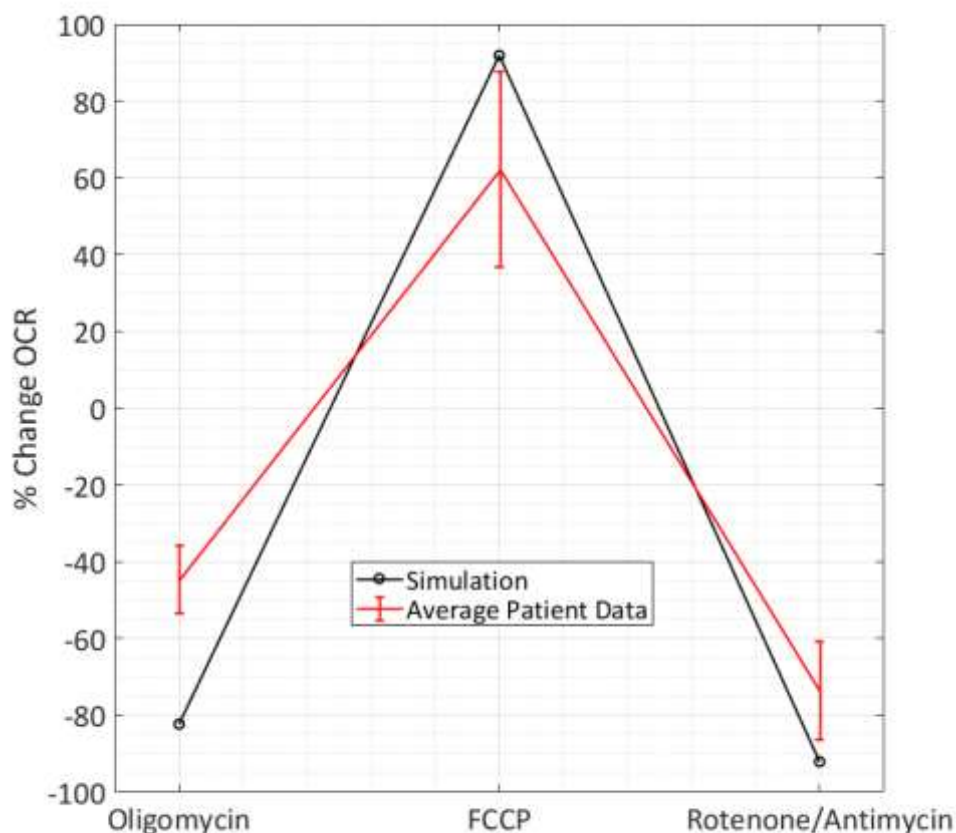


Figure 4-13: Three point reduced representation of simulated mitochondrial respiration stress test compared to average human primary hepatocyte data. Black line represents simulation and red line accompanied with standard deviation data represents *in vitro* data.

Initial quantitative insights into *in silico* - *in vitro* comparisons can be made from Figure 4-13. With the flux terms and model perturbations used to generate the OCR output, the initial *in silico* percentage decrease in OCR is -82.24 % compared to the *in vitro* -44.74% [± 8.77 %] for exposure to oligomycin. The model simulated a 91.87% increase in OCR compared to the *in vitro* 62.17% [± 25.35 %] change for FCCP injection. Finally, the model yielded a -92.12% decrease in OCR compared to the -73.63% [± 12.83 %] average decrease from the primary data. On all three points the model percentage change is outside of the error bounds of the *in vitro* data, although only moderately for the FCCP and AMA/Rotenone. This would suggest that inhibition of complex V by oligomycin in the *in vitro* experiments is less than a 100% inhibition,

with a similar assessment made for inhibition of complex I and III. Our estimated changes in $\Delta\Psi_m$ is also too high according to Figure 4-13.

4.3.2.2 Parameter Perturbation Sweep

Observing the changes in OCR as a function of the degree of perturbations of complex V, $\Delta\Psi_m$ and complexes I and III allows the sensitivity of the terms on OCR to be identified. These can then be used to simulate all patient data as well as the average data.

Changes in mitochondrial complex V flux as a function of percentage reductions between 0 and 100% were investigated, with the percentage change in OCR illustrated in Figure 4-14. Effects of changes in $\Delta\Psi_m$ flux as a function of percentage reductions between 10 and 20% are illustrated in Figure 4-15. Simultaneous changes in complex I and III flux as a function of percentage reductions between 0 and 100% are illustrated in Figure 4-16.

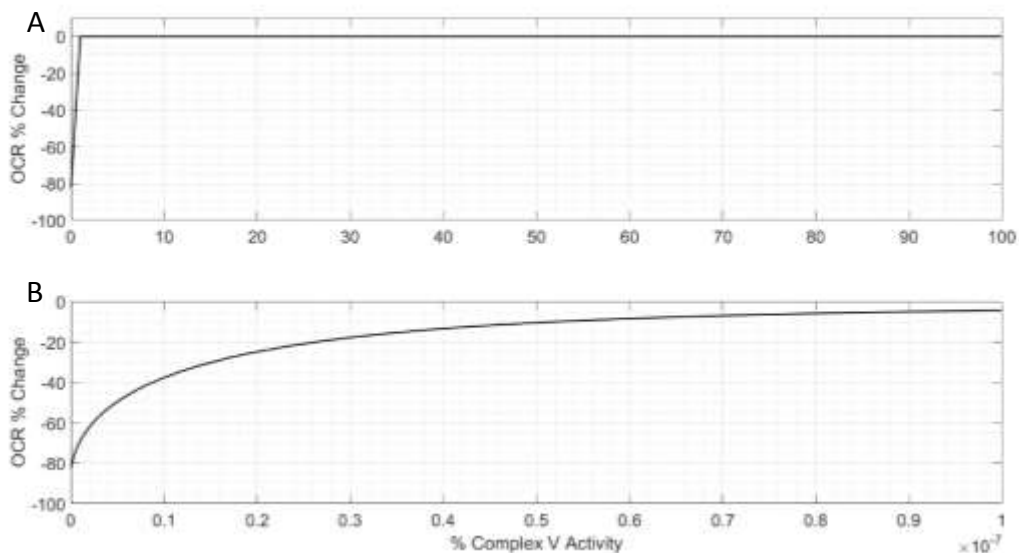


Figure 4-14: Percentage changes in OCR as a function of Complex V activity. OCR output is particularly sensitive to complex V activity, with changes between 0 and 1×10^{-7} % in transporter activity covering 0 to 100% activity change causing the majority of OCR variance. A shows the initial sweep from 0 to 100% activity, illustrating the need for a sweep at a much lower percentage activity, which is shown in B.

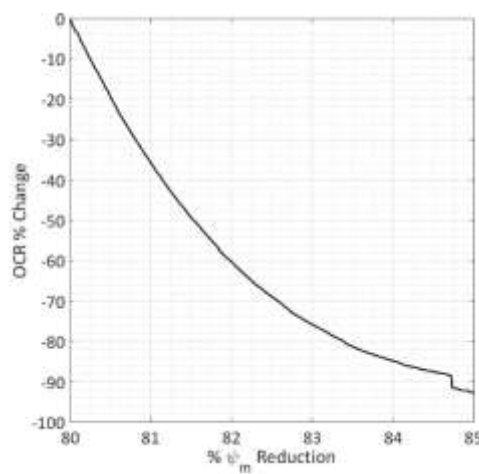


Figure 4-15: Percentage changes in OCR as a function of % $\Delta\psi_m$ reduction. 80 to 90 % reduction is necessary to reduce OCR from 0 to 100% of its original value.

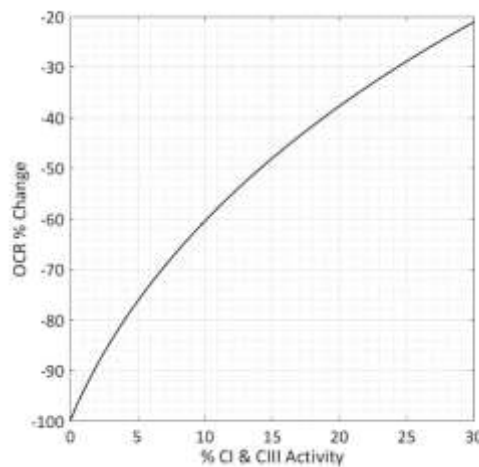


Figure 4-16: Percentage changes in OCR as a function of % complex I and III activity. Noticeable OCR effects can be observed when complex I and III are at 30% of original activity or less.

Figure 4-14 suggests that ATPsynthase complex V activity must be inhibited almost completely in order to observe noticeable reductions in OCR. This also suggests that in the model OCR is extremely resilient to changes in complex V activity. This finding is supported qualitatively as OCR arises from complex IV output, whereas complex V activity occurs after this in the electron transfer chain. Using this knowledge, it can be postulated that in the *in vitro* experiments oligomycin must cause near total inhibition of ATPsynthase activity and thus interpatient variation observed must arise from inter-patient differences rather than differences in inhibition. The effects of changes in $\Delta\Psi_m$ as a function of exposure to FCCP was simulated in Figure 4-15, highlighting the fact that most of the % changes in OCR occur when the membrane potential is reduced by at least 80%. Again, this suggests model OCR output is resilient to small changes in $\Delta\Psi_m$, with a 5% window where OCR is sensitive (80-85%).

Finally, simultaneous inhibition of complex I and III activity as a function of exposure to rotenone and antimycin A illustrates that a minimum of 70% reduction in activity of both complexes is required to significantly perturb model OCR output (Figure 4-16). Overall, such drastic inhibition of complex I, III, V and reduction of $\Delta\Psi_m$ required to perturb model % OCR output highlights the efficacy of the mitochondrial poisons oligomycin, FCCP, rotenone and AMA in inhibiting ETC target. Credence can be lent to this by simulating each individual patient data, obtaining complex inhibition parameters from the sweeps described in these figures. The percentage changes for the three-point reduced representation for each patient accompanied by the necessary parameter changes in the model required to simulate their parameter changes is shown in Table 4-6. The three columns A, B and C represent A; the percentage decrease from basal average OCR to post oligomycin injection, B; percentage average increase in OCR as a function of FCCP exposure and C; percentage OCR decrease as a result of exposure to rotenone and AMA respectively. For the

model parameter changes, A2, B2 and C2 are the values that the original model parameters X_{F0-F1} (A2), X_{C3} (B2) and X_{C1} (C2), must be multiplied by in order to elicit these corresponding percentage OCR changes.

A %	A2	B %	B2	C %	C2
-				-	
38.5754	9.52×10^{-9}	76.4952	0.8611	78.9068	0.0433
-				-	
54.0695	3.66×10^{-9}	68.6121	0.8700	76.1102	0.0520
-				-	
44.6846	6.71×10^{-9}	71.8525	0.8670	78.0131	0.0400
-				-	
47.6643	5.62×10^{-9}	71.1703	0.8675	75.9336	0.0450
-				-	
52.6002	4.10×10^{-9}	68.4237	0.8700	76.7239	0.0450
-				-	
49.6912	4.94×10^{-9}	64.2479	0.8770	72.4202	0.0680
-				-	
49.8789	4.90×10^{-9}	68.4757	0.8700	76.5267	0.0500
-				-	
42.8916	7.47×10^{-9}	60.2990	0.8860	72.8928	0.0700
-				-	
39.6959	9.00×10^{-9}	54.5831	0.8950	69.9251	0.0800
-				-	
31.2806	1.40×10^{-8}	53.7367	0.9030	73.5635	0.0650
-				-	
47.9389	5.50×10^{-9}	69.0614	0.8700	76.6628	0.0490
-				-	
46.4383	6.02×10^{-9}	69.4513	0.8710	75.8642	0.0530
-				-	
44.6232	6.75×10^{-9}	64.6309	0.8800	74.0634	0.0630
-				-	
44.8862	6.63×10^{-9}	81.0987	0.8450	82.7137	0.0290

-				-	
43.9016	7.03×10 ⁻⁹	62.6113	0.8820	70.4895	0.0850
-				-	
37.2431	1.00×10 ⁻⁸	66.2827	0.8820	77.0502	0.0550
-				-	
60.6792	2.25×10 ⁻⁹	73.6373	0.8580	82.1688	0.0280
-				-	
47.4495	5.66×10 ⁻⁹	71.8039	0.8675	82.9343	0.0270
-				-	
40.8283	8.39×10 ⁻⁹	61.7283	0.8864	75.7229	0.0550
-				-	
46.0041	6.19×10 ⁻⁹	63.7740	0.8800	73.1003	0.0700
-				-	
48.5816	5.30×10 ⁻⁹	65.9644	0.8750	74.7130	0.0620
-				-	
41.5176	8.07×10 ⁻⁹	70.2570	0.8720	79.3525	0.0430
-				-	
52.0076	4.26×10 ⁻⁹	70.4705	0.8660	77.3149	0.0470
-				-	
51.0439	4.54×10 ⁻⁹	61.4945	0.8800	73.4040	0.0620

Table 4-6: Table of patient average percentage OCR changes accompanied by the corresponding model parameter changes required to simulate each patient. Parameter changes are shown in grey columns while patient percentages are shown in white, each linked by letter.

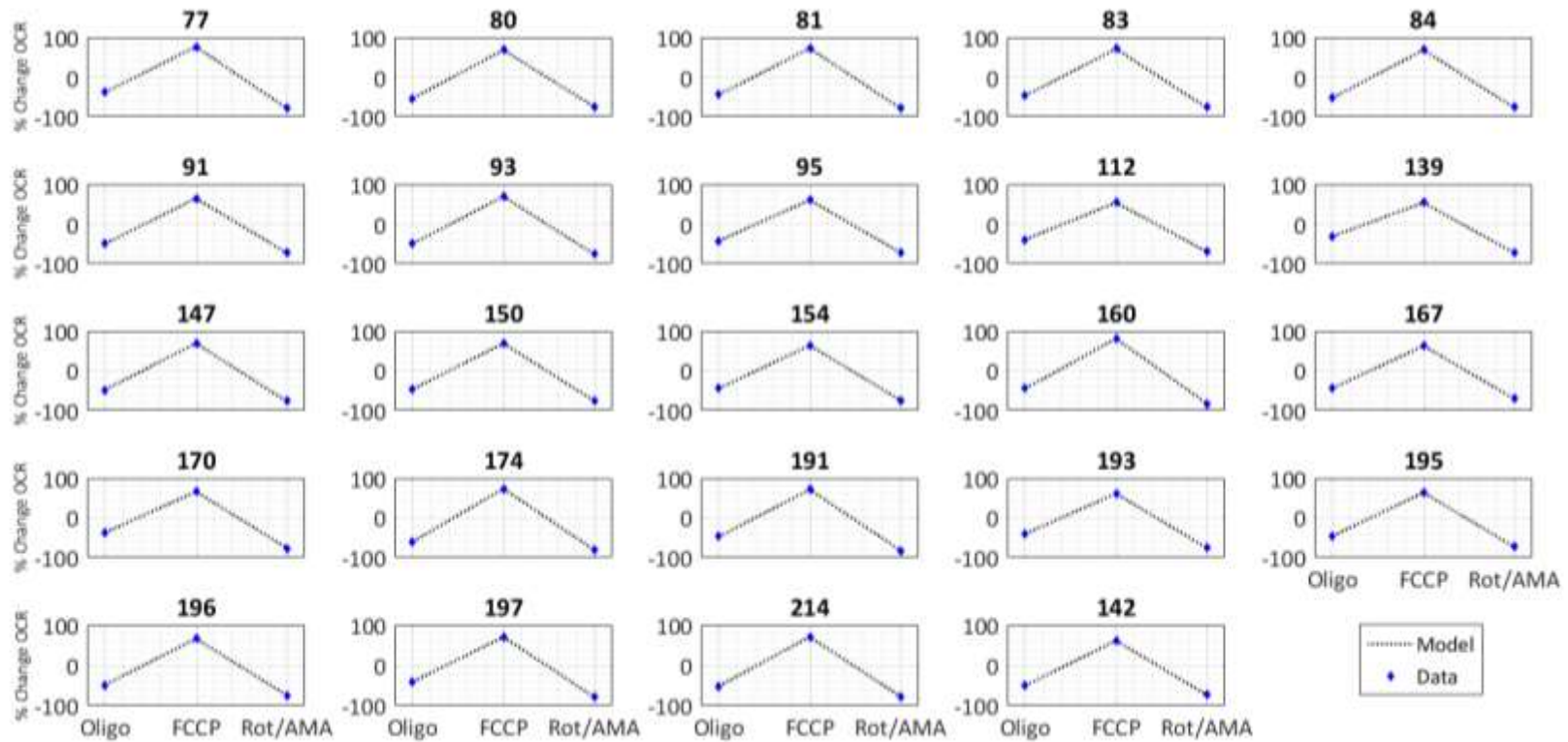


Figure 4-17: Model simulations of individual human primary hepatocyte data using a three-point reduced representation and parameters from Table 4-6.

Figure 4-17 demonstrates that the model is able to simulate each of the 24 patient % OCR data using the parameter changes as indicated in Table 4-6. We can now investigate if we can use the model to investigate the clinical importance of specific variables or parameters.

Mitochondrial bioenergetic functionality hinges on several important factors: integrity of the electron transport chain, integrity of proton motive force in the form of a membrane potential and bioenergetic metabolic precursors such as pyruvate and NADH.

4.4 Statistical Analysis

Accurately simulating the mitochondrial *in vitro* stress test data as a three-point reduced representation of percentage OCR changes, provides a platform from which statistical analysis may be performed. Such analysis allows investigation into the predictive power of the *in vitro* and *in silico* platforms, with regards to pharmacological outputs. The testable hypothesis is that patients with higher levels of reserve glycolytic capacity are better able to mitigate drug induced mitochondrial dysfunction. This is based fundamentally on the premise that glycolytic flux can compensate for a reduced mitochondrial ATP output to a certain extent. The following section describes the implementation of principal component analysis (PCA) and multinomial logistic regression as a statistical method of testing this hypothesis, with the aim of discerning whether the *in silico* model is better able to describe glycolytic reserve capacity values for each patient, compared to the raw experimental data.

4.4.1 Patient Glycolytic Reserve Capacity

The *in vitro* dataset obtained from the Chadwick group includes ECAR profiles for the mitochondrial stress test, as well as the ECAR glycolytic stress test. From this data, the reserve glycolytic capacity for each patient may be deduced. It is important to note that reserve capacity in this instance will be expressed as a proton production rate, rather than ECAR, by applying the same calculations with respect to extracellular

media buffering capacity, and accounting for respiratory contributions to extracellular acidification as described in section 3.3.3.

Glycolytic reserve capacity is used to describe the maximal glycolytic capacity after mitochondrial ATP synthesis is inhibited using the drug oligomycin. The glycolytic reserve capacity for each patient after conversion into PPR_{gly} , is presented in Table 4-7. Given the small data set, we base our analysis on attempting to predict the glycolytic reserve capacity within ranges (0 →15000, 15000 →29000 and > 29000 [$\text{pmol H}^+ \text{min}^{-1}$], which is low, moderate or high). The ranges were decided by plotting a histogram of the reserve capacities shown in Figure 4-18. Using a larger number of bins did not improve on representation of the patient reserve capacity data, nor the results of the statistical analysis. Our key aim is to determine whether the raw data or the *in silico* model is the better predictor of whether an individual’s glycolytic reserve capacity falls into one of these specified ranges.

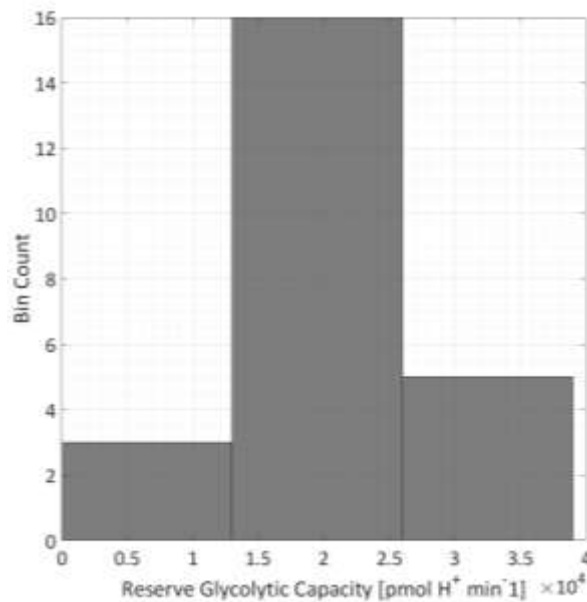


Figure 4-18: Reserve glycolytic capacity histogram for the 24 *in vitro* patients.

Patient	Reserve Capacity (pmol H+ / min)	Bin	Patient	Reserve Capacity (pmol H+ / min)	Bin
<hr/>					

170	3616.8	1	214	17974	2
165	6980.4	1	150	19010	2
167	11602	1	139	19051	2
81	13011	1	83	19404	2
196	13493	1	193	20259	2
160	14661	1	154	20458	2
191	14827	1	112	21353	2
84	15070	2	77	29421	3
93	15757	2	91	34783	3
95	16693	2	147	35778	3
197	17449	2	142	36547	3
195	17848	2	174	37507	3

Table 4-7: Table of patient reserve glycolytic capacities, after deduction of respiratory contributions to extracellular acidification. Each patient is allocated a bin, according whether their glycolytic reserve capacity falls within the ranges 0 →15000, 15000 →29000 and > 29000 [pmol H⁺ min⁻¹], identified as bins 1,2,3 respectively.

The data was used to see if reserve capacity could be separated (low, moderate, high) for each patient dependent on the experimental OCR changes. Since there are three predictor variables (columns A, B and C in table 4-6), a principal component analysis (PCA) was constructed in an attempt to visualize relationships in the data in 2 dimensions. Principal components were calculated using the covariance matrix. As a result, principal components 1 and 2 represents 96 – 98% of the total variance of the data, therefore we can have confidence that most of the information will be retained within the two dimensions. However, projecting the data onto these principal components (as seen in Figure 4-19), does not allow the (low, moderate, high) reserve capacity individuals to be clearly distinguished, nor does projecting the data on principal components calculated using the model parameter changes (columns A2, B2, C2 in table 4-6), instead of % OCR changes as predictor variables (wherein, 99.8% of total variance is represented in the first two principal components).

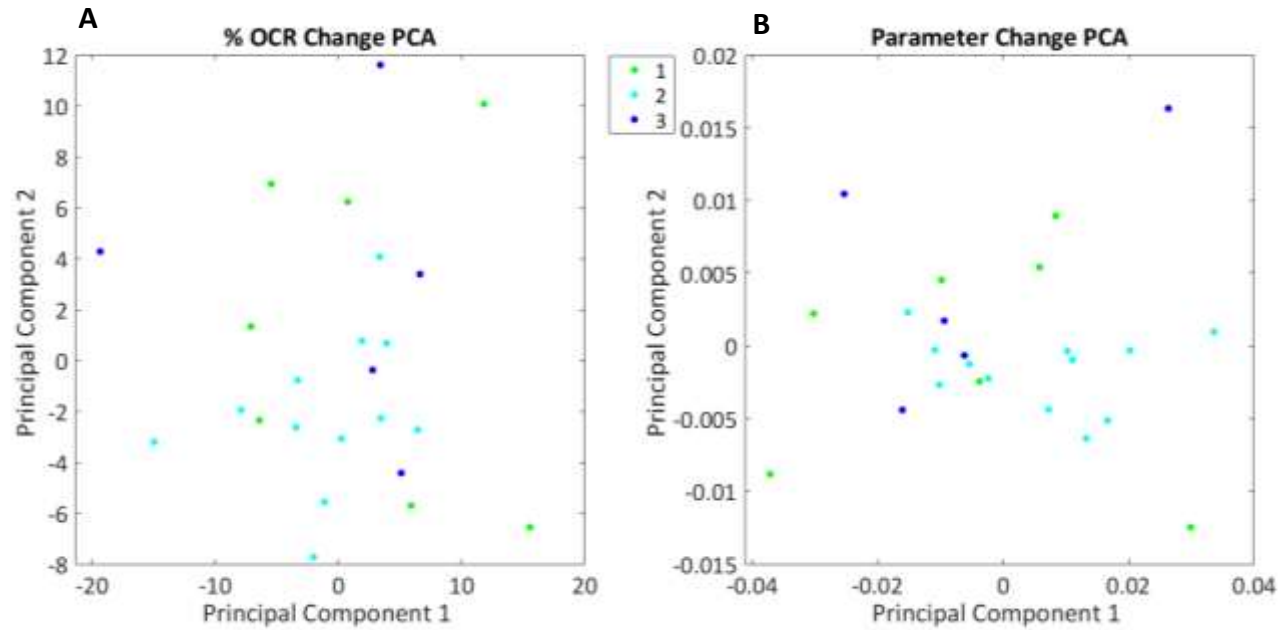


Figure 4-19: 2 dimensional PCA visualization of glycolytic reserve capacity in low (green), medium (light blue) and high (dark blue) individuals, with respect to % OCR changes (A) and corresponding model parameter (B) changes as given in Table 4-6, columns A,B,C and A2,B2,C2 respectively.

Our aim here was to test if using the model parameter changes, which are based on the mechanistic features within the model rather than observed % experimental changes, would enhance visualization, in that low, medium and high reserve glycolytic capacities individuals could be separated more accurately. Unfortunately, as we can see, Figure 4-19, this is not the case.

The principal component coefficients in the two cases (i.e. using % OCR or corresponding model parameter changes as predictors) are given in the Table 4-8.

A		
Predictor	Principal Component 1	Principal component 2
% Change in A	-0.5932	0.8028
% Change in B	0.7297	0.5048
% Change in C	-0.34	-0.3172

B		
Predictor	Principal Component 1	Principal component 2
Param change in A2	0.8648	-0.5019
Param change in B2	0.0244	0.0215
Param change in C2	0.5014	-0.8648

Table 4-8: Principal component coefficients in the case where % OCR (A) and model parameters (B) changes are used as predictors.

As separation could not be clearly observed, a multinomial logistic regression was used as a basis to get a quantitative understanding of the relationship between the OCR and model parameter predictors and glycolytic reserve capacity.

4.4.2 Multinomial Logistic Regression

Logistic regression measures the relationship between dependent variables and one or more independent variables. In this analysis it is assumed that the observed data (i.e. the patient glycolytic reserve capacity, Y) is a linear function of the explanatory/predictor variables (e.g. X_1 , X_2 and X_3 for % OCR changes in columns A, B and C, respectively, in table 4-6), e.g. using a generalised linear model:

$$Y = \beta_0 + \beta_1 X_1 + \beta_2 X_2 + \beta_3 X_3.$$

The idea of logistic regression is to find the parameters $\beta_0 - \beta_3$ that best fit the observed (glycolytic reserve) data. Because it is assumed that the data can be expressed as a generalised linear model then ordinary least squares can suffice as a fitting method.

To be able to use multinomial logistic regression a number of testing criteria need to be checked, as follows:

1. The dependent variable is measured on nominal level – this assumption holds since we have binned the reserve capacities into groups ‘1,2,3’ for low, moderate and high.
2. One or more of the independent variables are continuous, ordinal or nominal – we have 3 predictor variables (% OCR or parameter changes A or A2, B or B2, C or C2) all of which are continuous.
3. We have independence of observations, and dependent variable should have mutually exclusive/exhaustive categories (i.e. each observation can only be in one group, and every observation must belong to a group) – in our data, each patient is independent of one another, and each patient must fall into category 1,2 or 3 for reserve capacity.
4. There should be no multi-collinearity between predictor variables – we tested this using variance inflation factor methods as described below.
5. There should be no outliers/highly influential points – no outliers were detected.
6. Adequate sample size – a recommended sample size is 10 x the number of predictor variables. There are 3 predictor variables and 24 observations which means that we are 6 samples short. However, analysis with only 2 predictor variables showed no improvement so we continued with 3

predictor variables to allow a more complete comparison between all the OCR (and parameter) changes.

Again, whether patient glycolytic reserve can be better predicted using either the observed % OCR changes (columns A, B and C in table 4-6) or the corresponding model parameter changes (columns A2, B2 and C2 in table 4-6) was tested. Our first step is to test for multi-collinearity in both these cases. As highlight above, Variance Inflation Factor (VIF) test which quantifies the extent of multicollinearity in least squares regression analysis was used. It provides a measure of how much variance of an estimated regression coefficient is increased because of collinearity. The square root of the VIF value indicates how much larger the standard error is compared to what it would be if that variable was uncorrelated with the other predictor variables in the model. For example, a VIF value of a predictor variable of 4 means that the standard error for the coefficient of that predictor variable is $\sqrt{4} = 2$ times larger than it would be if that predictor variable was uncorrelated with the other predictor variables. As a rule of thumb, if the VIF value is greater than 1 and less than 10 then multicollinearity is considered to be low. The VIF values for the two cases (% OCR changes and model parameter changes) are given in Table 4-9. Each of the VIF values are within the desired range and therefore no multi-collinearity exists in independent variables.

	VIF		VIF
% change A	1.208	Param change A	1.425
% change B	3.646	Param change B	3.293
% change C	3.301	Param change C	2.71

Table 4-9: The VIF values for % OCR changes, and model parameter changes.

Consideration of whether predictor variables can predict the patient reserve capacity as univariate variables, i.e. considering if the glycolytic reserve data can be explained using the linear model $Y = \beta_0 + \beta_1 X_1$, where X_1 is given by either columns A, B or C alone (in the case of % OCR changes) or columns A2, B2 or C2 alone (in the case of model parameter changes). In each case, a Pearson Chi-square statistic to indicate goodness of fit of whether the model is a good fit to the data is used, as well as use of a Likelihood Ratio Chi-square test to examine if the fit is significantly improved by the full model ($\beta_0 + \beta_1 X_1$) compared to just the intercept (β_0) alone. The Likelihood Ratio Chi-square test is calculated by $-2L(\text{intercept alone model}) + 2L(\text{full model})$, where $L(\text{intercept alone model})$ is the log likelihood with just the intercept only and $L(\text{full model})$ is the log likelihood when the predictor value is included. The results are given in Table 4-10 and Table 4-11 for the cases of % OCR and model parameter changes.

	Goodness of fit		Likelihood ratio tests	
	Chi-square	Sig (p-value)	Chi-square	Sig (p-value)
% change A	48.812	0.286	1.111	0.574
% change B	48.224	0.306	1.718	0.424
% change C	49.833	0.253	5.999	0.05

Table 4-10: Degrees of freedom; 44 (goodness of fit); 2 (likelihood ratio tests) The p-values are calculated using the chi-square distribution defined by the given degrees of freedom.

	Goodness of fit		Likelihood ratio tests	
	Chi-square	Sig (p-value)	Chi-square	Sig (p-value)
Param change A	48.738	0.288	0.953	0.288
Param change B	36.059	0.206	0.986	0.206
Param change C	44.39	0.159	4.351	0.159

Table 4-11: Degrees of freedom; 44 (goodness of fit); 2 (likelihood ratio tests) The p-values are calculated using the chi-square distribution defined by the given degrees of freedom.

For the goodness of fit results, a large Chi-square indicates a poor fit for the model and, correspondingly, a significance (p-value) of less than 0.05 indicates that the model does not fit the data well. With the Likelihood ratio tests, a p-value of greater or equal to 0.05 indicates that the addition of the predictor variable does not significantly improve the model fit to the data compared to the intercept model alone. As we can see, in both cases (% OCR and model parameter changes; Table 4-10 and Table 4-11), each of the univariate models fit the data well (goodness of fit p-values all larger than 0.05) but none of the fits are improved by the addition of the predictor variable vs the intercept model alone. Therefore, there appears to be no statistically significant benefit to including the predictors as univariate variables in predicting patient reserve glycolytic capacity. The closest predictor variable to being significant is the % change C (p-value=0.05) and this outperforms the corresponding model parameter change as a predictor variable.

When using all the % OCR changes in a multivariate model to predict reserve glycolytic capacity, the Pearson Chi-square value is 57.36 (p-value=0.037<0.05, df=40) which indicates that the model does not fit the data does not fit the data well. The likelihood ratio chi-square (of the full multivariate model vs intercept only) is 10.132 (p-value=0.0119, df=6), confirming that all the % OCR changes as predictors provide no statistical to including none at all. The corresponding statistics for using all the model parameter changes as alternative predictors are: Pearson Chi-square value is

47.932 (p -value=0.182, df =40) and the likelihood ratio chi-square is 8.913 (p -value=0.179>0.05). Therefore, a similar pattern is seen to when using % OCR changes as predictors and, importantly, no improvement in significance is observed when using parameter rates in comparison to using the observed % OCR changes.

4.5 Model Predictions

The model has so far been validated against experimental data and used to simulate mitochondrial stress test profiles based on *in vitro* data from 24 individuals. The model can now be used to simulate perturbations in important physiological and pharmacological variables and processes and investigate the resulting effects on measurable experimental outputs.

4.5.1 Bioenergetic Model Perturbations

There are many important variables and reaction fluxes with respect to cellular bioenergetics within the mitochondria, and many ways in which bioenergetics status can be measured experimentally. For example, NADH in the mitochondrial matrix is responsible for providing reducing equivalents for OXPHOS, and can therefore be considered as vital for cellular energy production within the mitochondria. Similarly, cytoplasmic pyruvate (PYR) is the molecule that links glycolysis in the cytoplasm to oxidative phosphorylation in the mitochondria. While these two molecules are essential for cellular bioenergetics metabolism, they also have other important roles. For example, NADH makes one half of a redox couple that is used to maintain cellular ROS homeostasis, ultimately coined at the measure of cellular redox status. PYR, on the other hand, can be utilized during hypoglycaemia, by gluconeogenesis in order to buffer cytoplasmic glucose concentrations via the liver. As such, NADH and PYR homeostasis is vital for cellular homeostasis. The mitochondrial stress test inhibits all electron transport chain reactions, as well as dissipating $\Delta\Psi_m$. However, ETC complexes I and III are simultaneously inhibited by rotenone and AMA in the final step. While this occurs in order to completely shut down OXPHOS, it leaves little room

to discern single transporter (I or III) inhibition as a result of mitochondrial toxicity screening of new compounds.

In order to relate perturbations of these variables and fluxes to experimentally quantifiable experimental outputs, the model outputs as a result of perturbations in these variables are represented by measurable *in vitro* experimental outputs. Namely, $\Delta\Psi_m$, pH and OCR. It is important to align model predictions with outputs that can be confirmed experimentally to allow an experimental – *in silico* iterative process, whereby *in silico* works is used to guide experimental design (and vice versa). Therefore, mitochondrial matrix concentrations of NADH, cytoplasm concentrations of PYR and electron transport chain transporter fluxes CI and CIII were perturbed in the model, with output being focused on experimentally measurable changes in $\Delta\Psi_m$, pH and OCR.

4.5.1.1 pH Change Simulations

Changes in mitochondrial pH were examined as a function of NADH (matrix), PYR (cytoplasm), complex I and complex III perturbations. This simulation output therefore allows determination of sensitivity of each perturbation on mitochondrial pH. Note, that variable NADH and PYR perturbations consist of reductions ranging from their basal concentrations (2.5×10^{-3} M and 8.0×10^{-5} M, respectively) to zero, and ETC complex I and III activity is represented as 0 to 100 % background activity. The results shown in Figure 4-20 show steady state mitochondrial pH after a 1000 second simulation.

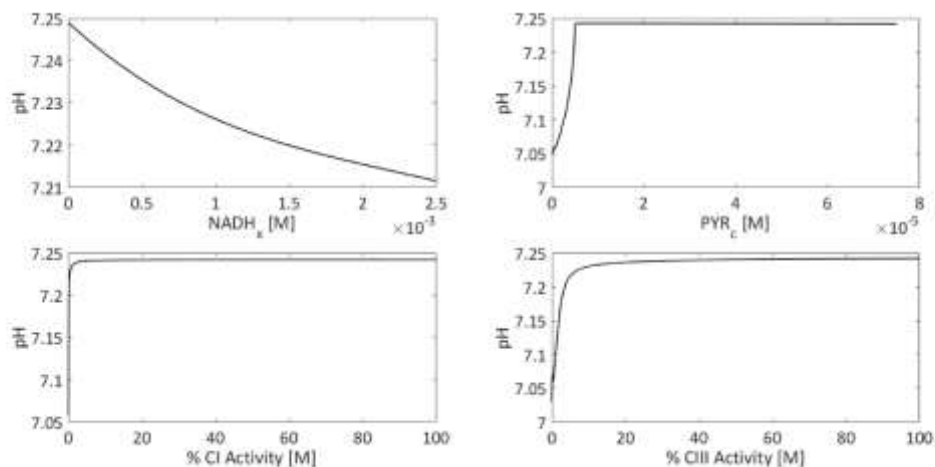


Figure 4-20: Resulting changes in mitochondrial pH as a function of perturbations in NADH, PYR, complex I and complex I. Variables denoted $_x$ and $_c$ represents matrix and cytoplasmic concentrations, respectively.

For complex I and III, decreases in transporter activity only appears impact pH at activities below 10% of baseline, with pH more sensitive to changes in complex III than complex I. Decreases in cytoplasmic pyruvate concentration has no immediate effect on mitochondrial pH until concentrations drop to 5.18×10^{-6} M or less, rendering pH as relatively insensitive to decreases in PYR. Also, decreases in mitochondrial matrix NADH results in only minor increases in pH. This makes sense intuitively as less NADH available for oxidative phosphorylation means less protons being pumped across the membrane resulting in an increase in pH.

4.5.1.2 $\Delta\Psi_m$ Change Simulations

Changes in mitochondrial $\Delta\Psi_m$ were then captured as a function of these perturbations NADH (matrix), PYR (cytoplasm), complex I and complex III perturbations.

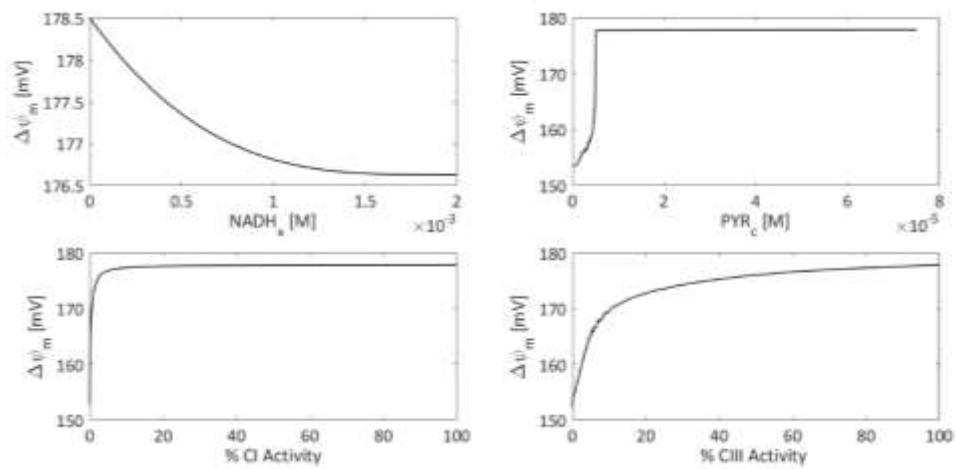


Figure 4-21: Changes in $\Delta\Psi_m$ as a function of perturbations in NADH, PYR, complex I and complex III. Variables denoted $_x$ and $_c$ represent matrix and cytoplasmic concentrations.

We see that $\Delta\Psi_m$ is much more sensitive to changes in complex III activity than to complex I activity, with little change in $\Delta\Psi_m$ until 6 % of complex I baseline activity. Similar to pH, $\Delta\Psi_m$ is relatively insensitive to changes to changes in cytoplasmic pyruvate concentration, with no noticeable changes in membrane until PYR drops to 5.3×10^{-6} M, at which point the decrease is rapid. Decrease in matrix NADH results in a small increase in membrane potential. This is most likely due to similar changes in pH, whereby the differences in protons across the membrane result in a different $\Delta\Psi_m$.

4.5.1.3 OCR Change Simulations

Finally, changes in model OCR were captured as a function of these perturbations Figure 4-22.

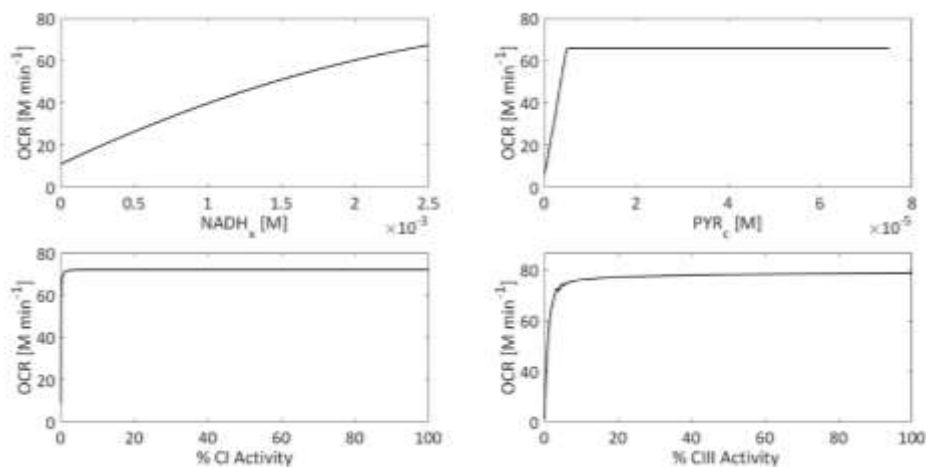


Figure 4-22: Changes in OCR as a function of perturbations in NADH, PYR, complex I and complex III. Variables denoted _x and _c represent matrix and cytoplasmic concentrations.

Perturbations of complex I and complex III result in little changes in OCR, with OCR being slightly more sensitive to complex III, most likely due to OCR being generated via complex IV flux, which would be more influenced by the ETC complex that precedes it (namely complex III). Model OCR is relatively insensitive to changes in cytoplasmic pyruvate, with only a significant decrease in OCR occurring once PYR concentration falls below 5.2×10^{-6} M, at which point OCR decreases from basal (65.75 M min^{-1}) to 7.5 M min^{-1} . Decrease in concentrations of NADH result in a steady decrease in OCR, indicating that OCR is the most sensitive to NADH out of the four outputs considered.

4.5.1.4 Simulation Discussion

Model simulations were intended to investigate changes in measurable experimental outputs as a function of mitochondrial matrix concentrations of NADH, cytoplasmic PYR and activities of ETC complex I and complex III fluxes. One objective was to investigate whether changes in pH, $\Delta\Psi_m$ and OCR were more sensitive to complex I or III, as the *in vitro* mitochondrial stress test inhibits both simultaneously. Out of our tests, complex I perturbations resulted in minimal changes in pH, $\Delta\Psi_m$ and OCR until almost complete inhibition. However, complex III perturbations induced more change in pH, $\Delta\Psi_m$ and OCR, especially $\Delta\Psi_m$. This suggests that it is

perhaps important to differentiate OCR measurements when investigating mitochondrial toxicity using extracellular flux analysis with respect to complex I and complex III activity, by not simultaneously inhibiting both.

Mitochondrial pH, $\Delta\Psi_m$ and OCR were found to be relatively insensitive to changes in cytoplasmic pyruvate perturbations, until PYR passed below a 5.2×10^{-6} M threshold. At this point, all three outputs decreased dramatically. This would suggest that pH, $\Delta\Psi_m$ and OCR are relatively resilient to cytoplasm pyruvate fluctuations, which makes sense intuitively, as PYR serves as an important molecule for other biological functions⁶¹. Finally, pH, $\Delta\Psi_m$ and OCR were found to be most sensitive to changes in matrix NADH concentrations. This bolsters the importance of maintaining cellular NAD/NADH redox state homeostasis, and highlights the downstream sensitivity as a result of NADH perturbations, which could occur as a result of ROS detoxification or, more specifically, as a result of futile redox cycling as discussed in Chapter 2.

4.6 Discussion

4.6.1 Chapter Discussion

In this chapter, a mitochondrial bioenergetics model that is thermodynamically driven using the BISEN toolset and literature-based kinetics was constructed. The model was validated against experimental data. The model is the first of its kind in simulating primary human hepatocyte *in vitro* oxygen consumption rate data from mitochondrial stress test assays. *In vitro* OCR data was expressed as a novel three-point reduced representation in order to facilitate model simulations of the percentage OCR changes as a function of exposure to oligomycin, FCCP, rotenone and AMA. The model was able to simulate each of the 24 human patient *in vitro* data, by mimicking relevant mechanistic pharmacological perturbations. Oligomycin, rotenone and AMA exposure were simulated by inhibiting ETC complexes V, I and III, while FCCP exposure was modelled by uncoupling model OXPHOS from the proton motive force and by removing the proton gradient between mitochondrial

membranes. The resulting *in silico* parameter changes that capture the mitochondrial stress test of the *in vitro* data were compared to the *in vitro* patient % OCR changes via statistical analysis, to test the hypothesis that patients with a higher glycolytic reserve capacity are better able to mitigate mitochondrial compromise, principal component analysis and multinomial logistic regression was performed. Each patient's reserve glycolytic capacity was converted to glycolytic only acidification by deducting respiratory contributions using the media buffering capacity method used in Chapter 2. Each patient was then assigned as having a low, moderate or high glycolytic reserve capacity. PCA showed no obvious visual correlation between the *in vitro* and *in silico* predictors, prompting the use of multinomial logistic regression to ascertain any quantitative relationships. Neither the *in vitro* % OCR changes nor the *in silico* model parameter changes yielded a significant result, suggesting that no link in this data, mitochondrial compromise and glycolytic reserve capacity.

Finally, the model was used to explore how perturbations in essential mitochondrial bioenergetic variables and fluxes affect experimentally measurable outputs. These simulations included perturbing mitochondrial matrix concentrations of NADH, cytoplasmic concentrations of pyruvate and reduction in complex I and III transporter activity, and monitoring the resulting changes in mitochondrial pH, $\Delta\Psi_m$ and OCR. Of all the perturbations, model simulations of pH, $\Delta\Psi_m$ and OCR were most sensitive to changes in NADH, suggesting that futile depletion of cellular reducing power, NADH, as a function of pharmacological or toxicological action can have significant effects on cellular bioenergetics. The differences between complex I and III on pH, $\Delta\Psi_m$ and OCR were investigated in order to discern if it is important during analysis of mitochondrial stress to separate inhibition of complex I and III. Our model shows that pH, $\Delta\Psi_m$ and OCR are more sensitive to complex III perturbations, particularly $\Delta\Psi_m$, suggesting that, when comparing mitochondrial toxicity of new or existing compounds to the mitochondrial stress test, more mechanistic insight could be gained if complex I and III were inhibited sequentially, rather than simultaneously. Finally, we found that $\Delta\Psi_m$, pH and OCR are relatively insensitive to changes in cytoplasmic pyruvate concentrations, until PYR decreases below a 5.2×10^{-6} M

threshold, whereby all three experimental outputs decrease rapidly. This would suggest that cytoplasmic PYR, although a TCA precursor, is relatively free to be utilized in other biological situations, until an approximate ten-fold decrease in concentration. These findings could therefore impact the way extracellular flux analysis is used to investigate mitochondrial toxicity, by providing a mechanistically detailed *in silico* platform from which experimentation and mechanisms of action can be investigated.

5 Chapter 5: Discussion & Future Work

It is widely accepted that pharmacological activity of certain classes of compounds (e.g. anticancer, antimalarial) is related to their ability to accept one or two electrons. However, pharmacological activity via redox cycling is an understated mechanism of toxicity associated with many classes of drugs. In particular, oxidative stress as a result of redox cycling plays a pivotal role in the cause of cardiac toxicity, specifically as a function of toxicity associated with the cellular bioenergetics. For example, doxorubicin is an anti-neoplastic used to treat cancer and has strong links to redox cycling induced cardiac toxicity, associated directly with promoting elevated levels of ROS and oxidative stress within the mitochondrial. Redox cycling, in general, uncouples oxidative phosphorylation resulting in mitochondrial dysfunction. The underlying pharmacology of redox cycling is very difficult to elucidate, owing to the fleeting existence of radical species, often being recycled rapidly back to their parent compound. As a result, redox cycling is difficult to identify during drug development. Insight into the coupling of the elusive redox cycling induced radical species formation, with biologically complex cellular bioenergetics can be aided by the utilization of quantitative systems pharmacology, a discipline that utilizes sophisticated *in silico* techniques combined with *in vitro* outputs. The inclusion of thermodynamics within the model allows consolidation of compound and generate kinetic rate constants and determination of energetically favourable and unfavourable processes. Furthermore, inclusion thermodynamic properties into large scale metabolic models of glycolysis and mitochondrial bioenergetics facilitates construction of pH-dependent mathematical models, capable of simulating dynamic pH time courses, as well as recapitulating changes in enzyme kinetics as a function of a thermodynamic based environment.

Chapter 2 describes the development of a novel *in silico* model of quinone redox cycling, with example drug doxorubicin that is thermodynamically based. The physiochemical properties of a plethora of quinones were consolidated into a mathematical framework from which compound specific reduction potentials and the corresponding equilibrium rate constants were obtained. Unknown kinetic parameters for the doxorubicin redox cycling model were obtained using a novel

surrogate *in vitro* extracellular flux analysis assay, where the rates of proton consumption and production were measured in real time. The model required additional mechanistic information in order to recapitulate the EFA data, specifically, the addition of a comproportionation reaction. This addition allowed the model to reproduce a number of different drug concentrations of EFA data, using only one concentration as the training data for model parameterisation. The model was expanded to include mitochondrial specific ROS detoxification mechanisms, centred on glutathione metabolism and superoxide dismutase. The model was also able to predict *in vitro* doxorubicin-induced mitochondrial ROS formation. For this, *in vitro* levels of mitochondrial ROS were quantified using the MitoSOX assay on HepG2 cells after exposure to doxorubicin.

This approach is the first of its kind. It proves that using thermodynamic and chemistry based methods, combined with experimental data, can facilitate *in silico* prediction of cellular organelle-specific doxorubicin induced ROS formation. This methodology opens the door for investigation of any compound that contains the quinone motif, with respect to redox cycling-induced mitochondrial ROS formation, given a single reduction potential or pKa value, coupled with the extracellular flux analysis. This is exciting, as the redox cycling of compounds old and new may now be investigated with this approach. Furthermore, thermodynamic and physicochemical properties of structurally similar motifs such as quinoneimines or 8-aminoquinolines, used predominantly to treat malaria, could be consolidated into a similar mathematical framework, allowing potential redox cycling-induced toxicity to be explored. This would have high clinical relevance, as redox cycling associated toxicity of these compound classes are known to prevent effective treatment of malaria in the third world.

Chapter 3 investigated the role of a lactate/H⁺ efflux as the predominant driving force of extracellular acidification rate (ECAR) during *in vitro* extracellular flux analysis (EFA), using a novel mathematical model of hepatic bioenergetics, which is pH-dependent with respect to reaction equilibria and enzyme kinetics. *In silico* ECAR was

modelled using the liver-specific monocarboxylate transporter 1 (MCT1) flux; recognising that lactic acid exists as its lactate anion and a proton at physiological pH. Glycolytic proton production rate (PPR_{gly}) was separated from *in vitro* ECAR measurements by accounting for the EFA media buffering power, followed by deducting calculated respiratory contributions to acidification. The model was validated with *in vitro* HepG2 cell EFA data and used to analyse PPR_{gly} as a function of MCT1 flux. Comprehensive computational models such as this require care when parametrizing and as such, sensitivity analysis revealed the most sensitive model parameters, with MCT1 transporter constants K_{eq} and V_{max} ranked as the two most sensitive parameters within the model. The validated model accurately simulated *in vitro* hepatic PPR_{gly} , eliciting lactate/ H^+ efflux via the MCT1 as a suitable driver of glycolytic rate. Further model predictions were used to explore the effects of *in vitro* media changes on glycolytic rate, highlighting that changes in extracellular concentrations of lactate and differences between the transient EFA microchamber and cell volumes result in large perturbations of PPR_{gly} and ECAR. The model emphasises the importance of separating PPR_{gly} from ECAR when scrutinizing *in vitro* EFA data quantitatively, especially when used to explore potential drug induced bioenergetic toxicity, due to ECAR also being a function of respiratory acidification.

This thermodynamically-driven pH-dependent model of hepatic glycolytic flux is the only model current that is coupled with EFA which can simulate glycolytic extracellular acidification. This is exciting because it offers a mathematical platform from which potential mechanistic insights can be obtained from often underutilized *in vitro* ECAR measurements. For example, the model could now be applied to investigate enzyme inhibition of glycolytic enzymes in anti-cancer therapy, since tumour cells are largely dependent on glycolysis for their energy requirements.

Chapter 4 describes the construction of a thermodynamic-based mitochondrial respiration model, used to simulate the *in vitro* primary human hepatocyte oxygen consumption rate (OCR) from mitochondrial stress test data. The experimental data was converted to a novel three-point reduced representation of the percentage

changes of OCR as a function to exposure to oligomycin, FCCP, rotenone and antimycin A. The model was able to recapitulate the data by mimicking the relevant mechanistic pharmacological perturbations. Oligomycin, rotenone and antimycin A exposure was simulated by inhibiting electron transport chain complexes V, I and III, while FCCP exposure was modelled by uncoupling model oxidative phosphorylation from the proton motive force and removing the proton gradient between mitochondrial membranes. The *in vitro* experimental OCR data and the model parameter changes required to simulate each patient was compared using statistical analysis in order to determine if either were capable of predicting each individual's glycolytic reserve capacity. This is founded by the hypothesis that patients with a higher glycolytic reserve capacity would be better able to mitigate mitochondrial compromise. Each patient was assigned a low, moderate or high reserve glycolytic capacity. Principal component analysis revealed no obvious visual correlations between the *in vitro* and *in silico* predictors. This was confirmed with the use of multinomial logistic regression, which showed no significant quantitative relationship. No significant result was yielded for the *in vitro* % OCR changes, nor the *in silico* parameter changes for predicting the glycolytic reserve capacity, suggesting no significant link between a patients glycolytic reserve capacity and their ability to mediate mitochondrial dysfunction. Finally, the model was used to investigate how perturbations in important bioenergetic variables and transporter fluxes effect experimentally measurable outputs. Namely, how changes in matrix NADH, cytoplasmic pyruvate and electron transport chain complexes I and III effect mitochondrial pH, $\Delta\Psi_m$ and OCR. Simulations show that pH, $\Delta\Psi_m$ and OCR are more sensitive to complex III than complex I, suggesting that, when investigating mitochondrial toxicity using the classic mitochondrial stress test, more mechanistic insight could be gained if complex I and III were sequentially inhibited, rather than simultaneously. It was also found that model pH, $\Delta\Psi_m$ and OCR are most sensitive to changes in matrix NADH concentration, suggesting that depletion of NADH during oxidative stress may have significant effects on cellular bioenergetics. Finally, pH, $\Delta\Psi_m$ and OCR were found to be relatively insensitive to changes in cytoplasmic

pyruvate, until a concentration-drop below a 5.2×10^{-6} M threshold. Pyruvate is a tricarboxylic acid cycle precursor that effectively links glycolytic and respiratory energy production and such a lack of sensitivity could suggest that pyruvate is relatively free to be utilised in other biological situations.

Now that the bioenergetic model has been validated, there is opportunity for it to be applied to mitochondrial toxicity testing, especially towards the reduction of the use of animal models. Integrated *in vitro* – *in silico* frameworks offer a unique approach for the investigation of bioenergetic toxicity mechanisms, especially through the use of thermodynamic-driven mechanistic models. Models such as these are able to easily investigate experimentally challenging concepts such as redox cycling toxicity, ROS formation and drug-induced perturbations in cellular bioenergetics, but only when combined with robust experimental data. As such, extracellular flux analysis provides a sturdy platform from which thermodynamic based changes in pH and oxygen concentration may be ascertained *in vitro*, and then coupled with *in silico* models for quantitative predictions. Therefore, taking a combined *in vitro* – *in silico* quantitative systems pharmacology approach augments and ameliorates both mathematical and experimental disciplines to be greater than what they would be alone.

6 Chapter 6: Abbreviations

Abbreviation	Definition
ROS	Reactive oxygen species
QSP	Quantitative systems pharmacology
[R]/[O]	Reduced / oxidised
EDG	Electron donating group
EWG	Electron withdrawing group
Q	Quinone
SQ ^{•-}	Semi quinone radical
H ₂ Q	Hydroquinone
O ₂ ^{•-}	Superoxide anion radical
GSH	Glutathione (reduced)
RNS	Reactive nitrogen species
GSSG	Glutathione disulfide (oxidised)
NADH	Nicotinamide adenine dinucleotide (reduced)
NADPH	Nicotinamide adenine dinucleotide phosphate (reduced)
NAD	Nicotinamide adenine dinucleotide (oxidised)
NADP	Nicotinamide adenine dinucleotide phosphate (oxidised)
PN	Pyridine nucleotide
•OH	Hydroxyl radical
MtDNA	Mitochondrial DNA
ΔS	Entropy
ΔG	Gibbs free energy
ΔH	Enthalpy
ATP	Adenosine triphosphate
ADP	Adenosine diphosphate
Pi	Inorganic phosphate
OXPHOS	Oxidative phosphorylation
TCA	Tricarboxylic acid cycle
ETC	Electron transport chain
ΔΨ _m	Mitochondrial membrane potential
FADH ₂	Flavin adenine dinucleotide
CYP	Cytochrome
BISEN	Biochemical Simulation Environment
EFA	Extracellular flux analysis
OCR	Oxygen consumption rate
ECAR	Extracellular acidification rate
PPR	Proton production rate
MitoSOX	Mitochondrial superoxide
UQ	Uncertainty quantification
SFEM	Stochastic finite elements analysis
RBO	reliability-based optimisation
LHS	Latin hypercube sampling

Abbreviation	Definition
PCA	Principal component analysis
MLR	Multinomial logistic regression
MCT1	Monocarboxylate transporter 1
SOD	Superoxide dismutase
PTQM	Physicochemical thermodynamic quinone model
GUI	Graphical user interface
Q-GSH	Quinone-glutathione adduct
BP	Buffering Power
HGP	Hepatic glucose production
HGU	Hepatic glucose utilisation
BC	Buffering capacity
glu/gal	Glucose / galactose
DILI	Drug-induced liver injury
DIMT	Drug-induced mitochondrial toxicity
NMr	non-mitochondrial respiration
tcmV	transient microchamber volume
AMA	Antimycin-A
FCCP	carbonylcyanide <i>p</i> -trifluoromethoxyphenylhydrazone
Complex V	F ₀ F ₁ -ATP synthase
IM	Mitochondrial inter-membrane space

7 Chapter 7: Appendix

7.1 Appendix A

Appendix A has the statistical analysis results for the EFA *in vitro* data described in 2.3.1.3. Significant changes between extracellular glucose concentrations were determined using Prism software as described in the methods section. One-way analysis of variance was determined using a one-way ANOVA with a Newman-Keuls Multiple comparison test to determine significance between all concentrations of glucose.

ECAR analysis

Table Analyzed	ECAR Normalized			
One-way analysis of variance				
P value	P<0.0001			
P value summary	***			
Are means signif. different? (P < 0.05)	Yes			
Number of groups	10			
F	384.2			
R squared	0.9665			
Bartlett's test for equal variances				
Bartlett's statistic (corrected)	5.51			
P value	0.7877			
P value summary	ns			
Do the variances differ signif. (P < 0.05)	No			
ANOVA Table	SS	df	MS	
Treatment (between columns)	2.287	9	0.2541	
Residual (within columns)	0.07937	120	0.000661	
Total	2.366	129		
Newman-Keuls Comparison Test	Multiple	Mean Diff.	q	Significant? P < 0.001? Summary
		234		

0 vs 5.0	-0.5022	70.4	Yes	***
		50.0		
0 vs 12.5	-0.3569	4	Yes	***
		48.7		
0 vs 15.0	-0.3478	6	Yes	***
		47.7		
0 vs 25.0	-0.3404	2	Yes	***
		43.9		
0 vs 10.0	-0.3137	8	Yes	***
		39.6		
0 vs 2.5	-0.2827	3	Yes	***
		34.2		
0 vs 7.5	-0.2442	3	Yes	***
		29.3		
0 vs 1	-0.2095	8	Yes	***
		16.0		
0 vs 0.1	-0.1145	5	Yes	***
		54.3		
0.1 vs 5.0	-0.3877	5	Yes	***
		33.9		
0.1 vs 12.5	-0.2425	9	Yes	***
		32.7		
0.1 vs 15.0	-0.2333	1	Yes	***
		31.6		
0.1 vs 25.0	-0.2259	7	Yes	***
		27.9		
0.1 vs 10.0	-0.1992	3	Yes	***
		23.5		
0.1 vs 2.5	-0.1682	9	Yes	***
		18.1		
0.1 vs 7.5	-0.1297	8	Yes	***
		13.3		
0.1 vs 1	-0.09508	3	Yes	***
		41.0		
1 vs 5.0	-0.2926	2	Yes	***
		20.6		
1 vs 12.5	-0.1474	6	Yes	***
		19.3		
1 vs 15.0	-0.1382	8	Yes	***
		18.3		
1 vs 25.0	-0.1308	4	Yes	***
		14.6		
1 vs 10.0	-0.1042	14.6	Yes	***
		10.2		
1 vs 2.5	-0.07315	6	Yes	***
		4.85		
1 vs 7.5	-0.03462	3	Yes	***
		36.1		
7.5 vs 5.0	-0.258	7	Yes	***
		15.8		
7.5 vs 12.5	-0.1128	1	Yes	***
		14.5		
7.5 vs 15.0	-0.1036	3	Yes	***
		13.4		
7.5 vs 25.0	-0.09623	9	Yes	***
		9.74		
7.5 vs 10.0	-0.06954	9	Yes	***

7.5 vs 2.5	-0.03854	5.40 3	Yes	***
2.5 vs 5.0	-0.2195	30.7 7	Yes	***
2.5 vs 12.5	-0.07423	10.4 1	Yes	***
2.5 vs 15.0	-0.06508	9.12 4	Yes	***
2.5 vs 25.0	-0.05769	8.08 8	Yes	***
2.5 vs 10.0	-0.031	4.34 6	No	**
10.0 vs 5.0	-0.1885	26.4 2	Yes	***
10.0 vs 12.5	-0.04323	6.06 1	Yes	***
10.0 vs 15.0	-0.03408	4.77 7	No	**
10.0 vs 25.0	-0.02669	3.74 2	No	**
25.0 vs 5.0	-0.1618	22.6 8	Yes	***
25.0 vs 12.5	-0.01654	2.31 9	No	ns
25.0 vs 15.0	-0.00739	--- 21.6	No	ns
15.0 vs 5.0	-0.1544	4	Yes	***
15.0 vs 12.5	-0.00915	--- 20.3	No	ns
12.5 vs 5.0	-0.1452	6	Yes	***

Table A1: Statistical analysis of *in vitro* EFA using different concentrations of glucose. Significance between average ECAR normalised to basal ECAR and protein content are shown, with P -values $< 0.05 = *$, P -values $< 0.01 = **$ and P -values $< 0.001 = ***$.

All concentrations of extracellular glucose were significant when compared to the control where the extracellular concentration of glucose is equal to zero (Figure A1).

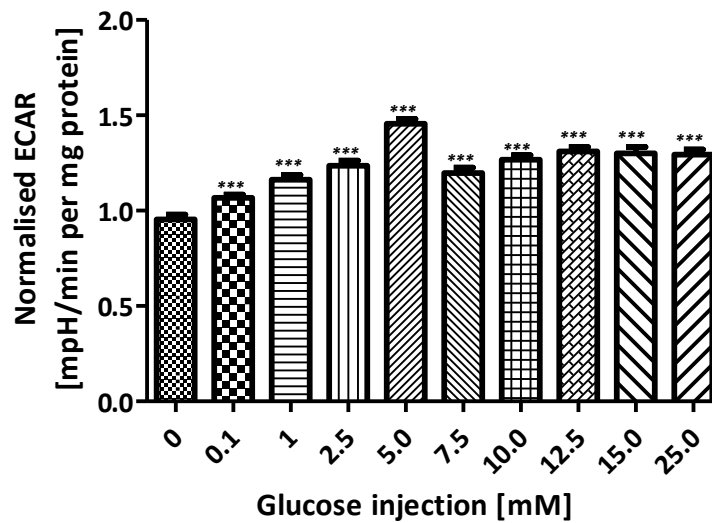


Figure A1: Statistical analysis of *in vitro* EFA ECAR using different concentrations of glucose showing all concentrations used above zero were significant. P -values < 0.001 = ***.

OCR analysis

Table Analyzed	OCR Normalized
One-way analysis of variance	
P value	P<0.000
P value summary	1
Are means signif. different? (P < 0.05)	***
Number of groups	Yes
F	10
R squared	15.88
	0.5436
Bartlett's test for equal variances	
Bartlett's statistic (corrected)	6.709
P value	0.6674
P value summary	ns
Do the variances differ signif. (P < 0.05)	No

ANOVA Table		SS	df	MS	
Treatment (between columns)		0.1026	9	0.0114	
Residual (within columns)		0.08615	120	0.000718	
Total		0.1887	129		
Newman-Keuls Comparison Test	Multiple	Mean Diff.	q	Significant? P < 0.001?	Summary
			12.0		
25.0 vs 0		-0.08932	2	Yes	***
			8.90		
25.0 vs 0.1		-0.06621	9	Yes	***
			8.66		
25.0 vs 1		-0.06442	9	Yes	***
			5.88		
25.0 vs 2.5		-0.04373	5	No	**
			3.90		
25.0 vs 5.0		-0.02905	9	No	ns
25.0 vs 12.5		-0.02263	---	No	ns
25.0 vs 15.0		-0.01409	---	No	ns
25.0 vs 10.0		-0.01156	---	No	ns
25.0 vs 7.5		-0.01	---	No	ns
			10.6		
7.5 vs 0		-0.07932	7	Yes	***
			7.56		
7.5 vs 0.1		-0.05621	3	Yes	***
			7.32		
7.5 vs 1		-0.05442	3	Yes	***
			4.53		
7.5 vs 2.5		-0.03373	9	No	*
7.5 vs 5.0		-0.01905	---	No	ns
7.5 vs 12.5		-0.01263	---	No	ns
7.5 vs 15.0		-0.00409	---	No	ns
7.5 vs 10.0		-0.00156	---	No	ns
			10.4		
10.0 vs 0		-0.07776	6	Yes	***
			7.35		
10.0 vs 0.1		-0.05464	3	Yes	***
			7.11		
10.0 vs 1		-0.05286	3	Yes	***
			4.32		
10.0 vs 2.5		-0.03217	9	No	*
10.0 vs 5.0		-0.01749	---	No	ns
10.0 vs 12.5		-0.01106	---	No	ns
10.0 vs 15.0		-0.00253	---	No	ns
			10.1		
15.0 vs 0		-0.07523	2	Yes	***
			7.01		
15.0 vs 0.1		-0.05212	4	Yes	***
			6.77		
15.0 vs 1		-0.05033	3	Yes	***
			3.98		
15.0 vs 2.5		-0.02964	9	No	*

15.0 vs 5.0	-0.01496	---	No	ns
15.0 vs 12.5	-0.00854	---	No	ns
		8.97		
12.5 vs 0	-0.06669	5	Yes	***
		5.86		
12.5 vs 0.1	-0.04358	4	Yes	***
		5.62		
12.5 vs 1	-0.04179	4	Yes	***
12.5 vs 2.5	-0.0211	2.84	No	ns
12.5 vs 5.0	-0.00642	---	No	ns
		8.11		
5.0 vs 0	-0.06027	1	Yes	***
5.0 vs 0.1	-0.03716	5	No	**
5.0 vs 1	-0.03537	4.76	No	**
5.0 vs 2.5	-0.01468	---	No	ns
		6.13		
2.5 vs 0	-0.04559	5	Yes	***
		3.02		
2.5 vs 0.1	-0.02248	5	No	ns
2.5 vs 1	-0.02069	---	No	ns
		3.35		
1 vs 0	-0.0249	1	No	ns
1 vs 0.1	-0.00179	---	No	ns
0.1 vs 0	-0.02311	---	No	ns

Table A2: Statistical analysis of *in vitro* EFA using different concentrations of glucose. Significance between average OCR normalised to basal OCR and protein content are shown, with P -values $< 0.05 = *$, P -values $< 0.01 = **$ and P -values $< 0.001 = ***$.

Significance between 0 mM and all other concentrations of extracellular glucose is shown in Figure A2.

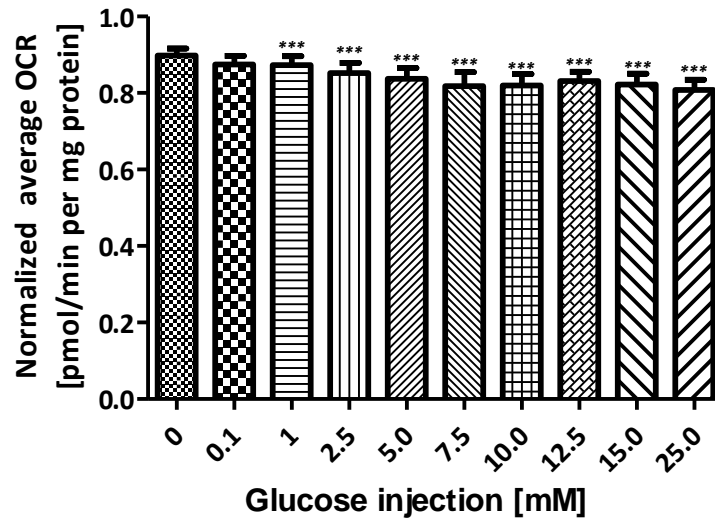


Figure A2 Statistical analysis of *in vitro* EFA OCR using different concentrations of glucose showing all concentrations used above zero were significant. P -values < 0.001 = ***.

8 Chapter 8: Bibliography

1. Rana, P., Naven, R., Narayanan, A., Will, Y. & Jones, L. H. Chemical motifs that redox cycle and their associated toxicity. *Medchemcomm* **4**, 1175–1180 (2013).
2. Silveira-Dorta, G. *et al.* Oxidation with air by ascorbate-driven quinone redox cycling. *Chem. Commun.* **51**, 7027–7030 (2015).
3. Bolton, J. L., Trush, M. A., Penning, T. M., Dryhurst, G. & Monks, T. J. Role of quinones in toxicology. *Chem. Res. Toxicol.* **13**, 135–160 (2000).
4. Krueger, F. R., Werther, W., Kissel, J. & Schmid, E. R. Assignment of quinone derivatives as the main compound class composing ‘interstellar’ grains based on both polarity ions detected by the ‘Cometary and Interstellar Dust Analyser’ (CIDA) onboard the spacecraft STARDUST. *Rapid Commun. Mass Spectrom.* **18**, 103–111 (2004).
5. Wang, Y. & Hekimi, S. Molecular Genetics of Ubiquinone Biosynthesis in Animals. *Crit. Rev. Biochem. Mol. Biol.* **48**, 69–88 (2013).
6. Fourie, J. *et al.* The effect of functional groups on reduction and activation of quinone bio-reductive agents by DT-diaphorase. *Cancer Chemother. Pharmacol.* **49**, 101–110 (2002).
7. Song, Y. & Buettner, G. R. Thermodynamic and kinetic considerations for the reaction of semiquinone radicals to form superoxide and hydrogen peroxide. *Free Radic. Biol. Med.* **49**, 919–962 (2010).
8. dos Santos, E. V. M., Carneiro, J. W. de M. & Ferreira, V. F. Quantitative structure-activity relationship in aziridiny-1,4-naphthoquinone antimalarials: study of theoretical correlations by the PM3 method. *Bioorg. Med. Chem.* **12**, 87–93 (2004).

9. Ehrhardt, K. *et al.* The Antimalarial Activities of Methylene Blue and the 1,4-Naphthoquinone 3-[4-(Trifluoromethyl)Benzyl]-Menadione Are Not Due to Inhibition of the Mitochondrial Electron Transport Chain. *Antimicrob. Agents Chemother.* **57**, 2114–2120 (2013).
10. Stepan, A. F. *et al.* Structural alert/reactive metabolite concept as applied in medicinal chemistry to mitigate the risk of idiosyncratic drug toxicity: a perspective based on the critical examination of trends in the top 200 drugs marketed in the United States. *Chem. Res. Toxicol.* **24**, 1345–1410 (2011).
11. Adam, A., Smith, L. L. & Cohen, G. M. An assessment of the role of redox cycling in mediating the toxicity of paraquat and nitrofurantoin. *Environ. Health Perspect.* **85**, 113–117 (1990).
12. Wijeratne, S. S. K., Cuppett, S. L. & Schlegel, V. Hydrogen peroxide induced oxidative stress damage and antioxidant enzyme response in Caco-2 human colon cells. *J. Agric. Food Chem.* **53**, 8768–8774 (2005).
13. Bonilla, I. M. *et al.* Differential effects of the peroxynitrite donor, SIN-1, on atrial and ventricular myocyte electrophysiology. *J. Cardiovasc. Pharmacol.* **61**, 401–407 (2013).
14. Auten, R. L. & Davis, J. M. Oxygen toxicity and reactive oxygen species: the devil is in the details. *Pediatr. Res.* **66**, 121–127 (2009).
15. Deavall, D. G., Martin, E. A., Horner, J. M. & Roberts, R. Drug-Induced Oxidative Stress and Toxicity. *J. Toxicol.* **2012**, 1–13 (2012).
16. Gewirtz, D. A critical evaluation of the mechanisms of action proposed for the antitumor effects of the anthracycline antibiotics adriamycin and daunorubicin. *Biochem. Pharmacol.* **57**, 727–741 (1999).
17. Davies, K. J. A. & Doroshow, J. H. Redox cycling of anthracyclines by cardiac mitochondria. I. Anthracycline radical formation by NADH dehydrogenase. *J.*

- Biol. Chem.* **261**, 3060–3067 (1986).
18. Šimůnek, T. *et al.* Anthracycline-induced cardiotoxicity: Overview of studies examining the roles of oxidative stress and free cellular iron. *Pharmacol. Reports* **61**, 154–171 (2009).
 19. Goormaghtigh, E., Chatelain, P., Caspers, J. & Ruyschaert, J. M. Evidence of a specific complex between adriamycin and negatively-charged phospholipids. *BBA - Biomembr.* **597**, 1–14 (1980).
 20. Pereira, G. C. *et al.* Drug-induced cardiac mitochondrial toxicity and protection: From doxorubicin to carvedilol. *Curr. Pharm. Des.* **17**, 2113–2129 (2011).
 21. Angsutararux, P., Luanpitpong, S. & Issaragrisil, S. Chemotherapy-Induced Cardiotoxicity: Overview of the Roles of Oxidative Stress. *Oxid. Med. Cell. Longev.* **2015**, 795602 (2015).
 22. Madeira, V. M. C. Overview of mitochondrial bioenergetics. *Methods Mol. Biol.* **810**, 1–6 (2012).
 23. Circu, M. L. & Aw, T. Y. REACTIVE OXYGEN SPECIES, CELLULAR REDOX SYSTEMS AND APOPTOSIS. *Free Radic. Biol. Med.* **48**, 749–762 (2010).
 24. Li, N. *et al.* Mitochondrial complex I inhibitor rotenone induces apoptosis through enhancing mitochondrial reactive oxygen species production. *J. Biol. Chem.* **278**, 8516–8525 (2003).
 25. Jones, D. P. Redox potential of GSH/GSSG couple: Assay and biological significance. *Methods in Enzymology* **348**, 93–112 (2002).
 26. Lushchak, V. I. Glutathione Homeostasis and Functions: Potential Targets for Medical Interventions. *J. Amino Acids* **2012**, 1–26 (2012).
 27. Ray, P. D., Huang, B.-W. & Tsuji, Y. Reactive oxygen species (ROS) homeostasis and redox regulation in cellular signaling. *Cell. Signal.* **24**, 981–990 (2012).

28. Gruber, J., Schaffer, S. & Halliwell, B. The mitochondrial free radical theory of ageing--where do we stand? *Front. Biosci.* **13**, 6554–6579 (2008).
29. Orrenius, S. Reactive oxygen species in mitochondria-mediated cell death. *Drug Metab. Rev.* **39**, 443–455 (2007).
30. Starkov, A. A. *et al.* Mitochondrial alpha-ketoglutarate dehydrogenase complex generates reactive oxygen species. *J. Neurosci.* **24**, 7779–7788 (2004).
31. Beard, D. A. & Qian, H. *Chemical Biophysics: Quantitative Analysis of Cellular Systems. Cambridge Texts in Biomedical Engineering* (Cambridge University Press, 2008). doi:DOI: 10.1017/CBO9780511803345
32. Bratic, I. & Trifunovic, A. Mitochondrial energy metabolism and ageing. *Biochim. Biophys. Acta - Bioenerg.* **1797**, 961–967 (2010).
33. Jonckheere, A. I., Smeitink, J. A. M. & Rodenburg, R. J. T. Mitochondrial ATP synthase: architecture, function and pathology. *J. Inherit. Metab. Dis.* **35**, 211–225 (2012).
34. Gaskell, H. *et al.* Characterization of a functional C3A liver spheroid model †Electronic supplementary information (ESI) available. See DOI: 10.1039/c6tx00101g Click here for additional data file. . *Toxicol. Res. (Camb)*. **5**, 1053–1065 (2016).
35. Diaz-Ruiz, R., Uribe-Carvajal, S., Devin, A. & Rigoulet, M. Tumor cell energy metabolism and its common features with yeast metabolism. *Biochim Biophys Acta* **1796**, 252–265 (2009).
36. Vander Heiden, M. G., Cantley, L. C. & Thompson, C. B. Understanding the Warburg Effect: The Metabolic Requirements of Cell Proliferation. *Science* **324**, 1029–1033 (2009).
37. Vanlier, J. *et al.* BISEN: Biochemical Simulation Environment. *Bioinformatics* **25**,

- 836–837 (2009).
38. Daniel. A. Beard, H. Q. *Chemical Biophysics*. (Chambridge Texts, 2008).
 39. Vinnakota, K., Kemp, M. L. & Kushmerick, M. J. Dynamics of Muscle Glycogenolysis Modeled with pH Time Course Computation and pH-Dependent Reaction Equilibria and Enzyme Kinetics. *Biophys. J.* **91**, 1264–1287 (2017).
 40. Vinnakota, K., Kemp, M. L. & Kushmerick, M. J. Dynamics of Muscle Glycogenolysis Modeled with pH Time Course Computation and pH-Dependent Reaction Equilibria and Enzyme Kinetics. *Biophys. J.* **91**, 1264–1287 (2006).
 41. Mookerjee, S. A. & Brand, M. D. Measurement and Analysis of Extracellular Acid Production to Determine Glycolytic Rate. *J. Vis. Exp.* 53464 (2015). doi:10.3791/53464
 42. Mookerjee, S. A., Goncalves, R. L. S., Gerencser, A. A., Nicholls, D. G. & Brand, M. D. The contributions of respiration and glycolysis to extracellular acid production. *Biochim. Biophys. Acta* **1847**, 171–181 (2015).
 43. Kamalian, L. *et al.* The utility of HepG2 cells to identify direct mitochondrial dysfunction in the absence of cell death. *Toxicol. Vitr.* **29**, 732–740 (2015).
 44. Brand, M. D. & Nicholls, D. G. Assessing mitochondrial dysfunction in cells. *Biochem. J.* **435**, 297–312 (2011).
 45. Wu, M. *et al.* Multiparameter metabolic analysis reveals a close link between attenuated mitochondrial bioenergetic function and enhanced glycolysis dependency in human tumor cells. *Am. J. Physiol. Cell Physiol.* **292**, C125-36 (2007).
 46. Mukhopadhyay, P., Rajesh, M., Yoshihiro, K., Haskó, G. & Pacher, P. Simple

- quantitative detection of mitochondrial superoxide production in live cells. *Biochem. Biophys. Res. Commun.* **358**, 203–208 (2007).
47. Riss, T. L. *et al.* Cell Viability Assays. in (eds. Sittampalam, G. S. *et al.*) (2004).
 48. Patelli, E. COSSAN: A Multidisciplinary Software Suite for Uncertainty Quantification and Risk Management. in *Handbook of Uncertainty Quantification* (eds. Ghanem, R., Higdon, D. & Owhadi, H.) 1–69 (Springer International Publishing, 2016). doi:10.1007/978-3-319-11259-6_59-1
 49. Koppenol, W. H., Stanbury, D. M. & Bounds, P. L. Electrode potentials of partially reduced oxygen species, from dioxygen to water. *Free Radic. Biol. Med.* **49**, 317–322 (2010).
 50. Svingen, B. A. & Powis, G. Pulse radiolysis studies of antitumor quinones: Radical lifetimes, reactivity with oxygen, and one-electron reduction potentials. *Arch. Biochem. Biophys.* **209**, 119–126 (1981).
 51. Lagarias, J., Reeds, J., Wright, M. & Wright, P. Convergence Properties of the Nelder–Mead Simplex Method in Low Dimensions. *SIAM J. Optim.* **9**, 112–147 (1998).
 52. Kembro, J. M., Aon, M. A., Winslow, R. L., O'Rourke, B. & Cortassa, S. Integrating mitochondrial energetics, redox and ROS metabolic networks: a two-compartment model. *Biophys. J.* **104**, 332–343 (2013).
 53. Bazil, J. N., Beard, D. A. & Vinnakota, K. C. Catalytic Coupling of Oxidative Phosphorylation, ATP Demand, and Reactive Oxygen Species Generation. *Biophys. J.* **110**, 962–971 (2016).
 54. Cohen, G. M. & d'Arcy Doherty, M. Free radical mediated cell toxicity by redox cycling chemicals. *Br. J. Cancer. Suppl.* **8**, 46–52 (1987).
 55. Fukai, T. & Ushio-Fukai, M. Superoxide dismutases: role in redox signaling,

- vascular function, and diseases. *Antioxid. Redox Signal.* **15**, 1583–1606 (2011).
56. Davies, K. J. A., Doroshov, J. H. & Hochstein, P. Mitochondrial NADH dehydrogenase-catalyzed oxygen radical production by adriamycin, and the relative inactivity of 5-iminodaunorubicin. *FEBS Lett.* **153**, 227–230 (1983).
 57. Sauerbeck, A. *et al.* Analysis of regional brain mitochondrial bioenergetics and susceptibility to mitochondrial inhibition utilizing a microplate based system. *J. Neurosci. Methods* **198**, 36–43 (2011).
 58. Beeson, C. C., Beeson, G. C. & Schnellmann, R. G. A high-throughput respirometric assay for mitochondrial biogenesis and toxicity. *Anal. Biochem.* **404**, 75–81 (2010).
 59. Coordinators, N. R. *et al.* Database resources of the National Center for Biotechnology Information. *Nucleic Acids Res.* **42**, D7–D17 (2014).
 60. Gille, C. *et al.* HepatoNet1: a comprehensive metabolic reconstruction of the human hepatocyte for the analysis of liver physiology. *Mol. Syst. Biol.* **6**, 411 (2010).
 61. Konig, M., Bulik, S. & Holzhutter, H.-G. Quantifying the contribution of the liver to glucose homeostasis: a detailed kinetic model of human hepatic glucose metabolism. *PLoS Comput. Biol.* **8**, e1002577 (2012).
 62. Yang, Y. *et al.* MITOsym®: A Mechanistic, Mathematical Model of Hepatocellular Respiration and Bioenergetics. *Pharm. Res.* **32**, 1975–1992 (2015).
 63. Halestrap, A. P. & Wilson, M. C. The monocarboxylate transporter family--role and regulation. *IUBMB Life* **64**, 109–119 (2012).
 64. Bionumbers. Diameter of HepG2/C3A (Liver) Cell. (2013).
 65. Overmoyer, B. A., McLaren, C. E. & Brittenham, G. M. Uniformity of liver

- density and nonheme (storage) iron distribution. *Arch. Pathol. Lab. Med.* **111**, 549–554 (1987).
66. Technologies, A. Transient Microchamber Video. (2016). Available at: [https://www.agilent.com/en-us/products/cell-analysis-\(seahorse\)/transient-microchamber](https://www.agilent.com/en-us/products/cell-analysis-(seahorse)/transient-microchamber).
 67. Diaz-Ruiz, R., Rigoulet, M. & Devin, A. The Warburg and Crabtree effects: On the origin of cancer cell energy metabolism and of yeast glucose repression. *Biochim. Biophys. Acta* **1807**, 568–576 (2011).
 68. Mookerjee, S. A. & Brand, M. D. Measurement and Analysis of Extracellular Acid Production to Determine Glycolytic Rate. *J Vis Exp* 53464 (2015). doi:10.3791/53464
 69. Liu, A. M. *et al.* miR-122 targets pyruvate kinase M2 and affects metabolism of hepatocellular carcinoma. *PLoS One* **9**, e86872 (2014).
 70. Kato, Y. *et al.* Acidic extracellular microenvironment and cancer. *Cancer Cell Int.* **13**, 89 (2013).
 71. Abrahams, M., Eriksson, H., Björnström, K. & Eintrei, C. Effects of propofol on extracellular acidification rates in primary cortical cell cultures: application of silicon microphysiometry to anaesthesia. *BJA Br. J. Anaesth.* **83**, 467–469 (1999).
 72. Dietl, K. *et al.* Lactic acid and acidification inhibit TNF secretion and glycolysis of human monocytes. *J. Immunol.* **184**, 1200–1209 (2010).
 73. Nuttall, F. Q., Ngo, A. & Gannon, M. C. Regulation of hepatic glucose production and the role of gluconeogenesis in humans: is the rate of gluconeogenesis constant? *Diabetes. Metab. Res. Rev.* **24**, 438–458 (2008).
 74. Radziuk, J. & Pye, S. Hepatic glucose uptake, gluconeogenesis and the

- regulation of glycogen synthesis. *Diabetes. Metab. Res. Rev.* **17**, 250–272 (2001).
75. Cryer, P. E. Glucose counterregulation: prevention and correction of hypoglycemia in humans. *Am. J. Physiol.* **264**, E149-55 (1993).
 76. Feher, J. 2.10 - ATP Production II: The TCA Cycle and Oxidative Phosphorylation BT - Quantitative Human Physiology. in 180–190 (Academic Press, 2012). doi:<https://doi.org/10.1016/B978-0-12-382163-8.00021-9>
 77. Feher, J. 2.9 - ATP Production I: Glycolysis. in *Quantitative Human Physiology* 171–179 (Academic Press, 2012). doi:<http://doi.org/10.1016/B978-0-12-382163-8.00020-7>
 78. Jackson, V. N. & Halestrap, A. P. The kinetics, substrate, and inhibitor specificity of the monocarboxylate (lactate) transporter of rat liver cells determined using the fluorescent intracellular pH indicator, 2',7'-bis(carboxyethyl)-5(6)-carboxyfluorescein. *J. Biol. Chem.* **271**, 861–868 (1996).
 79. Okamoto, T. *et al.* Establishment and characterization of a novel method for evaluating gluconeogenesis using hepatic cell lines, H4IIE and HepG2. *Arch. Biochem. Biophys.* **491**, 46–52 (2009).
 80. Aleo, M. D. *et al.* Human drug-induced liver injury severity is highly associated with dual inhibition of liver mitochondrial function and bile salt export pump. *Hepatology* **60**, 1015–1022 (2014).
 81. Luo, G., Shen, Y., Yang, L., Lu, A. & Xiang, Z. A review of drug-induced liver injury databases. *Arch. Toxicol.* **91**, 3039–3049 (2017).
 82. Marroquin, L. D., Hynes, J., Dykens, J. A., Jamieson, J. D. & Will, Y. Circumventing the Crabtree Effect: Replacing Media Glucose with Galactose Increases Susceptibility of HepG2 Cells to Mitochondrial Toxicants. *Toxicol. Sci.* **97**, 539–547 (2007).

83. Nadanaciva, S. *et al.* Assessment of drug-induced mitochondrial dysfunction via altered cellular respiration and acidification measured in a 96-well platform. *J. Bioenerg. Biomembr.* **44**, 421–437 (2012).
84. Hynes, J. *et al.* Investigation of Drug-Induced Mitochondrial Toxicity Using Fluorescence-Based Oxygen-Sensitive Probes. *Toxicol. Sci.* **92**, 186–200 (2006).
85. Thompson, R. A. *et al.* Risk assessment and mitigation strategies for reactive metabolites in drug discovery and development. *Chem. Biol. Interact.* **192**, 65–71 (2011).
86. Kass, G. E. N. Mitochondrial involvement in drug-induced hepatic injury. *Chem. Biol. Interact.* **163**, 145–159 (2006).
87. Boelsterli, U. A. & Lim, P. L. K. Mitochondrial abnormalities--a link to idiosyncratic drug hepatotoxicity? *Toxicol. Appl. Pharmacol.* **220**, 92–107 (2007).
88. Dykens, J. A. *Drug-Induced Mitochondrial Toxicity*. (Wiley, 2008).
89. Zajtchuk, R. New technologies in medicine: biotechnology and nanotechnology. *Dis. Mon.* **45**, 449–495 (1999).
90. Dykens, J. A. & Will, Y. The significance of mitochondrial toxicity testing in drug development. *Drug Discov. Today* **12**, 777–785 (2007).
91. Beard, D. A. A Biophysical Model of the Mitochondrial Respiratory System and Oxidative Phosphorylation. *PLOS Comput. Biol.* **1**, (2005).
92. Beard, D. A. Modeling of Oxygen Transport and Cellular Energetics Explains Observations on In Vivo Cardiac Energy Metabolism. *PLoS Comput. Biol.* **2**, e107 (2006).
93. Wu, F., Yang, F., Vinnakota, K. C. & Beard, D. A. Computer modeling of mitochondrial tricarboxylic acid cycle, oxidative phosphorylation, metabolite

- transport, and electrophysiology. *J. Biol. Chem.* **282**, 24525–24537 (2007).
94. Beard, D. A., Vinnakota, K. C. & Wu, F. Detailed Enzyme Kinetics in Terms of Biochemical Species: Study of Citrate Synthase. *PLoS One* **3**, e1825 (2008).
 95. Wu, F., Zhang, E. Y., Zhang, J., Bache, R. J. & Beard, D. A. Phosphate metabolite concentrations and ATP hydrolysis potential in normal and ischaemic hearts. *J. Physiol.* **586**, 4193–4208 (2008).
 96. Wu, F., Zhang, J. & Beard, D. A. Experimentally observed phenomena on cardiac energetics in heart failure emerge from simulations of cardiac metabolism. *Proc. Natl. Acad. Sci.* **106**, 7143–7148 (2009).
 97. Vinnakota, K. C., Bazil, J. N., den Bergh, F. Van, Wiseman, R. W. & Beard, D. A. Feedback Regulation and Time Hierarchy of Oxidative Phosphorylation in Cardiac Mitochondria. *Biophys. J.* **110**, 972–980 (2016).
 98. Vanlier, J. *et al.* BISEN: Biochemical Simulation Environment. *Bioinformatics* **25**, 836–837 (2009).
 99. Smith, C. M. & Williamson, J. R. Inhibition of citrate synthase by succinyl-CoA and other metabolites. *FEBS Lett.* **18**, 35–38 (1971).
 100. Kohn, M. C. & Garfinkel, D. Computer simulation of metabolism in palmitate-perfused rat heart. II. Behavior of complete model. *Ann. Biomed. Eng.* **11**, 511–531 (1983).
 101. Bose, S., French, S., Evans, F. J., Joubert, F. & Balaban, R. S. Metabolic network control of oxidative phosphorylation: multiple roles of inorganic phosphate. *J. Biol. Chem.* **278**, 39155–39165 (2003).
 102. JM, B. *Biochemistry*. (2002).
 103. Agilent. How Agilent Seahorse XF Analyzers Work. (2017). Available at: <http://www.agilent.com/en-us/products/cell-analysis->

%28seahorse%29/how-seahorse-xf-analyzers-work (29/09/2017).

104. Agilent. The fundamental parameters of mitochondrial function. (2017). Available at: [http://www.agilent.com/en-us/products/cell-analysis-\(seahorse\)/mitochondrial-respiration-the-xf-cell-mito-stress-test](http://www.agilent.com/en-us/products/cell-analysis-(seahorse)/mitochondrial-respiration-the-xf-cell-mito-stress-test) (29/09/2017).
105. Shchepina, L. A. *et al.* Oligomycin, inhibitor of the F₀ part of H⁺-ATP-synthase, suppresses the TNF-induced apoptosis. *Oncogene* **21**, 8149–8157 (2002).
106. To, M.-S. *et al.* Mitochondrial uncoupler FCCP activates proton conductance but does not block store-operated Ca²⁺ current in liver cells. *Arch. Biochem. Biophys.* **495**, 152–158 (2010).
107. Kenwood, B. M. *et al.* Identification of a novel mitochondrial uncoupler that does not depolarize the plasma membrane(). *Mol. Metab.* **3**, 114–123 (2014).
108. Han, Y. H., Kim, S. H., Kim, S. Z. & Park, W. H. Antimycin A as a mitochondrial electron transport inhibitor prevents the growth of human lung cancer A549 cells. *Oncol. Rep.* **20**, 689–693 (2008).
109. Ai, Q. *et al.* Rotenone, a mitochondrial respiratory complex I inhibitor, ameliorates lipopolysaccharide/D-galactosamine-induced fulminant hepatitis in mice. *Int. Immunopharmacol.* **21**, 200–207 (2014).